ARISTOTLE UNIVERSITY OF THESSALONIKI
SCHOOL OF GEOLOGY
DEPARTMENT OF GEOPHYSICS

ELENI A. TOKMAKTSI
Geologist

GROUND PENETRATING RADAR (GPR) DIRECT WAVE STUDY

MASTER THESIS

POSTGRADUATE STUDIES PROGRAMME 'APPLIED GEOLOGY',
DIRECTION: 'APPLIED GEOPHYSICS & SEISMOLOGY

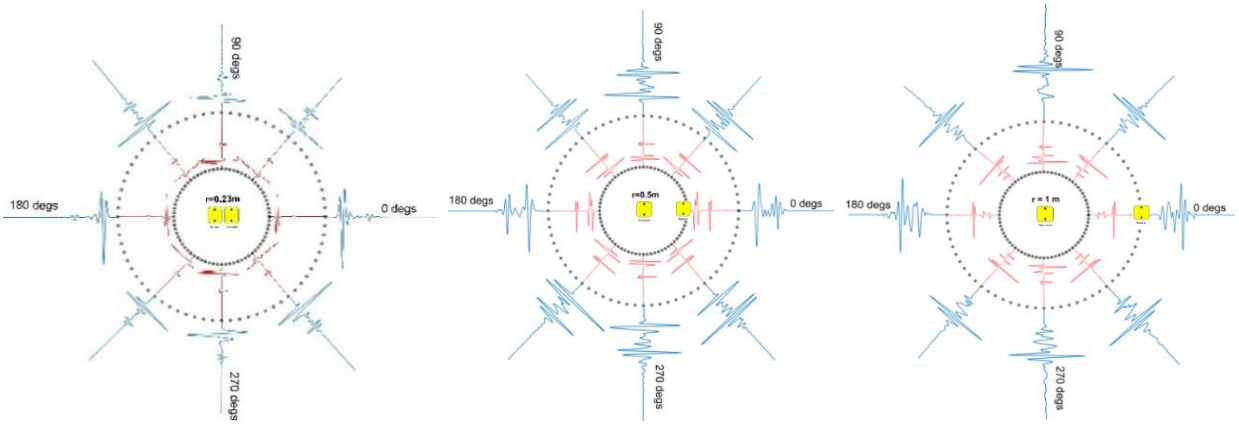

THESSALONIKI
2021

ELENI A. TOKMAKTSI
ΕΛΕΝΗ Α. ΤΟΚΜΑΚΤΣΗ
Πτυχιούχος Γεωλόγος

GROUND PENETRATING RADAR (GPR) DIRECT WAVE STUDY
ΜΕΛΕΤΗ ΤΩΝ ΑΠΕΥΘΕΙΑΣ ΚΥΜΑΤΩΝ ΣΤΗ ΜΕΘΟΔΟ ΤΟΥ ΡΑΝΤΑΡ ΥΠΕΔΑΦΟΥΣ

Υποβλήθηκε στο Τμήμα Γεωλογίας στα πλαίσια του Προγράμματος Μεταπτυχιακών Σπουδών ‘Εφαρμοσμένη Γεωλογία’, Κατεύθυνση ‘Εφαρμοσμένη γεωφυσική και σεισμολογία’

Ημερομηνία Προφορικής Εξέτασης: 20/07/2021
Oral Examination Date: 20/07/2021

Advisory & Examining Board

Dr. Nectaria Diamanti, Aristotle University of Thessaloniki: Supervisor
Associate Professor, Georgios Vargemezis, Aristotle University of Thessaloniki: Board Member
Dr. Antonios Giannopoulos, The University of Edinburgh: Board Member

Τριμελής Συμβουλευτική & Εξεταστική Επιτροπή

Δρ. Νεκταρία Διαμαντή, Ε.ΔΙ.Π. Α.Π.Θ.: Επιβλέπουσα
Αναπληρωτής Καθηγητής, Γεώργιος Βαργεμέζης, Α.Π.Θ.: Μέλος Τριμελούς Επιτροπής
Δρ. Αντώνης Γιαννόπουλος, Πανεπιστήμιο του Εδιμβούργου: Μέλος Τριμελούς Επιτροπής

GROUND PENETRATING RADAR (GPR) DIRECT WAVE STUDY– *Master Thesis*

ΜΕΛΕΤΗ ΤΩΝ ΑΠΕΥΘΕΙΑΣ ΚΥΜΑΤΩΝ ΣΤΗ ΜΕΘΟΔΟ ΤΟΥ ΡΑΝΤΑΡ ΥΠΕΔΑΦΟΥΣ – *Μεταπτυχιακή Διπλωματική Εργασία*

Citation:
Tokmaktsi E. A., 2021. – Ground Penetrating Radar (GPR) Direct wave study. Master Thesis, School of Geology, Department of Geophysics, Aristotle University of Thessaloniki.
Τοκμακτσή Ε. Α., 2021. – Μελέτη των Απευθείας κυμάτων στη μέθοδο του ραντάρ υπεδάφους. Μεταπτυχιακή Διπλωματική Εργασία, Τμήμα Γεωλογίας, Τομέας Γεωφυσικής, Α.Π.Θ.

Cover Figure:……

Contents

Abstract

Ground Penetrating Radar (GPR) is a geophysical method based on the emission and reception of electromagnetic (EM) waves. A transmitting antenna (Tx) is emitting EM signals and a receiving antenna (Rx) is recording these signals' reflections caused by changes in the electrical properties of the subsurface. When the Tx-Rx antenna pair is at near proximity, as it is usually the case during GPR surveys, and the subsurface targets are located at shallow depths, the strong in amplitude direct EM signal recorded by the GPR receiver (i.e., the direct wave – DW) may mask the reflections (reflected wave – RW) coming from the in ground targets.

In this study, the major aim is to examine the spatial distribution of the EM signals around the GPR Tx antenna. Since the recorded signals are mostly dictated by the strong direct wave signal, we have focused on the study of this response, attempting to locate areas around the Tx where the direct wave becomes minimum, while the signal strength of the reflected wave remains ideally unchanged. The location of those local minima in the direct signal may give rise to advantageous Tx-Rx configurations, where a clear reflection can be obtained with the least possible involvement of the direct wave.

To perform such a study, field testing was performed at a site where a mostly horizontal subsurface reflector was located. This was confirmed by carrying out GPR grid measurements and validated using the electrical resistivity tomography (ERT) method. Wide Angle Reflection and Refraction (WARR) measurements were also performed to estimate the average EM wave velocity in the uppermost layer and define more precisely the depth of the subsurface features in the survey area. Having found an almost horizontal layer in the field, both the direct and reflected waves were studied by collecting static GPR data around a circle. This way both the direct and reflected waves were studied in terms of (a) changing the Tx-to-Rx antenna orientation (i.e., broadside and endfire), (b) changing the Tx-to-Rx antenna separation (with varying the circle's radius) and (c) changing the Tx-to-Rx antenna angular position (one antenna was placed at a fixed location in the circle's center while the other was moved radially in fixed angle steps around the first one).

In addition to field testing, numerical modelling was performed to study these three (3) aforementioned factors that are known to impact the EM signal distribution around the GPR transducers. For the numerical modelling work, the GPR antennas were represented either by ideal Hertzian dipoles (point dipoles) or by resistively loaded bare dipoles.

1.Introduction

Ground Penetrating Radar (GPR) is an active, non-invasive geophysical method well known for its high resolution and mostly applied to detect both natural and man-made buried targets at shallow depths. The method is relying on the emission of electromagnetic (EM) pulses into the subsurface. The emitted signal interacts with the in-ground materials, reflected and recorded. From an engineering/hardware point of view, GPR is a system which in its standard form consist of two transducers which convert propagating EM waves to electrical signals, and vice versa. The GPR transducers are the transmitter (Tx) and the receiver (Rx), which transmit and receive the GPR pulses, respectively.

The transmitter, through a transmitting antenna radiates radio waves (in the 10-1500MHz frequency range) which propagate through the earth's subsurface. This propagation is mostly governed by the EM properties of the media that the signal is passing through. The most important physical properties for GPR are the dielectric permittivity, electrical conductivity, and magnetic permeability. These properties are responsible for almost every distortion of the transmitted signals in the way that these undergo transmission, reflection or/and refraction phenomena (these will be described on a following chapter).

The history of the GPR method starts when the German physicist Heinrich Hertz built the first antennas to validate James Clerk Maxwell's electromagnetic theory (Skolnic, 1980). In 1910, Gotthelf Leimbach and Heinrich Löwy submitted the first patent for a system to emit continuous radio waves in order to map the subsurface. The idea of using radio pulses rather than continuous signals was born in 1926 by Dr. Hülsenbeck and a glacier's depth was successfully first measured in 1929 by W.Stern with the use of a GPR system. From 1955 to 1960 researchers focused on applying radio waves to study ice, motivated by altimeter errors that the United States Air Force reported, when inaccurately tried to land an aircraft on Greenland's ice sheet (Waite and Schmidt, 1962). GPR applications were limited to applying radio echo sounding in prospecting ice until 1973, when Cook introduced the use of the method in coal mines. Additionally, Holser et al. (1972), Unterberger (1978), and Thierbach (1973) used GPR to detect and derive the depth of salt deposits. In general, the technology of GPR was rapidly developed during and after the World War II for military purposes. It is also worth mentioning the Apollo 17 lunar exploration program which included GPR technology to map the Moon's subsurface as it exhibits a similar electrical behavior to ice (Annan, 1973). Much further development of the GPR method occurred between 1995 and 2000 with the evolution of computers. Since then, GPR hardware components, software for acquisition and processing of data, numerical models and commercial interest are all constantly rising (Grasmueck 1996, Annan et al. 1997, Annan 2002).

From its infancy until now, GPR's applications are numerous. Some of them serve archeological and environmental studies (e.g., Nuzzo et al., 2002; Brewster and Annan, 1994). Others include the qualitatively characterization of man-made structures such as detection of fractures in a pavement or voids in concrete (e.g., Diamanti et al., 2010). The method is

furthermore applicable in hydrological studies, geological stratigraphy mapping, mining, subsurface structure visualizing etc. (e.g., Annan 2005, Batayneh et al., 2014, Francke and Yelf, 2003; Kadioğlu and Daniels, 2008).

One of the most challenging issues with GPR is data interpretation. This thesis focuses on studying the various GPR signals reaching the GPR receiver and mainly, the first arrival on a GPR recording, the direct wave (DW). The direct wave, although it is very helpful to record as it is helping define the time-zero or else, the true ground surface for a GPR survey, being the strongest response in a GPR record it may mask or interfere in some cases with the reflected signals (i.e., reflected wave – RW) which are indicators for in-ground targets. To help with GPR data interpretation, this thesis focuses in the study of mainly the DW as well as the RW, in an attempt to suggest an advantageous transmitter-receiver arrangement where the DW becomes minimum while the RW remains almost unchanged.

To make the scope and results of this work comprehensible, a fundamental comprehension of the GPR background theory is required. The propagation of EM waves in a medium is quantitatively descripted by Maxwell's equations and the interaction of an EM wave with the subsurface is ruled by the EM physical properties of the materials. Beyond these, the emission and the reception of EM waves also depend on the nature of the GPR antennas. All of these topics will be discussed in more detail on a later chapter. For more information about the structure of this thesis a general overview follows.

1. General overview

The purpose of this thesis is to examine the behavior of mainly the GPR DW and also, the RW events, when the Tx and Rx relative position and orientation are changing. To serve this purpose, field measurements were performed, and also, GPR synthetic data were produced to image the spatial distribution of EM signals in terms of their amplitude and shape. The chapters of this dissertation are as follows:

- The second chapter describes the theory of the GPR method. More specifically, an introduction to the basic physical principles (i.e., the equations of Maxwell) will be presented and the electromagnetic properties of the materials will be analyzed. The EM material properties will be linked to Maxwell's equations through the constitutive equations. In addition, a short discussion on the sources of noise in GPR data will be made. Also, the various regions of the EM fields when moving away from an EM source will be listed as in this thesis we study the impact of the Tx-to-Rx distance on the GPR responses.
- In the third chapter, an introduction to GPR antennas will be given. The ways that EM signals can be polarized will be listed and the concept of the antenna pattern will be analyzed in detail because this work is inspired by the theoretical antenna pattern issues.
- In the fourth chapter, the typical GPR assumptions which are usually valid for a GPR survey will be discussed enlightening the limitations of the method.
- In the fifth chapter the materials and the methods of this study will be presented. The survey area will be presented from a geological point of view. The set-up of both the field tests and the synthetic experiments will be presented. In addition, the processing for both the observed and the synthetic data will be given.
- In the sixth chapter, the results from the synthetic and the observed data will be listed and discussed.
- In the seventh chapter, the results from the synthetic and the observed data will be cross correlated and discussed at a common basis.
- In the eighth chapter, the conclusions of this study will be given.
- Appendices A, B and C include data and images during data acquisition, and results from both the synthetic and observed data that are not included into the main body of this thesis.

At this point, I would like to express my gratitude to my supervisor Dr. Nectaria Diamanti as she was more than devoted to this work and she has been always available for every kind of question. I would also like to thank Dr. Antonis Giannopoulos and Dr. Georgios Vargemezis for their meaningful observations and conversations about this work. In addition, I would like to express my thankfulness to Sensors & Software Inc. for providing access to the necessary GPR hardware equipment and software and more specifically, Dr A. Peter Annan who provided feedback on this work. Lastly, I am also beholden for everything my family has done for me during all these years and I am thankful to my classmates who also supported me during the field measurements of this study.

2. Theoretical Considerations

In this chapter, a brief Introduction into the concepts of the physical background of GPR will be attempted. A qualitatively description of the phenomena of generation, propagation, and interaction of EM waves with materials are required to understand how a GPR system works and in extend, the substance of this thesis. To succeed into the above, Maxwell's equations for EM fields and physical properties of materials with great importance for GPR will be presented. Taking a deep dive into the mathematical part of electromagnetics is beyond the scope of this work. More information about quantitative clarification of the physics can be found in Chapter 2 of the book "The Finite Difference Time Domain Method for Electromagnetics" by Karl S. Kunz and Raymond J. Luebbers (1993). A more focused mathematical approximation on the method of GPR can be found in the book chapter "Ground Penetrating Radar Principles Procedures and Applications" by Peter A. Annan (Annan, 2003).

2.1 The concept of GPR

As it was previously mentioned in the Introduction, GPR is a geophysical EM method which has the ability to detect targets in the subsurface and map them with high resolution using EM waves. A GPR system consists of two transducers: the transmitter (Tx) and the receiver (Rx) which can be either placed in the same or different boxes. Single transducer box GPRs are easier to be transported but separate transducer systems offer a variety of arrangements and hence, GPR measurements (e.g., Common Mid-Point (CMP) and Wide-Angle Reflection Refraction (WARR) arrangements).

EM waves travel in the vacuum with the speed of light ($c \approx 3\ 10^8$ m/s). The electromagnetic spectrum covers a range of frequencies and GPR is operating in the high frequency range of the radio sub-spectrum (i.e., ~10MHz-1GHz). GPR systems produce radio waves and more specifically, radio pulses of short duration with specific characteristics (Wielopolski et al. 2000, Daniels 2004). These pulses are emitted from a transmitting antenna, travel in the subsurface interacting with materials and then, received by a receiving antenna.

The result of the interaction between EM waves and subsurface inhomogeneities is the generation of reflected and/or refractive waves received by a GPR receiver. Some of the energy that is not reflected back is travelling deeper (transmitted wave). The direct GPR wave is comprised by two parts: the part that travels straight from the Tx through the air to the Rx antenna (i.e., direct air wave – DAW) and the part that travels marginally in the subsurface, very close to the air-ground interface (i.e., direct ground wave – DGW). So, the DGW is dependent on the dielectric properties of the near surface medium. A portion of the initial emitted energy is lost due to physical phenomena which govern the EM waves transmission such as: geometrical spreading, scattering, attenuation etc. More information about the principles of reflection and refraction of EM waves will be given in a following chapter. The whole concept can be visualized in Figure 1 where a receiving antenna is placed at a distance X from a transmitting antenna, above a two layered earth model. The DAW is denoted with black dashed line and the DGW wave with a blue dashed line. The green dashed line corresponds to the reflected wave and the red one to the refracted EM wave.

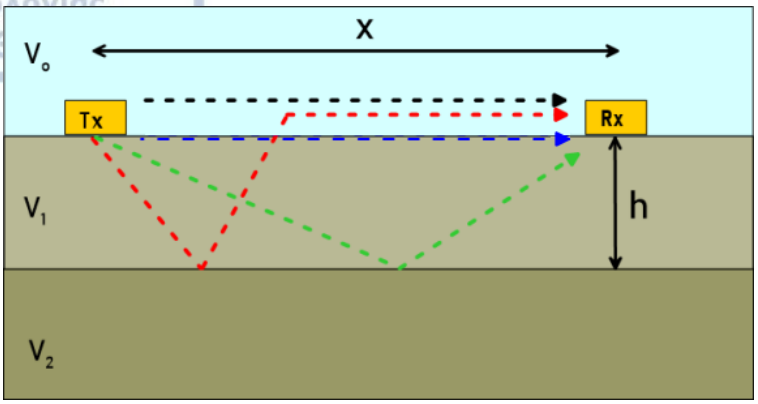

Figure 1: Different ray paths for an emitted EM wave travelling from a transmitting antenna to a receiving antenna for a two layered earth model. V_0 is the velocity of the EM wave in air (equal to c), V_1 the velocity in the first medium and V_2 the velocity in the second medium.

For GPR systems that have their antennas in separate boxes, three basic modes of GPR operation can be deployed which are the: common-offset (CO) reflection, CMP (or WARR) and transillumination modes (Figure 2). GPR systems that have both their Tx and Rx antennas included in a single box can only operate in the CO reflection mode, which is the mostly used (Annan, 2003).

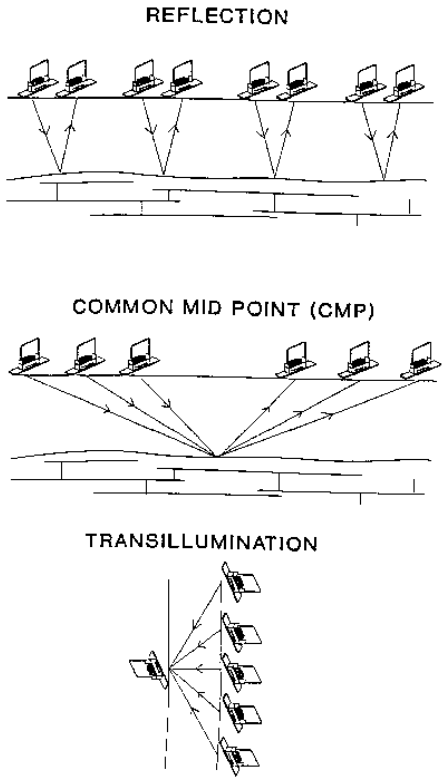

Figure 2: The three basic modes of GPR operation (Annan, 2003).

For the CO mode, the antennas have a fixed distance between them and by dragging them along the surface of the ground, GPR data are collected at various spatial positions. By combining these data, an image is formed known as radargram or a cross section, like the example depicted in Figure 3. In a radargram, one can see the direct ground and air waves (usually as a non-separated arrival) and the reflected EM waves generated by differences in the dielectric properties of the subsurface materials. That is why GPR reflections are typically indicators of subsurface targets, interfaces, and heterogeneities.

At the radargram of Figure 3, the spatial position of the measurements is indicated along the top ruler (m), the time axis is on the right in nanoseconds (ns) and the corresponding depth is on the left in meters (m). The time axis indicates the time that the GPR signals take to travel from the Tx in the subsurface, reflect, and travel back to the GPR Rx. When the velocity of the GPR signal propagation in the subsurface is known, this time axis can be converted into a depth axis. As seen in Figure 3, the direct air and direct ground waves are united, depicted from 0 to ~3 ns and the reflection starting at ~11ns corresponds to the interface between layer 1 and layer 2. The interface is approximately located at 0.75m using a GPR wave velocity equal to V1=0.143m/ns. The black and white bands of the signals indicate the polarity of EM waves. Positive signals (peaks) are represented by white colors and negative signals (troughs) by black. It is defined by GPR manufacturers whether the pulse of the direct air wave will first arrive with a trough or a peak.

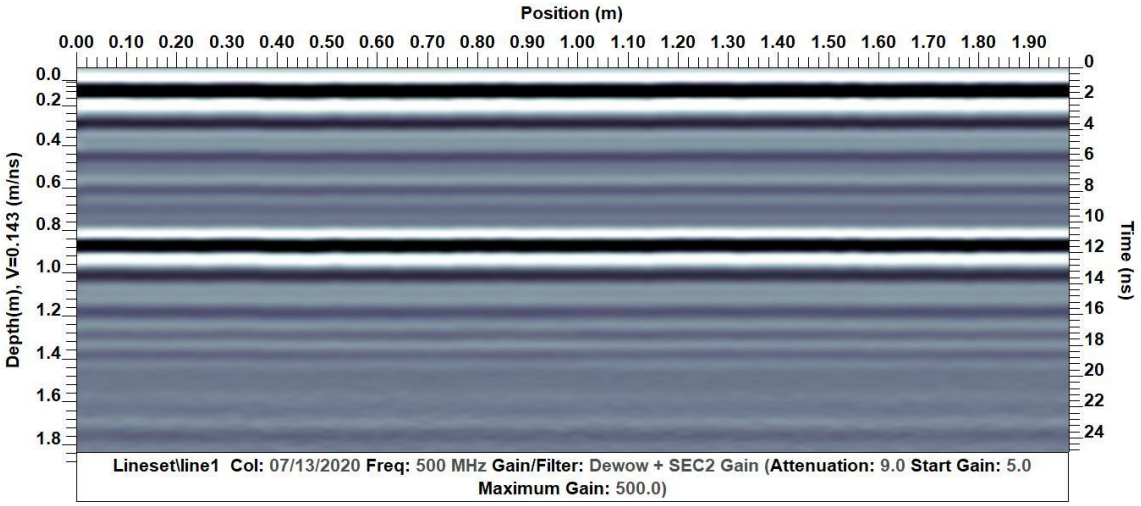

Figure 3: A typical image of a radargram in grey scale when GPR is operating in CO reflection mode. The spatial position of the measurements is indicated along the top ruler (m), the time axis is on the right in nanoseconds (ns) and the corresponding depth is on the left in meters (m).

It is important to know the velocity that EM waves travel in the subsurface in GPR surveys as knowing this velocity provides the user with information about the dielectric properties of the materials under study and also, provides information about the depth of target(s). The link between the EM wave velocity and the dielectric properties will be discussed later. To perform detailed velocity estimations, it is essential to carry out multi-offset surveys such as the CMP and WARR modes that lead to generating a GPR tomography (Annan, 2003). When GPR is operating in the standard CO reflection mode, velocity can be derived only by a hyperbolic shaped like

reflection (if there is any) and appropriate hyperbola fitting. A typical image from a WARR survey is depicted in Figure 4, where the Rx antenna is moving away from the Tx antenna.

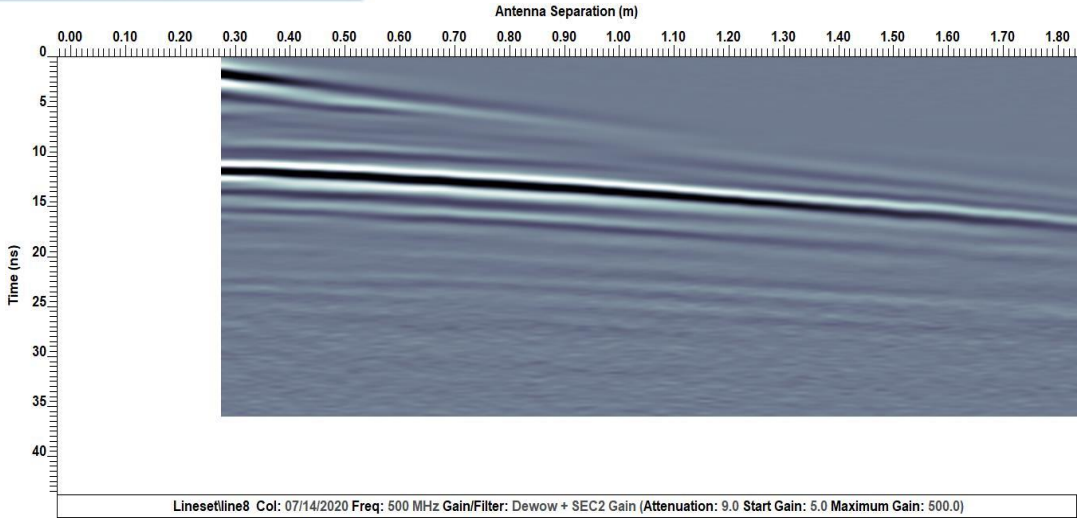

Figure 4: Data resulting from a multi-offset survey (WARR).

From the recorded signals in Figure 4, the direct air wave (DAW), direct ground wave (DGW) and the reflected wave (RW) events can be identified. The DAW is travelling with the speed of light in a straight line from Tx to Rx and thus, it is always the first arrival reaching the receiver. The time it takes this wave to arrive to the receiver is given by:

$$t_{air} = \frac{x}{c} \tag{2.1}$$

where, x is the distance between the Tx and Rx antennas.

The DGW has also a straight-line shape (like the air wave) as it follows a direct line ray path from the transmitting to the receiving antenna. Although, it travels within the ground with the velocity of the uppermost layer (V_1), the ray path it follows is located at near proximity to the air-ground interface. As V_1 will always be less than the speed of light, the direct ground wave will always arrive after the direct air wave. The time which corresponds to the arrival of this wave to the receiver can be calculated as:

$$t_{ground} = \frac{x}{V_1} \tag{2.2}$$

The RW also travels with velocity V_1 from the Tx in the subsurface and back to the Rx. Unsimilar to the direct air and ground waves, it travels through a longer ray path and thus, it is a later arrival. Its curvy shape makes this wave quite distinguishable from other signals. The time it takes for a reflection to reach the receiver is given by:

$$t_{reflected} = \frac{\sqrt{x^2+4h^2}}{V_1} \tag{2.3}$$

where, h is the depth of the uppermost layer, as depicted in Figure 1.

2.2 Physical Basics

2.2.1 Maxwell's Equations

In 1873, the Scottish physicist James C. Maxwell deployed the work that had already been done by André-Marie Ampère and Michael Faraday on electricity and magnetism suggesting the unity between those two fields (Maxwell, 1873; Goldstein, 2017). The EM fields relation is described by the following equations.

Divergence equations: *Curl equations:*

$$\nabla \cdot \vec{B} = 0 \text{ (a)} \qquad \nabla \times \vec{H} = \vec{J} + \frac{\partial \vec{D}}{\partial t} \text{ (c)}$$

$$\nabla \cdot \vec{D} = \rho \text{ (b)} \qquad \nabla \times \vec{E} = -\frac{\partial \vec{B}}{\partial t} \text{ (d)} \qquad (2.4)$$

where,

- $\vec{E}$ is the electric field vector ($^{V}/_{m}$)
- $\vec{H}$ is the magnetic field vector ($^{A}/_{m}$)
- $\vec{B}$ is the flux density vector or magnetic induction (Vs/m^2)
- $\vec{D}$ is the electric displacement field vector (As/ m^2)
- ρ is the charge density distribution (C/m^3)
- $\vec{J}$ is the electric current density (A/m^2)

Equations (2.4) reveal what produces these fields; the sources of the EM waves are the charge density distribution ρ, and the electric current density $\vec{J}$ (e.g., Klenk, 2012). They also physically show that a time changing electric field induces a time changing magnetic field and vice versa (Baker et al., 2007). Maxwell's equations explain the most of what happens in a GPR's transmitting antenna and how does electromagnetic (radio in our case) pulses are formed and afterwards emitted by a transmitter. Further details about the electronics of antennas are beyond of the aim of this thesis.

2.2.2 Physical Properties of Natural materials

The most important electromagnetic properties for the method of GPR are the electrical permittivity (Ɛ), the magnetic permeability (μ) and the electrical conductivity (σ). After the generation of radio pulses in the transmitting antenna every other process until the reception of the signal is closely related or depended mainly on these electromagnetic material properties. The ability of GPR to detect an in-ground target is controlled by the electromagnetic nature of the geological formations lying into the subsurface. For this reason, this chapter is analyzing

physical properties of the materials, which are present in every aspect concerning the GPR method and this thesis.

Permittivity (Ɛ) is the ability of mater to resist when being under the impact of an external electric field. This ability depends on a material's structure and it is measured in F/m. Materials that are highly resistive to an electric field are called dielectrics (or insulators) and materials which are easily allowing an electric field to pass through them are known as conductors. The higher the resistance of a matter is, the higher the value of the permittivity for this material. Note that the permittivity of free space is denoted as $Ɛ_0$ and it is equal to 8.854 10^{-12} F/m.

When an external electric field is applied through a dielectric material, its electrons are shifted until the creation of an internal electric field, which is trying to cancel the external one and brings balance to the system. This process is generating two physical phenomena simultaneously occurring when an insulator is exposed to an electric field. The first one is the energy storage (e.g., capacitors) because a charge is building up. The second one is energy dissipation via heating due to the displacement of electrons described above. That is why a more accurate definition of permittivity would be that it describes the ability of a material to polarize, support polarization, and store energy in response to an external electric field (Olhoeft, 1998 retrieved by Baker et al., 2007).

Mathematically, the phenomena of storage and dissipation accompanying permittivity are expressed through a complex number. The real component (ε') is related to energy storage while the imaginary part (ε'') is for the release of energy. The imaginary component of permittivity has usually value greater than 0 but less than the real part (Hewlett Packard, 1992):

$$Ɛ' = Ɛ_r \, Ɛ_0 \, (F/m) \tag{2.5}$$

where, $Ɛ_r$ is the relative permittivity (or else, dielectric constant), a dimensionless quantity which will be analyzed later. The imaginary part of permittivity is:

$$Ɛ'' = \frac{\sigma}{\omega} \ (F/m) \tag{2.6}$$

where, ω is the angular frequency (rad/s) and σ the conductivity of the medium (mS/m). The values of the equations (2.5) and (2.6) can be combined to form the so-called loss tangent or tan(δ). The loss tangent describes the "lossiness" of a material when an electric field is present, and it is the ratio of the diffusive character of a mater to its ability of energy storage.

$$\tan(\delta) = \frac{Ɛ''}{Ɛ'} = \frac{1}{Q} \ \text{(dimensionless)} \tag{2.7}$$

The value of the loss tangent is a very valuable number to decide whether the method of GPR is efficient to be applied or not. It is the reciprocal of the quality factor (Q) for seismic methods and closely related to the attenuation (α) of the signal of GPR (Baker et al., 2007). Under low-loss conditions, the loss tangent can be simplified as: $\tan(\delta) = {}^{\sigma}/_{\omega Ɛ}$. When it is <<1 it is assumed that

there is very little attenuation for the signal of GPR and that conduction currents are small (Annan, 2005; Ward and Hohmann,1991). Hence, the GPR method is applicable.

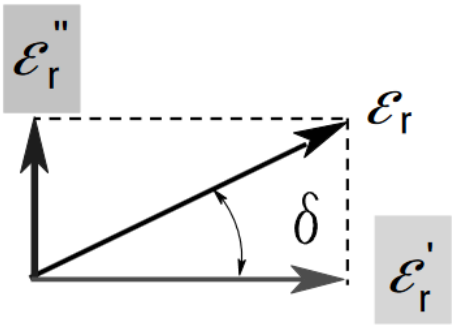

Figure 5: A vector diagram describing the relationship between the real (Ε') and the imaginary (Ε'') components of the relative permittivity to the loss tangent δ (Hewlett Packard, 1992).

As mentioned above, another commonly mentioned quantity for the GPR method is the relative permittivity ($Ε_r$) also referred to as dielectric constant or dielectric permittivity ($κ_r$). The relative permittivity for a complex material is relating the real and the imaginary parts of permittivity (Baker et al., 2007):

$$Ε_r = [\frac{ε'}{ε0} - i\frac{ε''}{ε0}] \text{ (dimensionless)} \quad (2.8)$$

Relative permittivity is a much more convenient way to express the permittivity (it is a constant, dimensionless value) and it is also more handheld for materials to be compared in that way (Annan, 2003). In Table 1 some values for the most common materials for GPR are presented (Meyer et al. 2008). Considering most GPR applications, we assume that the medium in which the signal is passing through, is a linear, isotropic, non-complex material satisfying the low loss criteria ($\frac{\sigma}{\omega\varepsilon}$ <<1) (Annan, 2003). That is why, practically, permittivity at low frequencies (≤ 1GHz) is made of only its real part and so Ε is equivalent to Ε' (Chen and Zhang, 2009):

$$Ε_r = \frac{ε}{ε0} \quad (2.9)$$

Equation (2.9) is a fundamental one for GPR because permittivity has a strong impact on the estimation of the velocity of EM waves (as it will be discussed below) and it is also an important parameter for the electromagnetic impedance and finally, the reflectivity calculation.

It is worthwhile mentioning that the moisture content of a medium has a tremendous influence on its relative permittivity, as water is the highest $ε_r$ material. As can be seen in Table 1, dry masonry has a much smaller value of $Ε_r$ compared to a moist one.

Table 1: Relative permittivity at a center frequency of 1 GHz for materials which could be present during a GPR survey (Meyer et al. 2008).

Material	Relative Permittivity (ε_r)
Air	1
Dry Masonry	3-5
Moist Masonry	5-26
Dry Concrete	5-8
Moist Concrete	8-16
Asphalt	3-5
Granite	5-7
Basalt	8
PVC	3
Dry sands/dry clay	4-8
Wet sands/wet clay	16-32
Ice	3-5
Water	81

Likewise permittivity, the magnetic permeability (μ), measured in H/m, is also a complex number where its real component is describing energy storage and the imaginary one the diffusive character of a material when it is subject to a magnetic field (Powers, 1997).

For most sediments, rocks and soils which consist of non-ferromagnetic minerals, the value of magnetic permeability is small and approximately equal to the magnetic permeability of the vacuum ($\mu_0=10^{-7}$ H/m) (Ulaby, 2001). Obviously, geological formations with high content of magnetic materials or their derivative**s** (i.e., magnetite, hematite, Fe_20_3) are excluded from this assumption. The relative magnetic permeability is defined as:

$$\mu_r = \frac{\mu}{\mu 0} \text{ (dimensionless)} \qquad (2.10)$$

Since Earth's upper crust materials, in most of the cases, are non-magnetic, $\mu = \mu_0$ and equation (2.10) leads to μ_r being equal to unity. In that way, some fundamental equations such as the velocity of an EM wave in a non-ferromagnetic and a non-conductive soil can be simplified (Reppert, 2000). Equation (2.11) is for the wave velocity through a magnetic and/or highly conductive material and equation (2.12) describes the velocity of a radio wave in a non-magnetic and low-loss material.

$$V = \frac{c}{\sqrt{\frac{\varepsilon r \mu r}{2}\left(\sqrt{1+(tan(\delta))^2}+1\right)}} \qquad (2.11)$$

$$V = \frac{c}{\sqrt{\varepsilon r}} \text{ (m/s)} \qquad (2.12)$$

The later equation is what is used to define the velocity of the signal for the majority of GPR applications. We can also define the EM pulse wavelength (λ) through the signal propagation velocity as:

$$\lambda=\frac{V}{f}\ (m) \tag{2.13}$$

From equations (2.12) and (2.13) it is understood that a low value of relative permittivity means a high propagation velocity of the radio wave and so, a large wavelength favoring the depth of the investigation but allowing for lower resolution at the same time.

Conductivity describes how easily an electron moves in a material when the last is under the impact of an external electric field (Saarenketo, 1998). Conductivity has a strong influence on GPR considering the propagation and penetration of the signal, because the larger it is, the higher wave attenuation is and thus, the less the GPR skin depth as it will be shown below (Baker et al., 2007).

For wet or moist materials, we can approximate conductivity, σ, through Archie's law for electrolytic conduction (Archie, 1942):

$$\sigma = \alpha\phi^{m}s^{n}\sigma_{w}+\sigma_{c}\ (S/m) \tag{2.14}$$

where,

- m is a constant (1.3–2.5)
- a is a constant (0.4–2)
- s is the saturation of water (fractional)
- n is a constant (~2)
- σ_w is the conductivity of pore fluid (S/m)
- σ_c is the surface conductivity of a soil's matrix (S/m)

We can now define attenuation (α) as the rate of loss in amplitude for an EM wave that propagates through a material. Attenuation depends on the electromagnetic properties of a mater and on the angular frequency (Stratton and Chu, 1941):

$$\alpha = \omega\ (\frac{\mu\varepsilon}{2}[(1+\frac{\sigma^2}{\omega^2\varepsilon^2})^{\frac{1}{2}}-1])^{½}\ (Np/m) \tag{2.15}$$

It is generally preferred to express the attenuation in dB/m. Considering a low-loss medium equation (2.15) can be redefined as (Annan, 2003):

$$\alpha = 1.64\frac{\sigma}{\sqrt{\varepsilon_r}}\ (dB/m) \tag{2.16}$$

From equation in (2.15) another important parameter for GPR can be extracted which is the skin depth. Skin depth (δ) points the distance that a wave is travelling before its amplitude reduced to 1/e:

$$\delta = \frac{1}{\alpha} \tag{2.17}$$

Similarly, equation (2.17) for the skin depth, can be simplified for cases where small conduction currents are dominated (Ward and Hohmann, 1991) as:

$$\delta = \sqrt{\frac{2}{\omega\mu\sigma}} \tag{2.18}$$

It is obvious that the GPR wave depth of penetration is minimum if the conductivity is high. In general, a maximum skin depth requires a combination of minimum frequency of the transmitter antenna and a low value of conductivity for the environment where GPR is applied. Highly conductive materials would cause a rapid attenuation for the signal and in this case the method would fail to detect any in-ground target or subsurface stratigraphy.

The frequency of operation of GPR antennas is also a parameter which needs to be considered. In some cases, GPR might operate at frequencies between low-loss and the quasi-static profile, where a loss tangent of <<1 and >>1 does not longer describe the low loss criteria and the quasi-static conditions, respectively. Considering this, the provided simplified equations are no longer valid to estimate the wave parameters (Hatch et al., 2013).

At this point, it is also worth noting that the conductivity of ground water depends on its concentration of total dissolved solids (TDS). The higher this concentration is, the higher the value of water conductivity. GPR surveys can succeed in imaging the water table quite well (and many times below it) as long as water has a low value of TDS (i.e., fresh water). In Table 2, the values of relative permittivity, conductivity, velocity, and attenuation for some common geological materials are presented. The water type and content in a formation are important parameters resulting in higher dielectric constant and conductivity values, as shown for dry and saturated sands in the table below (Annan, 2003).

Additionally, the imaginary part of electrical permittivity is related to the diffusion component of the EM energy and it is proportional to the cation exchange capacity (CEC) of a formation (e.g., Saarenketo, 1998). That is why soils made of materials with high CEC, such as clays, may present a high signal attenuation. On the contrary, non-clay but clayed-sized formations, do not attenuate the GPR signal that rapidly, making the naturally occurring fraction of clay in a soil an important parameter for the application of the method of GPR (Baker et al., 2007).

Table 2: Values for relative permittivity (K_r or ε_r), electrical conductivity (σ), velocity (v), and attenuation (a) for some common geological materials (Annan, 2003).

Material	K_r or ε_r	σ (ms/m)	v (m/ns)	a (dB/m)
Air	1	0	0.3	0
Distilled Water	80	0.01	0.033	3×10^{-3}
Fresh Water	80	0.5	0.033	0.1
Sea Water	80	3×10^{3}	0.01	10^{3}
Dry Sand	3-5	0.01	0.15	0.01
Saturated Sand	20-30	0.1-1.0	0.06	0.03-0.3
Limestone	4-8	0.5-2	0.12	0.4-1
Shales	5-15	1-100	0.09	1-100
Silts	5-30	1-100	0.07	1-100
Clays	5-40	2-1000	0.06	1-300
Granite	4-6	0.01-1	0.13	0.01-1
Dry Sand	5-6	0.01-1	0.13	0.01-1
Ice	3-4	0.01	0.16	0.01

2.2.3 Constitutive Equations

So far, it has been highlighted that the propagation of EM waves is closely related to the physical properties of the materials that these waves are passing through. The constitutive relations mathematically provide the macroscopic description of how electrons, atoms and molecules of a material react under the impact of an EM field (Tzanis, 2015). In this section, the mathematical link between the electromagnetic properties of the media and the propagation of the EM waves will be described.

The constitutive equations demonstrate the interaction between EM fields and material properties and are presented in the following form:

$$\vec{D}_{(t)} = [\varepsilon_{(t)}] * \vec{E}_{(t)}$$

$$\vec{B}_{(t)} = [\mu_{(t)}] * \vec{H}_{(t)}$$

$$\vec{J}_{(t)} = [\sigma_{(t)}] * \vec{E}_{(t)} \qquad (2.19)$$

where,

- ε is the permittivity of the medium ($^{F}/_{m}$)
- μ is the magnetic permeability of the medium ($^{H}/_{m}$)
- σ is the electric conductivity of the medium ($^{mS}/_{m}$)
- [] means tensor

- * means convolution

For the applications of GPR, the parameters of Ɛ, μ and σ are considered as scalar quantities and therefore, the convolution sign in equations (2.19) can be substituted by a simple multiplication. Assuming a linear, isotropic, and non-dispersive material, relations in (2.19) can be written as follows:

$$\vec{D} = \varepsilon \vec{E} \qquad \vec{B} = \mu \vec{H} \qquad \vec{J} = \sigma \vec{E} \qquad (2.20)$$

Supposing that no charges or current sources are present, the constitutive relations in (2.19) become the Maxwell's equations (2.21):

$$\nabla \times \vec{H} = \varepsilon \frac{\partial \vec{E}}{\partial t} \qquad \nabla \times \vec{E} = -\mu \frac{\partial \vec{H}}{\partial t} \qquad (2.21)$$

In physical terms, equations in (2.21) suggest that if we have a large permittivity, it will take a large curl to induce the same change in electric field.

A quantity that links the permittivity of the medium (Ɛ) and the magnetic permeability (μ) is the refractive index (n) (Griffiths, 2005):

$$n = \sqrt{\frac{\varepsilon\mu}{\varepsilon_0\mu_0}} = \sqrt{\varepsilon_r\ \mu_r} \quad \text{(dimensionless)} \qquad (2.22)$$

Considering equation (2.22) and a non-ferromagnetic material, we can define a relationship for the refractive index and the wave velocity of the form:

$$n = \frac{c}{V} \qquad (2.23)$$

2.2.4 EM wave propagation

In the previous sections, the Maxwell's equations and the electromagnetic properties of the materials were presented. This chapter combines both these subjects to introduce the wave equations, meaning the mathematical description (function) of how an EM wave propagates through materials with respect to time and space.

Propagation of oscillatory EM waves requires frequencies which exceed the material's transition frequency (f_t) defined as (Baker et al., 2007):

$$f_t = \frac{\sigma}{2\pi\varepsilon_0\ \varepsilon_r} \qquad (2.24)$$

A concept describing the importance of the transition frequency for GPR applications and its relationship to the signal attenuation for a material above its transition frequency (where the curve of attenuation is flattened at high frequencies), is shown in Figure 6. In realistic

heterogenous materials, EM signals will be rapidly absorbed, and scattering losses and water relaxation will dominate (Sensors & Software, 2016).

To obtain the wave solutions and describe the propagation of a radio wave in space and time, Maxwell's equations and constitution relations are needed. Taking the curl of equations (2.4c) and (2.4d) and excluding the electromagnetic properties of the medium when they are considered to be constant values, the wave equations result in:

$$\nabla^2\vec{E} = -\frac{1}{c^2}\frac{\partial^2\vec{E}}{\partial t^2} \text{ (a)}$$

$$\nabla^2\vec{H} = \frac{1}{c^2}\frac{\partial^2\vec{H}}{\partial t^2} \text{ (b)} \qquad (2.25)$$

Equations (2.25a) and (2.25b) are called wave equations and they are pointing that a change of space (term 1) will yield a change in time (term 2). To simplify further equations (a) and (b) for plane wave equations, time harmonic Maxwell's equations should be used (i.e., functions that are periodic with time). We can write the electric (2.26a) and magnetic (2.26b) fields as periodic functions:

$$\bar{\bar{E}}=\bar{E}(x,y,z)\, e^{i\omega t} \text{ (a)}$$

$$\bar{\bar{H}}=\bar{H}(x,y,z)e^{i\omega t} \text{ (b)} \qquad (2.26)$$

Equations (2.26a) and (2.26b) indicate that the magnitude of the electric ($\bar{E}$) and magnetic ($\bar{H}$) fields in a direction (x,y,z), "wiggles" with respect to time ($e^{i\omega t}$). By plugging (2.26a) and (2.26b) into Maxwell's equations, the following relations are resulted in frequency domain:

$$\nabla^2\vec{E} = i\omega\mu(\sigma+i\omega\varepsilon)\vec{E} \text{ (a)}$$

$$\nabla^2\vec{H} = i\omega\mu(\sigma+i\omega\varepsilon)\vec{H} \text{ (b)} \qquad (2.27)$$

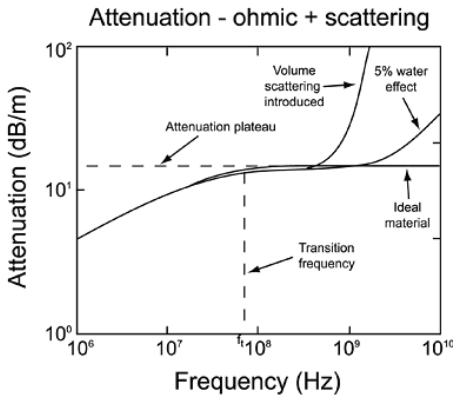

Figure 6: For an "ideal" material, attenuation plateaus above the transition frequency. In real environments, water and/or volume scattering cause attenuation to increase with frequency. The onset of high frequency losses is very site specific (Sensors & Software, 2016).

Equations (2.27a) and (2.27b) are known as Helmholtz equations. The properties of travelling EM waves depend on the wave number (k) which is a synonymous definition to the propagation constant and can be also seen denoted as γ.

$$k=\sqrt{\mu\varepsilon\omega^2 - i\mu\sigma\omega} = \pm (\alpha + i\beta) \quad (2.28)$$

where, β is the propagation constant or wave number or phase term and it is defined as $\beta=2\pi/\lambda$ (rad/m). For the wave regime and low loss conditions, the iμσω term can be ignored (Annan, 2005; Ward and Hohmann, 1991). For this case, α is approximately equal to zero and k, β can be written as (Hatch et.al, 2013):

$$k\approx\beta=\omega\sqrt{\varepsilon\mu} \text{ (rad/m)} \quad (2.29)$$

By defining (2.28) and using equations (2.27a) & (2.27b), it is obvious that the propagation of time harmonic EM waves is influenced by the wave number:

$$\nabla^2\vec{E}=k^2\vec{E} \text{ (a)} \qquad \nabla^2\vec{H}=k^2\vec{H} \text{ (b)} \quad (2.30)$$

The plane wave solutions for (2.30a) and (2.30b) can be extracted for a homogenous medium and with a sinusoidal time dependence on the general form shown below (Ward and Hohmann, 1991, Hatch et.al, 2013):

$$E=E_0e^{-i(kz-\omega t)} \text{ (a)} \qquad H=H_0e^{-i(kz-\omega t)} \text{ (b)} \quad (2.31)$$

where, E_0 and H_0 are the initial electric and magnetic field magnitudes, and z is the depth of penetration (in meters). Equations (2.31a) and (2.31b) are fundamental for GPR. They describe a travelling EM wave whose electric and magnetic field is changing with time and space according to the electromagnetic properties of the medium(s) encountered. The electric and the magnetic fields are perpendicular to one another and also, perpendicular to the propagation vector of the resulting EM wave. The wave impedance (Z) is expressed as the ratio of the electric and magnetic fields, which compose an EM plane wave (2.32).

$$Z=\frac{E}{H} \quad (2.32)$$

For the quasi-static regime, the impedance can be written as:

$$Z=\sqrt{\frac{i\omega\mu}{\sigma}} \quad (2.33)$$

In this case, the electric field lags the magnetic field having a phase difference of $\pi/4$ (radians). For the region where conductivity is not important (the wave regime), wave impedance is given by:

$$Z=\sqrt{\frac{\mu}{\varepsilon}} \quad (2.34)$$

In this case, the magnetic and electric fields are in phase with one another. From equations (2.33) and (2.34), it is noticeable that electrical impedance is governed by changes in the relative permittivity (considering μ=1). This can explain that reflections for a downward propagating EM planewave are generated due to variations of the impedance in the ground (Annan, 2003)

2.3 Source Signal Characteristics

As it was previously discussed, GPR does not send a continuous signal into the subsurface, it sends out pulses. These signals contain various radio waves emitted around a specific frequency, called the GPR center frequency (f_c). Typically, the pulses radiated have frequencies of 0.5 to 1.5 times the center frequency (Annan, 2003). For example, an antenna of f_c =500 MHz emits signals of minimum frequency (f_{min}) at ~250 MHz or lower and of maximum frequency (f_{max}) at ~750 MHz or higher.

Electric and magnetic fields form sinusoidal EM waves in a range of frequencies that are packed in one form called the wavelet (Figure 7). The range of frequencies which are present in the wavelet is called bandwidth (B) and the time duration of this wave-like oscillation is the pulse width (W). The relationship between the bandwidth and pulse width is: $B=1/W$.

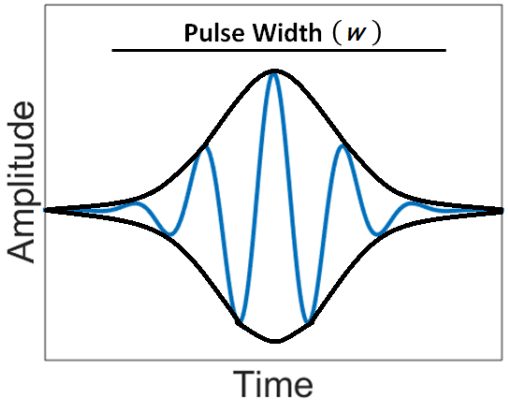

Figure 7: The form of a wavelet (pulse) with blue solid line, the corresponding envelope with black solid line and the pulse width (w) of the representing radio pulse.

The physical length of a pulse is known as the wavelength, sometimes also referred το as spatial length. In Figure 7 the concepts of a wavelet and its pulse width are depicted. The black solid line which encloses the pulse is called the envelope. For a pulse width of Δt duration, the center frequency can be estimated as: $f_c = 1/\Delta t$. From equations (2.12) and (2.13) the wavelength can be redefined as:

$$\lambda=\frac{c}{f_c\sqrt{\varepsilon_r}} \quad (2.35)$$

This expression shows that if the signal is propagating through a material with a high dielectric permittivity, it will move slower and it will have a larger wavelength.

Considering that GPR systems operate mostly in the range of approximately 100MHz to 1GHz this corresponds to a range of 1-10ns of pulse width. Figure 8 summarizes the relationships between the different characteristics of the source signal (bandwidth/energy spectrum, pulse-width, envelope).

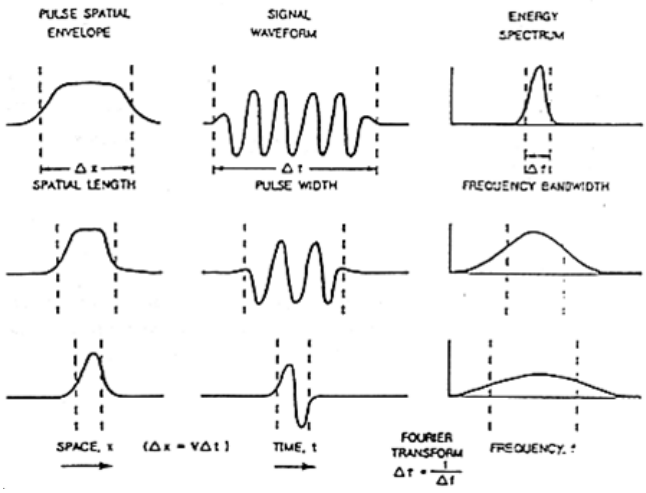

Figure 8: Illustration of the relationship between the source signal characteristics which control resolution (Annan, 2003)

Radio waves emitted from a GPR transmitter in the form of wavelets, propagate through the ground and exhibit the physical phenomena of EM wave transmission, reflection, refraction, and/or scattering. Then, the resulting EM waves are recorded as a returning signal by the GPR receiver.

To discriminate whether one or more targets are present in a GPR record (Figure 9), the recorded events (i.e., two in this example) must be adequately separated in time to be explicitly recognized as two different targets rather than one entity (Berkhout,1984, Knapp,1991, Kallweitt & Wood,1982). When the travel time for the pulse to reach two individual objects is similar, then the pulses and their envelopes are crossing, and the resulting signal could be confusing. It is generally accepted that GPR can recognize two independent events if they have a time difference at least equal to W/2 (Figure 10).

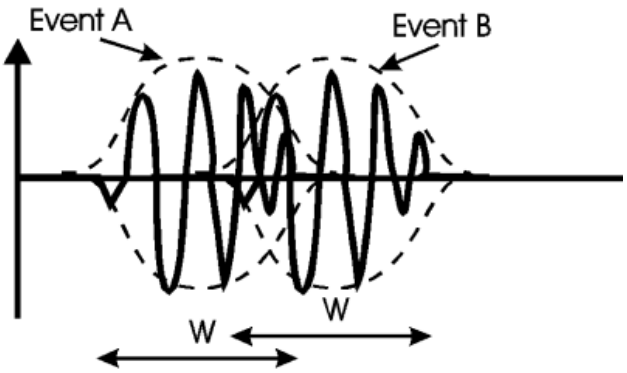

Figure 9: Two events overlapping each other in terms of time making the resulted signal difficult to be interpreted (Annan,2003)

Figure 10: Considering the pulse envelope, two events could be well resolved if they are separated in time by W/2 (Annan, 2003)

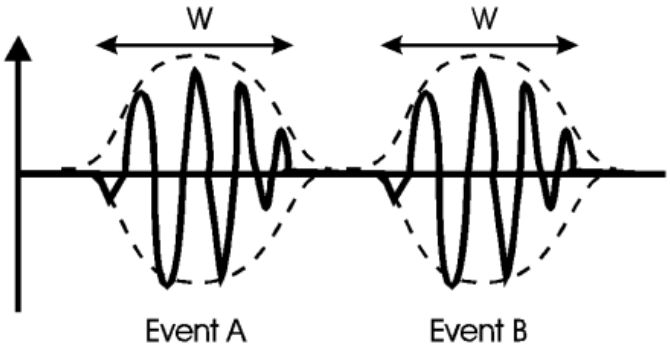

Figure 11: Clearly separated pulses and envelopes in time give rise to two well resolved targets (Annan, 2003)

2.4 Reflection, Refraction and Transmission of Radio waves

It has already been discussed that when a downward propagating EM wave reaches an interface or generally a change in the electromagnetic properties of the ground, portions of the initial signals undergo reflection, refraction, and transmission.

The reflection coefficient (R) can be defined as the amplitude of the reflected wave to the amplitude of the incident wave. If the incident wave hits a boundary perpendicularly, then the reflection coefficient is given by:

$$R=\frac{Reflected\ Amplitude}{Incident\ Amplitude} \tag{2.36}$$

Equation (2.36) can also be expressed as a function of the relative permittivity of the respective materials which are forming an interface:

$$R=\frac{\sqrt{\varepsilon_1}-\sqrt{\varepsilon_2}}{\sqrt{\varepsilon_1}+\sqrt{\varepsilon_2}} \quad (2.37)$$

The magnitude of R reveals the portion of the initial energy that has been reflected. From equation (2.37) it is obvious that if ε_1 and ε_2 have quite different values, most of the incident wave will undergo reflection $(\varepsilon_2 \ll \varepsilon_1)\ or\ (\varepsilon_1 \ll \varepsilon_2)$. Conversely, if ε_1 and ε_2 are similar, then, most of the initial incident energy will continue its path deeper in the subsurface. The reflection coefficient can take either positive or negative values and it is in the range of -1 to 1. Negative values show reverse of polarity of the signal. As a result, if the reflected wave has a value of R<0, then $\varepsilon_1 < \varepsilon_2$ and if the returning signal is represented by a value of R>0, then $\varepsilon_1 > \varepsilon_2$. At highly conductive boundaries, radio waves can only experience total reflection as they cannot propagate through an extremely conductive medium (such as metal).

The energy that keeps a downward propagation path is represented by the transmitted wave and the corresponding transmission coefficient (T) is:

$$T=\frac{Transmitted\ Amplitude}{Incident\ Amplitude}=\frac{2\sqrt{\varepsilon_2}}{\sqrt{\varepsilon_1}+\sqrt{\varepsilon_2}} \quad (2.38)$$

Refraction describes the deviation of a radio wave's direction. The angle of the reflected EM wave can be directly obtained from the angle of the incident ray (Figure 12). The angle of the refracted portion can be approached by Snell's law and for planar waves is given by:

$$\frac{\sin\theta_1}{V_1}=\frac{\sin\theta_2}{V_2} \quad (2.39)$$

From equation (2.12), Snell's law for radio waves can be rephrased as:

$$\sqrt{\varepsilon_1}\sin\theta_1=\sqrt{\varepsilon_2}\sin\theta_2 \quad (2.40)$$

When $V_2 > V_1$ (hence, $\varepsilon_2 < \varepsilon_1$) the wave is refracting towards the dotted line (Figure 12) and the resulted wavefront is spreading out. If $V_1 > V_2$, then the wave tends to follow the line of the interface between layer 1 (ε_1, V_1) and layer 2 (ε_2, V_2) and the wavefront is shrinking.

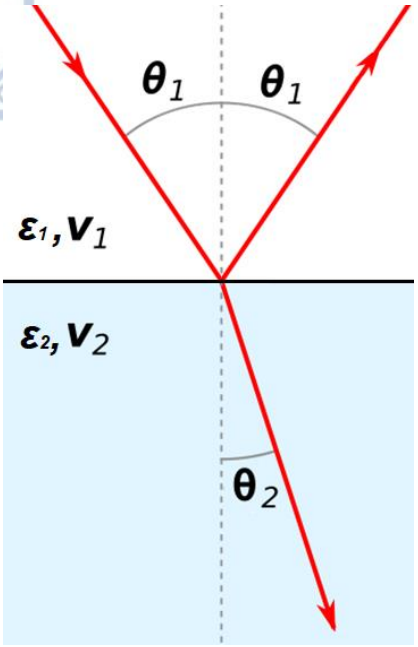

Figure 12: Reflection and Refraction of a radio wave at an interface.

Like with seismic waves, radio waves can also experience critical refraction (Figure 13) if the incident angle is such that the refracted wave is propagating along a boundary with the velocity of the 2nd layer (V_2). A wave generated by the mechanism of critical refraction is called head wave and the critical angle (θ_c) that must occur to trigger such waves is given by:

$$\sin\theta_c = \frac{V_1}{V_2} \tag{2.41}$$

Critical refraction can only take place if $V_1 < V_2$.

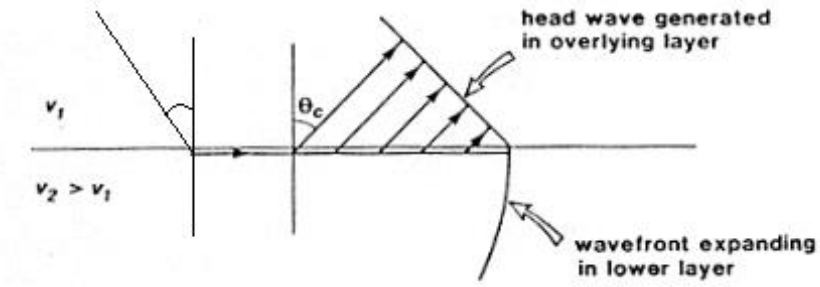

Figure 13: Critically refracted waves at an interface generating head waves.

2.5 GPR depth of penetration & resolution

It was previously mentioned that the skin depth defines the distance that a radio wave is travelling before its amplitude reduced to 1/e (Equations 2.17, 2.18) and thus, the probing

distance for a GPR survey. For materials which are characterized by larger skin depths, radio pulses can penetrate deeper into the subsurface and yet provide a strong returning signal. For example, rocks and sediments saturated with sea water have sufficiently smaller probing distances than rocks and sediments saturated with fresh water (Equation 2.18). In general, for hard rocks such as granite, limestone and schist, the skin depths are quite large as it is depicted in Figure 14.

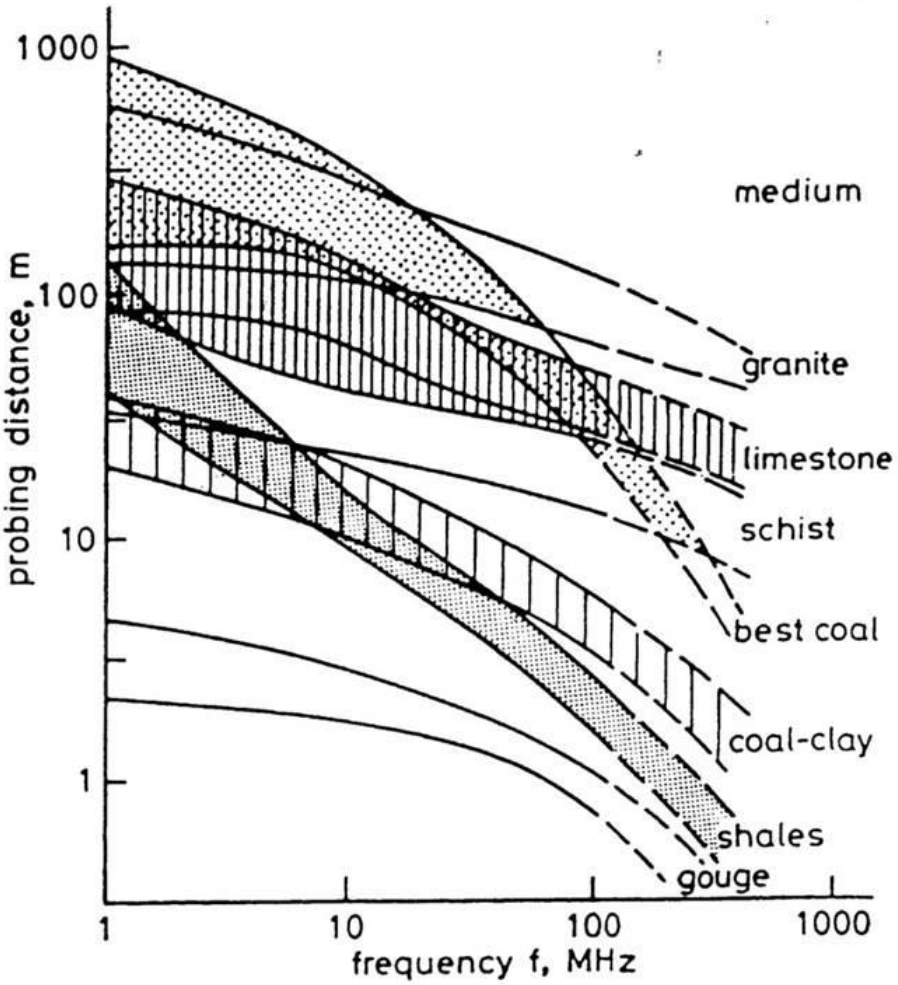

Figure 14: Probing distance (skin depth) for various materials in a range of frequencies from 1MHz to 1000MHz (Cook, 1975)

GPR resolution is characterized by two aspects: the transmitter blanking and the dual target horizontal and vertical discrimination (or else, resolution). Transmitter blanking is the situation when the receiver is unable to detect returning signals until after the GPR transmitter has finished its transmission. This phenomenon occurs because the transmitter antenna initially emits a very large (direct) signal. The receiver is usually in close proximity to the transmitter and thus the receiver can only see this large direct emission which is covering the rest of the resulting pulses for a specific interval of time (i.e., very early times). In this case, the electronics of the receiver are overloaded and reflected waves are not detectable until the emission of the direct signal has stopped (Annan, 2003).

The second aspect considering the resolution is the discrimination of two targets in horizontal and vertical plane. It has already been mentioned that the pulse width (W) of the source signal can influence GPR resolution. We can now use W to define the vertical and the horizontal resolution of GPR. A schematic concept of the vertical and the horizontal resolution is depicted in Figure 15.

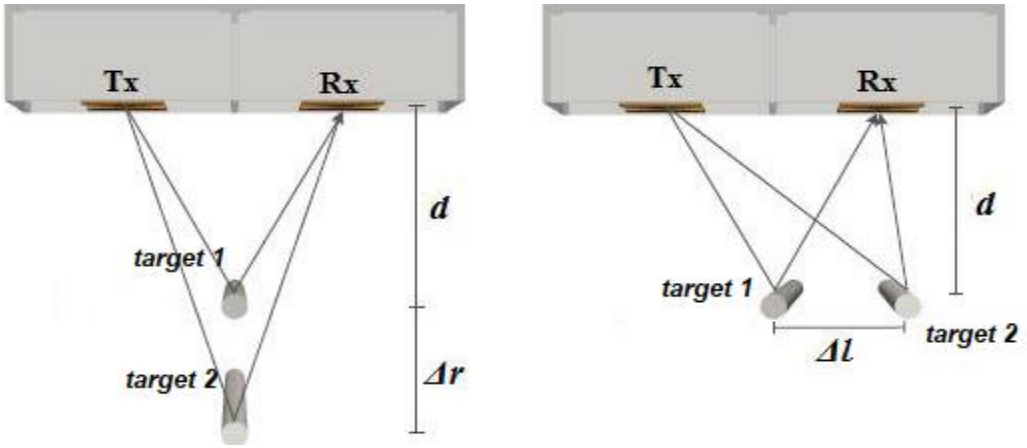

Figure 15: A schematic illustration of the vertical (left) and horizontal (right) GPR resolution considering the discrimination of two targets (Tzanis, 2015).

For vertical resolution, we assume that Δt (the time difference of the signal to reach target1 and target2) is greater than W/2 and the distance (m) between them is almost equal to one quarter of the wavelength (corresponding to the center frequency of Tx). The travel times for the pulse to reach target1 (t_1) and target2 (t_2) are given by:

$$t_1=\frac{2d}{V} \quad (2.42)$$

and,

$$t_2=\frac{2d+2r}{V} \quad (2.43)$$

from (2.42) and (2.43) we get that:

$$\Delta t=\frac{2r}{V} \quad (2.44)$$

We also know that Δt=W/2 and thus:

$$\frac{w}{2}=\frac{2r}{V} \rightarrow \Delta r \geq \frac{VW}{4} \quad (2.45)$$

From equation in (2.45) it is obvious that the vertical resolution of GPR is a function of pulse width (W) and the propagation velocity of the pulse in a medium and thus, for the same medium the vertical resolution for two targets is different for GPR antennas of different center frequencies.

Making the assumption that ΔL<< d (where, d is the target depth – Figure 15), and following the same logic as for the vertical resolution concept, the minimum horizontal distance between two targets to be discriminated by GPR, is given by:

$$\Delta L \geq \sqrt{\frac{VdW}{2}} \quad (2.46)$$

It is also worth to mention that when dealing with layers, then a general rule is that a layer should have a thickness at least equal to 1/4 the wavelength of the emitted wavelet to be detectable by GPR. For the case of very thin layers (e.g., thickness less than λ/4), multiple reflections are occurring in the top and the button of this thin layer resulting at a reflection coefficient which is influenced by constructive and destructive components (Baker et al., 2007).

2.6 Sources of Noise in GPR data

In the previous sections, some of the limitations of GPR considering the physical properties of the materials which are governing the depth of penetration, the target resolution, and the nature of the returning radio waves/signals (e.g., reflection, transmission, and refraction) were discussed. In this section, the sources of noise in GPR data will be pointed out.

GPR data are suffering from specific types of noise either in an external form or caused by the GPR system equipment itself, sometimes making the detection of targets difficult. Diamanti and Annan (2019) have identified five types of noise often occurring when GPR is employed:

1. External interference noise: radio waves from various sources, other than GPR, may occur while conducting a GPR survey. These external signals exist in the same range of frequencies with GPR and thus, can be measured by the receiver and mask responses from targets. Sources of this noise may be phones, radio towers and any other systems which transmit information in the form of radio waves. Applying stacking in GPR data reduces this kind of noise (Figure 16).

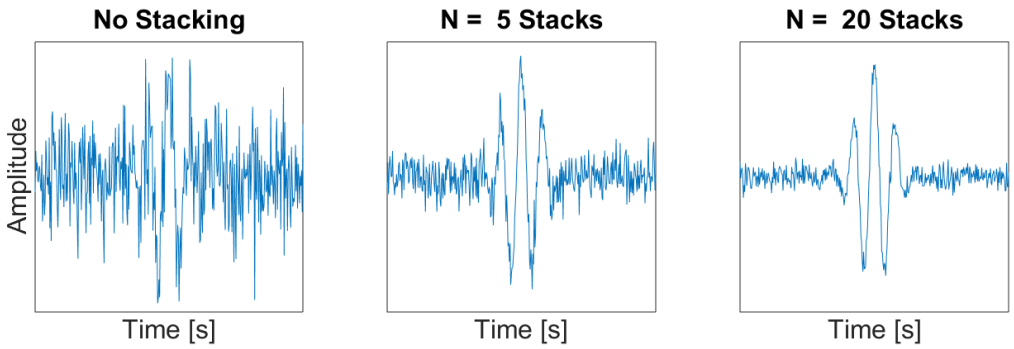

Figure 16: Example of an improved returning signal (increasing the signal to noise ratio-SNR) by stacking which is averaging multiple traces for a specific spatial position
(Copied from: https://em.geosci.xyz/content/geophysical_surveys/gpr/data.html#processing)

2. In-ground clutter noise: localized non-uniformities in the ground cause GPR signal to scatter. Scattering is referring to deviations in the path of the transmitted GPR signal and generates responses which are not coming from the desired targets. Any responses

resulting from undesired objects are considering as noise (Figure 17). Stacking is unable to reduce this type of noise in GPR data.

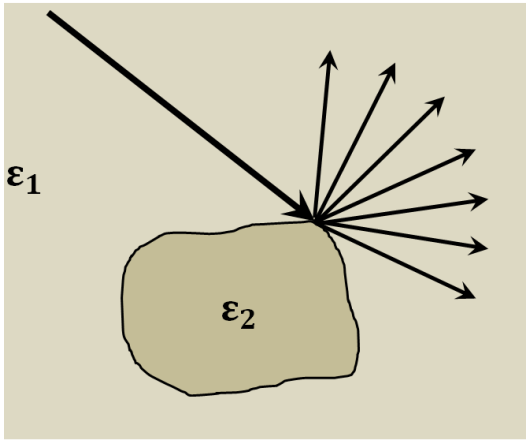

Figure 17: Example of scattering from irregular surface texture
(Copied from: https://gpg.geosci.xyz/content/GPR/GPR_fundamental_principles.html#scattering)

3. Airwave clutter noise: this type of noise is also referring to scattering but this time from objects above the ground. Stacking is unable to reduce this type of noise in GPR data. To avoid measuring signals such as these, shields should be used on the transmitter and receiver and also, coupling of the GPR antennas closely to the ground surface.
4. Time-invariant coherent system noise and "time-variant coherent system noise": a type of noise generated by the GPR support system itself (e.g., ancillary cables, connections, synchronized internal signal leakage, etc.) whose components are interacting with the emissions coming from the transmitter antenna. The term "time-invariant" and "time-variant" is because this noise may be coherent for a specific observation, but it may also be present with minor variations from observation to observation. Unfortunately, stacking cannot improve data including such types of noise.
5. Incoherent system noise: traces not coherent with the surrounding ones may be present in GPR data and these are related to the GPR electronics system.

Before GPR data are composed to form an image of a radargram, some techniques can be applied to eliminate some of the noise types described above. Stacking has already been mentioned and its impact is depicted in Figure 16, where the more the traces that are averaged, the more the returning signal seems to be improved. Stacking is not always beneficial for some types of noise as it can only boost incoherent GPR signals. Incoherent random noise may be also improved applying "smoothing" to the data (using a moving average of some neighboring points) as depicted in Figure 18.

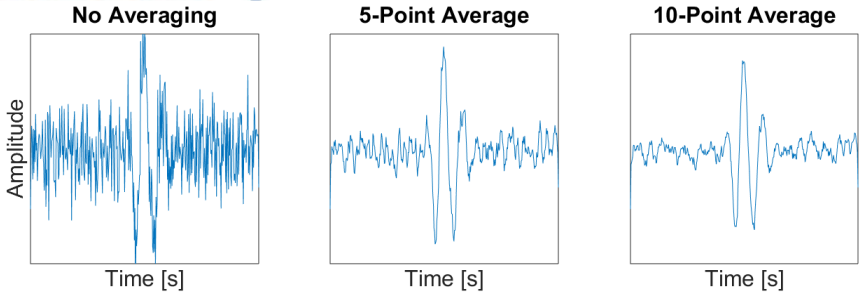

Figure 18: Example of smoothing a trace using a moving average
(Copied from: https://em.geosci.xyz/content/geophysical_surveys/gpr/data.html#processing)

2.7 Regions of the EM field

In previous sections, a type of categorization regarding the GPR operation has been identified: the quasi-static regime ($\frac{\sigma}{\omega\varepsilon}$ >>1), where conductivity is dominant and GPR application should be avoided, and the wave or low-loss regime ($\frac{\sigma}{\omega\varepsilon}$ <<1) where the dielectric permittivity and the wave properties of the EM wave dominate making the use of GPR possible.

Another aspect of great importance for GPR has to do with the distance of an EM signal from its source of emission (for this case the transmitting GPR antenna). EM waves present a different behavior with respect to the distance from their source and they tend to get unpredictable and complex the closer they are to the immediate surrounding area of the antenna. In addition, in close vicinity to the source, fields that decay at different orders of 1/r are observed. The summation of the effects and characteristics of the various EM waves present near the source characterized by exponentially decaying components ($C_1 + C_2/r + C_3/r^2 + C_4/r^3$...) are called the evanescent fields (Umenei, 2011). Due to the complexity and the confusion that dominates this region, the receiver antenna of a GPR need to be placed at distances such that the method can be physically simplified. Additionally, understanding the behavior of the EM waves with distance from the antenna, is very helpful for the construction of finite-sized models (Diamanti and Annan, 2013).

According to Kraus (1988), two zones are observed with respect to the distance between an EM signal and its source: the “near field” and the “far field”. The near field is divided into a non-radiative zone referring as the “reactive near field region”, where energy has a storing character. The other part of the near field is the “radiative zone” or “Fresnel zone” where radiation fields are dominant, and the distribution of energy is dependent on the distance from the source. The far-field or Fraunhofer region is where the fields are independently distributed, and the EM components behave as plane waves (Figure 19). In the far field and the radiative part of the near field, the strength of the electric (E) and magnetic (B) components decreases with distance by the inverse-distance and/or inverse-distance squared. Controversy, in the non-radiative part of the near field, the E and B field’s strength decreases more rapidly with distance (by the inverse distance cubed). This rapid drop in power observed in the near reactive region, ensures that phenomena such the evanescent fields mentioned above are vanished (or almost vanished) at greater distances.

The boundary between the far-field and the near-field Fresnel region is given by:

$$\text{Radius} = \frac{2d^2}{\lambda} \quad (2.47)$$

where, Radius is the distance from an antenna's feed point (the center of a dipole source) and d is the largest dimension of the antenna, or it is equal to λ, whichever is greater. That means that for relatively short antennas (according to the wavelength) the boundary condition in (2.47) can be rewritten as R=2λ. Because GPR systems are ultra-wide band (UWB), the wavelength can vary from $2\lambda_c$ to $\lambda_c/2$ as it is the case for the center frequency (f_c) earlier mentioned. Thus, considering $4\lambda_c$ as the distance from the antenna to the start of the far field region would be closer to the reality (Diamanti and Annan, 2013).

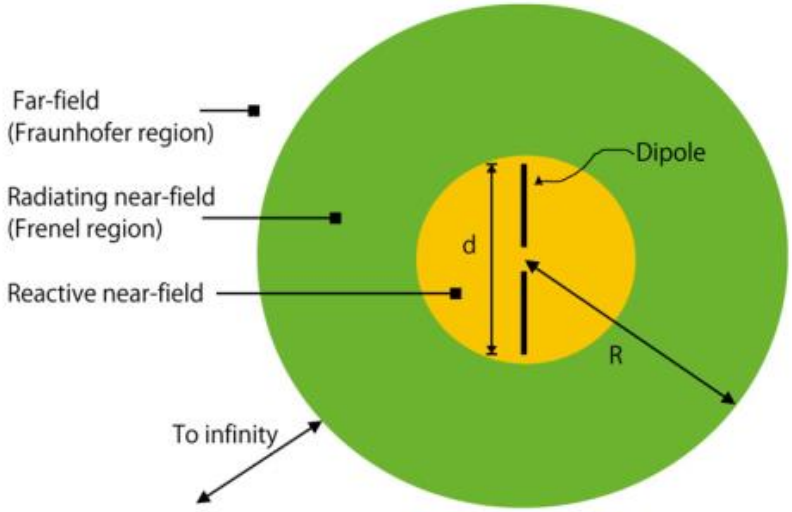

Figure 19: A schematic illustration of the antenna field regions according to the distance (R-Radius) from the fed point of a dipole antenna, with length=d (Kraus, 1988 retrieved by Diamanti & Annan, 2013)

The wave impedance in the near field is also a function of the source, whereas in the far field it depends only on the medium. Charges that are not moving and charges with a constant velocity can only produce reactive fields (e.g., static EM fields) and thus, store energy. An exception is when another circuit is present where there is a storing and a transferring behavior. Charges that are accelerating can produce radiative fields that is the reason why AC sources are required to produce EM radiation (e.g., changing EM fields). Radiating fields emit energy outwards from the source regardless of whether there is a receiving antenna to record the resulting signal or not.

3.An introduction to GPR antennas

Antennas control the emitted and recorded signals of GPR and thus, are the most important hardware component of the system (Diamanti & Annan, 2013). As it was previously mentioned, a transmitting antenna is one which converts electrical signals into EM pulses of short duration and radiates them outwards, and a receiving antenna is converting EM pulses from the received beam into electrical signals. Antennas can be examined by many aspects, some of them will be discussed in this chapter.

3.1 Polarization of GPR signals

Commercially available GPR antennas radiate polarized EM waves. The most common types of polarization are linear, elliptical, and circular (Figure 20). Linearly polarized EM waves are mostly used where the electric and the magnetic fields do not experience a phase difference between each other, and they sinusoidally vary in magnitude as propagating in a medium. In linearly polarization, the E-field does not rotate with time and thus, the only way to observe a change in its orientation in an isotropic material is to reorientate the antennas, e.g., the transmitting and/or the receiving one (Baker et al., 2007). That is why in the case of linear polarization, antenna orientation has a strong impact on a survey. This is not the case for the elliptical or circular (a special case of elliptical) types of polarization, where, the E field is rotating (e.g., the field direction changes) and the amplitude is also varying with respect to time. In this case an ellipse is observed in the field plane and an elliptical spiral is forming with time (Radzevicius and Daniels, 2000; Annan, 2003).

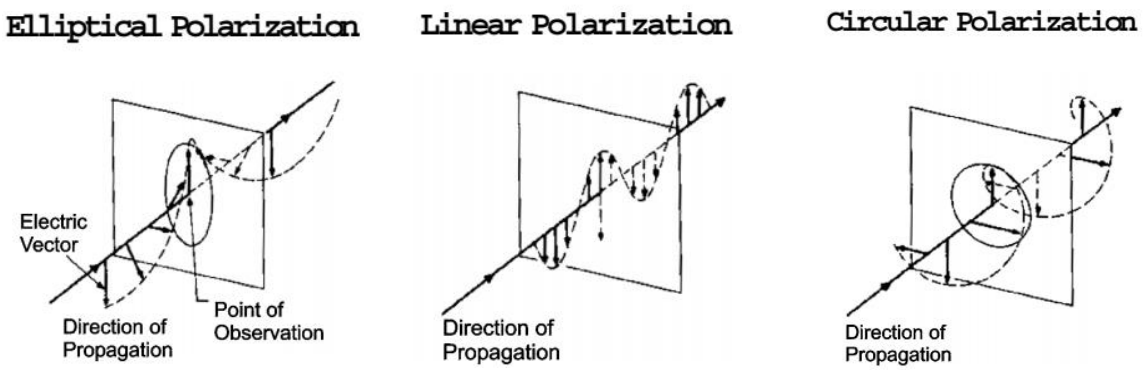

Figure 20: Antennas generate polarized EM waves. The three most common types of polarization are linear (middle), elliptical (left) and circular (right) (Annan, 2003).

Focusing on the linear polarization, as the antennas that are mostly used in GPR are of dipolar nature, EM waves are broadcasted on a single plane (usually the horizontal) and they can experience depolarization when reflecting from some types of surfaces, such as rough interfaces or curve shaped ground (Balanis, 2012; Baker et al., 2007). When reflection occurs, the linear polarized wave will be separated into two components. Its first component will remain in the same direction as the original emitted pulse, while the second component will be orthogonal to the first one. The ratio between those two components is an indicator of the heterogeneity of the medium that the linear polarized wave is travelling through. The discussion made above

concerning the linear, elliptical, and circular EM wave polarization is referring to as polarization due to the antenna construction. Polarization of GPR signals can also be accomplished due to antenna and target orientation.

Polarization due to the antenna orientation is described by the location of the E (electric) and H (magnetic) fields in comparison to the vertical plane of incidence. When changing the orientation of GPR antennas, changes are also observed in the direction of E and H components. For dipole, half wave and center fed antennas, the E-field is broadcasted parallel to the long axis of the dipole source while the H-field is located perpendicular to the long axis of the antenna. There are two types of polarization due to the antenna orientation commonly used in GPR surveys based on the observation of the maximum strength of E and H fields relative to a reference plane (usually the direction of propagation). When E is located on a horizontal plane which is perpendicular to the plane containing the incidence, then this type of polarization is cited as E-horizontal (EH) or transverse electric (TE). When E is contained in a vertical plane parallel to the plane of incidence, then this type of polarization is called E-vertical (EV) or transverse magnetic (TM). The terms “E-plane” and “H-plane” are also frequently used in GPR literature. E-plane stands for the parallel to the length of the antenna plane which contains the dipole. H-plane is used to define the plane which is perpendicular to the dipole and bisecting it (Millard et.al., 2002).

Various antenna configurations (and hence, various polarizations) can be used during a GPR survey and they are characterized by the antennas’ position relative to the direction of the survey line. Assuming that dipole, half wave and center fed antennas are used, to generate and record TE (or else, EH) signals, the transmitting and receiving antennas are placed side by side (with the long axis of the transmitting antenna parallel to the long axis of the receiving antenna) and both being perpendicular to the survey direction. This antenna configuration is the so-called broadside perpendicular (BD-PR) mode. To generate and record TM (or else, EV) signals, antennas must be oriented end to end (the dipole of the TX and the dipole of Rx are aligned) and both placed parallel to the survey line. This antenna arrangement is called endfire parallel (EF-PL). Collecting EH and EV polarized data simultaneously is also possible but not preferred as the signal is neutralized. To do so, the long axis of the Rx antenna is oriented perpendicular to the long axis of the Tx antenna, or reversely. This type of antenna arrangement is known as crossed dipole orientation (Ulaby, 2001; Balanis, 2015; Baker et al., 2007). For GPR, the magnitude and direction of E fields are usually more important than those of H fields. Consequently, the TE and TM mode terms are commonly used because the main interest is weighted more in E rather than H (Jordan and Baker, 2003). The most common antenna arrangements relative to a GPR survey direction are given in Figure 21.

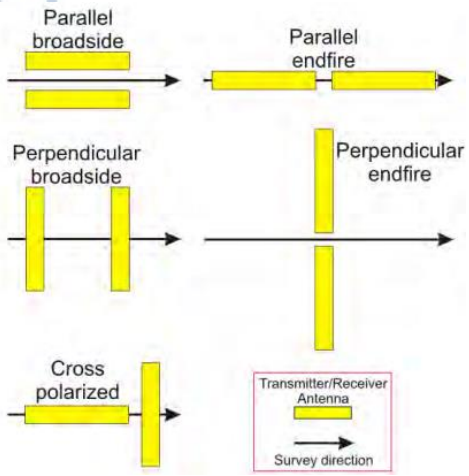

Figure 21: An illustration of commonly used Transmitter/Receiver antenna configurations comparing to the direction of a GPR survey line (Annan, 2005)

Antenna polarization and collection of either EH or EV or both EH and EV waves are all based on the theory of reciprocity which will be discussed later and which ensures that the receiving antenna records the same way in which the transmitting antenna emits. It is also worth to mention that it has been proved that the broadside configuration produces a higher signal to noise ratio compared to the endfire arrangement and thus, it is the most commonly used type of antenna orientation. This can be partially explained from the concept of the footprint of GPR which has the form of an ellipse (Figure 22). The major axis (A) and the minor axis (B) of this illuminated ellipse can be estimated as:

$$A=\frac{\lambda}{4}+\frac{D}{\sqrt{\varepsilon_r-1}} \quad (3.1)$$

$$B=\frac{A}{2} \quad (3.2)$$

where, D is the depth of the projection of the eclipse in the subsurface. From the concept of the GPR footprint it can be observed that when antennas are oriented in the parallel broadside comparing to the line of a survey, then the major axis (A) will be also located parallel to the survey line tracking down target(s) in the preferred direction. On the other hand, when collecting data using a parallel end-fire antenna arrangement, the elongated A axis will be located perpendicular to the survey line increasing the possibility for the returning signal to include off-line and unwanted responses (Baker et al., 2007).

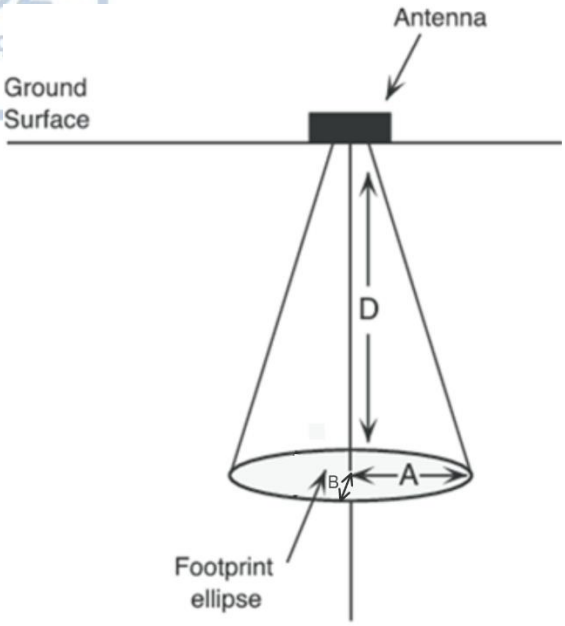

Figure 22: A schematic diagram of the GPR footprint ellipse in depth D from the surface (modified from Neal, 2004)

Knowing in advance the orientation of underground targets would be apparently ideal, as this would make clear how to orientate the antennas and generate pronounced E fields in the appropriate direction. Therefore, any a priori information on the subsurface situation of survey sites is important to have.

3.2 Antenna Radiation Patterns, Directivity & Gain

The term "radiation pattern" stands for the representation of the distribution of the radiated or received energy from an antenna as a function of direction. Radiation can be plotted in terms of power density represented by a poynting vector ($\vec{P}$) usually in a dB scale, as a function of angular position (in polar coordinates: θ, ϕ) and as radial distance from the antenna (Balanis, 1997).

From a three-dimensional (3D) point of view, one can imagine a large sphere which encloses a source/antenna at its center (spherical coordinate system) and as its radius becomes infinity, the far field is approached. The antenna emits EM waves outwards cutting the surface of the sphere. At any point of this imaginary sphere, the E and H fields are tangential to its surface. The E and H field vectors are then decomposed into two components following the directions of $\hat{\theta}$ and $\hat{\varphi}$ unit vectors which are also tangential to the surface of the sphere and perpendicular to one another. The concept of the generation of a far field antenna pattern is shown in Figure 23.

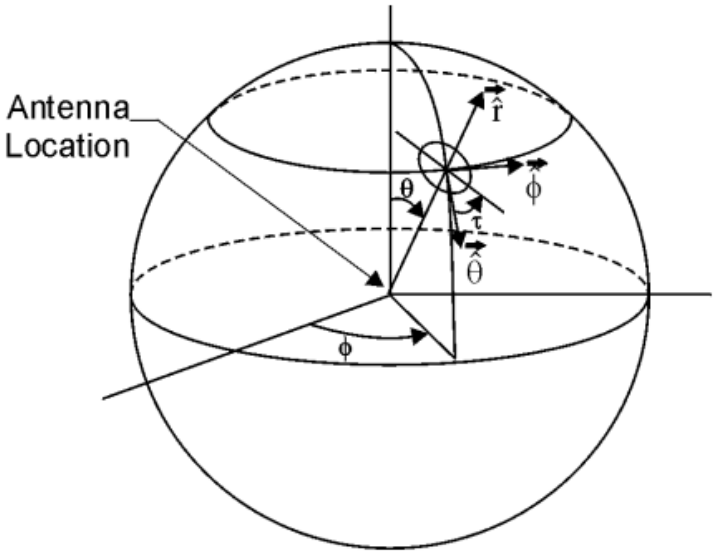

Figure 23: Far field antenna pattern represented by the EM fields (E & H) crossing the surface of a large sphere (Copied from Annan, 2003)

The power patterns are plotted as a function of square of the magnitude of electric and magnetic fields (Annan, 2003):

$$\vec{P} = \vec{E} \times \vec{H} = \frac{|E|^2}{Z} \quad (3.3)$$

They are plotted on logarithmic or commonly on dB scale where the power is increasing from the inner most to the outer most plane of the surface which represents the maximum level of power (0 dB). $\vec{P}$ indicates the power radiating directly outwards at all points composing the sphere. The total radiated power can be calculated as an integration over the surface of the sphere as (Annan, 2003):

$$\iint \vec{P} \cdot \hat{r} dA \quad (3.4)$$

where, $\hat{r}$ is the unit vector in the radial direction.

Antenna patterns are usually graphically depicted as 2D plots dividing the 3D pattern into horizontal and vertical planes. Consequently, a 3D antenna pattern can be mainly decomposed into two 2D figures as indicated in Figure 24, where a schematic diagram of an antenna pattern for a dipole source antenna located in free space is shown from a side and top/end view.

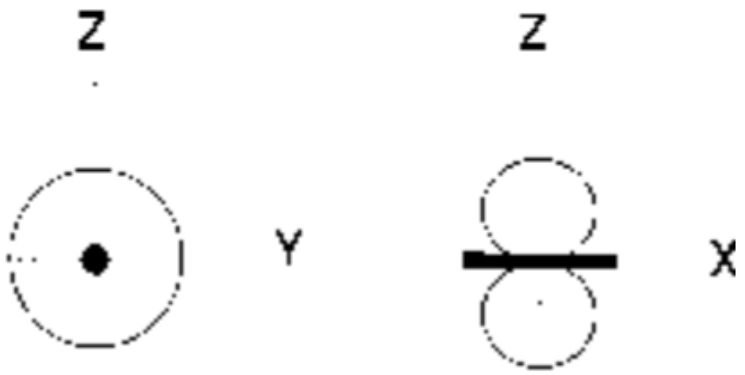

Figure 24: 2D radiation pattern, top view (TE mode- left) and side view (TM mode- right), for a dipole located in free space. The antenna is in the XY plane (Annan, 2003)

It has been already highlighted that GPR antennas do not radiate in an omnidirectional trend. This means that the energy is distributed favoring some directions and thus, knowing the antenna pattern gives the chance to recognize "sensitive" directions and areas in the subsurface where GPR can better image (Annan, 2003). GPR antennas interact with the materials in the ground as they are usually placed on the ground surface or very close to it (0.1 times the wavelength or less). As a result, the antenna pattern is also influenced by the electromagnetic properties of these in-ground materials (Diamanti and Annan, 2013). A schematic diagram of antenna patterns is shown in Figure 25, where the antennas are placed on the air-ground interface.

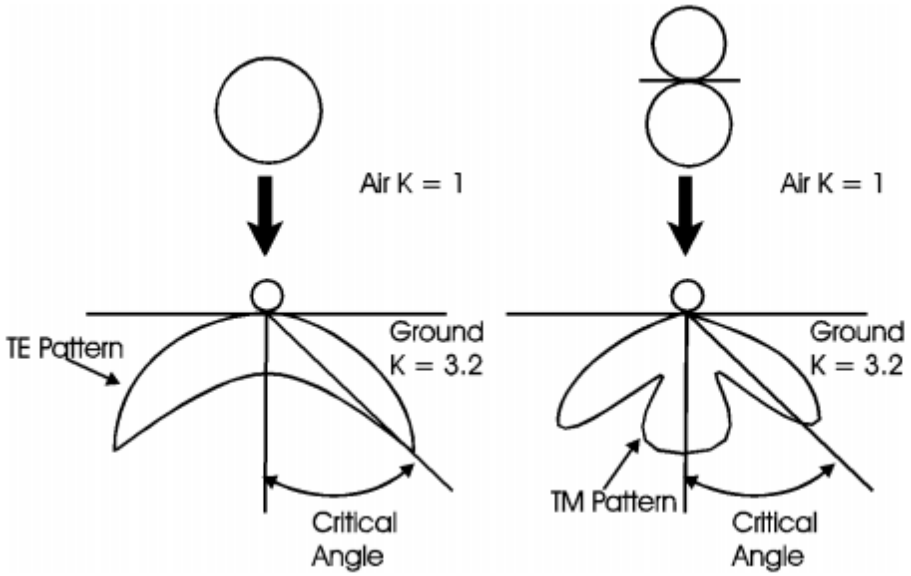

Figure 25:Generalized 2D antenna patterns for a dipole placed on the air-ground interface for TM mode (right) and TE mode (left). The analogous radiation patterns when a dipole is placed in free-space are also shown on the top part of the figure (Annan, 2003)

In Figure 25 it can be observed that when antennas are ground-coupled most of the energy radiated by the antenna goes downwards, into the ground. In the TE pattern of Figure 25, a major lobe of energy is located in the ground at the critical angle between an air / half-space interface

with a relative permittivity (K or ε_r) equal to 3.2. The TM pattern has nulls and the maximum radiation intensity is directly downwards from the antenna at normal incidence. The null points in the TM pattern divide it into the major and minor (or side) lobes (those lobes are not present in the TE pattern). The angle where the energy dramatically decreases in the TM pattern is known as the Brewster angle and it is given by (Baker et al., 2007):

$$\sin\varphi = \sqrt{\frac{1-\left(\frac{\varepsilon r_1 \mu r_1}{\varepsilon r_2 \mu r_2}\right)}{1+\left(\frac{\varepsilon r_1}{\varepsilon r_2}\right)^2}} \ (radians) \qquad (3.5)$$

The maximum intensity of the antenna radiation (the edge of the major lobe) is measured in terms of directivity. Directivity is expressed as the ratio of the intensity in a specific direction and the intensity averaged over all directions from the antenna (Baker et al., 2007). A similar concept to the antenna directivity is the antenna gain. Antenna gain is a measure of power radiated in a particular direction (the peak value of the major lobe in an antenna pattern). A perfectly directive antenna would have only one narrow major lobe without any other distribution of energy, but it is impossible to design such an antenna. Thus, minor lobes are always present in a radiation pattern of a real antenna. The shape of the lobes is changing due to variations in the relative permittivity of the ground (Diamanti and Annan, 2013). More specifically, as the relative permittivity increases the directionality of the antenna is increasing too (Figure 27). As a result, more energy is going straight downwards, and the major lobe becomes narrower (Annan, 2003). Antenna patterns also change when the height of the antenna from the ground changes. As height increases, the energy entering the ground decreases and the distribution of energy into the air is increasing (Diamanti and Annan, 2013).

It is obvious from the TE and TM mode antenna patterns (Figure 25) that a difference in radiation intensities will exist when collecting data with antennas-oriented in an end-fire or a broadside mode. Radiation patterns are commonly defined in the far field region of an antenna and they can be divided into two categories: as power patterns (Equation 3.6) or field (strength) patterns (Equation 3.7), both in a decibel (dB) scale (Millard et al. 2002):

$$\text{Relative Power (dB)} = 10\log_{10}\left(\frac{P}{P_{max}}\right) \qquad (3.6)$$

or,

$$\text{Relative Energy (dB)} = 20\log_{10}\left(\frac{E}{E_{max}}\right) \qquad (3.7)$$

where, P and E are the power and the electric field values - for a specific antenna center frequency - at a specific radius and angle from the antenna, and P_{max}, E_{max} are the maximum observed power and E-field values, respectively. To deal with the ultra-wide band (UWB) nature of GPR, Diamanti and Annan (2013) proposed the use of the total energy instead, throughout the whole frequency spectrum and not only at the antenna's center frequency (Diamanti and Annan, 2013):

$$\text{Relative Energy (dB)} = 10\log_{10}(E_{total}) \qquad (3.8)$$

and

$$E_{total} = \int_{t=0}^{T} E_{(r,\theta)^2} \quad (3.9)$$

where, E_{total} is the total energy at a specific radius (r) and angle (θ). The summation is made over the total duration of the response (from t=0 to the end of the pulse duration T). E is the electric field value at a specific radius (r) and angle (θ) (Diamanti and Annan, 2013 modified by: Warren and Giannopoulos, 2017).

Antenna patterns are usually produced in a computational way (3D or 2D plots) by parametrizing a domain of finite size with the use of a software. The source (Tx) is either an infinitesimal dipole or a model containing the characteristics of a real antenna structure. The Rx antenna is moving at a distance r (which is assumed to be in the far-field region) and captures the fields at various angles around the Tx antenna (e.g., completing a circle around it). This circle is a cross-section which contains the air and the half space region. The Tx antenna is located at the center of this circle and traditionally, antenna patterns are plotted for a single frequency equal to the center frequency of the antenna. The data measured by the Rx antenna are used to produce the antenna pattern which is equal to the Tx antenna pattern due to the theory of reciprocity. Reciprocity ensures that an antenna can be used as both a transmitting or a receiving one. This is because the properties of the transmitting and receiving antennas that exhibit the reciprocity are:

- Equality of antenna patterns
- Equality of antenna directivities/gains
- Equality of antenna effective lengths or effective apertures (how much power is captured from the plane wave and delivered by the antenna).
- Equality of antenna impedances (the output impedance of the Tx is equal to the input impedance in Rx).

In Figure 27, the results of such a simulation are presented for the E and H plane shown in Figure 26. These are antenna patterns close to reality as a model containing the characteristics of a real antenna was used to compute those. The simulation was made for a distance simulating the transition zone between the near and far fields (which is usually the case for the most GPR targets and applications). These plots were created taking into account the UWB range of frequencies of the GPR signals. The results were computed according to equation (3.9) divided by an electromagnetic impedance (Z) value.

More specifically, the input results for generating Figure 27 ((a) and (b)) were obtained by the software GprMax3D (Giannopoulos, 2005), which is a GPR wave simulator using the finite-difference time-domain (FDTD) method (Taflove, 1995; Yee, 1966). This figure shows the antenna field patterns of a resistively loaded and shielded antenna (dipole) located in a finite size domain. The Tx-Rx pair was located at height 2cm off the air-ground interface (90^o-270^o axis) and the half-space (below the 90^o-270^o axis) was modelled employing various electric permittivity values. As mentioned above, to generate the patterns of Figure 27, the radiated energy per steradian was

divided by the input energy at the source. The results were plotted in dB at a logarithmic scale and the radiated energy was computed over the whole frequency content of an antenna of f_c equal to 1000MHz. In both E-plane and H-plane of Figure 27, one can see the back lobes (above the 270°-90° axis) which is the distribution of energy into the air. It is also obvious, that for both patterns the major lobe of energy is located directly under the antenna (at 180°) and as the electric permittivity increases, the main lobe becomes more focused (an increase of directivity and gain is achieved) and at the same time, the energy emitted into the air is slightly increased. In the E-plane pattern, the minor side lobes are obvious and the distribution of energy is symmetric. For the H-plane, the pattern is slightly asymmetrical because the Rx antenna and its shield are not symmetric to the Tx center (i.e., feed point). The spike shaped structure observed in the E-plane between the air and the half-space is an artifact because a single value of Z was used (Diamanti and Annan, 2013).

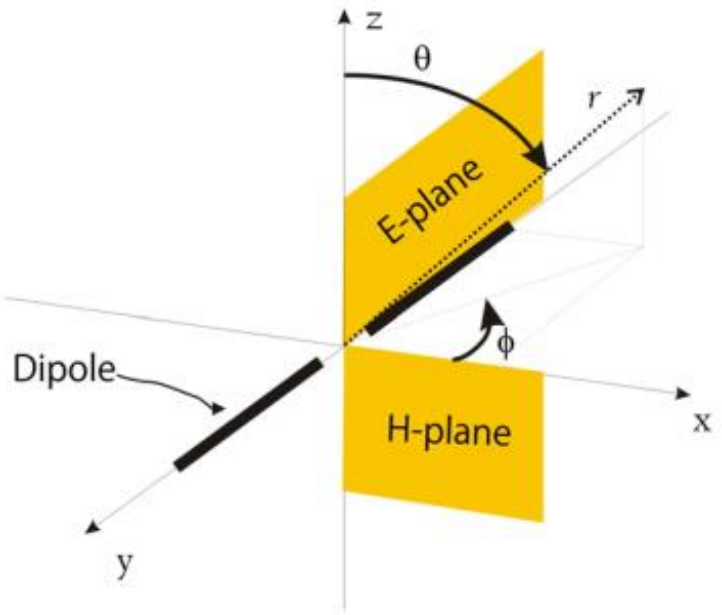

Figure 26: E- and H-planes of a dipole oriented along the y-axis (copied from Diamanti and Annan, 2003)

To summarize, it is very important for a GPR survey to know how the energy of the antenna is spatially distributed and take advantage of the position of local maxima or minima (major and minor lobes) of the emitted power. It is worth to mention that antenna patterns are mostly influenced by the arrival of the direct wave because of its large and powerful response. As it was previously mentioned, antenna patterns are governed by many factors such as the height of the antenna from the air-ground interface, the electromagnetic properties of the subsurface, the orientation of the antennas and even the topography or the anisotropy of the ground (Giannopoulos and Diamanti, 2005,2008; Lampe and Holliger, 2003; van der Kruk et al., 2012).

This thesis was inspired by the concept of the GPR direct wave – the wave that reaches the Rx antenna first. The fact that it is the strongest response in a GPR record, often shadowing other important responses from the subsurface, made us want to study it further. Our major purpose

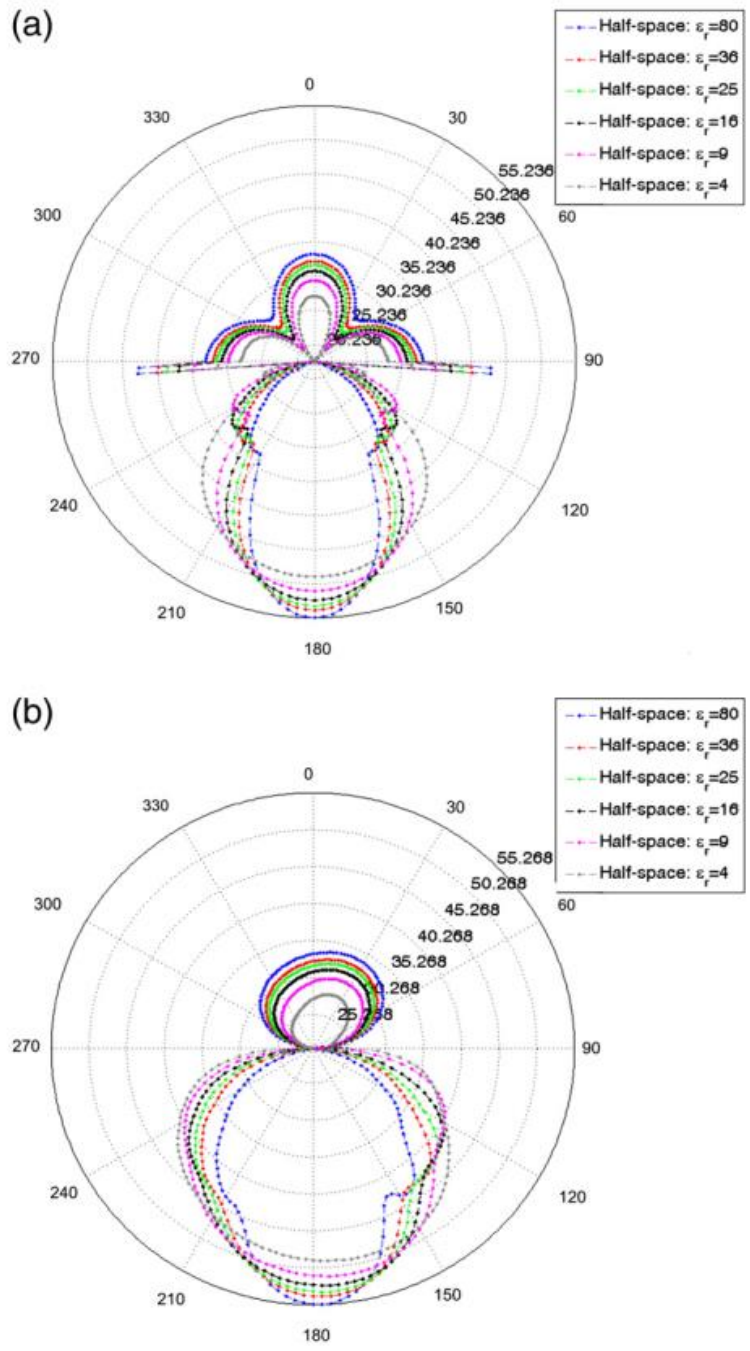

Figure 27: The distribution of energy for a shielded antenna located above a half-space with various dielectric properties (a)E-plane (b) H-plane (copied from Diamanti and Annan, 2003)

was to discover if there would be an optimum position of the Rx antenna relative to the position of the Tx antenna where a local minimum of the GPR direct wave could be measured in another than the standard mode of GPR antenna configuration, the broadside perpendicular mode. So, it was desired to find a possible Tx-Rx antenna orientation/position that the direct wave would be minimum but yet, the energy coming from the reflected events would not dramatically change.

4.Typical GPR assumptions

Field regions and conditions of low loss or quasi-static criteria were previously defined in an effort to understand the characteristics of GPR signals. To simplify the quantitative approach for the GPR method, some typical GPR assumptions are made. These assumptions are listed below and are valid for this thesis too:

1. The materials of the subsurface are homogenous and isotropic and due to the antenna reciprocity, the EM waves are considered to travel in a two-dimensional space.
2. In every survey, GPR is assumed to perform in a range of frequencies where the emitted signals exceed the transition frequency of the materials and the materials are nonmagnetic, as it is usually the case.
3. GPR is also assumed to perform under low-loss conditions where displacement currents are dominant and are favoring propagation and reflection of EM waves, rather than phenomena of induction. Thus mathematic relations for the quasi-static region are neglected.

These criteria should be considered before a GPR survey to decide whether GPR is a useful tool for imaging the subsurface. Especially for the assumption of number 3, performing GPR in an area where the low-loss criteria are violated, will result in a very few cycles (if any) of EM waves oscillation and thus, using GPR as a reflection imaging technique will be challenging or even impossible (Baker et al., 2007).

5.Materials and Methods

This thesis focuses on the study of the behavior of the direct wave (DW) which is the first signal to arrive from the transmitting to the receiving antenna of a GPR system. This DW consists of two parts: the direct air wave (DAW) and the direct ground wave (DGW). Many studies have been published in the past, highlighting the use of the direct ground wave in measurements considering the variation of soil moisture and soil water content (e.g., Marcak et al., 2018; Klenk, 2012; Grote et al., 2010; Galagedara, 2003; Huisman et al., 2003). In practice, the Tx and Rx pair are usually in near proximity between each other when a GPR survey is performed and thus, the direct air and direct ground waves are usually recorded united, generating a powerful signal which may mask the reflections from desirable in-ground targets. Commercially available processing software for GPR data is equipped with filters that can remove the DW from a radargram (e.g., background average subtraction - BAS) but during this processing, useful data may be eliminated too. The major aim of this work is to study the behavior of the DAW and DGW as a common arrival (i.e., DW) and as separated entities, in order to detect weak spots of energy in their distribution at early times while at the same time, the signal from underground reflectors (reflected wave – RW) remains almost unchanged in amplitude.

As seen from the radiation patterns of the previous chapter, the GPR antennas' emitted energy, which is mostly represented by the direct wave, is weak in some specific polar coordinates around the Tx antenna. Relying on this fact, field measurements were designed and also, synthetic data were produced in an appropriate trend. More specifically, a homogenous (as possible) piece of earth was spotted in the field, hosting a reflector which was horizontal at its most part. The area was found after GPR measurements (in the reflection mode) were performed in a 5m×5m grid using the SmartCart GPR bistatic system from Sensors & Software. The antennas were oriented in the broadside perpendicular configuration and had a center frequency of 500MHz. The structure of the subsurface was also validated from an electrical resistivity tomography (ERT) performed in one parallel and one perpendicular line following the GPR lines, crossing the center of the GPR grid with the use of the multichannel system Syscal Pro of Iris instruments at a dipole-dipole electrode arrangement. WARR measurements were also conducted to estimate the velocity of the upper layer and the arrival times for each of the Rx responses were calculated according to the equations (2.1), (2.2) and (2.3).

A SmartCart is a bistatic GPR system configuration designed by Sensors & Software and consists of the antenna pair, a Digital Video Logger (DVL) unit which displays and stores the collected data?. All the cable connections of the system, including power, are connecting to the DVL (Tx and Rx ports, Battery port, Serial port for GPS, Odometer Cable). The source of power is the SmartCart 12V (9 Amp-hr) battery and the odometer is a distance calculator attached to the SmartCart wheel. Even though the odometer is calibrated in the factory, it is essential to calibrate it periodically to ensure accuracy of position. This is of great importance because the calibration can change when using the SmartCart on different surface materials that have varying smoothness (e.g., pavement, grass, sandy soil etc.). The GPR system will trigger the transmitter to fire and collect a data trace either by the odometer (as the odometer wheel moves one step size), manually (in difficult terrain where antennas cannot be moved easily or at regular time

intervals) or at a free run mode which allows the system to pulse based on a specified time interval or continuously in cases where collecting data with the odometer is impractical or impossible (e.g., collecting data from a boat). The optional SmartCart GPS mount is designed to mount a GPS receiver, which can log GPS information during data collection (Sensors & Software, 2005).

The Syscal Pro is a product from Iris Instruments. It is an all-in-one multinode resistivity and induce polarization (IP) sounding and profiling system used for environmental and engineering geophysical studies. Its source can provide a maximum of voltage of 800V and current of maximum intensity of 2.5A. The receiver can calculate the voltage difference between 10 dipoles simultaneously with accuracy of 1Mv and an error of 0.2%. The system can host 48 electrodes and the measurements are pre-designed by protocols included in the instrument and created by appropriate software (e.g., Electre Pro). These protocols include the various arrangements of the electrodes that can be applied in a survey. Images from the Syscal Pro instrument and the SmartCart GPR system are illustrated in appendix A.

To identify the weak spots of energy (in terms of polar coordinates), the Tx antenna was placed above the ground at the center of the horizontal part of the reflector according to the results of the grid. The Tx-Rx distance and the orientation of the antennas are critical factors that impact the distribution of the EM signals around the transmitter, as discussed earlier, and thus, the experiment was performed for both the perpendicular broadside (PR-BD) and parallel end-fire (PL-EF) antenna orientations (from now on they will be mainly referred to as broadside and endfire for brevity)and for various Tx-Rx radial distances (0.23m, 0.5m and 1m). More specifically, the Rx was initially placed at a radius distance of 0.23 m and at 0^0 from the transmitter completing a circle around it with a step of 10^0. The antennas were initially oriented at the PR-BD mode along the 0^0-180^0 line. The same process was repeated with the antennas been oriented in the PL-EF mode along the 0^0-180^0 line. Following the same logic, the 0.5m and 1m radial distances were performed, where for the radius distance equal to 1m a sample step of 5^0 was used for both the PR-BD and PL-EF configurations. The results were visualized by the software EKKO_project V5 (Sensors & Software, 2017).

Apart from the field data, synthetic data were also produced using the GprMax v3.1.5 software (Warren et al., 2016). gprMax is a GPR simulator that employs 3D FDTD numerical modelling (Taflove, 1995; Yee, 1966) and it has been applied for various cases of GPR numerical modelling, such as modelling pavement cracks (Diamanti and Redman, 2012), rough interfaces and subsurface heterogeneities (Giannopoulos and Diamanti 2008) and modelling real GPR antenna systems (Diamanti et al., 2012; Warren and Giannopoulos, 2011). For this study, a 3D half space with a horizontal interface was modelled. Above the half space a source of EM energy was placed and the Rx antenna received signals at radial distances of 0.23m, 0.5m and 1m with a step of 5 degrees around a circle. In the following sections more information about the area of interest, the field measurements and the production of the synthetic data will be presented.

5.1 Field Measurements

5.1.1 Area of Interest

Field measurements were performed on the 13th and 14th of July, 2020 at the administrative district of Chalkidiki, Greece, and more specifically nearby the lagoon of Agios Mamas settlement, as depicted in Figure 28 from Google Earth.

Figure 28: The field test area annotated by the red square and located in Agios Mamas settlement (Chalkidiki, Greece)

Agios Mamas is located in the North-East part of Greece and from a geotectonic point of view, it belongs to the wider tectonic zone of Axios (or Vardar zone). Axios zone is a part of Internal Hellinides and it is divided into three subzones from East to West: Peonia, Paiko and Almopia sub-zones (Mercier, 1966), as indicated in Figure 29. The geological setting of the area where the field experiment was performed corresponds to Peonia's subzone lithology.

Peonia subzone mostly consists of Mesozoic sedimentary and igneous rocks and a variety of metamorphic rocks and ophiolites (including Oreokastro ophiolites) with mélanges. Oreokastro ophiolites with the ophiolites of Guevguely are forming the Innermost Hellenic Ophiolite Belt (Bebien et al., 1986). The presence of ophiolites partially explains the geotectonic evolution and it is therefore, crucial for the still controversially discussion about the geodynamic interpretation of the whole Hellenides (Kostaki et al., 2013).

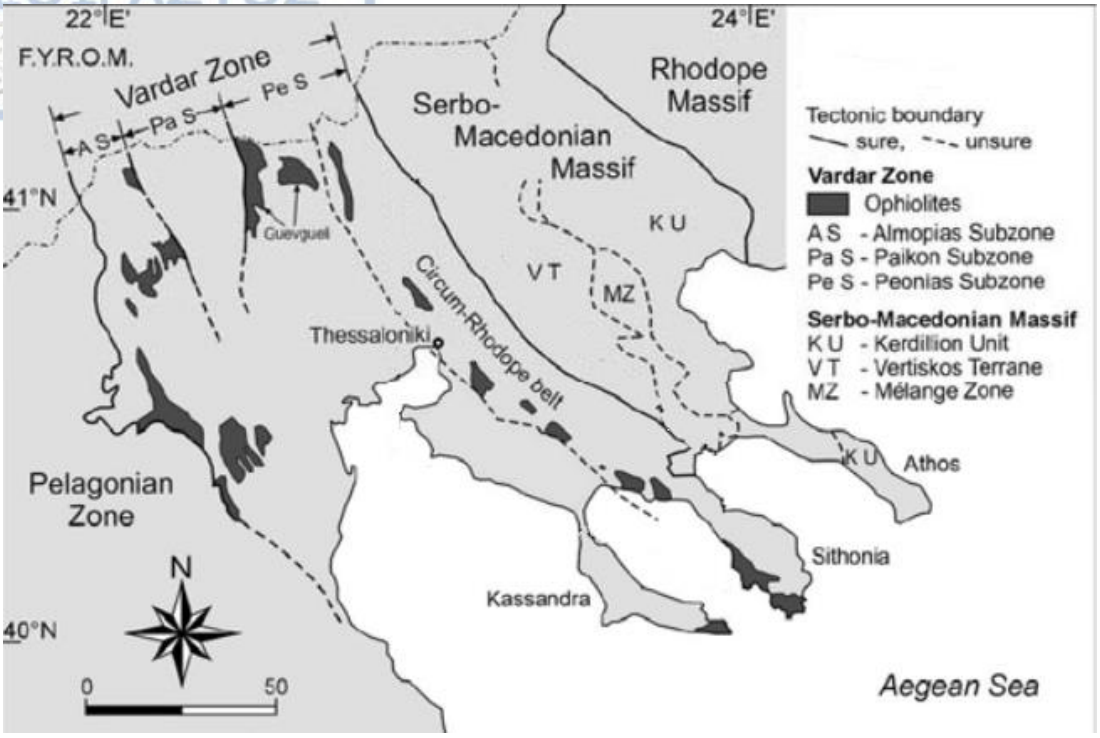

Figure 29: Map indicating the geotectonic framework of the area of interest in the Vardar zone of northern Greece including the main neighboring geotectonic zones (Kockel et al., 1977 modified by G. Meinhold et al., 2009)

The area was chosen because an almost flat, homogenous layer was detected in the subsurface by using both the GPR and ERT methods, as previously discussed. This horizontal-like reflector allowed for carrying out the GPR measurements where we wanted to study the behavior of both the GPR direct wave and reflected wave events without them being influenced by surface and/or subsurface toughness and increased scattering due to layer heterogeneity.

5.1.2 GPR grid

A 5m×5m GPR grid (Figure 30 & Figure 31) was deployed in the XY plane using a SmartCart and antennas of fc equal to 500MHz with a broadside arrangement, from Sensors & Software. More specifically, ten GPR lines at reflection mode, with 0.5m spacing were performed at the SW-EN direction (x-lines) and ten lines at reflection mode with 0.5m spacing were performed at SN-EW direction (y-lines). The EM wave velocity was initially chosen at 0.100 m/ns, which is a typical GPR wave velocity in the subsurface. As it will be discussed below, we carried out WARR measurements to define this velocity more accurately. From the GPR grid depth slices, a square-like area of approximately 2m×2m where the reflector seemed to be horizontal (Figure 31b) was isolated and chosen as the appropriate location for carrying out the experimental part of the study. In Figure 31, the depth slices generated from the grid and visualized by the EKKO_Project software are illustrated at 0m, 0.60m and 1m. In Figure 31b, the most horizontal part of the reflector is annotated by the solid black square. According to the radargrams, using a typical velocity of 0.100m/ns, the almost horizontal reflector is located at a depth of almost 0.55m-0.60m. More information about the acquisition of the GPR grid is presented in Table 3.

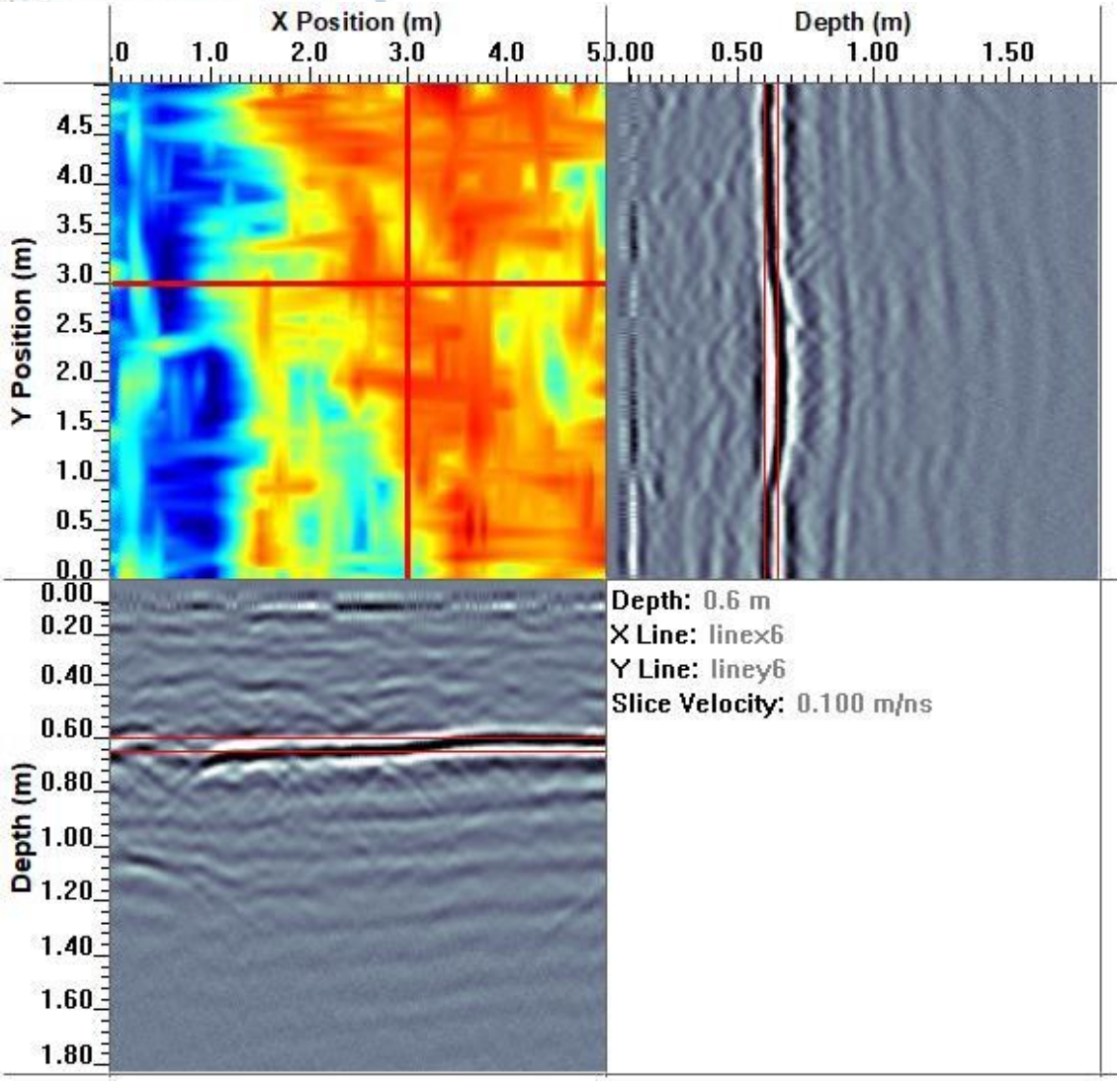

Figure 30: 3D Preview of grid lines x6 and y6. The red solid lines in the GPR cross sections indicate the depth at which a GPR slice is shown (i.e., the 0.6m depth slice)

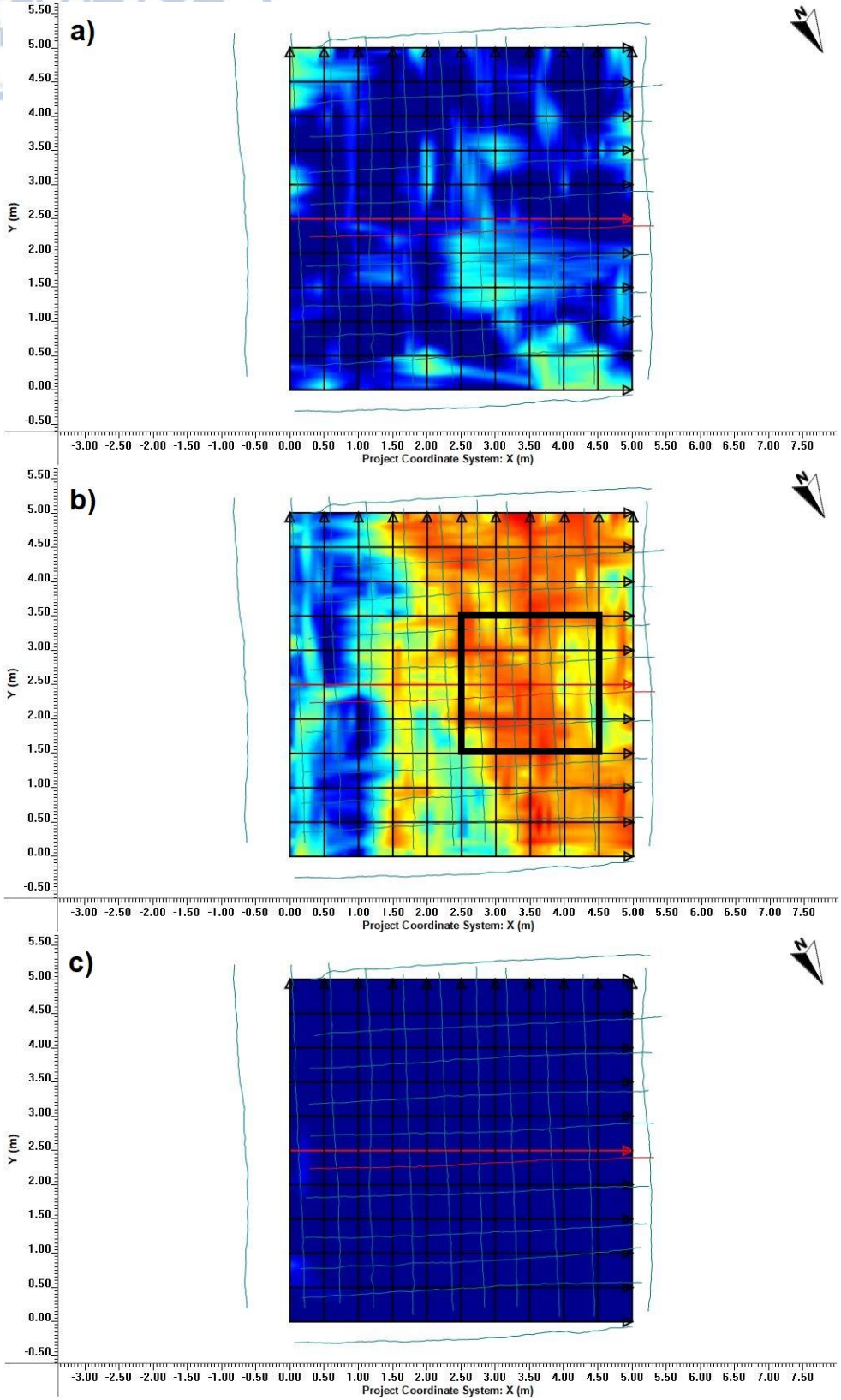

Figure 31: Depth slices from the GPR grid – from top to bottom: a) depth slice at 0m b) depth slice at 0.60m c) depth slice at 1m. In the middle depth slice, the area where the GPR measurements around a circle were performed is depicted with a black solid square.

Table 3: Information on the data acquisition of the GPR grid

Survey Type	*Reflection*
Frequency (MHz)	*500*
Time Window (ns)	*40*
Start Position (m)	*0*
End Position (m)	*5*
Step Size (m)	*0.02*
Number of Traces	*251*
Points per Trace	*200*
Antenna Separation (m)	*0.23*

5.1.3 Wide Angle Reflection Refraction (WARR) measurements

After the area hosting an almost horizontal subsurface reflector was spotted from the GPR grid results, WARR measurements were performed with the pulseEKKO PRO GPR system. This system has its Tx and Rx transducers separated, a fact which permits to carry out such measurements that lead to estimating a more representative GPR velocity in the upper layer and calculating more properly the arrival times for each of the GPR responses (DAW, DGW and RW). To perform WARR measurements, the Tx is placed at a stable position and the Rx is moving away from the Tx at a fixed step (Figure 32). In this case, antennas of f_c equal to 500MHz were used, the Tx-Rx starting antenna separation was 0.275m and the Rx step size was set to 0.02m.

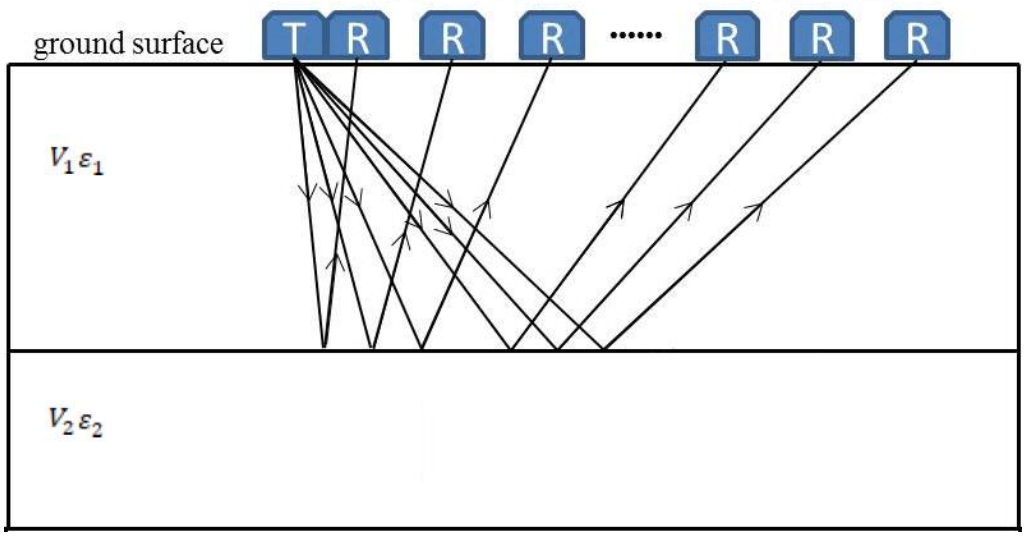

Figure 32: Schematic illustration of WARR measurements performance where the Tx antenna is stable at one position and the Rx antenna is moving away at a specific spatial step. The uppermost layer corresponds to V_1, ε_1 and the second layer is characterized by V_2, ε_2. The returning signal is the reflected wave (RW) between the interface of layer1 and layer2. The reflection is captured at various angles (modified after Du et al., 2020).

At a SN-EW direction a WARR line was performed with the antennas-oriented in the PD-BD mode. Hyperbola fitting was applied at the RW from the subsurface interface using the EKKO_Project software and the new velocity obtained was 0.143m/ns, as it is indicated in Figure 33. WARR measurements were performed at various Tx-Rx angles in respect to the subsurface interface and using various Tx-Rx orientations. The output images from these results are given in Appendix B.

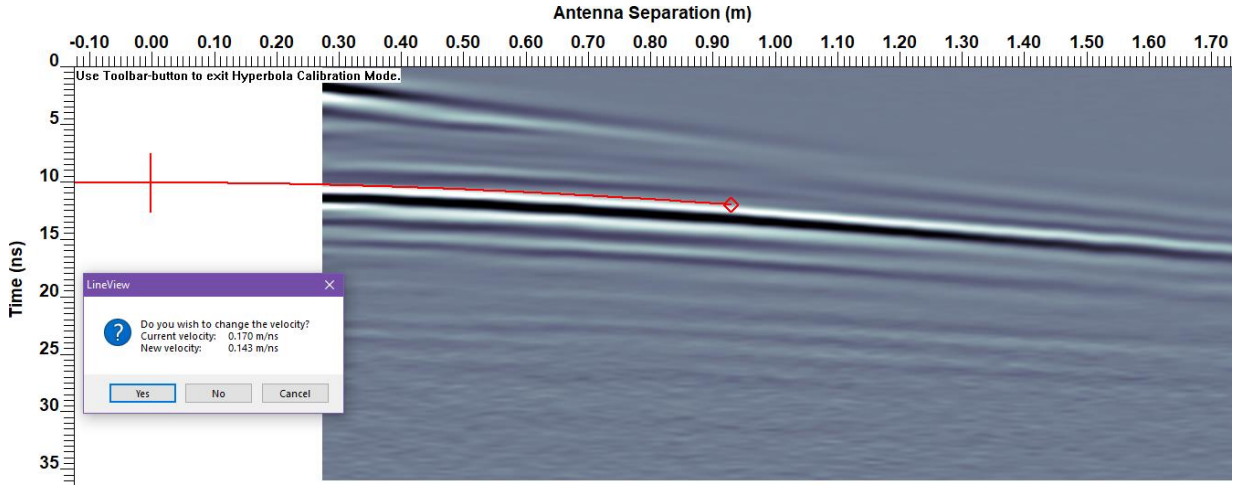

Figure 33: Hyperbola fitting in WARR measurements applied to the RW from the subsurface interface to estimate a more representative GPR wave velocity of the uppermost layer. In the horizontal axis the antenna separation is presented in meters and the vertical axis is showing the time in ns. The new velocity is estimated at 0.143m/ns

After the calculation of a more representative velocity of the GPR waves in the uppermost layer, the depth of this reflector needs to be re-estimated. When applying v=0.143m/ns instead of the initial, typical value of v=0.100m/ns used, the depth of the reflector is estimated at ~0.75-0.8 m instead of the range of ~0.55-0.60 m that was estimated before the hyperbola fitting on the WARR type measurements (Figure 34).

Using equations in (2.1), (2.2) and (2.3), the arrival times at the Rx for the DAW, DGW and RW events can be calculated for a fixed Tx-Rx distance. In Table 4, the arrival time for each of the three responses and for Tx-Rx distances equal to x= 0.23, 0.5 and 1m are shown (Table 4). Note that these distances represent the three radii that we performed our field measurements around a circle. For the calculations of Table 4, the depth of the reflector (h) was chosen at 0.75m and the velocity of the upper layer (V_1) was considered equal to 0.143m/ns.

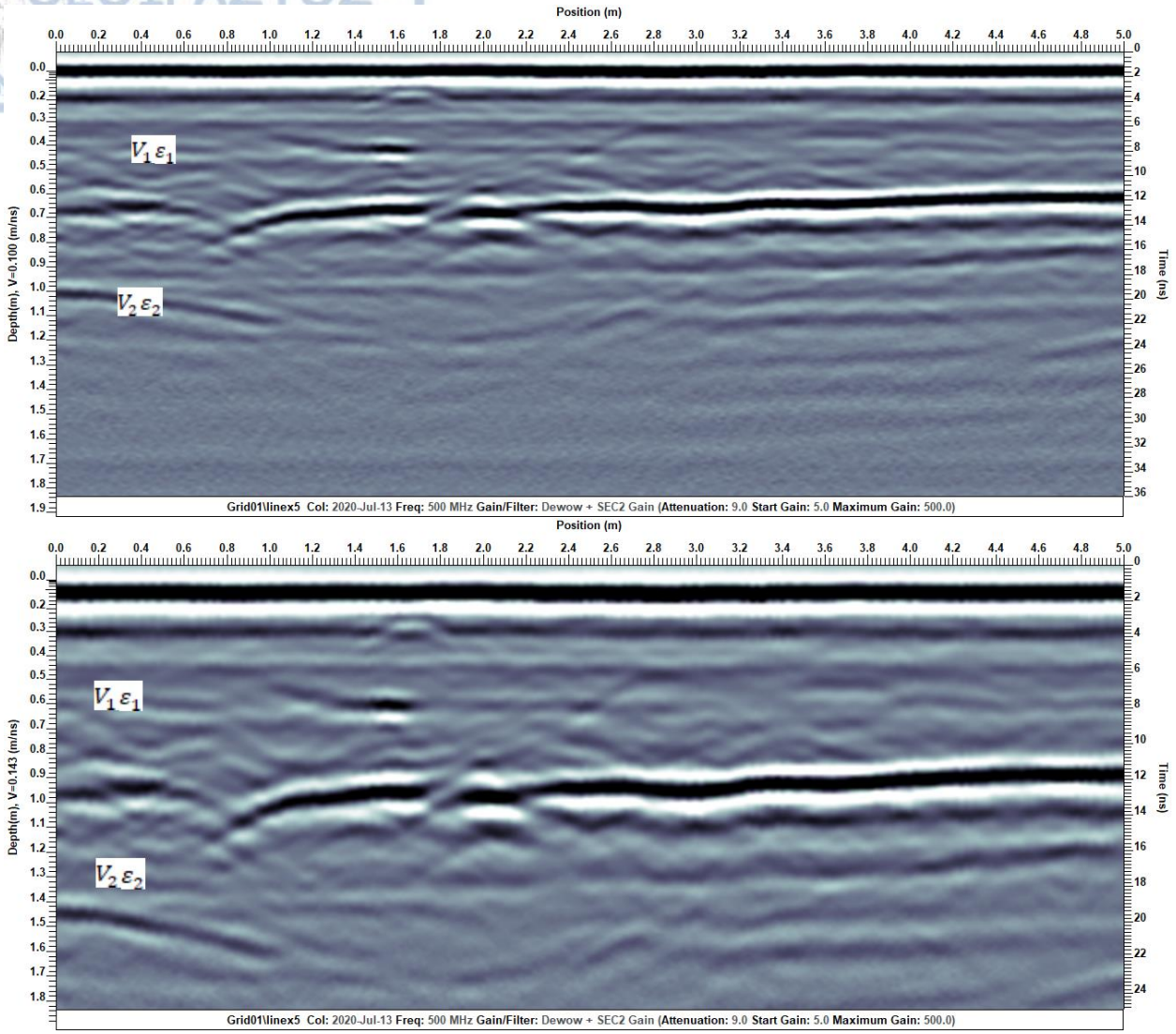

Figure 34: Line x5 from the GPR grid before (top) and after (bottom) applying the velocity estimated from the WARR measurements (v=0.143m/ns). The new depth estimation is revealing that the reflector is located at approximately 0.75-0.8m under the ground surface. The uppermost layer is indicated in the picture with V_1, ε_1 and the second layer is represented by V_2, ε_2. The x axis shows the position of the measurements (m) along the measured line and the vertical axis is depth (m).

Table 4: The arrival times at the Rx (in ns) for the direct air (t_{air}), direct ground (t_{ground}) and reflected ($t_{reflected}$) waves, for Tx-Rx distances of 0.23, 0.5 and 1m

Radius (m)	**0.23**	**0.5**	**1**
t_{air} (ns)	0.76	1.66	3.33
t_{ground} (ns)	1.61	3.50	6.99
$t_{reflected}$ (ns)	10.61	11.05	12.60

5.1.4 Electrical Resistivity Tomography (ERT)

An Electrical Resistivity Tomography (ERT) was performed in the area to validate the structure of the subsurface described by the GPR grid. The first ERT (DD1) was deployed following the x5 line of the GPR grid. The second ERT (DD2) was carried out almost perpendicular to the first one, following the y5 line of the GPR grid.

ERT belongs to the geoelectrical methods which are capable of mapping the subsurface at great depths through the variations of the geoelectrical properties of the subsurface. Electrical resistivity ρ (Ohm·m) is the opposition of a material to the electrical flow currents. To perform a single resistivity measurement, two pairs of electrodes are placed on the ground. The first pair are the electrodes needed to induce in the subsurface current (usually denoted as: A and B or C_1 and C_2), and the other two electrodes (M and N or P_1 and P_2) are used to measure the potential difference, as it is illustrated in Figure 35. When a series of single measurements with 2 pairs of electrodes, based on a given predefined protocol of measurement sequence, this type of acquisition is called ERT and it produces a 2-D image of the subsurface in terms of electrical resistivity variations (Tsourlos, 1995).

The ohmic resistance of the ground can be calculated as:

$$R=\frac{V}{I} \tag{5.1}$$

where I, is the intensity of the current injected into the ground through the A, B electrodes, and V is the potential difference captured by the electrodes M, N. The electrical resistivity of a cylindrical-shaped sample of a conductor is given by:

$$\rho = \frac{RS}{\mathrm{L}} \tag{5.2}$$

where, S is the cross-sectional area and L is the length of the sample.

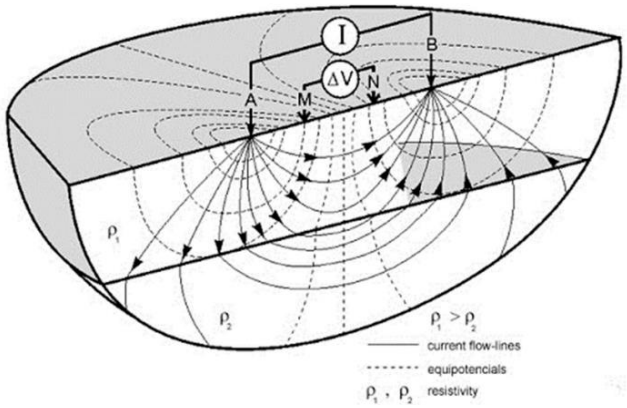

Figure 35: A schematic diagram of the performance of a single resistivity measurement where: A, B are the electrodes used to inject an amount of current (I) into the earth, M, N are the electrodes used for the calculation of the potential difference (ΔV) and ρ_1, ρ_2 are the electrical resistivities corresponding to the first and the second layers, respectively (Knödel et al., 2007 retrieved by Nivorlis, 2020).

The four electrodes needed to perform a geoelectrical survey can be arranged at various positions depending on the aim of a survey and/or the geology of an area prospected. Every arrangement has a unique geometry characterized by the so-called geometrical factor (G or K). When the position of the electrodes is taken into account, the equation in 5.2 can be redefined as:

$$\rho = \frac{2\pi V}{I} \cdot \frac{1}{\frac{1}{AM} - \frac{1}{BM} - \frac{1}{AN} + \frac{1}{BN}} = \frac{2\pi V}{I} \cdot G \qquad (5.3)$$

The electrical resistivity calculated from equation (5.3) corresponds the true electrical resistivity only when homogeneous and isotropic media are considered. Earth is, in almost all cases, heterogeneous so, the previous estimations do not generally correspond to the true electrical resistivity of the subsurface. The electrical resistivity calculated by equation (5.3) represents a type of weighted average of the resistivities of the different in-ground materials and is therefore called the apparent resistivity (Cook and Van Nostrand, 1954; Tsourlos, 1995). The values of the real resistivity can be obtained through the inversion of the apparent resistivity with the use of specific software. In this thesis, the DC2Dpro software (Kim, 2010) was used.

In Figure 36, the most typical arrangements of electrodes are presented with their corresponding geometrical factors. For this study, the dipole-dipole arrangement was used (Figure 36D) where the electrodes were located at a straight line (i.e., axial dipole array). The dipole-dipole electrode array is sensitive to changes in the resistivity of the materials with depth (Tselentis and Paraskeuopoulos, 2013).

The resistivity of a soil or rock is dependent on several factors that include the amount of interconnected pore water, the porosity, the amount of total dissolved solids (TDS) such as salts and clays (Saad et al., 2012). More information about the 2-D DC resistivity method is given by Zohdy and others (1974), Reynolds (2011) and Rubin and Hubbard (2006).

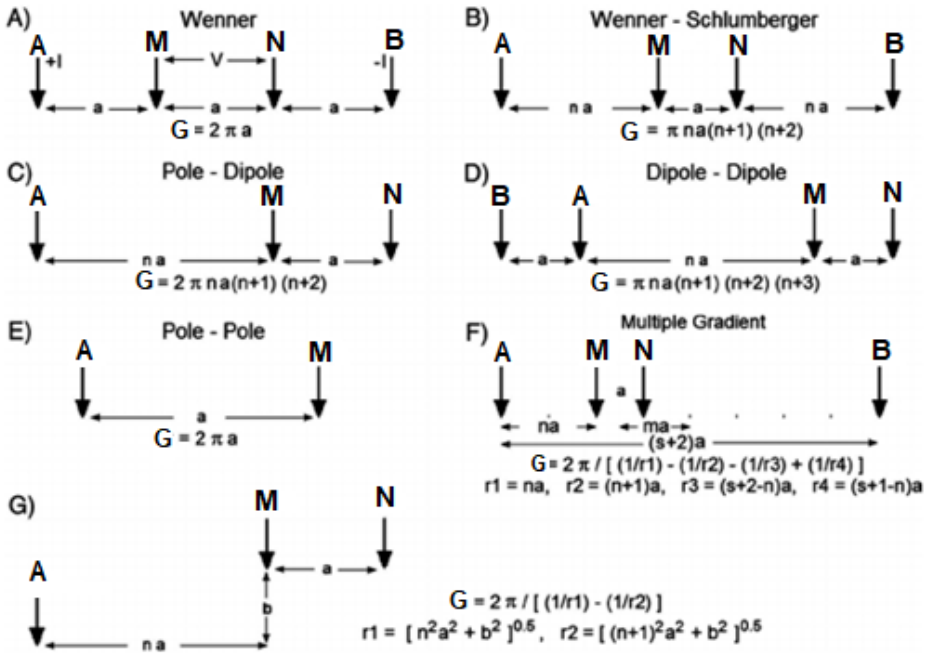

Figure 36: The most common arrangements of electrodes for an ERT application with their corresponding geometrical factors. A, B is the position of the electrodes needed to inject current, M, N is the position of electrodes needed to measure the potential difference and G is the geometrical factor characterizing each of the arrays (modified after Loke et al., 2013)

After carrying out the two ERTs, the results of their inversion show a good correlation with the grid lines from GPR. The comparison of DD1 with the corresponding x5 GPR grid line and of DD2 with the y5 grid line is depicted in Figure 37 and Figure 38, respectively. Each of the ERT is illustrated with rainbow color scale where with dark red colors high values of resistivity are presented and with light blue colors low values of resistivity and thus, high conductive materials are depicted. Both DD1 and DD2 indicate the existence of an uppermost layer of high resistivity values (~700-1000 Ohm·m, dark red color) and with a thickness of ~0.7-0.8m. This layer corresponds to a sandy soil which was visible in the surface. Below this almost horizontal reflector, there appears to be a second layer that has low to intermediate values of resistivity (~8-68 Ohm·m, green color). At approximately 1.8m depth, a quite conductive medium is depicted with blue color (~2-3 Ohm·m) which could be either the salty water table or saturated sandy-clay soil.

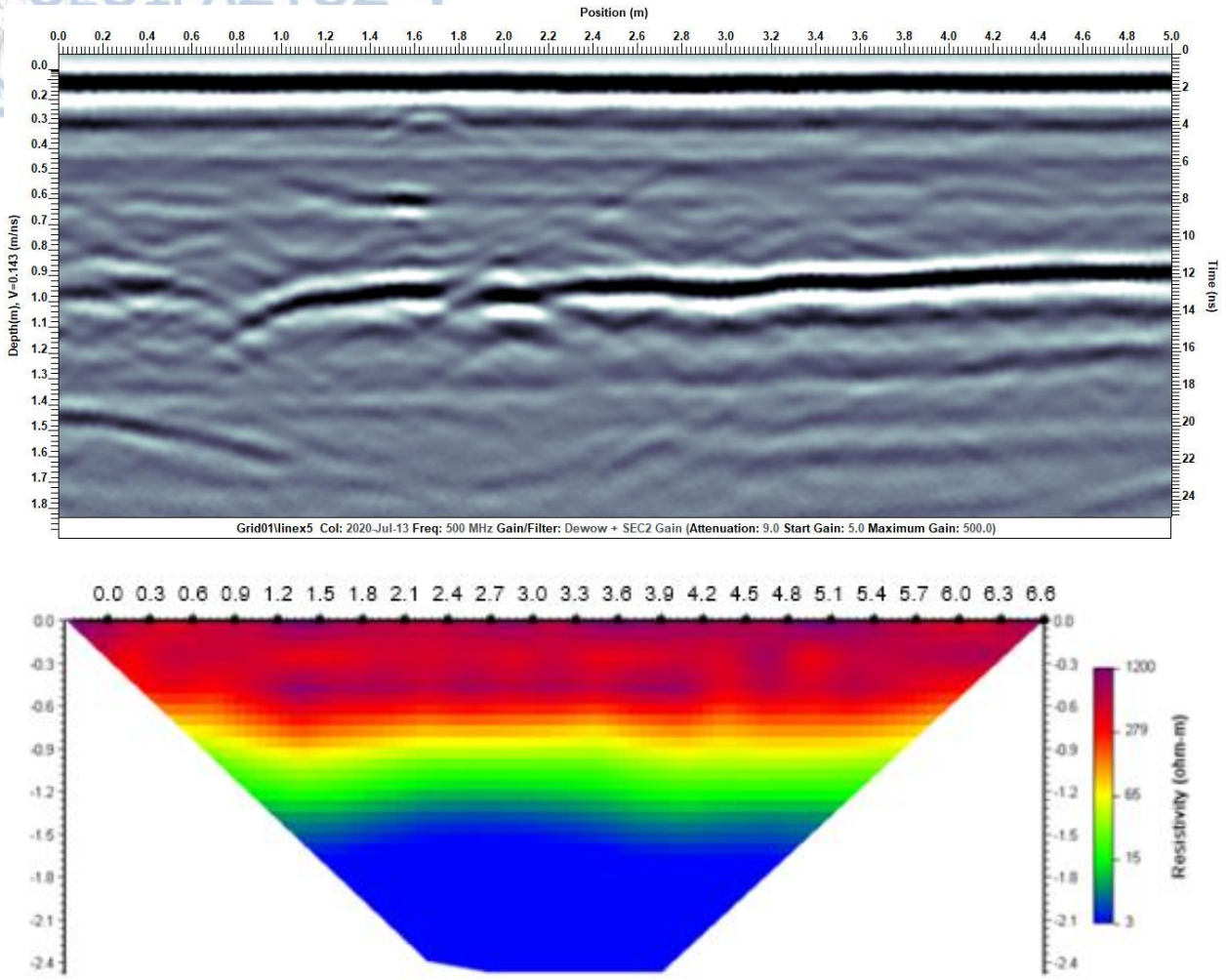

Figure 37: The x5 GPR grid line (top) where the top axis is for the position of each measurement in m and the two vertical axes correspond to the time in ns (right axis) and to the depth for a GPR wave velocity equal to 0.143m/ns (left axis). The almost horizontal subsurface layer is seen at ~0.8m depth. The corresponding ERT to the x5 GPR line is DD1, shown at the bottom with rainbow color scale (in Ohm.m). The x axis is the position of each measurement in m and at the left and right axes the corresponding depth in m is shown.

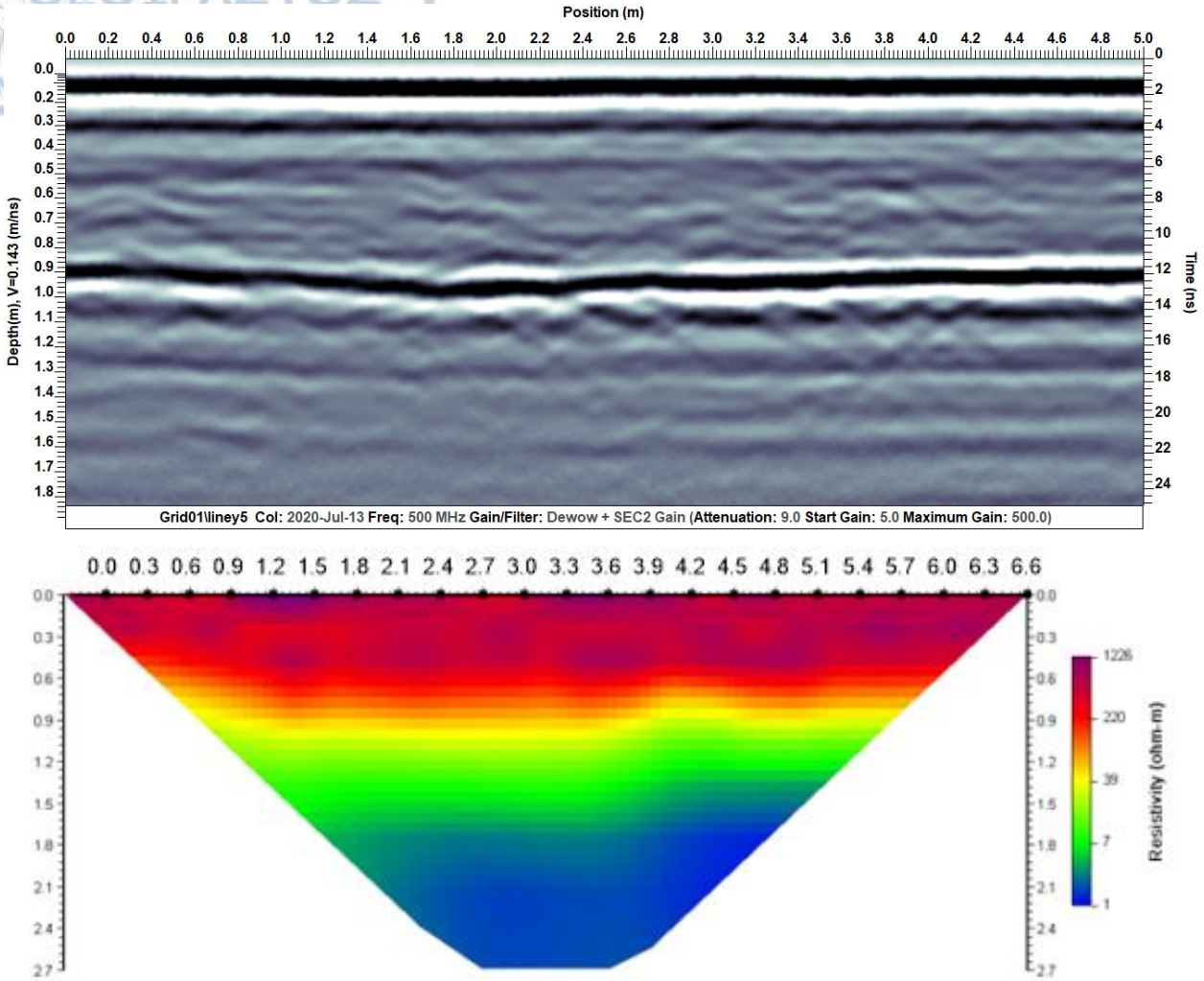

Figure 38: The y5 GPR grid line (top) where the top axis is for the position of each measurement in m and the two vertical axes correspond to the time in ns (right axis) and to the depth using GPR wave velocity equal to 0.143m/ns (left axis). The corresponding ERT to the y5 GPR line is DD2, shown at the bottom with rainbow color scale (values of resistivity in Ohm.m). The x axis shows the position of each measurement in m and at the left and right axes the corresponding depth in m is shown.

In general, both the ERT and the GPR grid results indicate an interface at approximately 0.75m depth from the ground surface. This reflector has a part where it is almost horizontal and so, it is considered appropriate to perform the experimental part of this study (i.e., the GPR measurements around a circle).

5.1.5 GPR static & radial data acquisition

The detection and mapping of an almost horizontal subsurface reflector in the field was done and cross validated by both the GPR grid data and the ERT, as shown in the previous section. To study the spatial distribution of the EM signals emitted by the GPR Tx antenna and recorded by the Rx antenna, in terms of polar coordinates, changing the radial distance and the orientation of Tx in relation to the Rx were considered as these are critical factors impacting the way that the energy is spatially distributed. For this reason, the field experiment was conducted over the horizontal subsurface reflector where all the DAW, DGW and RW events were studied by

collecting static GPR data around a circle. The Tx was placed at the circle's center and the Rx recorded data by moving circularly around the Tx. Since the Rx was moving at specific angular steps around the Tx, the relative antenna-to-antenna orientation was constantly changing. Also, three radial distances were chosen for the data collection around the circle: these were equal to r=0.23m, 0.5m and 1m. The angular Rx step was set to 10^0 for the 0.23m and 0.5m radii and 5^0 the 1m radial distance. The Tx was placed at the center of the black solid square of Figure 31b with the Rx antenna completing three concentric circles around it clockwise. Figure 39 (top) shows the initial transducer position for the circle of Tx-Rx radial distance equal to 0.23m. At this initial position, the GPR antennas were oriented in the broadside configuration along the 0^0-180^0 line, as indicated. Then, from this position, the Rx was moved counterclockwise with a step equal to 10^0 around the fixed Tx, till a complete circle was fulfilled. At each angular position – for all data collected around each circle – 100 GPR traces were collected for a total time window of 40ns. When the Rx antenna reached the 270^0 location, the Tx-Rx antenna configuration becomes endfire, as seen in Figure 39 (bottom). In Appendix A, more photos from the field measurements are provided.

Each set of measurements collected around a circle starts with placing the Rx antenna at 0^o at a specific radial distance away from the Tx (which is fixed in the circle's center) and with a specific starting antenna-to-antenna orientation (either broadside or endfire). This starting orientation is obviously changing when the Rx moves radially around the circle and when it is located at the 90^o and 270^o the starting broadside antenna configuration becomes endfire and vice versa. From now on, when referring to a broadside or endfire Tx-Rx antenna configuration, their orientation at the 0^0-180^0 will be considered. For the GPR data around a circle with an angular step of 10^o (i.e., r=0.23 & r=0.5m), datasets from 37 positions were recorded and were comprised of 100 traces each. For the circle with radius equal to 1m where an angular step of 5^o, 73 datasets were collected with 100 traces each. As it will be presented below, collecting the data this way, has allowed to study how the EM signals are distributed at a plan view, how this distribution is influenced by the antenna-to-antenna orientation and also, the impact of the distance from the source. In Table 5 information on the radial and static GPR data acquisition is given.

Table 5: Information about the GPR static & radial data collected in the field

Antenna orientation (at the 0^0-180^0 line)	Broadside	Broadside	Broadside
Tx-Rx distance-x (m)	0.23	0.5	1
spatial Rx step (degrees)	10	10	5
Antenna orientation (at the 0^0-180^0 line)	Endfire	Endfire	Endfire
Tx-Rx distance-x (m)	0.23	0.5	1
spatial Rx step (degrees)	10	10	5

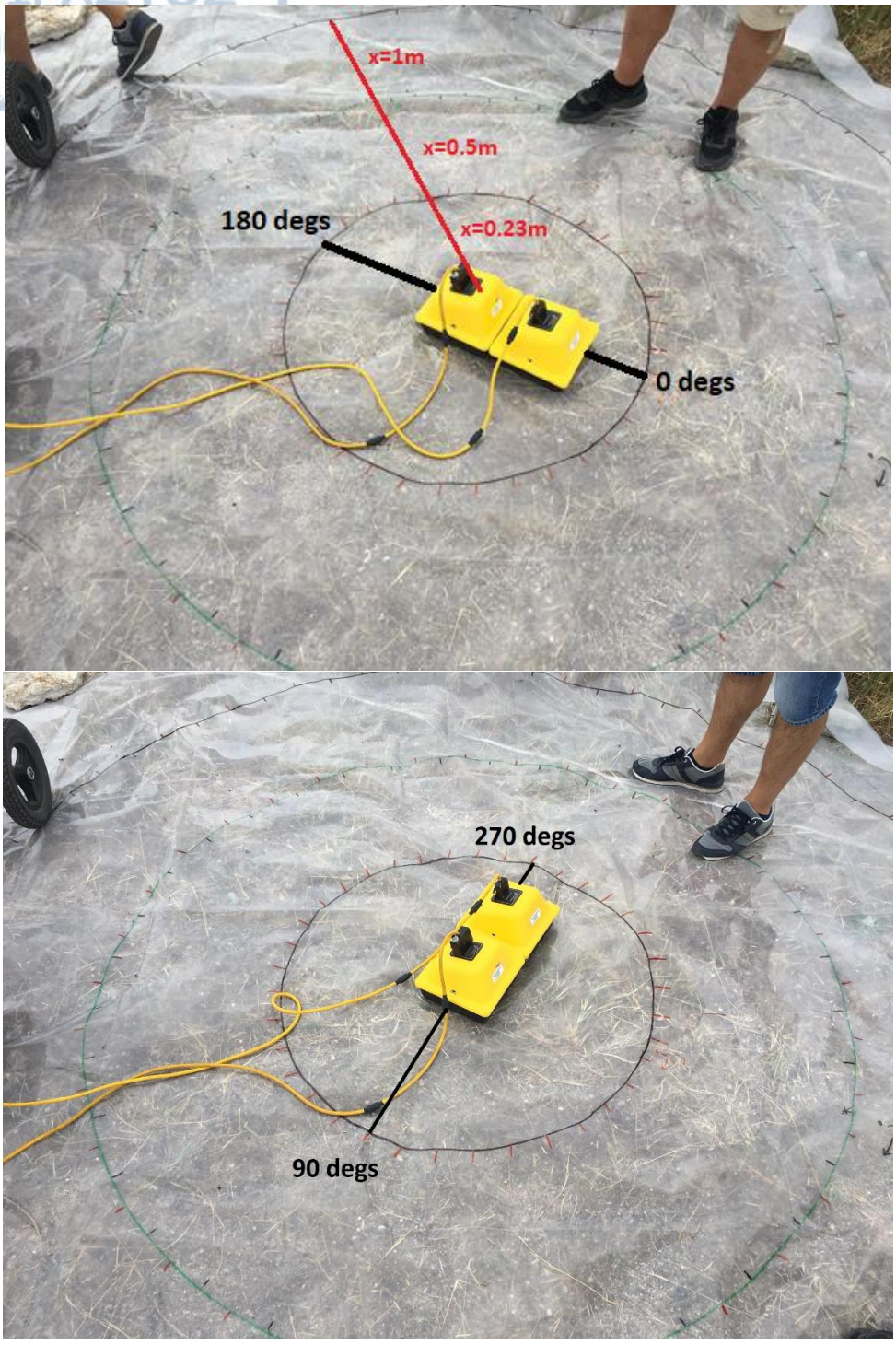

Figure 39: Data acquisition for the circle of radius equal to 0.23m where the antennas were oriented in the broadside configuration along the 0-180^o line (black solid line-top). With moving the Rx around the circle the Tx-Rx configuration becomes endfire along the 90-270^o line (black solid line-bottom). At the top image, with red solid line the various radial distances (x) are indicated.

Synthetic data were also produced in an effort to mimic the field data conditions, using gprMax, in order to capture the EM signals distribution. Both Hertzian point dipoles as well as realistic dipole sources were used to simulate the GPR antennas. A 3D half space was modelled with a

GPR source placed above the ground in the center of the domain. The Rx antenna was placed broadside to the Tx source at 0^0 and a single trace was calculated every 5^0 around a circle of all three aforementioned radii (i.e., r=0.23, 0.5 and 1m). The same process was repeated for the endfire antenna configuration (starting at 0^0 along the 0^0-180^0 line). In Figure 40, the three concentric circles for the broadside antenna orientation (top) and the three concentric circle for the endfire antenna orientation (bottom) are presented. With blue and red solid lines the traces collected from the observed data and the synthetic data are shown respectively, at the 0, 50, 90, 130, 180, 230, 270 and 310 degrees. More information on the production of the synthetic data is presented later.

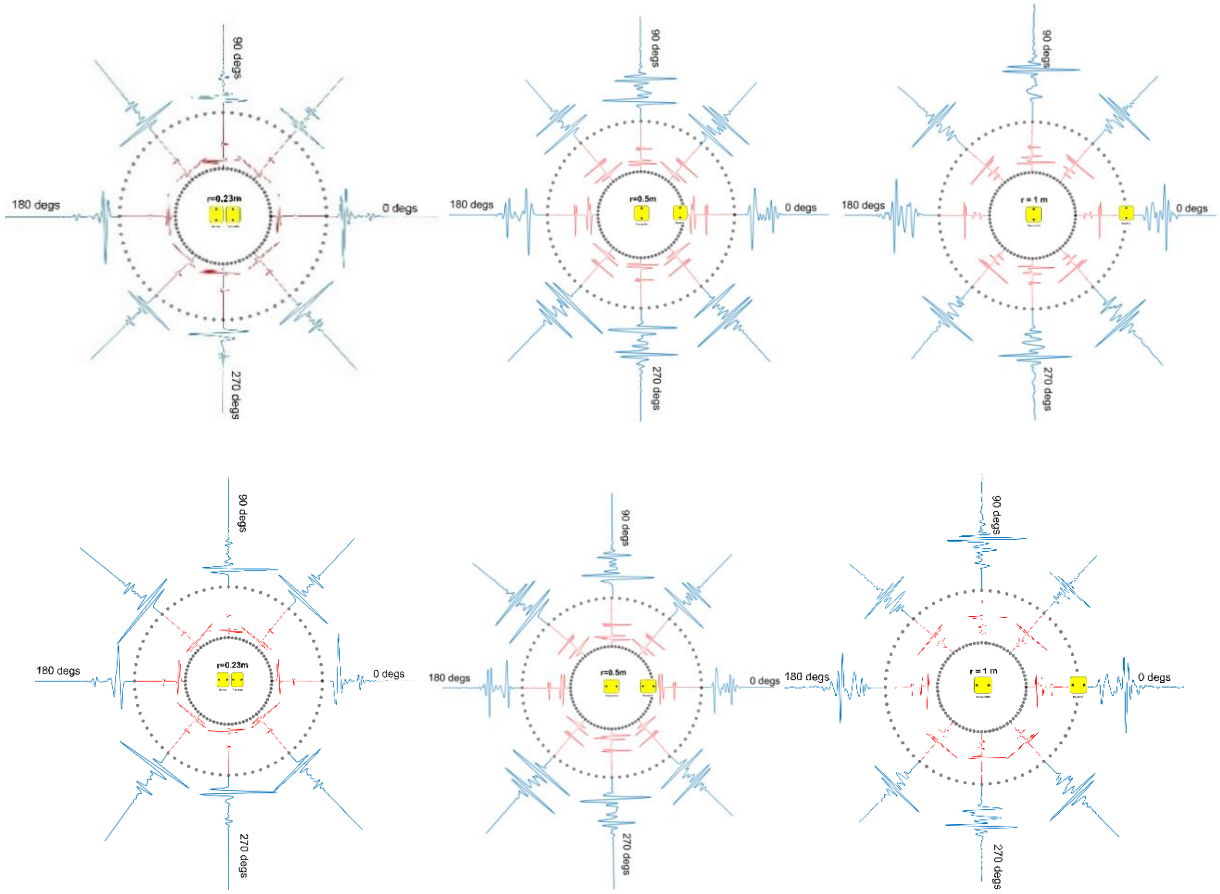

Figure 40: The traces collected at 0, 50, 90, 130, 180, 230, 270 & 310 degrees are shown. From left to right – top: circles with r=0.23, 0.5 and 1m, broadside antenna orientation. From left to right – bottom: circles with r=0.23, 0.5 and 1m, endfire antenna orientation. In all plots, with blue solid line are the traces from the observed data and with red solid line the traces for the synthetic data.

Every collected trace consists of the main three responses: the direct air wave (DAW), the direct ground wave (DGW), and the reflected wave (RW). To study the behavior of each of the three responses when the antenna orientation and the distance between the antennas are changing, these responses must be isolated from the GPR recordings. The direct wave (DW – which is the combination of DAW and DGW) is the response that first arrives to the Rx and the RW is the signal from in-ground targets (mainly dictated by the response from the relatively flat, subsurface layer

in our case). Studying at all these signals around a circle, an attempt is made to identify a Tx-Rx position where the direct wave is minimized (or, ideally null-coupled), while the RW stays ideally intact.

5.1.6 Data processing

Collecting static GPR data around a circle with an angular step of 10^0 or 5^o and at a specific Tx-Rx distance (0.23m, 0.5m or 1m), gave rise to 37 or 73 radargrams (or lines), respectively, all being comprised of 100 traces each. Every trace had a time window of 40ns and time step of 0.2ns along the trace. An example of such a radargram collected in the field is shown in Figure 41 for the broadside Tx-Rx antenna configuration and for the circle of radius equal to 0.23m. This radargram is collected when the Rx antenna is placed at the 0^0. Note that even though the x-axis indicates the position in meters, the antennas do not move and stationary data are collected over a period of time and until 100 traces are collected at each Rx position. At the right y-axis, the time from the start of the recording window is shown in nanoseconds (note that the full time window was set equal to 40 ns, however, the first 24ns are shown). The left y-axis shows the corresponding depth using a GPR wave velocity equal to 0.143m/ns (V_1) (which was inferred from the WARR measurements). The DW is limited by the blue solid parallelogram and the RW is pointed by the red solid parallelogram. The uppermost layer is characterized by V_1 and ε_1 and the second layer corresponds to V_2, ε_2.

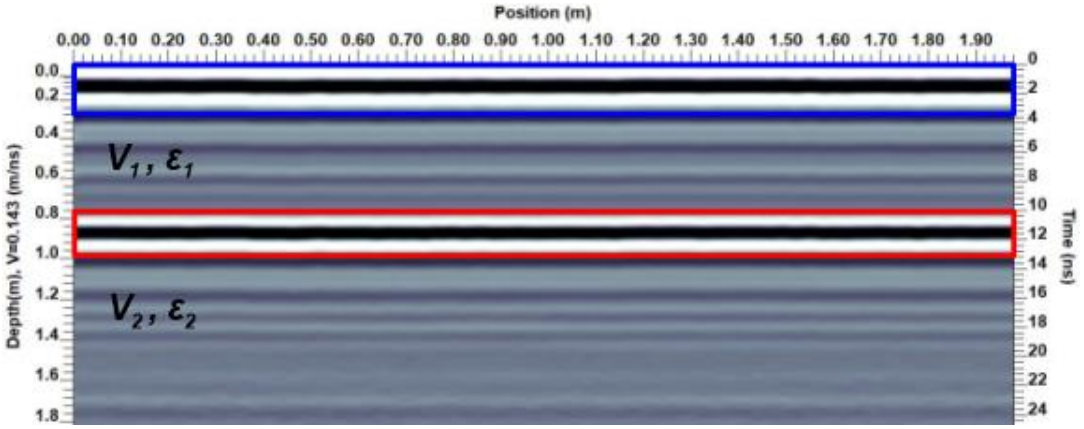

Figure 41: Field line collected at a broadside mode for the circle with r=0.23m when the Rx antenna was at the 0^0 location. The right y-axis shows the time from the start of the recording in ns and the left y-axis is the corresponding depth using a velocity of 0.143m/ns (i.e., the velocity of the uppermost layer- V_1). The blue solid parallelogram contains the response from the DW and the RW is limited by the red parallelogram. The uppermost layer is characterized by V_1, ε_1 and the second layer by V_2, ε_2.

During the field test, the datasets which were collected around a circle every 10^0 consist of 37 lines similar to the line of Figure 41 (i.e., line 1 is the recording where the Rx antenna was at 0^0 and line 37 is the recording collected when the Rx antenna was at 360^0 – essentially back at the 0^0 position). For the datasets collected every 5^0 around the circle, 73 lines were produced. To isolate the DW and the RW wave for each recording, all traces in a single line (as the one of Figure 41, for example), were averaged to produce one single trace for each Rx position around the circle. In order to get an average trace for each line as indicated in Figure 41, the EKKO_Project software by Sensors & Software was used.

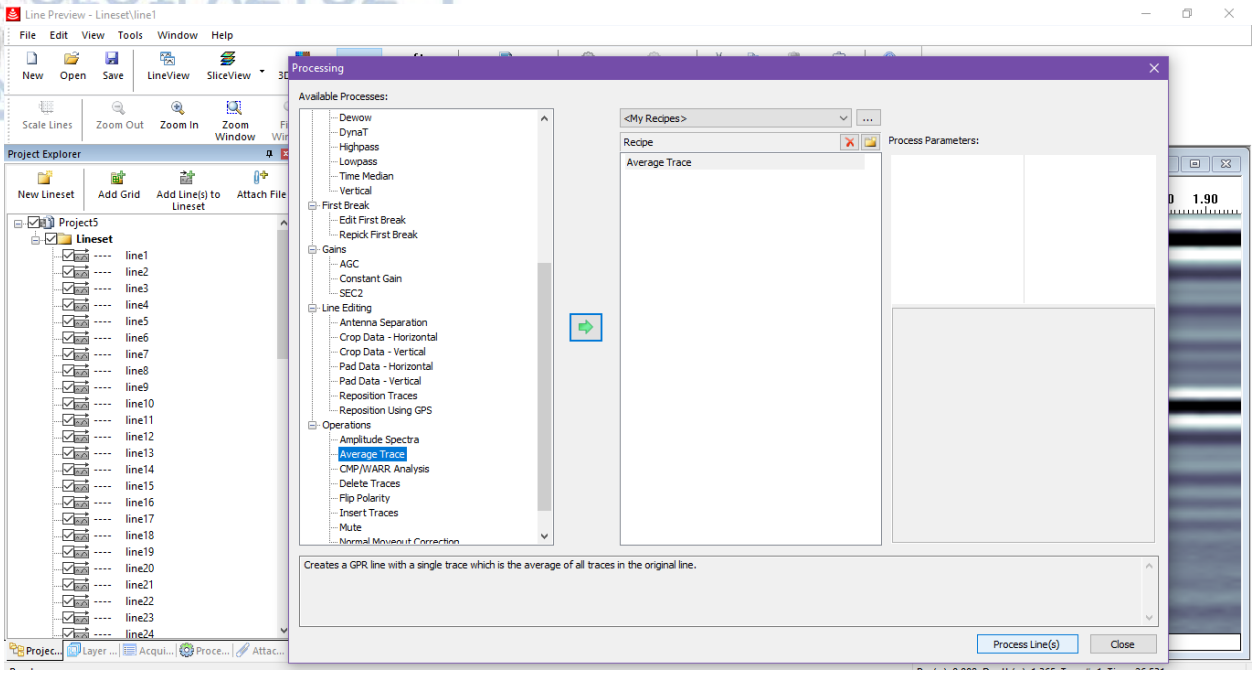

Figure 42: Image from EKKO_Project indicating the "Average Trace" operation which was applied to every line collected (left) at each angular antenna position.

After this process was performed, a single trace plot was generated for every angular position (i.e., each line) around the circle. For example, line 1 of Figure 41 after applying the "Average Trace" operator, the trace plot of Figure 43 is produced.

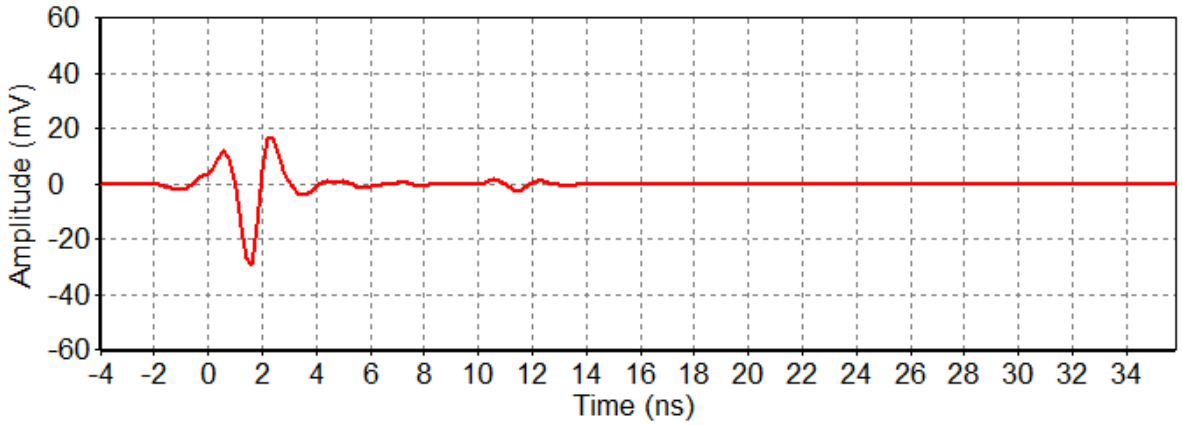

Figure 43: The derived trace plot for line 1 at the 0^0 Rx position of the data of Figure 41 after applying the "Average Trace" operator. The y-axis shows the GPR signal amplitude in millivolts (mV) and in x-axis is the time in nanoseconds (ns) from the start of the recording window. The Tx-Rx antenna separation equals to 0.23m. The strong reflection at the start of the trace is the combination of the DA and DG waves. The reflected event is the weak reflection that arrives at the GPR receiver at ~10 ns.

Regardless the antenna orientation, we collected 37 lines for the circles of r=0.23m and r=0.5m and 73 lines for the circles of r=1m. Every trace plot consists of mainly the DW and the RW events, as indicated in Figure 44 for various angular positions around the circle.

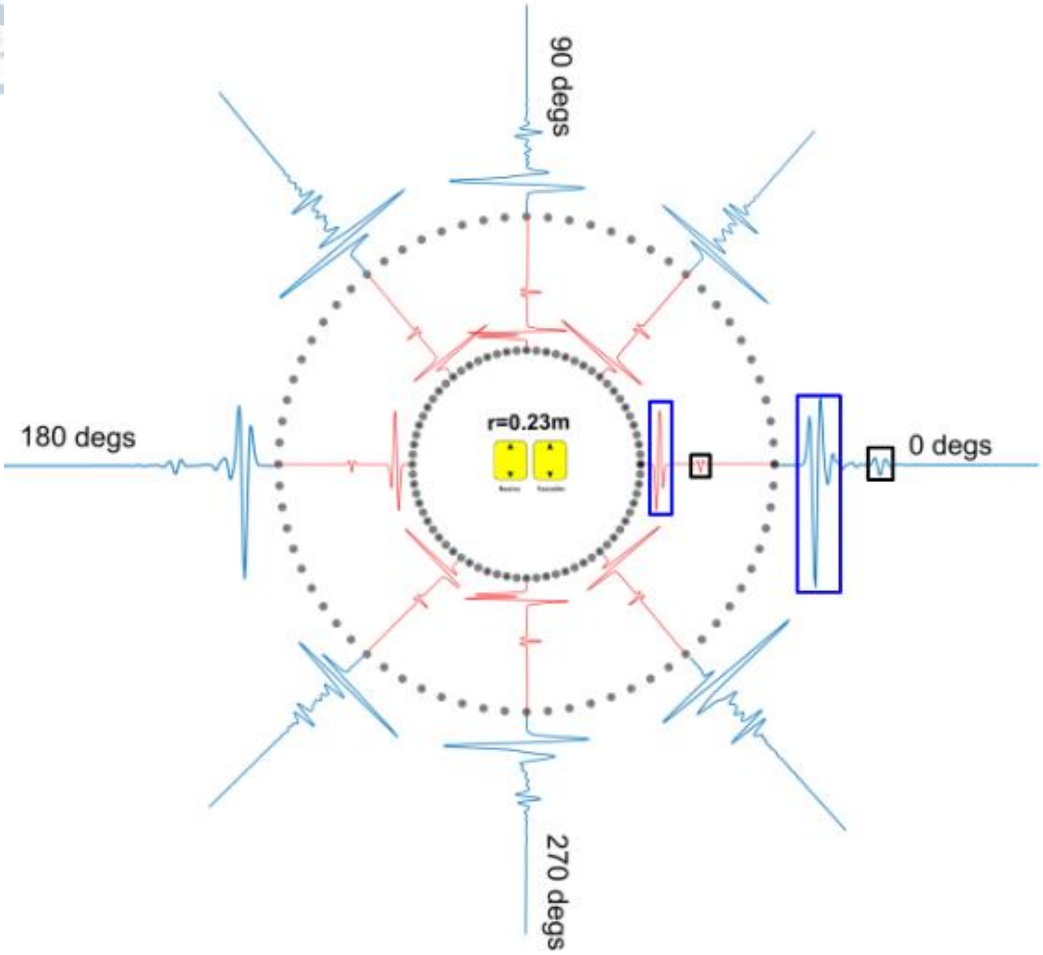

Figure 44: Trace plots for the circle of r=0.23m with the antennas-oriented at the broadside at the starting 0^0 position. Blue traces are the ones collected in the field and red traces are the synthetic ones. The DW is limited by the blue solid parallelograms and the black solid parallelograms contain the RW in both the observed and the synthetic data.

Figure 45 shows the averaged traces recorded in the field from 0^0 to 90^0 for the circle of r=0.5m and for the broadside antenna configuration. As it can be seen from this figure, it is hard to "isolate" the various DAW, DGW and RW events. Therefore, to properly crop and isolate the direct and reflected waves from every recording, we used the arrival times at the Rx as presented in Table 4 for the direct ground (t_{gr}) and reflected (t_{ref}) waves, taking into account the Tx-Rx antenna separation each time. The GPR wave velocity we used was set equal to V_1=0.143m/ns which was estimated by the WARR measurements.

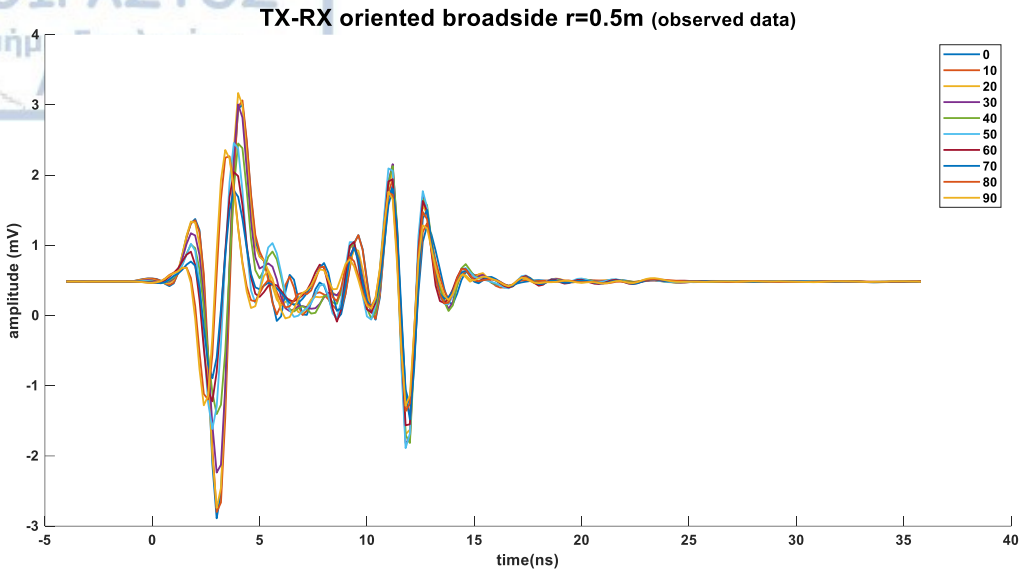

Figure 45: Traces collected from 0^0 to 90^0 for the broadside antenna orientation and for the circle of r=0.5m. In the x axis the time from the start of the recording window is indicated in ns. In the y axis the amplitude of the GPR signal in millivolts is presented.

A code was created in MATLAB which crops and isolates the direct air wave, the direct ground wave and the reflected wave from every single recording. In Figure 46 the direct wave (both DAW & DGW events) for the broadside configuration and for the circle of r=0.5m is presented for all the 37 collected traces which are composing the full circle (angular step of 10^0). Each trace corresponds to one color of the rainbow color scale indicated at the right side of the plot. Figure 47 illustrates the cropped reflected wave of all averaged collected traces for the broadside antenna orientation and for the circle of r=0.5m. Every trace of Figure 46 and Figure 47 corresponds to a specific spatial position of the Rx around the Tx and at a specific radial distance (antenna separation).

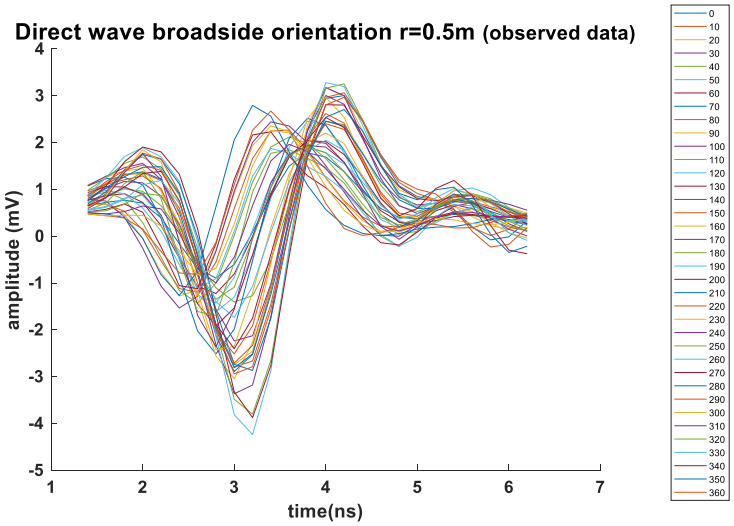

Figure 46: The direct wave isolated for every collected trace around the circle of r=0.5m for the broadside antenna orientation. The legend shows the traces for every location in angular steps of 10^0.

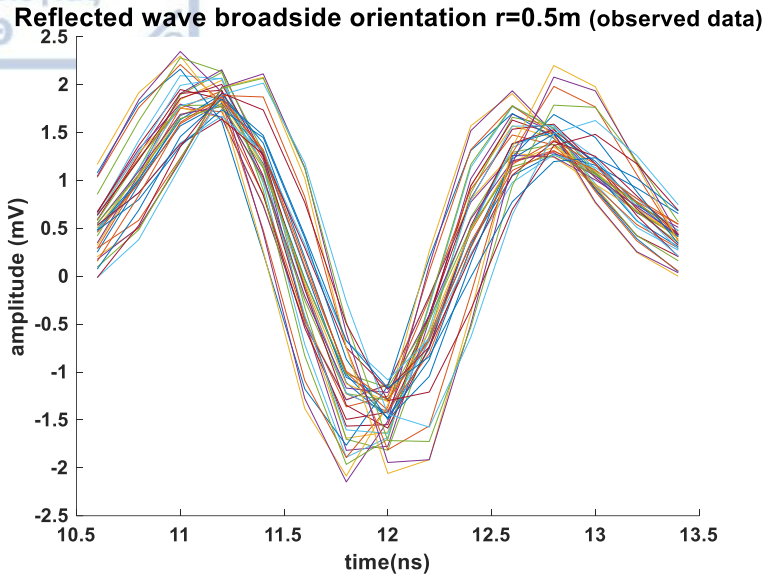

Figure 47: The reflected wave of all averaged collected traces for the broadside antenna orientation and for the circle of r=0.5m. The 37 traces are indicated with the same rainbow color scale as depicted in Figure 46.

To illustrate the variations in the electric field spatial distribution for each of the GPR recorded events (i.e., DW & RW) when the polar coordinates are changing, we calculated (a) the average of the absolute value, (b) the maximum of the absolute value and (c) the Root Mean Square (RMS) value for each event (during their respective, properly cropped time windows) and for every recording location around the circle. By doing so, every trace is transforming to a single unique value of amplitude representing the value of the EM signals in a specific position. For example, applying this analysis to every trace collected at the time windows of (a) the direct wave and (b) the reflected wave, for the circle of r=0.5m and for the broadside antenna orientation, we get:

1. 37 averaged absolute values of amplitude in millivolts (each at every 10^0s) for the direct wave, and 37 averaged absolute amplitude values in millivolts (each at every 10 degrees) for the reflected wave (Figure 48).
2. 37 maximums from the absolute amplitude values in millivolts (each at every 10 degrees) for the direct wave, and 37 maximums from the absolute values of amplitude in millivolts (each at every 10 degrees) for the reflected wave.
3. 37 RMS values of amplitude in millivolts (each at every 10 degrees) for the direct wave, and 37 RMS values of amplitude in millivolts (each at every 10 degrees) for the reflected wave.

When the angular step is equal to 5^0 (i.e., circle of r=1m broadside and endfire antenna configurations), the traces and the corresponding values of the analysis described above are 73 instead of 37.

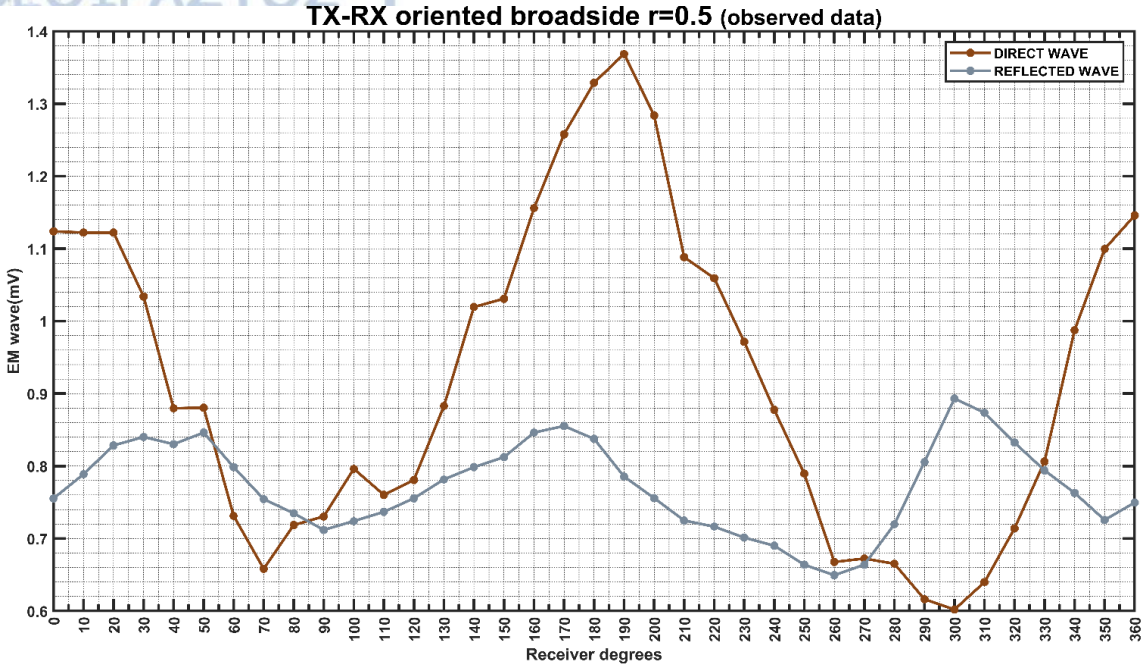

Figure 48: The mean of the absolute values of amplitude in millivolts (y axis) of the direct wave (brown solid line) and the reflected wave (grey solid line) around the circle of r=0.5m and for the broadside antenna orientation (angular step of 10^0).

To study the behavior of the direct wave in terms of the two different events it is comprised of (i.e., the DAW and the DGW) the analysis described above was again applied and the results for the three different events are shown in Figure 49.

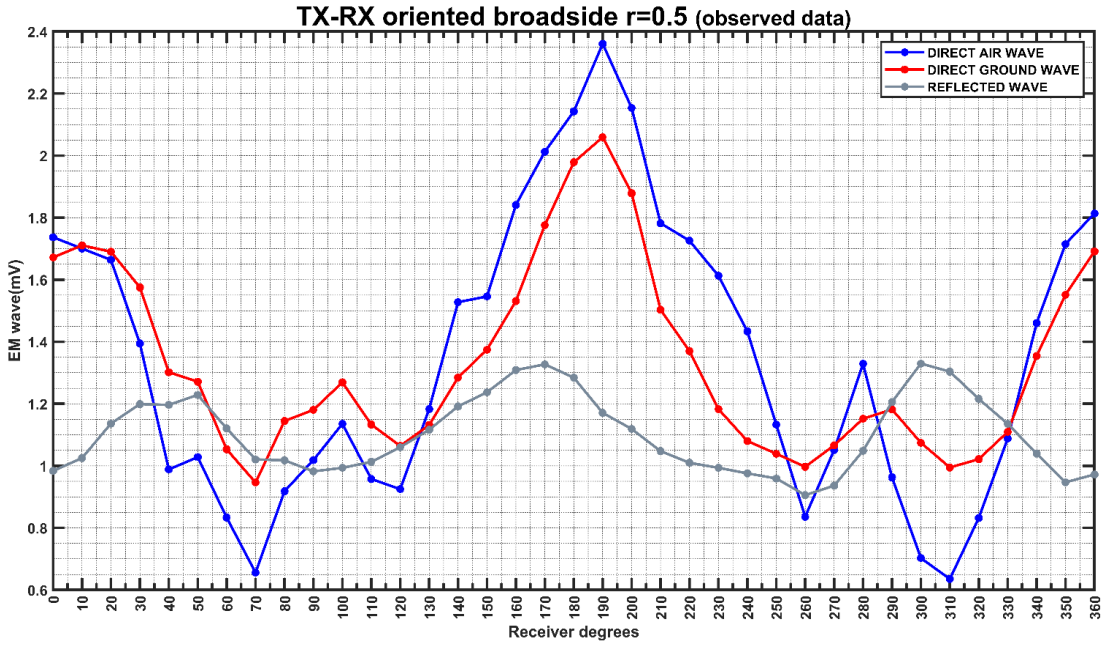

Figure 49: The mean of the absolute values of amplitude in millivolts (y axis) around the circle of r=0.5m for the direct air wave (blue solid line), the direct ground wave (red solid line) and the reflected wave (grey solid line), for the broadside antenna orientation.

The same analysis was applied for the static lines collected for all the circles and for all antenna-to-antenna configurations and antenna separations. As a result, 9 diagrams were generated in total for the broadside antenna orientation (i.e., for the 3 separate events of every radial distance). Each of these diagrams depicts the radial distribution of the direct air wave, direct ground wave and the reflected wave with the distance from the source. In addition, 9 more diagrams were generated for the endfire antenna configuration.

In the Discussion section, comparing those results between each other and also, between the numerically simulated data, we attempt to clarify the impact of antenna-to-antenna orientation, the Tx-Rx distance, and the Tx-Rx angular position on the spatial distribution of the signals for the DAW, DGW wave and RW events.

5.2 Synthetic Data

Synthetic data were produced using gprMax (Warren et al., 2016). A 3D half space was modelled of total size of x= 2.4 m, y=2.4 m and z=1.4 m. The discretization of space in all the x, y and z directions was dx=dy=dz=0.005m and the time window for every simulation was set to 30ns with a time step of 0.009624 ns. The first layer was built to have thickness h= 0.75m to match the thickness of the uppermost layer defined by the observed data (Figure 50- blue color). According to equation 2.12 for the velocity V_1 equal to 0.143m/ns (estimated by the WARR measurements), the relative permittivity of the upper layer is $\varepsilon_1 = 4.4$ and the relative permittivity of the second layer is $\varepsilon_2 = 9$. The ε_2 value was chosen after evaluating the layer1/layer2 reflection coefficient from the field GPR data. For the first set of models, an infinitesimal hertzian dipole was used as an EM source emitting a signal of the form of the normalized first derivative of a Gaussian waveform. The EM source was placed at 0.01m from the surface and at the center of the domain. The receiving antenna was set to record one trace every 5^0 around a full circle. Data were modelled for three Tx-Rx antenna separations (hence, around three circles of different radii): 0.23, 0.5 and 1m. Also, two antenna configurations were modelled at the starting position (i.e., at 0^0) along the 0^0-180^o line: the broadside (Figure 51-left) and the endfire (Figure 51-right). As a result, the data for every circle and for each antenna configuration consisted of 73 single traces (i.e., 1 trace every 5^0).

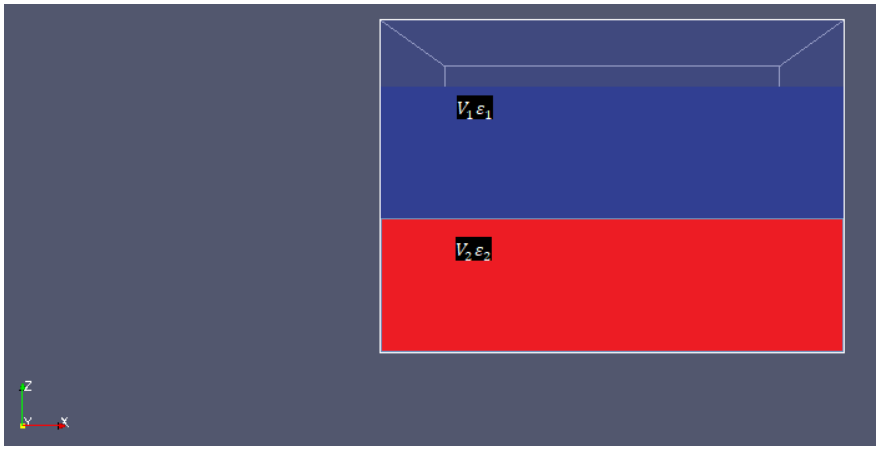

Figure 50: Side view of the 3D half space modelled using gprMax. Model size: x=2.4m, y=2.4m and z=1.2m. The upper layer (blue) was set to have a velocity of V_1= 0.143m/ns and $\varepsilon_1 = 4.4$. The second layer (red) was modelled with V_2= 0.100 m/ns and $\varepsilon_2 = 9$.

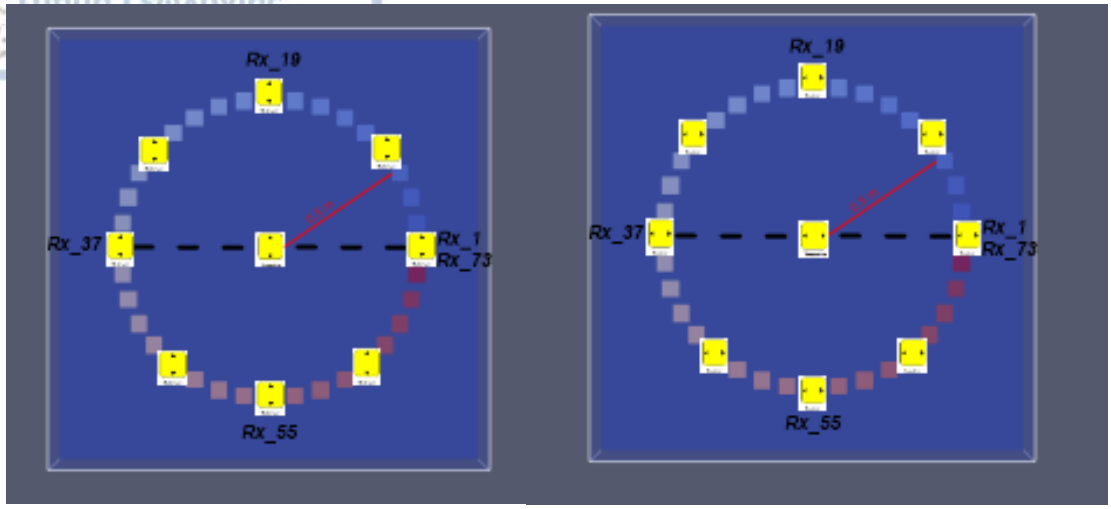

Figure 51: Plan view of the 3D half space depicted in Figure 50. This is an example for the circle of r=0.5m (red solid line) for the broadside (left) and the endfire (right) antenna orientation. The black dashed line is the 0^0-180^0 line. The Tx antenna is placed in the middle of the circle and the Rx antenna is moved around the Tx one in steps of 5^0, collecting traces at each position. As a result, every circle consists of 73 single traces. Rx_1, Rx_19, Rx_37, Rx_55 and Rx_73 are the positions of the Rx antenna at 0, 90, 180, 270 and 360 degrees, respectively.

For every set of traces collected at each position around the circle, the DAW, the DGW and the RW are identified, as shown in Figure 52.

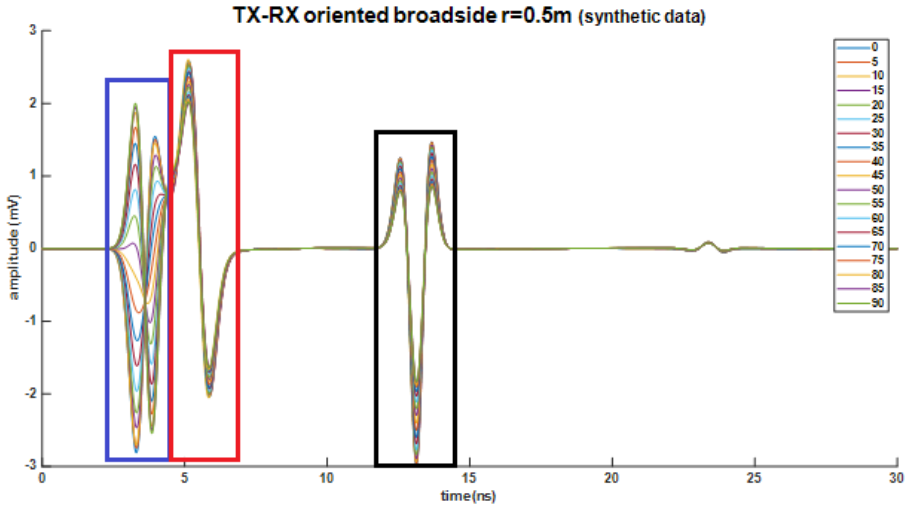

Figure 52: Example for the simulated traces from 0^0 to 90^0 (with an angular step of 5^0) for the circle of r=0.5m and for the broadside antenna orientation. Every trace corresponds to a specific angle (in degrees) as indicated by the legend. The direct air wave is limited by the blue parallelogram, the direct ground wave is limited by the red parallelogram and the reflected wave is pointed by the black parallelogram. The traces have been collected using point dipole antennas.

A Matlab script was created to properly crop each trace at the time windows annotated by the rectangles of the Figure 52 and isolate each of the DAW, DGW and RW events for both the modelled and field data. The part of the trace which is forming the direct air wave, the direct

ground wave, and the reflected wave (Figure 53, Figure 54, Figure 55) is chopped and three unique values of amplitude are calculated for each part of the trace (i.e., the mean(abs), the max(abs) and the RMS values) as depicted in Figure 56. As a result, every circle has 73 traces * 3 values, where each calculated value is the overall amplitude at a specific position around the circle and at a specific distance away from the Tx antenna. Plotting those values around the circle, an image of the spatial distribution of the amplitude is created. In Figure 57, the mean absolute values of amplitude for the direct (both DAW & DGW) and the reflected waves for the broadside antenna orientation and for the circle of r=0.5m are presented, plotted over the corresponding angles around the circle. In Figure 58, the mean absolute values of amplitude for the DAW, DGW and RW events are plotted, for the broadside antenna orientation and for the circle of r=0.5m. The same process was applied to both the numerically simulated and field data.

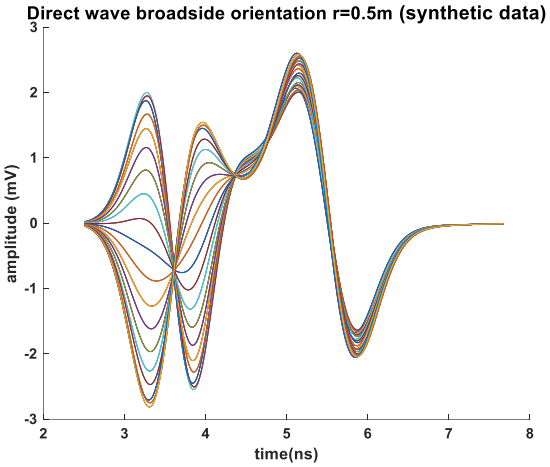

Figure 53: The direct wave for the first 18 (out of the 73) simulated traces for the broadside antenna orientation and for the circle of r=0.5m.

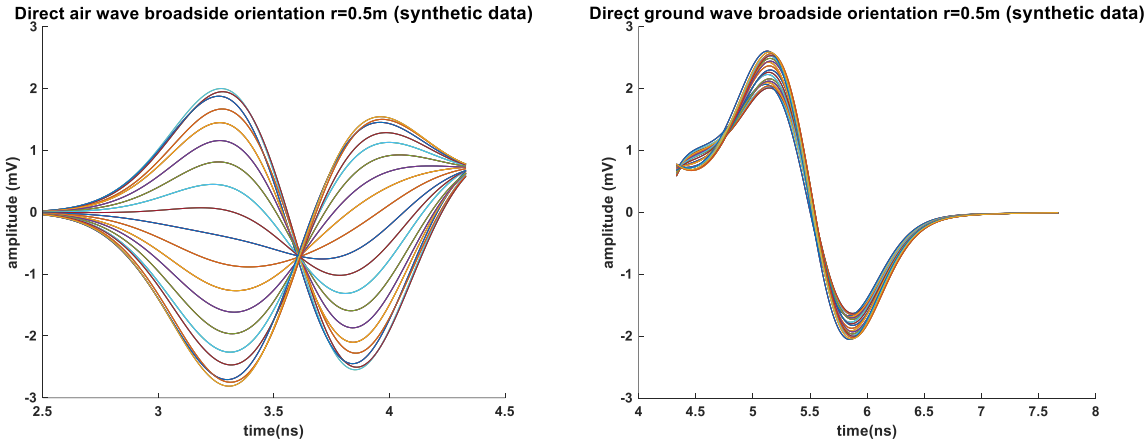

Figure 54: The direct air wave (left) and the direct ground wave (right) for the first 18 (out of the 73) simulated traces for the broadside antenna orientation and for the circle of r=0.5m.

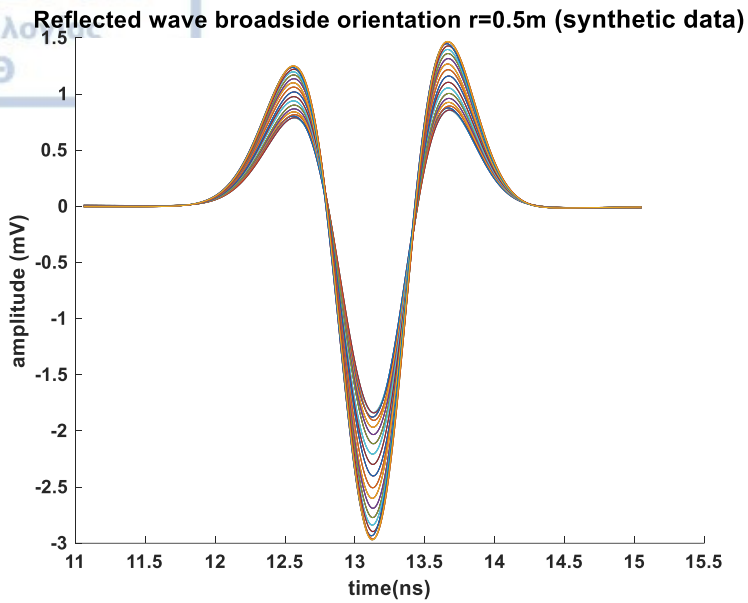

Figure 55: The reflected wave for the first 18 (out of the 73) simulated traces for the broadside antenna orientation and for the circle of r=0.5m.

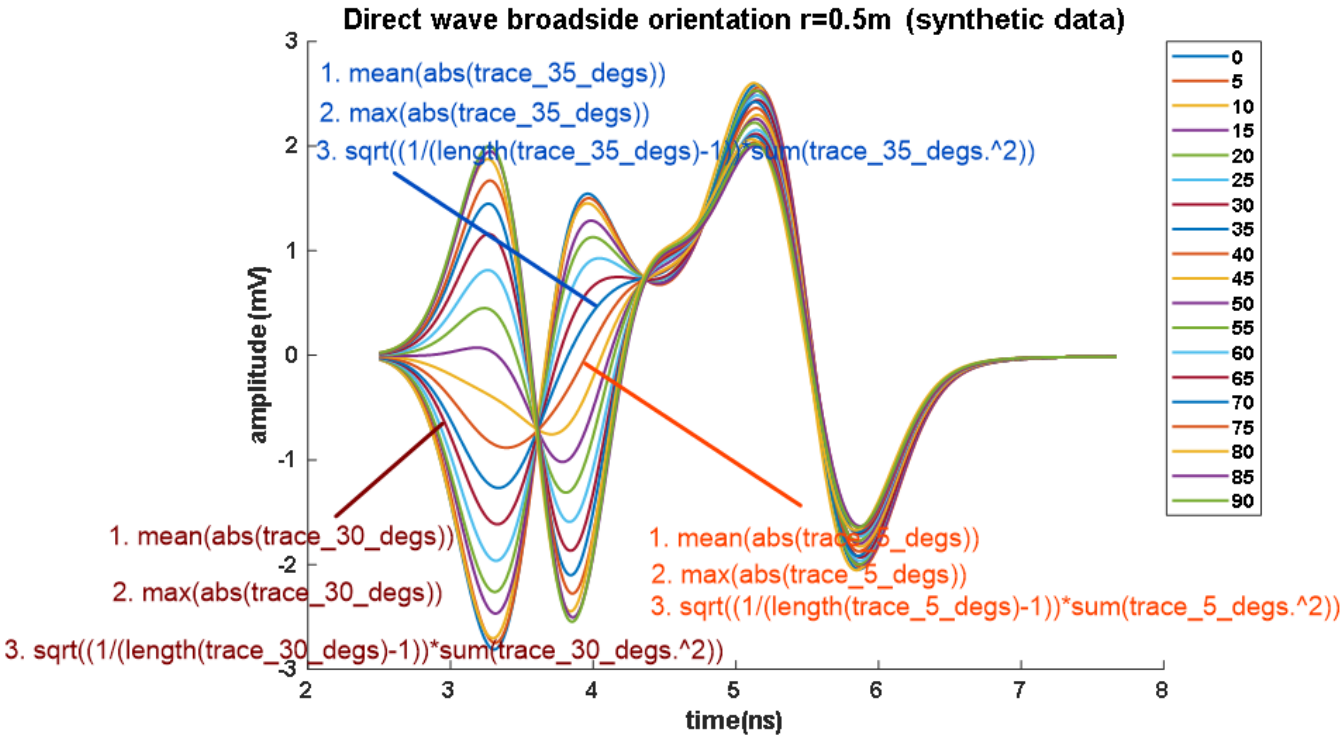

Figure 56: Visualization of the process applied to the traces of 5, 30 and 35 degrees for the direct wave (circle of r=0.5m) for the broadside orientation. The same process is applied to all the events of the trace, from 0^0 to 360^0. Each trace corresponds to one angle around the circle as annotated by the legend. The traces have been collected with point dipole antennas.

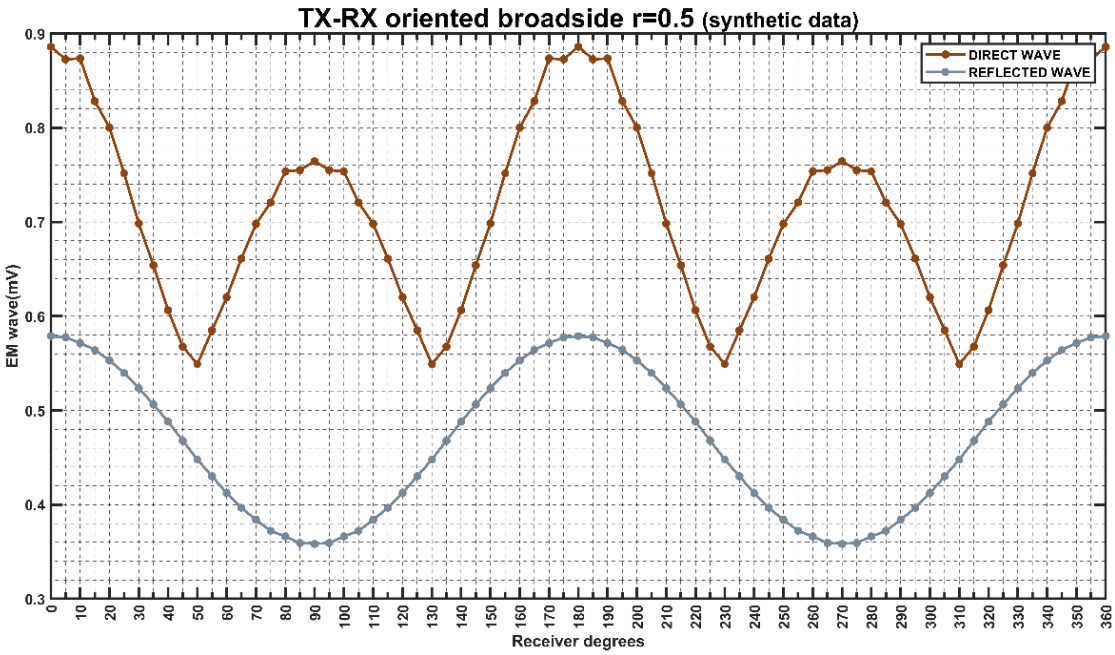

Figure 57: The mean of the absolute values of amplitude in millivolts (y axis) of the direct wave (brown solid line) and the reflected wave (grey solid line) for the circle of r=0.5m and for the broadside antenna orientation. The minor grid lines perpendicular to the x axis are at every 5^0. The traces have been collected with point dipole antennas.

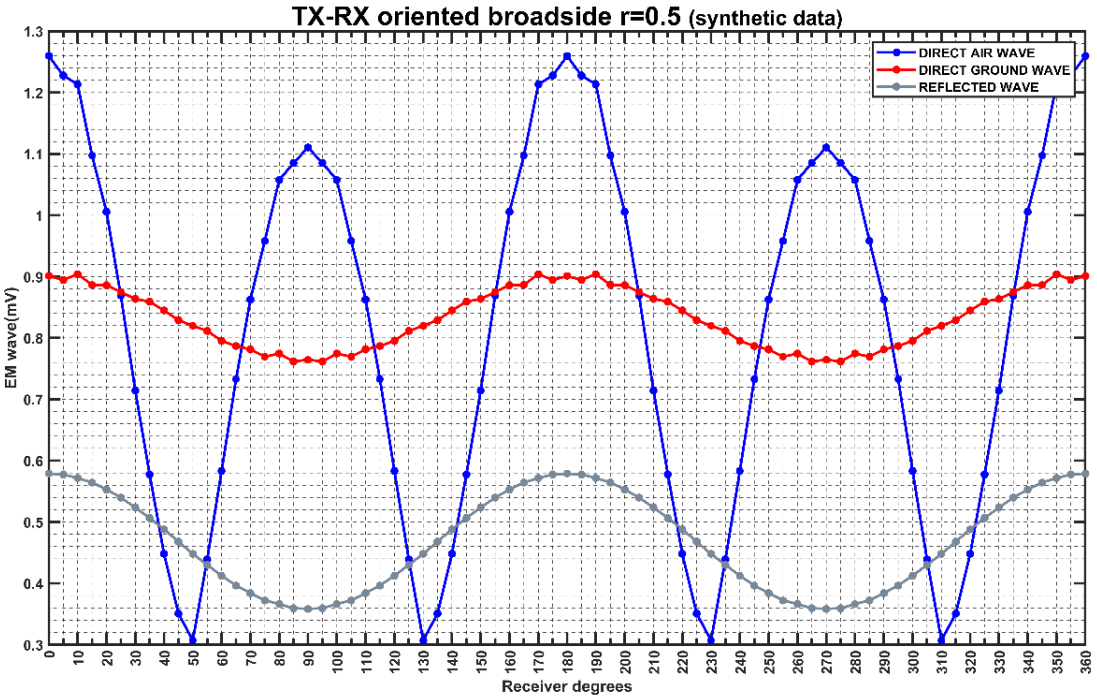

Figure 58: The mean of the absolute values of amplitude in millivolts (y axis) of the direct air wave (blue solid line) the direct ground wave (red solid line) and the reflected wave (grey solid line) for the circle of r=0.5m and for the broadside antenna orientation. The minor grid lines perpendicular to the x axis are at every 5 degrees. The traces have been collected with point dipole antennas.

To further study the impact of the antennas in the distribution of the EM signals, bare dipole antennas (i.e., unshielded resistively loaded dipoles) were also modeled. Bare dipoles are a much better representation of real antennas that are used to collect GPR data in the field, than infinitesimal EM dipole sources (which are most of the time used to produce synthetic GPR data). For the traces created employing bare dipoles as antennas, the same analysis was made as described earlier. For these models, only the traces for the first two quadrants of each circle were modeled with an angular step of 10^0 (i.e., from 0 to 180 degrees), as the rest of the responses (the other half of the circle) would provide symmetrical results. Bare dipoles were only used to model the broadside antenna orientation for the radial distances of 0.23, 0.5 and 1m. In Figure 59, the plan view for the model using bare dipole antennas for the circle of r=0.5m and for the broadside antenna orientation is indicated. The same model as this of Figure 59 was produced for the broadside antenna orientation for the semicircles of radius of 0.23m and 1m.

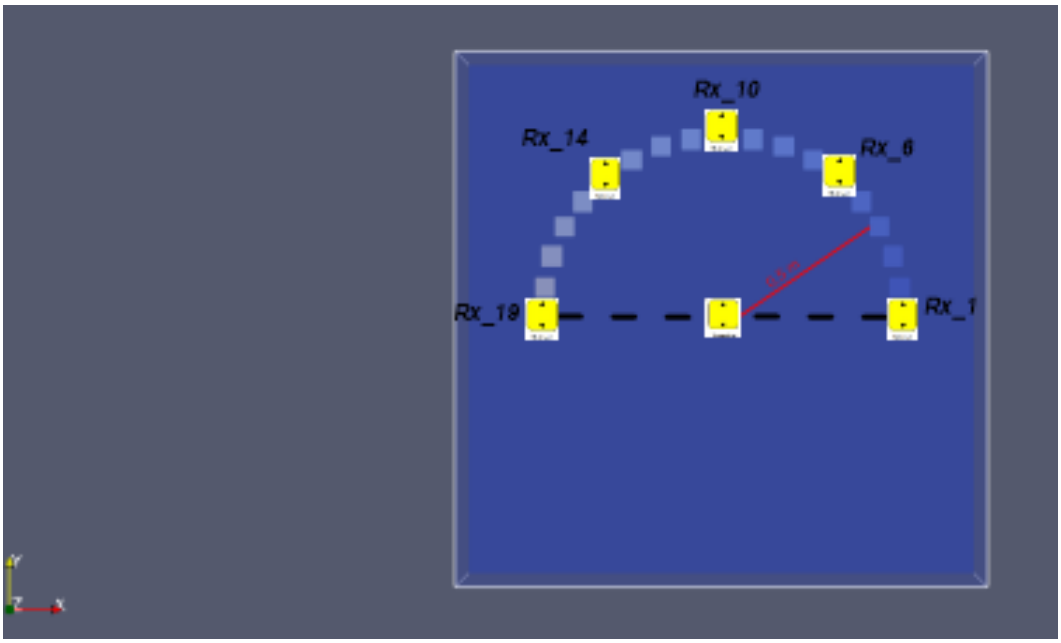

Figure 59: Plan view for the 3D half space modelled using bare dipole antennas. This is an example for the circle of r=0.5m (red line) for the broadside antenna orientation. The positions of the Rx antenna at 0, 50, 90, 130 and 180 degrees are indicated with Rx_1, Rx_6, Rx_10, Rx_14 and Rx_19, respectively.

Every semicircle consists of 19 traces, each for every 10^0. The traces collected from 0^0 to 90^0 for the broadside antenna orientation and for r=0.5m are presented in Figure 60.

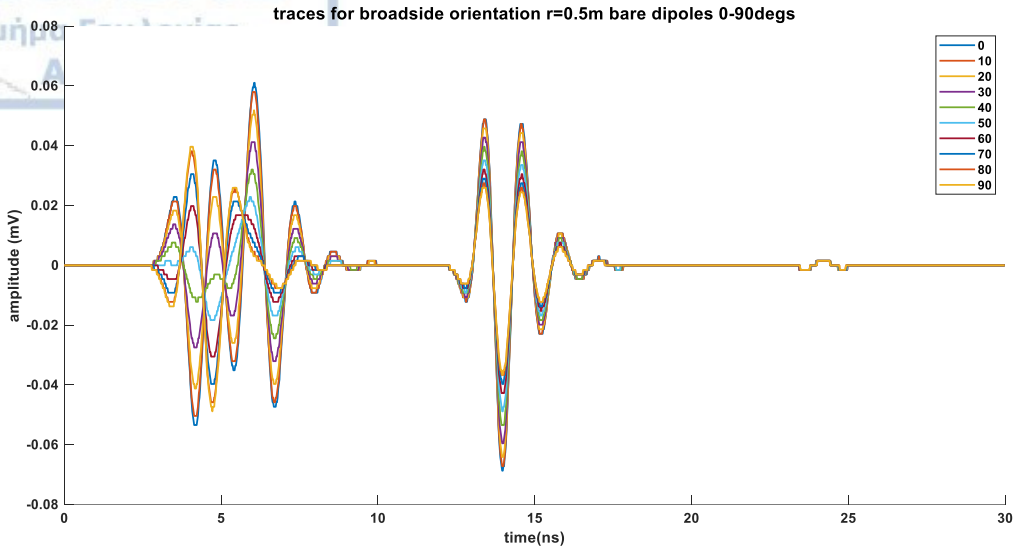

Figure 60: Example for the simulated traces from 0 to 90 degrees (angular step of 10^0) for the circle of r=0.5m and for the broadside antenna orientation. Every trace corresponds to a specific angle (in degrees) as indicated by the legend. The traces have been generated using bare dipole antennas.

Using the time of the arrival for the direct air wave, direct ground wave and the reflected wave, each of these responses can be identified and isolated (Figure 61, Figure 62, Figure 63) and the analysis previously described is applied at each part of the trace which is forming the main three GPR signals (i.e., DAW, DGW and RW). Therefore, for every trace a unique value is calculated for each of these events which can be plotted with the corresponding degrees around the circle, indicating the changes in the spatial distribution of the EM signals for each of the GPR waves (Figure 64).

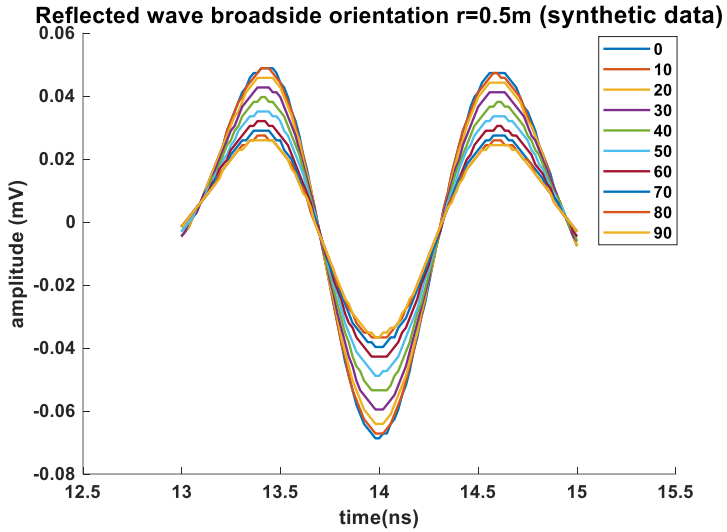

Figure 61: The simulated reflected wave for the 10 traces from 0 to 90 degrees, for the broadside antenna orientation and for the circle of r=0.5m. In the x axis is the time in ns and in the y, axis is the amplitude of the GPR signal in mV. The angular position around the circle for the 10 traces is indicated by the legend. The traces have been created using bare dipole antennas.

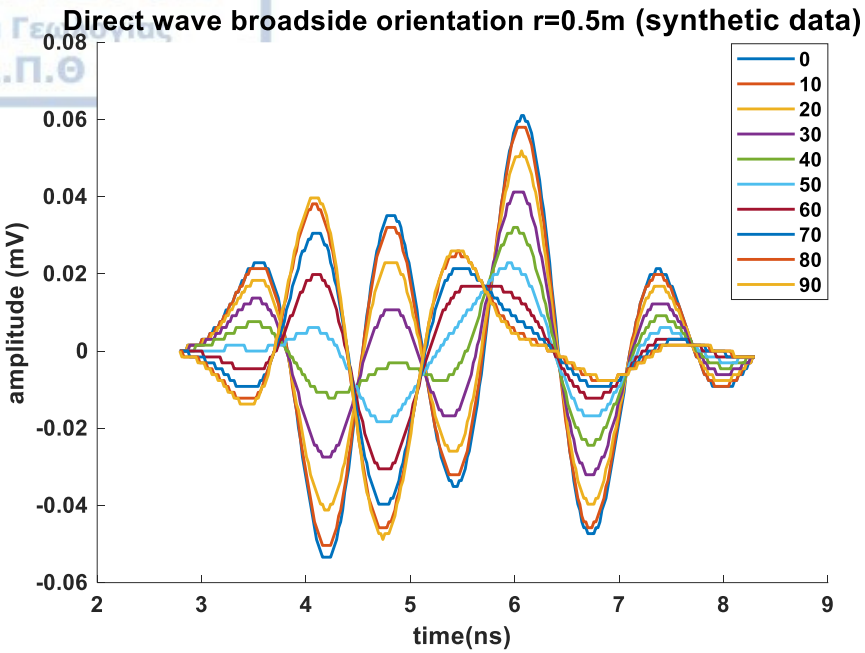

Figure 62: The simulated direct wave (DW) for the 10 traces from 0 to 90 degrees, for the broadside antenna orientation and for the circle of r=0.5m. In the x axis is the time in ns and in the y, axis is the amplitude of the GPR signal in mV. The 10 traces correspond to the degrees around the circle indicated by the legend. The traces have been generated employing bare dipole antennas.

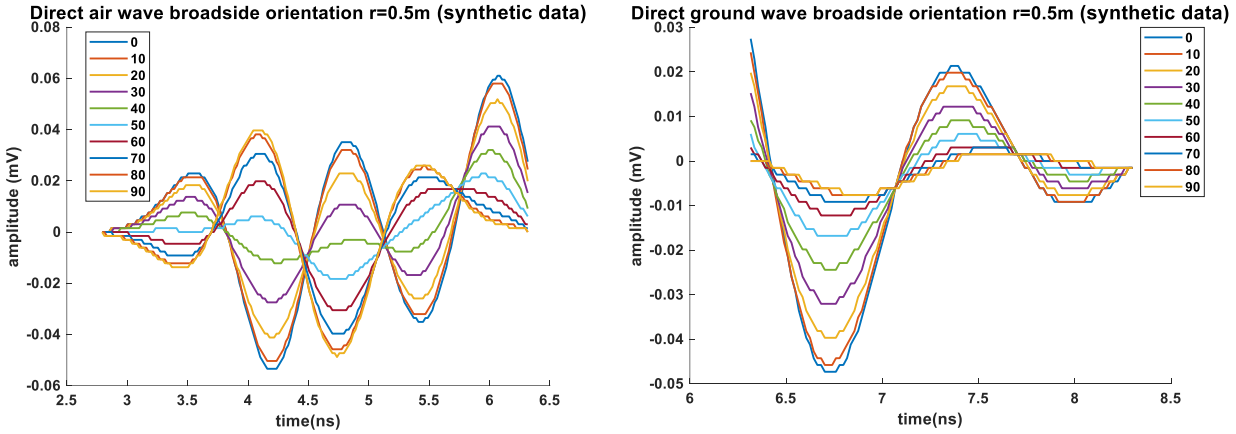

Figure 63: The simulated DAW (left) and the DGW (right) for the 10 traces collected from 0 to 90 degrees, for the broadside antenna orientation and for the circle of r=0.5m. In the x axis is the time in ns and in the y, axis is the amplitude of the GPR signal in mV. The 10 traces correspond to the angular position indicated by the legend. The traces have been generated using bare dipole antennas.

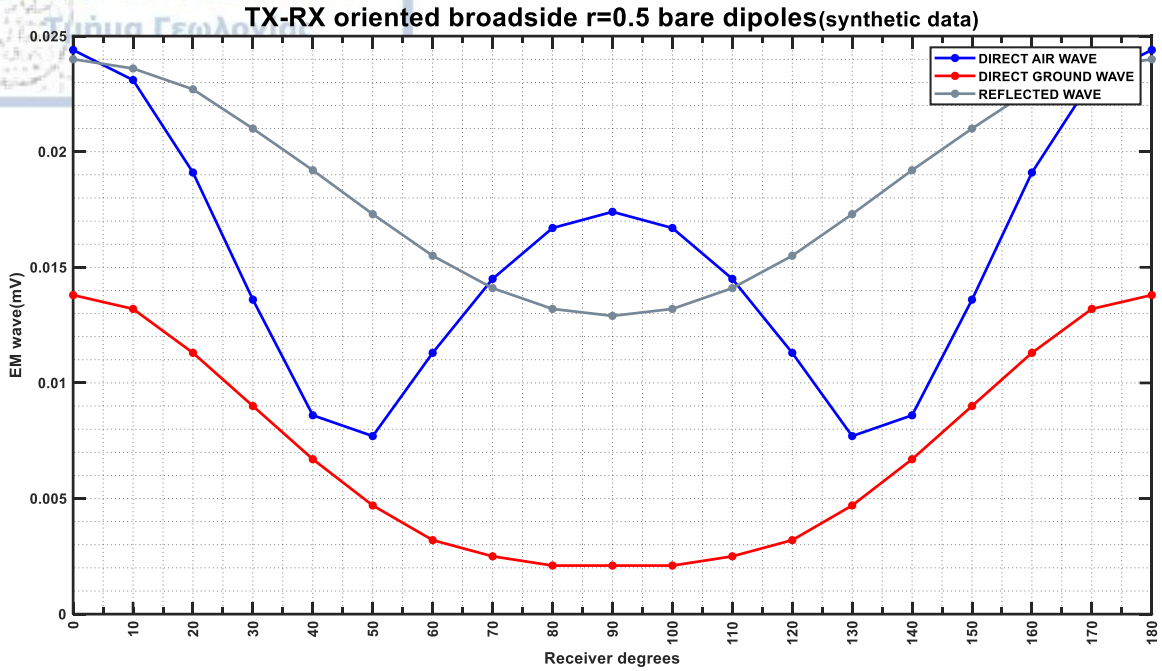

Figure 64: The mean of the absolute amplitude values in millivolts (y axis) of the DAW (blue line), the DGW (red line) and the RW (grey line) for the circle of r=0.5m and for the broadside antenna orientation. These values are plotted over the angular position around the half-circle (i.e., from 0^0 to 180^0, angular step of 1^0) as indicated in the x axis. The minor grid lines in the x axis are at every 5 degrees. The simulated traces have been generated using the bare dipole antennas.

To conclude, GPR data were simulated around three circles of radii r=0.23, 0.5 and 1m for both the broadside (PD-BD) and the endfire (PL-EF) antenna orientations, with spatial step of 5^0 using point dipole EM sources (i.e., Hertzian dipoles). Also, three semicircles of r=0.23, 0.5 and 1m were produced for the PD-BD antenna orientation with a spatial step of 10^0 using bare dipole antennas. For the models generated using point dipoles, 73 single traces were collected and the DAW, DGW and the RW were individually cropped, analyzed and 73 single values were calculated according to the analysis previously described. For the models generated using bare dipoles as the EM sources, 19 single traces were calculated and the same process was performed and at the end 19 single values were obtained. In Figure 65, a schematic diagram is presented summarizing the generation of both the synthetic (top) and the observed data (bottom).

The variations in amplitude of the DAW, DGW and RW around the circle reflect the way that the EM signals for each of these responses are spatially distributed. Such plots are presented in the next chapter.

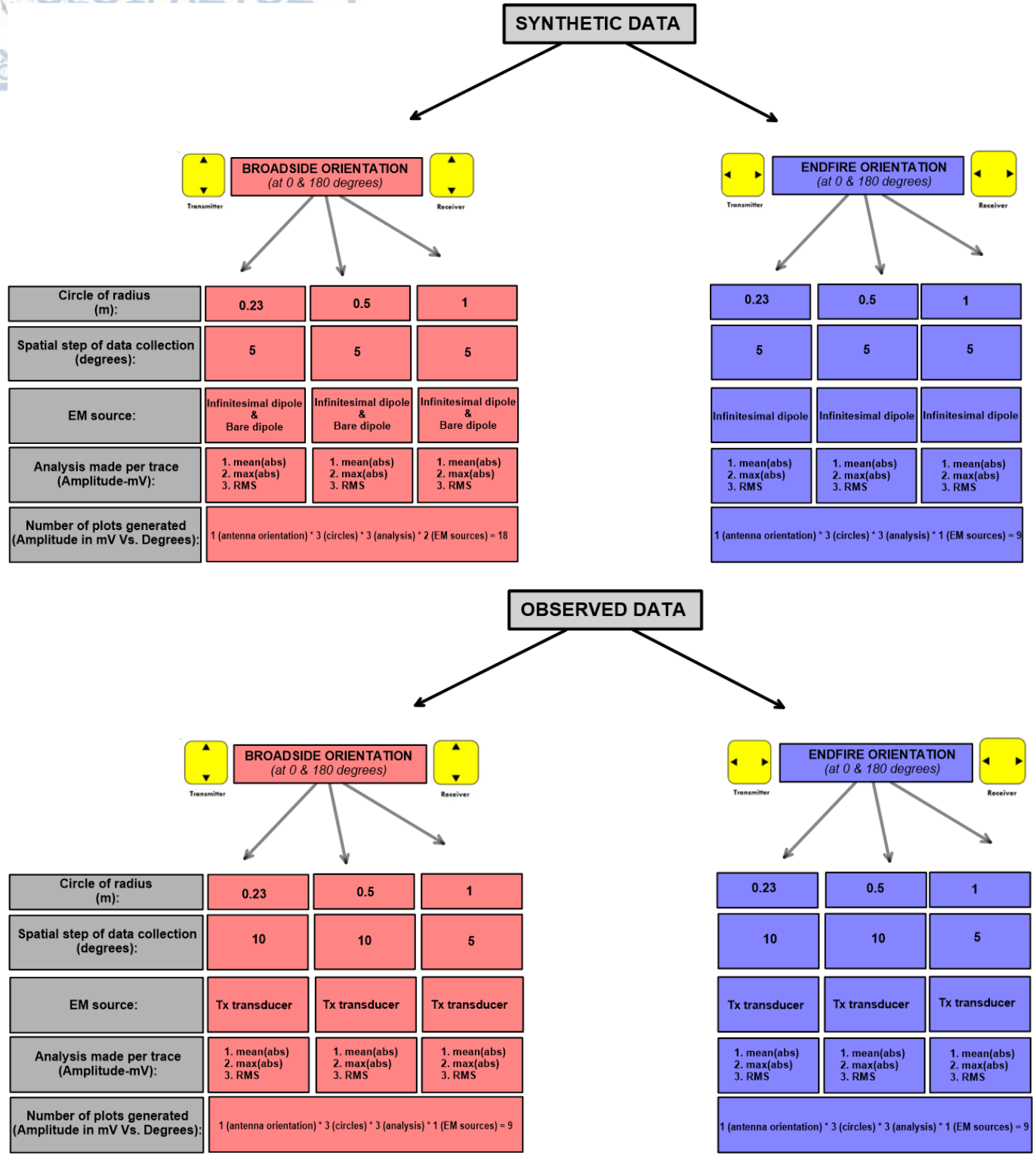

Figure 65: Schematic diagram summarizing the generation of both the synthetic (top) and the observed data (bottom).

6.Results

In this chapter, the results of the study will be presented. More specifically, both for the synthetic and the observed data results will be presented for each of the antenna orientations (i.e., PD-BD and PL-EF) and for all the circles (i.e., radii of 0.23, 0.5 and 1m) in a trace plot format from 0 to 90 degrees and also, in the form of plots of the mean absolute amplitude values in mV versus the angular step. The additional results for the maximum absolute values of amplitude in mV and the RMS values versus angle around the circle are given in appendix C.

6.1 Synthetic data *(point dipole EM source)*

Starting with the synthetic data, the trace plots from 0^0 to 90^0 for the broadside (PR-BD) antenna orientation and for all the circles are indicated in Figure 66. The results are obtained using an infinitesimal dipole EM source to excite the numerical models. Each plot corresponds to a specific position around the Tx antenna and distance from it.

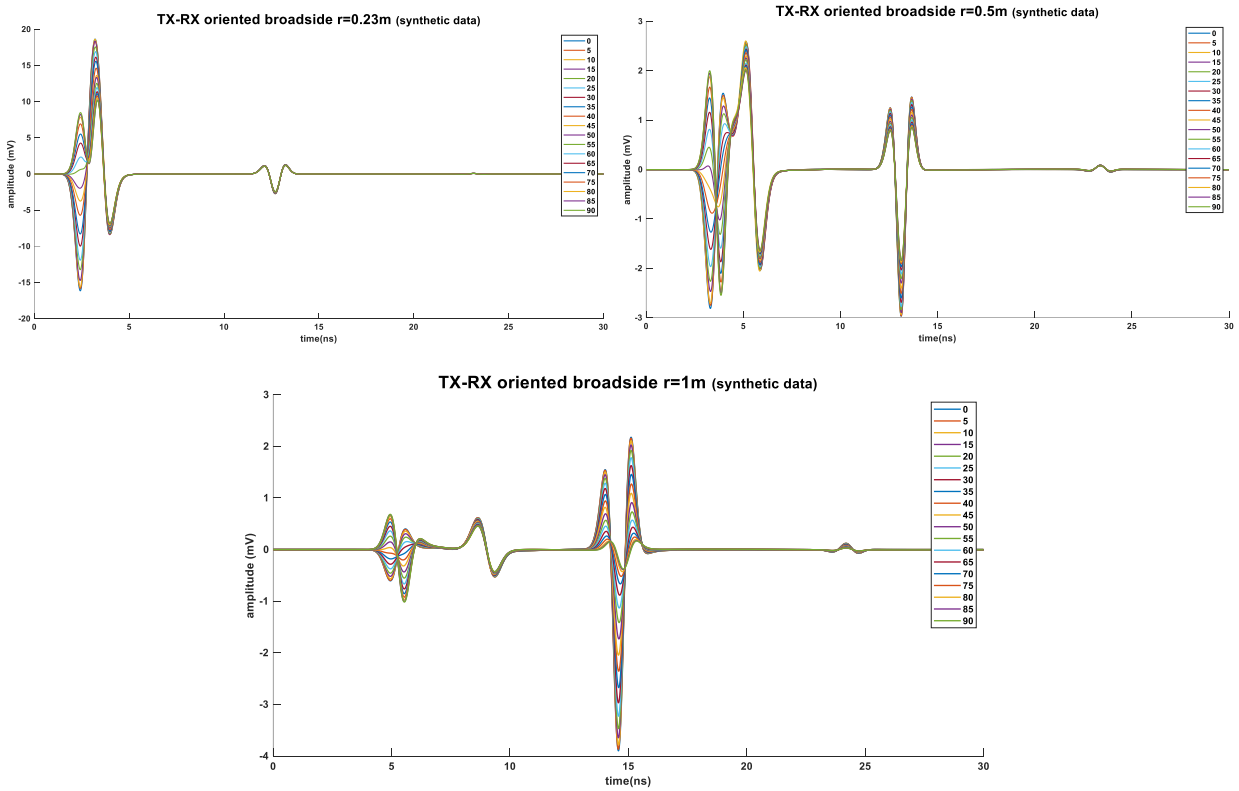

Figure 66: Trace plots for the traces simulated from 0^0 to 90^0, for the broadside antenna orientation and for the circles of r=0.23m (top left corner), r=0.5m (top right corner) and for r=1m (bottom). These traces were generated using an infinitesimal dipole EM source. The x-axis indicated the time in ns and the y-axis shows the amplitude in mV. Each trace corresponds to a specific angular position around the Tx antenna, as indicated by the legends.

From the plot for r=0.23m, one can observe that the separation of the direct air wave (DAW) and the direct ground wave (DGW) is not so straightforward. Using the time of the arrivals of each of these responses, the DAW is approximately limited from ~1.9 to ~2.8 ns. For this part of the plot (Figure 66-top left corner), a range in amplitude and in the signal polarity can be seen. The rest

of the direct wave (i.e., the DGW) is limited from ~2.8 to ~5.5 ns is more stable in terms of amplitude and signal polarity. The reflected wave (~10.5 to ~15 ns) has almost no change in amplitude. For the plot of r=0.5m (Figure 66-top right corner) the separation between the DAW (~2.4 to ~4.4ns) and the DGW (~4.4 to~7.5ns) is more obvious. The DAW has a similar behavior to the DAW for r=0.23m; its amplitude varies extensively around the circle and this is the case for its polarity too. The DGW is again more stable in amplitude and in polarity. The reflected wave (~11 to ~15.3ns) starts to change in amplitude compared to its amplitude range depicted in the plot for r=0.23m. It should be noted that the y-axis scale is different for the various plots. For the plot of r=1m (Figure 66-bottom), the DAW (~4 to ~7.5ns) and the DGW (~7.5 to ~11.5ns) are clearly separated. The DAW still exhibits a great range in amplitude and polarity changes. The DGW does not change by much in both its polarity and amplitude. The reflected wave (~12.5 to ~17 ns) changes more radically in amplitude compared to the results for r=0.23 and r=0.5m.

All of the above can be also observed in Figure 67 that shows the plots of the average absolute values of amplitude for the DAW (blue line), the DGW (red line) and the RW (grey line), for all the circles. These plots are derived from the synthetic data and for the PD-BD antenna configuration.

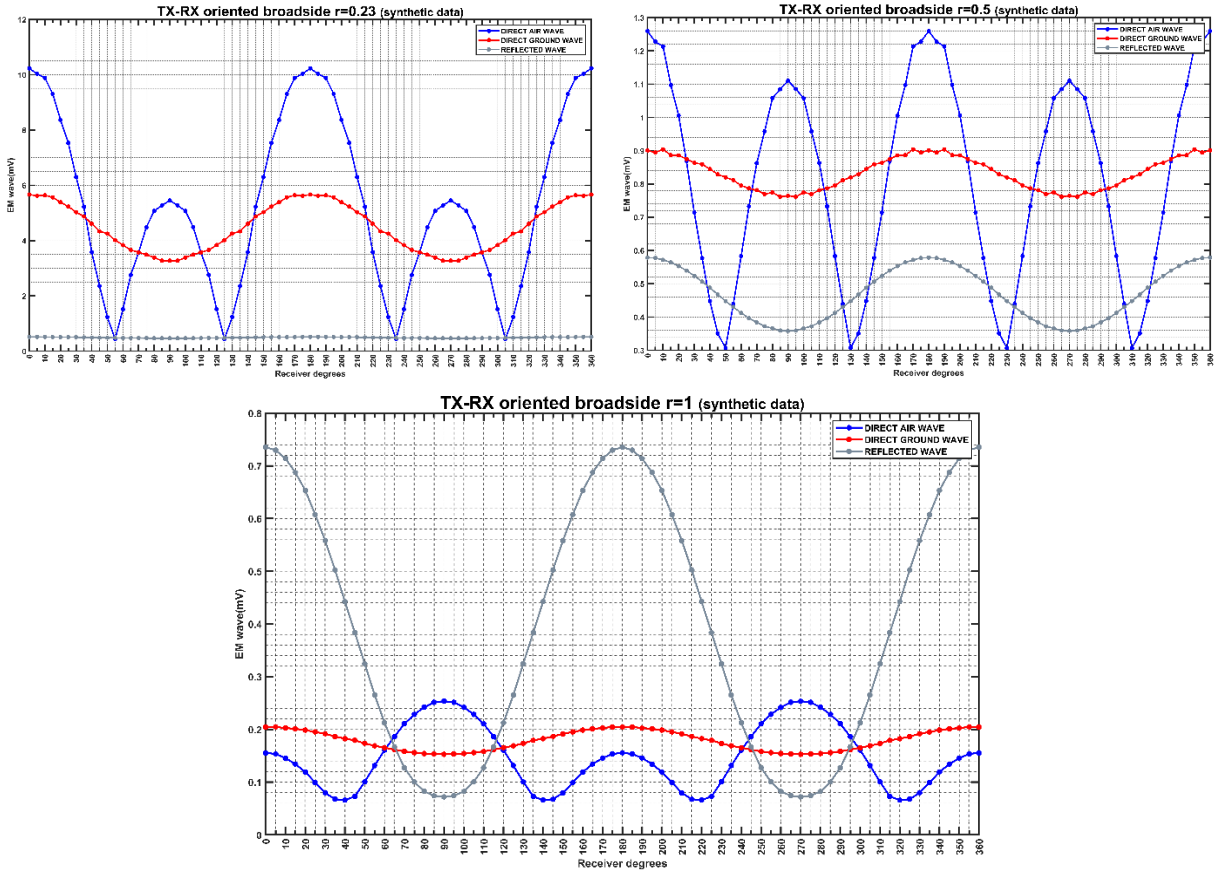

Figure 67: The mean of the absolute amplitude values in millivolts (y axis) of the DAW (blue line), the DGW (red line) and the RW (grey line) for the circles of r=0.23m (top left corner), r=0.5m (top right corner) and r=1m (bottom), for the broadside antenna orientation. These values are plotted over the angular position around the circle (i.e., from 0^0 to 360^0), as indicated in the x axis. These results are obtained from numerical data where a point dipole EM source was employed to excite the models.

In the plot for the circle of r=0.23m (Figure 67-top left corner), the DAW shows a range of amplitude from ~0.5 to approximately 10.25 mV. Its trend consists of major lobes at 0^0 (same as at 360^0) and at 180^0 and two minor lobes at 90^0 and 270^0. This shape resembles the broadside antenna pattern. The local minima for the DAW amplitude are seen at ~55^0, 125^0, 235^0 and 305^0. As the synthetic data are completely symmetrical to the quadrants of each circle, from now on, only the local minimum and the lobes of the first quadrant will be discussed. The DGW presents a different behavior compared to the DAW. It has a smaller range in amplitude variation (from ~5.6 to 2.8mV) and major lobes at 0^0 (same as at 360^0) and at 180^0. Also, no minor lobes are present. The RW is unchangeable around the circle.

For the circle of r=0.5m, the major and minor lobes for the DAW are seen at the same angles around the circle as seen for the circle of r=0.23m at 90. Also, for this case, the relative amplitude change between the major and minor lobes is smaller than this change between the lobes for r=0.23. The local minimum for the DAW has shifted to 50^0 compared to the local minimum which is at ~55^0 for the case of r=0.23m. The range in amplitude for the DAW is from ~0.3 to ~1.26mV. The DGW amplitude ranges from ~0.76 to 0.9mV and it presents similar behavior to the DGW for the circle of r=0.23m (i.e., its major lobes are seen at 0^0 and 180^0 and no minor lobes are present). The RW is quite different for the circle of r=0.5m. Its amplitude starts to change with angular position and ranges from ~0.58 to 0.36 mV. The trend in the shape of the RW resembles the shape of the DGW.

For the circle of r=1m, the amplitude of the DAW ranges from ~0.06 to 0.26 mV and its major lobes are seen at 90^0 and 270^0, which is where the minor lobes for the circles of 0.23 and 0.5m radii where seen. Minor lobes exhibit a similar behaviour. The local minimum for the DAW has shifted further, to 40^0, when compared to the local minima for the cases of r=0.23 and 0.5m. The DGW amplitude ranges in amplitude from ~0.16 to 0.2mV and its shape does not change by much with angle. The RW amplitude ranges from ~0.08 to 0.74 mV. Although the amplitude change of the RW at r=1m is larger than its change at 0.5m, the trend in their shape is similar.

Observing the three responses (i.e., the DAW, the DGW and the RW) with respect to the Tx-Rx separation for the broadside antenna orientation, the DAW has a high range of amplitude variation and its shape does not remain stable as its major lobe is initially located at 0 and 180 degrees and ends up at 90 and 270 degrees when the Tx-Rx distance is r=1m. The local minima of the DAW change position from ~55 to ~40 degrees, when changing the antenna separation from 0.23m to 1m, respectively. The DGW has a more stable behaviour for every circle. It always has a smaller range in amplitude compared to the DAW and its shape is similar for every Tx-Rx separation. The RW is unchangeable for r=0.23m and then, when the Tx-Rx distance is increased, it gradually changes. Its shape at r=0.5 and r=1m is similar but the observed changes in amplitude are larger as the Tx-Rx distance increases. All these GPR signals are characterized by the same polarity when they arrive to the Rx antenna.

The mean normalized absolute amplitude values in mV for the direct wave as a whole entity (i.e., DAW and DGW combined) is shown in Figure 68 for the broadside antenna orientation and for the circles of r=0.23m (bright green line), 0.5m (green line) and 1m (orange line). The x-axis

indicates the angular position of the traces (0^0 to 360^0) and the y-axis shows the normalized mean absolute values of the DW in mV.

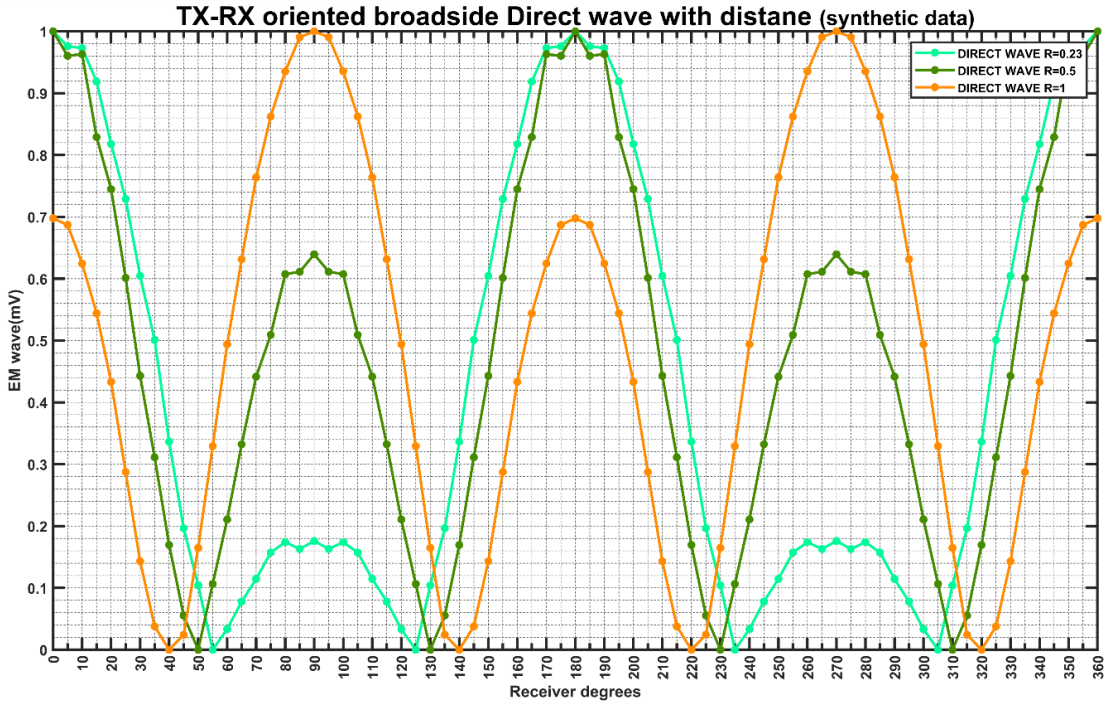

Figure 68: The normalized absolute mean values of the DW (y-axis) with respect to the spatial step of the simulated traces (i.e., per 5^0) as indicated in the x axis for the broadside antenna orientation and for the circles of r=0.23m (bright green line), r=0.5m (green line) and r=1m (orange line). The minor grid lines in the x axis are at every 5^0.

It can be clearly seen in Figure 68 that the local minima are shifting from 55^0 when r=0.23m to 50^0 when r=0.5m and then, to 40^0 when r=1m. Another observation is that the shape of the DW is mostly influenced by the DAW rather than the DGW (also see Figure 67).

The normalized mean absolute amplitude values of the DW presented in Figure 68 were interpolated using the Kriging formula to produce a general plan view of the amplitude spatial distribution for the DAW with distance from the Tx source (Figure 69). Kriging is an interpolation method which weights the surrounding measured values to derive a prediction for an unmeasured location. The general formula for both interpolators is formed as a weighted sum of the data (Borga and Vizzaccaro, 1996):

$$\hat{Z}(d_0) = \int_{j=1}^{N} \lambda_j \, Z(d_j) \qquad (8.1)$$

where:
$Z(d_j)$: is the measured value at the jth location
λ_j: is an unknown weight for the measured value at the jth location
d_0: is the prediction location
N: is the number of measured values

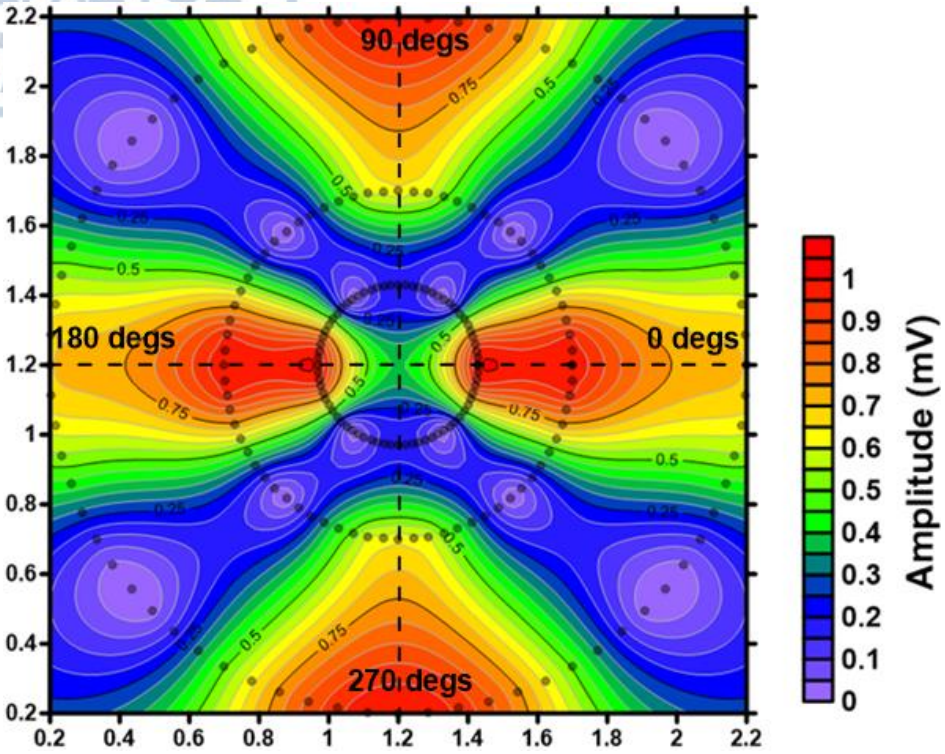

Figure 69: The simulated normalized mean absolute amplitude values (mV) for the DW and for the broadside antenna orientation, interpolated using the Kriging method. The inner dotted circle is for r=0.23m, the middle dotted circle is for r=0.5m and the outer dotted circle is for r=1m. The x and the y axis are the relative coordinates of the circles in meters. The normalized mean absolute amplitude values are indicated by the rainbow color scale.

The interpolated image of Figure 69 clearly shows the major lobe of the DW at 0^0 and 180^0 for r=0.23 and r=0.5m. Also, for r=1m it is obvious that the major lobe moves towards the 90^0 and 270^0 position. The local minimum for the DW for r=0.23m reaches a value of zero at 55^0, as it is also indicated in Figure 67 (top left corner) and in Figure 68. For r=0.5m, the minimum amplitude values are ranging from 35^0 to 60^0, reaching a zero value at 50^0 (also see: Figure 67-top right corner, and Figure 68). For r=1m, the minimum amplitudes for the direct wave are from 25^0 to 55^0, reaching a zero value at 40^0 (also see: Figure 67-bottom and Figure 68).

The trace plots from 0^0 to 90^0 for the endfire antenna configuration and for the circles of r=0.23m (top left corner), r=0.5m (top right corner) and for r=1m (bottom) are indicated in Figure 70. The synthetic results are generated using infinitesimal dipole EM sources as both the transmitting and receiving antennas. Each plot corresponds to a specific position around the Tx antenna.

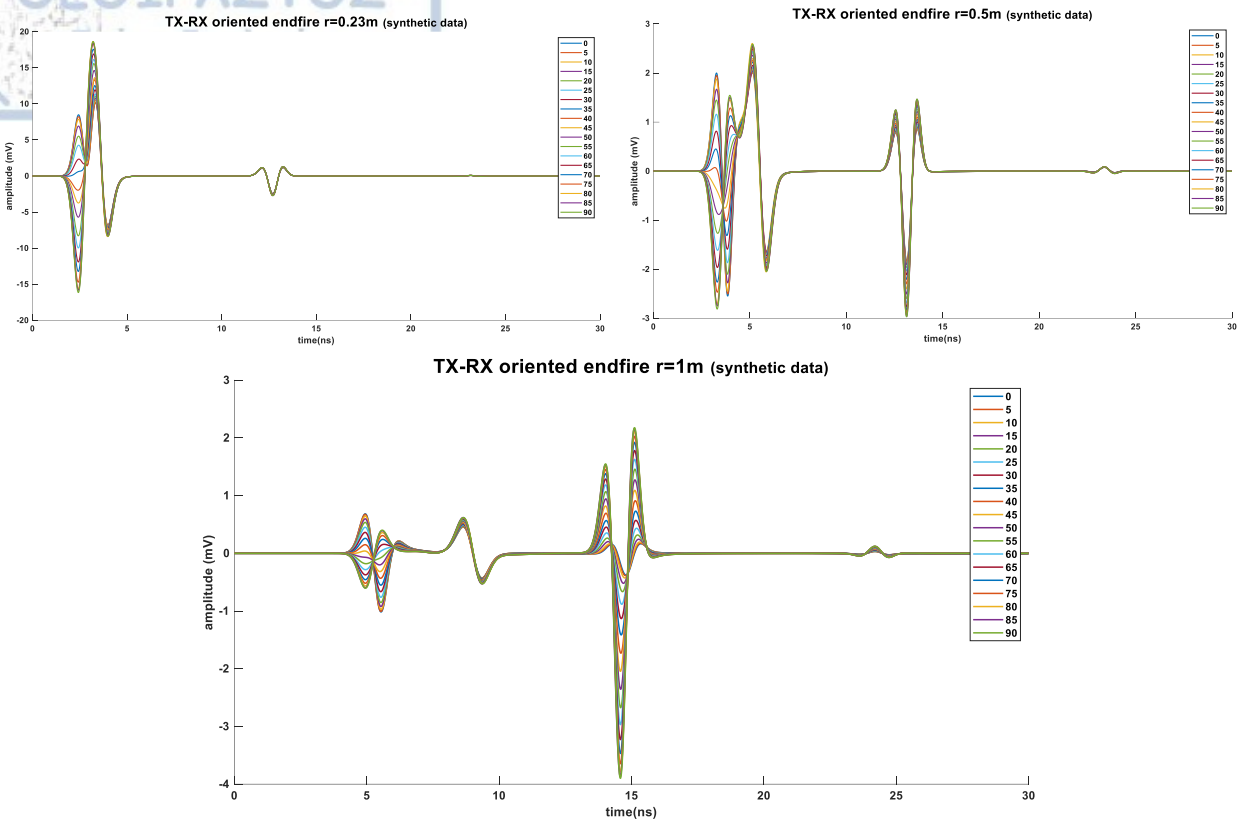

Figure 70: Simulated trace plots for the traces collected from 0^0 to 90^0, for the endfire antenna orientation and for the circles of r=0.23m (top left), r=0.5m (top right) and for r=1m (bottom). Traces were generated using an infinitesimal dipole EM source. In the x-axis the time in ns is indicated from the start to the end of the simulation and the y-axis is the amplitude in mV. Each trace corresponds to a specific angular position around the Tx antenna, as indicated by the legends.

The responses simulated for the endfire antenna orientation (i.e., the DAW, the DGW and the RW) are characterized by a similar behavior to the broadside antenna configuration. Note that while the Rx antenna is moving around the Tx, the endfire antenna configuration at the 0^0-180^0 line becomes the broadside antenna configuration at the 90^0-270^0. More specifically, the DAW has a high range in amplitude changes and also, in polarity changes, for all the Tx-Rx distances. The DGW seems to be the most stable signal in terms of amplitude and polarity. The RW is almost unchangeable when r is equal to 0.23m but for r=0.5m and r=1m, changes in its amplitude are observed. For r=0.23 m, it is harder to distinguish the DAW and the DGW. For r=1m, these two events are completely separated (Figure 70, bottom). Both of the DAW and DGW amplitudes are getting smaller as the Tx-Rx distance increases. The arrival time of the DAW, DGW and the RW for r=0.23m, 0.5m and 1m are the same as for the broadside antenna configuration.

The plots of the average absolute amplitude values for the DAW (blue line), the DGW (red line) and the RW (grey line) plotted over the angular position of the simulated traces for the endfire antenna orientation are shown in Figure 71.

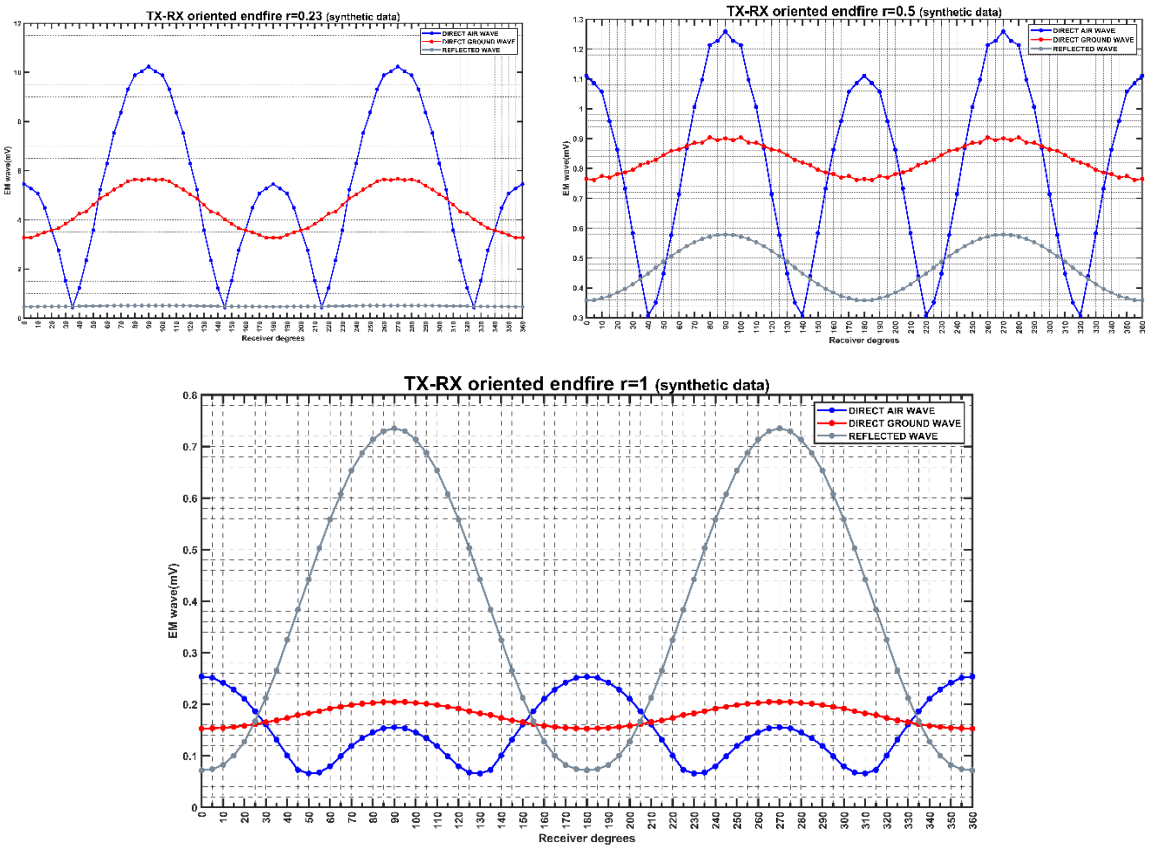

Figure 71: The mean, absolute amplitude values in millivolts (y axis) for the DAW (blue line), the DGW (red line) and the RW (grey line) for the circles of r=0.23m (top left), r=0.5m (top right) and for r=1m (bottom) for the endfire antenna orientation over the angular position of the simulated traces (i.e., per 5^0). The traces have been generated using a point dipole EM source.

The DAW for r=0.23m and for the endfire antenna orientation reaches a maximum amplitude of 10.25 mV and a minimum of 0.5 mV at 90^0 and 35^0 degrees, respectively, for the first quadrant of the circle. The shape of the DAW has a major lobe at 90^0 and a minor lobe at 0^0 which is a similar trend to an endifire antenna pattern. The DGW reaches the receiver with the opposite polarity of the DAW and it has smaller changes in amplitude. Regarding the shape of the DGW, its major lobe is located at 80^0 and minor lobes are not observed. The RW is stable as it is the case for r=0.23m and for the broadside antenna orientation. For r=0.5m (Figure 71-top right), the DAW has the same range in amplitude as in the the broadside antenna orientation. The minor lobe at 0^0 increases in amplitude and the major lobe is located at 90^0. The local minimum of the DAW has shifted from 35^0 degrees (r=0.23m) to 40^0. The DGW has maintained its shape from r=0.23m to r=0.5m and the changes in its amplitude are the same to the changes of the DGW for r=0.5m of the broadside antenna orientation. The RW has also the same range in amplitude changes as for the broadside antenna orientation (Figure 67-top right). The shape of the RW follows the shape of the DGW and therefore, both of these responses have the same polarity. For r=1m (Figure 71-bottom), the DAW has the same amplitude changes as the direct air wave for r=1m and for the broadside antenna orientation (Figure 67-bottom). Its shape has changed with the major lobe located at 0^0 and the minor lobe at 90^0, which is a similar trend to a broadside antenna pattern. The local minimum of the DAW has shifted from 40^0 (r=0.5m) to 50^0. The DGW

has maintained its shape and it reaches the receiver with the reverse polarity compared to the DAW. The RW shows the same changes in amplitude as the RW of r=1m for the broadside antenna orientation. Its shape follows the shape of the DGW and both of these responses have the same polarity.

Observing the three responses (i.e., the DAW, DGW and the RW) with respect to the Tx-Rx distance and for the endfire antenna orientation, the DAW has a high range of amplitude changes and its shape changes as its major lobe, initially located at 90^0 and 270^0, is gradually shifting and ends up at 0^0 and 180^0 when the Tx-Rx distance is r=1m. The DGW shows a more stable behaviour for all circles. It always has a smaller range in amplitude changes compared to the DAW and its shape is similar for every Tx-Rx distance. The RW is almost unchangeable for r=0.23m and it is gradually changing with distance. Its shape at r=0.5 and r=1m is similar but the observed changes in amplitude are larger as the Tx-Rx distance is increasing. The DGW and the RW have the same polarity which is reversed compared to the DAW.

The normalized mean absolute values of amplitude in mV for the DW as a whole entity (i.e., DAW and DGW combined) are presented in Figure 72 for the endfire antenna orientation.

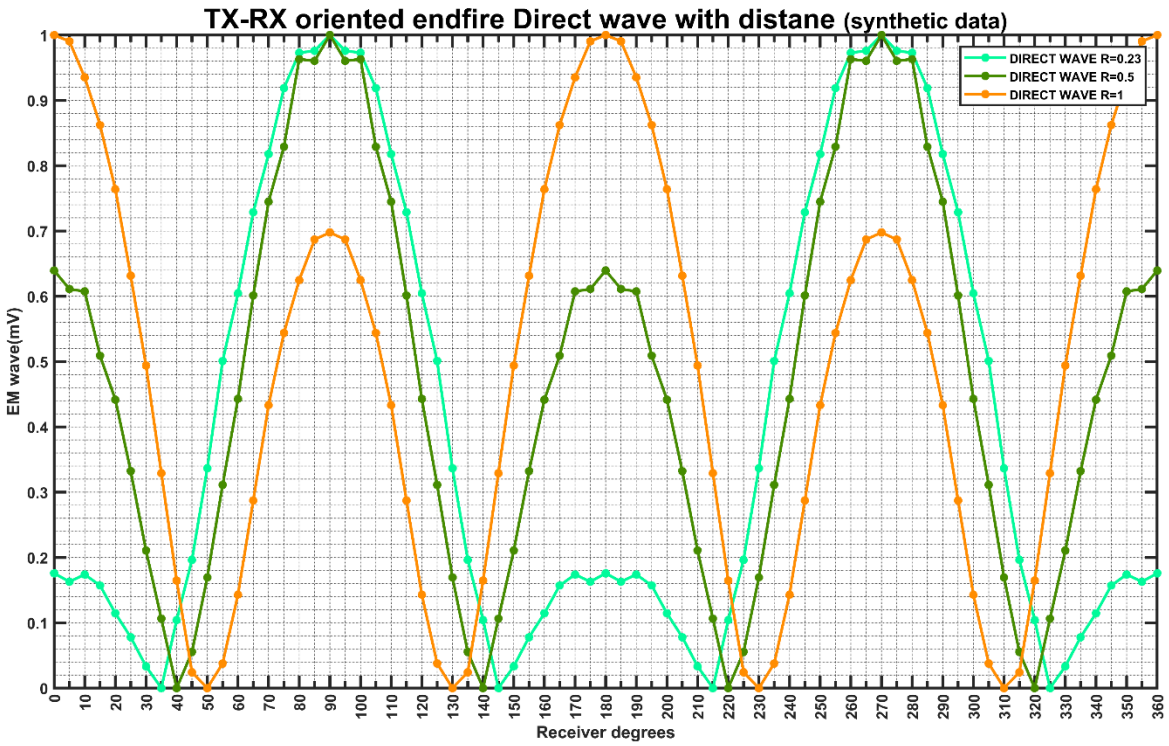

Figure 72: The normalized absolute mean values of the DW (y-axis) with respect to the spatial step of the simulated traces (i.e., per 5^0) as indicated in the x axis for the endfire antenna orientation and for the circles of r=0.23m (bright green line), r=0.5m (green line) and r=1m (orange line). The minor grid lines in the x axis are at every 5 degrees.

As it can be seen in Figure 72, the minor lobes of the DW for r=0.23m are increasing in amplitude with distance and end up governing the shape of the DW when r=1m. The local minima are

shifting from 35^0 when r=0.23m to 40^0 when r=0.5m and to 50^0 when r=1m. Another observation is that the shape of the direct wave is mostly influenced by the DAW rather than the DGW.

The normalized mean absolute amplitude values for the DW presented in Figure 72 were interpolated using the Kriging formula presented in Equation 8.1, to produce a general plan view of the spatial amplitude distribution for the DW with distance from the source, as shown in Figure 73.

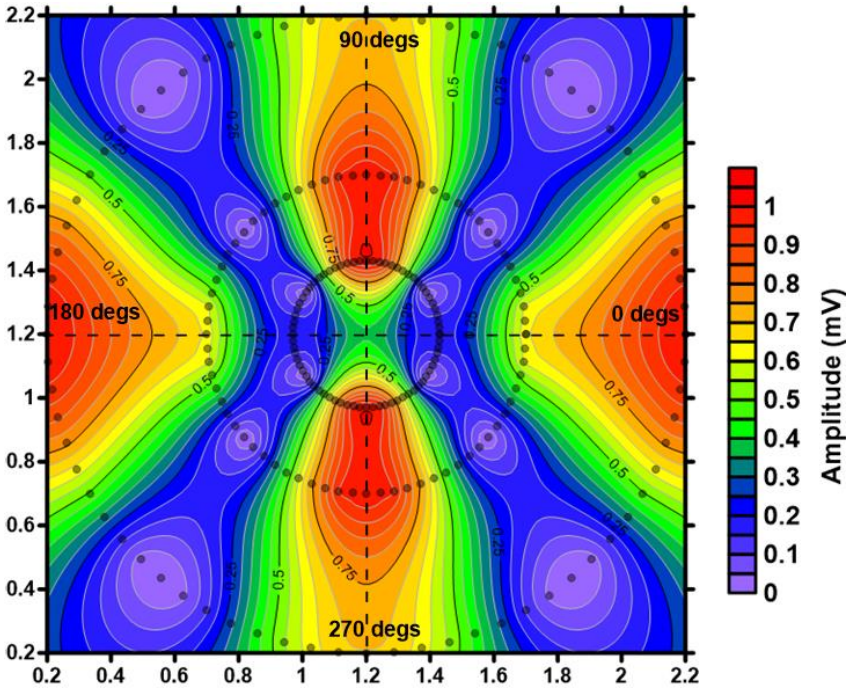

Figure 73: The simulated normalized mean absolute amplitude values (mV) for the DW and for the endfire antenna orientation, interpolated using the Kriging method. The inner dotted circle is for r=0.23m, the middle dotted circle is for r=0.5m and the outer dotted circle is for r=1m. The x and the y axis are the relative coordinates of the circles in meters. The normalized mean absolute amplitude values are indicated by the rainbow color scale.

The interpolated image of Figure 73 clearly shows the major lobe of the direct wave at 90^0 and 270^0 for r=0.23 and r=0.5m and also, the major lobe of the DW at 0^0 and 180^0 for r=1m. The local minima for the direct wave for r=0.23m are ranging from 0^0 to 35^0 reaching a value of zero at 30^0 degrees. For r=0.5m, the minimum values of amplitude for the DW range from 25^0 to 45^0 angular position, reaching a zero value at 35^0-40^0, which agrees with the DW behavior of Figure 72 and the DAW results presented in Figure 71. For r=1m, the minimum of the DW amplitude is at 40^0 to 65^0 angular position reaching a zero value at 50^0 (which agrees with the DW results of Figure 72 and the DAW of Figure 71-bottom).

6.2 Synthetic data *(bare dipole EM source)*

Apart from the point dipole sources used for our modelled data, one more set of numerical models was created employing bare dipole antennas to excite the models. Models were created for the three circles of r=0.23m, r=0.5m and r=1m, consisting of only the two first quadrants (i.e.,

from 0^0 to 180^0). Also, only the broadside configuration was treated for these models and the angular step for the simulated traces was equal to 10^0.

The simulated trace plots from 0 to 90 degrees for the broadside antenna orientation and for the semicircles of r=0.23m (Figure 74-top left corner), r=0.5m (Figure 74-top right corner) and for r=1m (Figure 74-bottom) are indicated in Figure 74. In the x-axis the time in ns is indicated from the start to the end of the recording window. In the y-axis the amplitude in mV is presented. Each plot correspond to a specific position around the Tx antenna and the degrees are indicated by the rainbow color scale located at the right top corner of each plot.

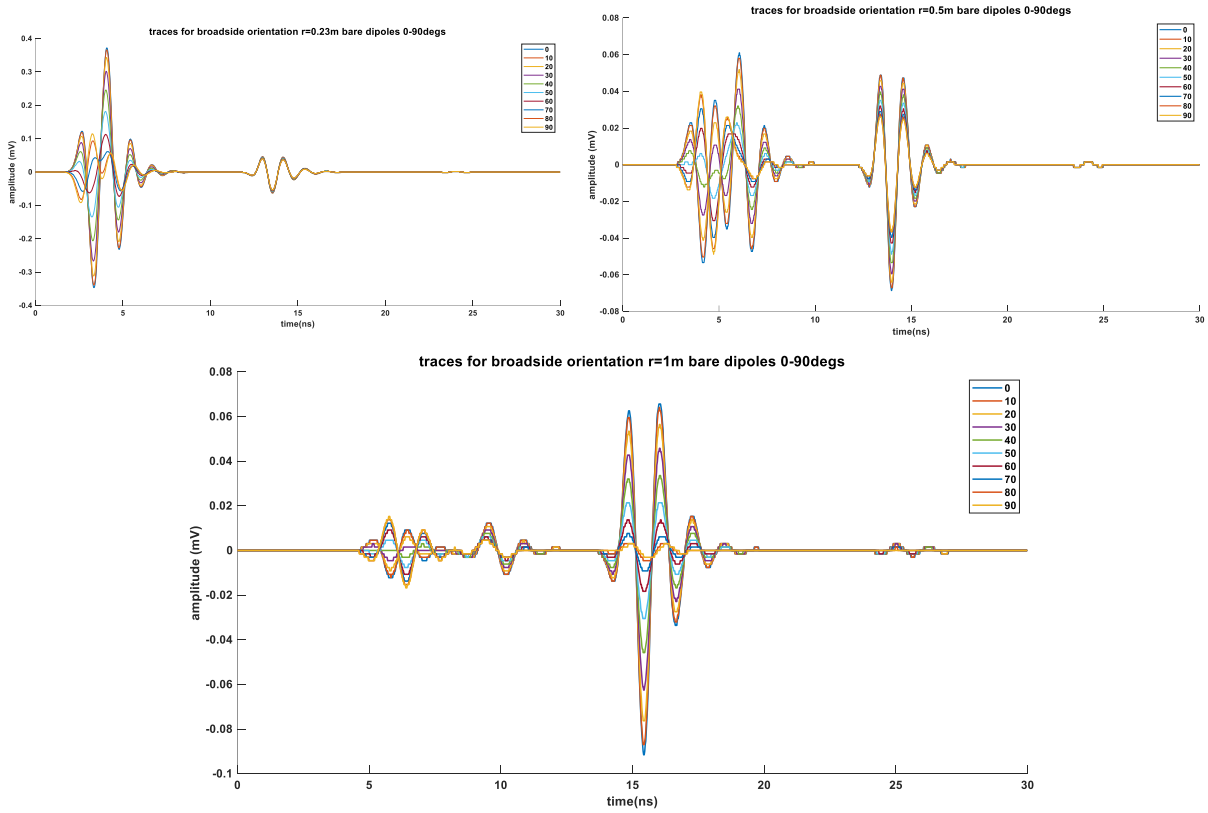

Figure 74: Simulated trace plots for the traces collected from 0^0 to 90^0, for the broadside antenna orientation and for the semicircles of r=0.23m (top left), r=0.5m (top right) and for r=1m (bottom). Traces were generated using bare dipoles both for the source and the receiving antenna. In the x-axis the time in ns is indicated and the y-axis is the amplitude in mV. Each trace corresponds to a specific angular position around the Tx antenna, as indicated by the legends.

For r=0.23m (Figure 74-top left), and for r=0.5m (Figure 74-top right) it is hard to distinguish the DAW from the DGW. For the RW, the changes in amplitude for r=0.23m (~12.5-14.5ns) to r=0.5m (~13-15.5ns) are obvious. For r=1m (Figure 74-bottom), the DAW (~4.5-9ns) and the DGW (~9-11.5ns) are clearly separated. The DAW for r=1m is changing in amplitude and polarity in contrast to the DGW which has a more stable behavior in terms of amplitude and polarity changes. The RW also changes in amplitude with angular position. The behavior of these three GPR signals (i.e., DAW. DGW and RW) when bare dipoles are used for the simulations is similar to when point dipoles are used (Figure 66).

The same processing sequence was applied to these numerical data and the plots of the average absolute amplitude values for the various events are shown in Figure 75. The results for the average maximum values and the RMS amplitude values can be found in Appendix C.

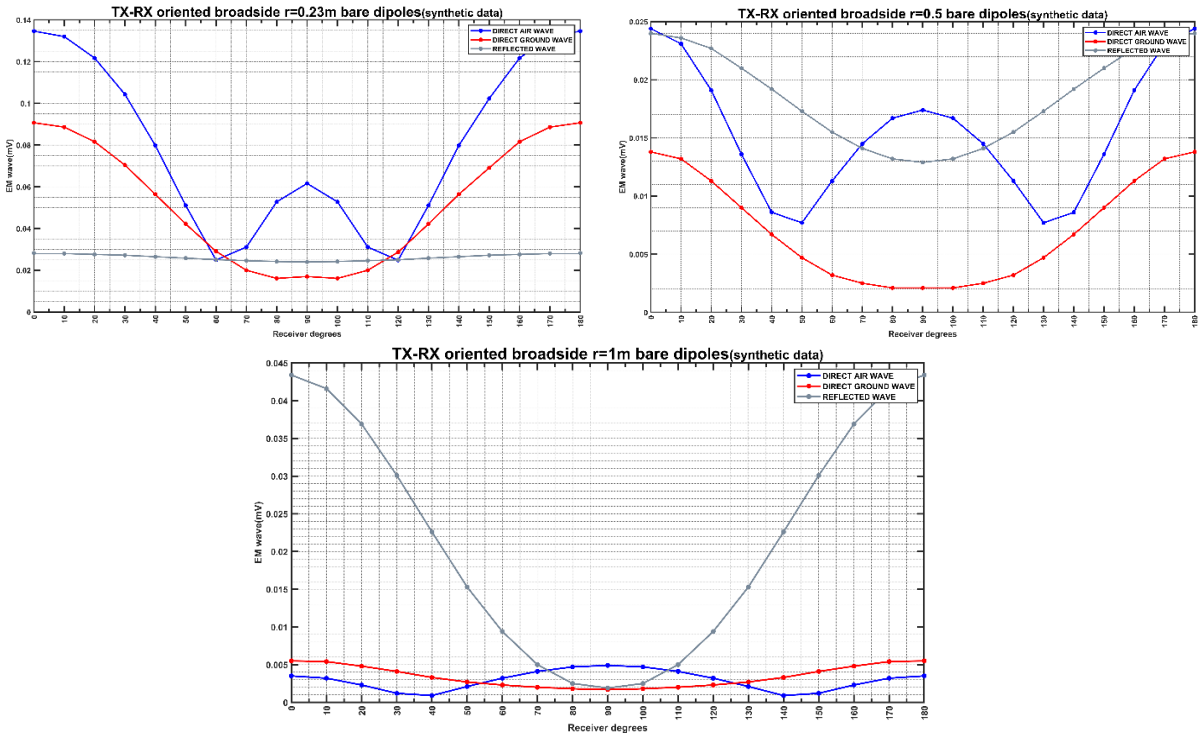

Figure 75: The mean, absolute amplitude values in millivolts (y axis) for the DAW (blue line), the DGW (red line) and the RW (grey line) for the circles of r=0.23m (top left), r=0.5m (top right) and for r=1m (bottom) for the broadside antenna orientation over the angular position of the simulated traces (i.e., per 10^0). The traces have been generated employing in the models bare dipoles as the Tx and Rx antennas.

For r=0.23m, the DAW (Figure 75-top left) changes in amplitude from 0.025 to 0. 135 mV. The local minimum is located at 60^0. The major amplitude lobe is indicated at 0^0 and 180^0 and a minor lobe is also observed at 90^0, forming a shape similar to a broadside antenna pattern. The DGW for r=0.23m ranges in amplitude from 0.015 to 0.09 mV. It is recorded having the same polarity to DAW; it has a major lobe at 0^0 and 180^0 and a small minor lobe at 90^0. The RW is generally unchangeable with a very small amplitude change (~0.025-0.0275 mV). For r=0.5m (Figure 75-top right), the DAW ranges in amplitude from 0.008 to 0.025 mV and its local minimum has shifted at 50^0. Its major lobe is still located at 0^0 and 180^0 and its minor lobe has become significantly higher in amplitude. The DGW ranges in amplitude from 0.002 to 0.015 mV. Its shape is characterized by a major lobe at 0^0 and 180^0. The RW ranges in amplitude from 0.013 to 0.024 mV. All the three GPR events are reaching the Rx antenna with the same polarity. For r=1m (Figure 75-bottom), the DAW has a amplitude change in the range of 0.001 to 0.005 mV with a local minimum at 40^0. Its shape has changed as the major lobe is now at 90^0 and the minor lobe is at 0^0 and 180^0. The DGW amplitude ranges from 0.002 to 0.005 mV, the major lobe is seen at 0^0 and 180^0. The RW amplitude ranges from 0.002 to 0.043 mV and it generally follows the shape of the DGW. All of these three GPR events are reaching the Rx antenna with the same polarity.

6.3 Observed data

The observed data were collected in the field as described in Chapter 5.1. Data were collected employing the broadside and endfire antenna configurations using the 500MHz transducers by Sensors & Software. Three concentric circles of r=0.23m, r=0.5m and r=1m were formed moving the Rx around the Tx. Traces were collected per 10^0 for r=0.23m and 0.5m, and per 5^0 for r=1m, for both the broadside and endfire antenna configurations.

The field data trace plots from 0^0 to 90^0 for the broadside antenna orientation are illustrated in Figure 76. Each trace corresponds to a specific Rx position around the Tx. For r=0.23m (Figure 76-top left) and for r=0.5m (Figure 76-top right) it is difficult to discriminate the DAW and the DGW. For r=1m, the DAW and the DGW can be separated but it is surely harder to distinguish them when compared to the clinical modelled responses.

The arrival times for the DAW (t_{air}), the DGW (t_{gr}) and the RW (t_{ref}) estimated by the WARR measurements presented in Table 4 can be used to isolate those three responses and generate the spatial amplitude distribution for each of them.

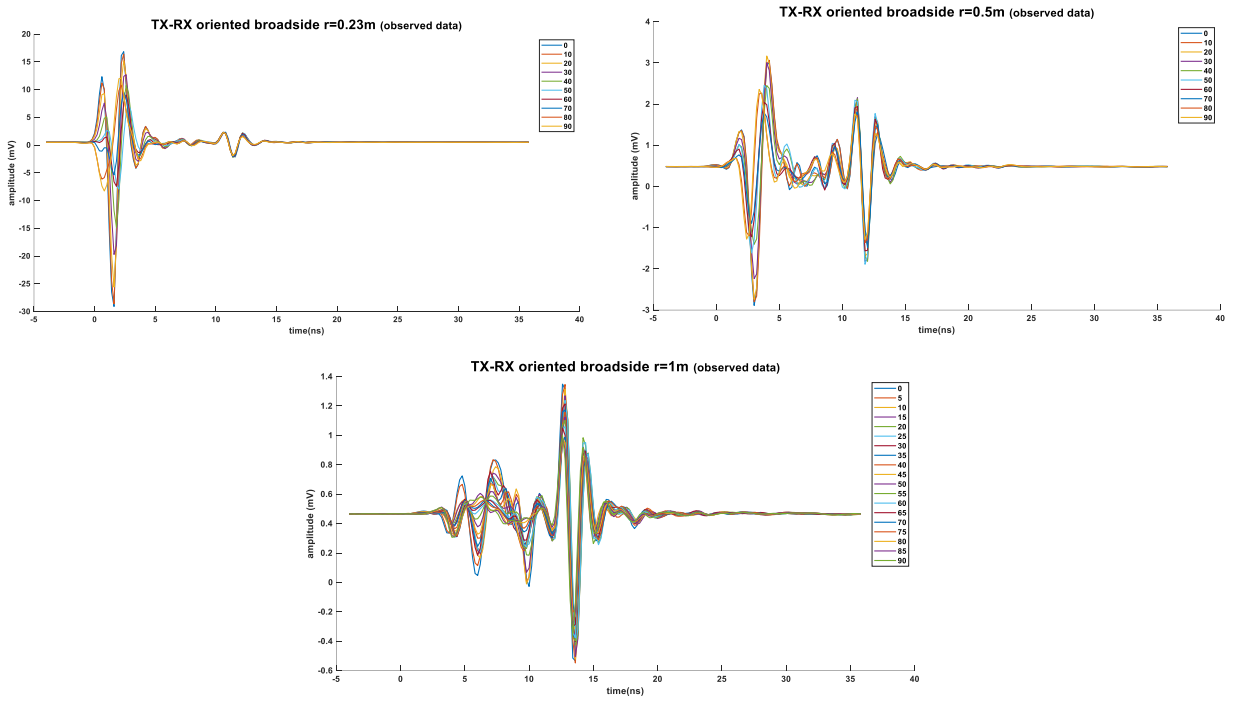

Figure 76: Field data trace plots for the traces collected from 0^0 to 90^0, for the broadside antenna orientation and for the circles of r=0.23m (top left), r=0.5m (top right) and for r=1m (bottom). In the x-axis the time in ns is indicated and the y-axis is the amplitude in mV. Each trace corresponds to a specific angular position around the Tx, as indicated by the legends.

The plots of the average absolute amplitude values for the DAW, the DGW and the RW versus the angular position of the collected traces for the broadside antenna orientation and for all the circles are shown in Figure 77. The results for the average maximum values and the RMS values of amplitude for all these three events can be found in Appendix C.

For r=0.23m, the DAW amplitude (Figure 76- top left and Figure 77) ranges from 0.4 to 9.4 mV reaching a minimum value at 70^0. The shape of the DAW is characterized by a major lobe at 0^0 and 180^0 and the minor lobes at 90^0 and 270^0 are shown to have quite high amplitude values.

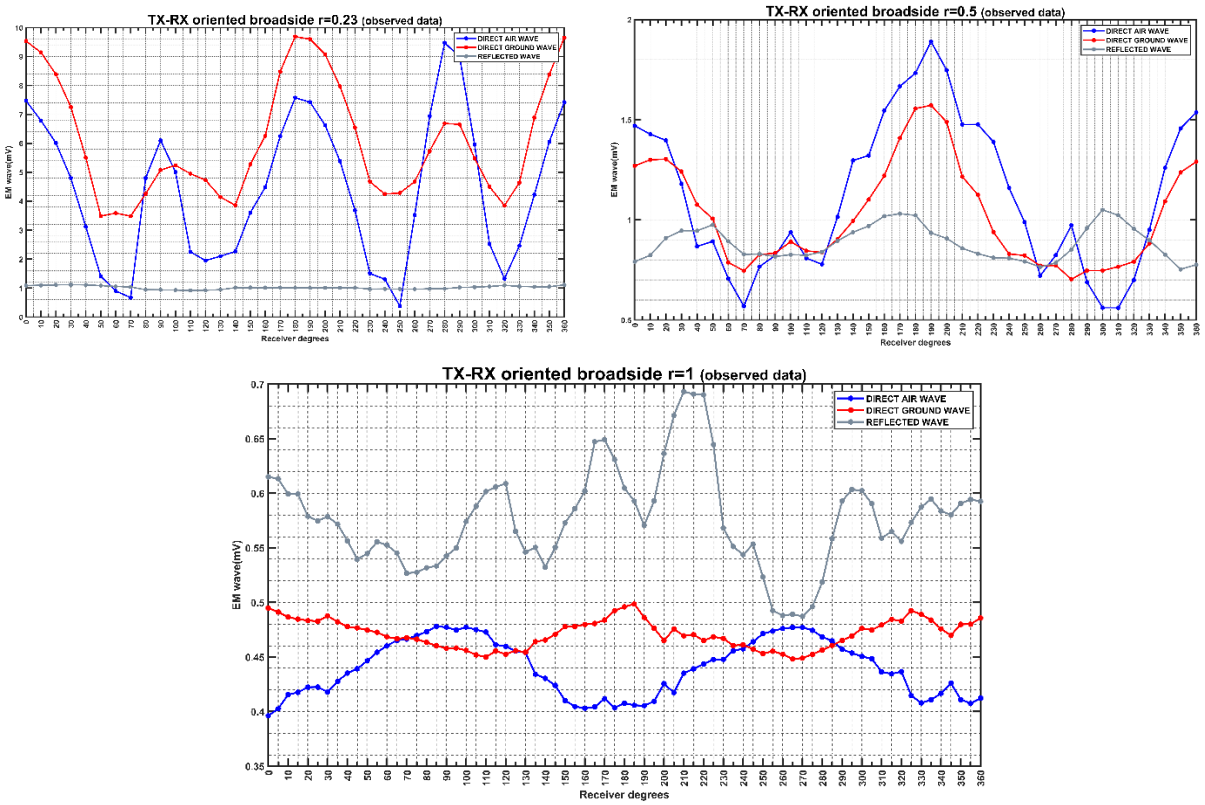

Figure 77: The mean, absolute amplitude values in millivolts (y axis) for the DAW (blue line), the DGW (red line) and the RW (grey line) for the circles of r=0.23m (top left), r=0.5m (top right) and for r=1m (bottom) for the broadside antenna orientation over the angular position of the field collected traces (i.e., per 10^0 for r=0.23 and r=0.5m and per 5^0 for r=1m).

The DGW amplitude ranges from 3.4 to 9.6 mV. The trend of the DGW generally follows the shape of the DAW clearly indicating a major lobe at 0^0 and 180^0 and minor lobes at ~90^0 and 270^0. The RW is stable in amplitude with a range of ~1-1.02mV. The DAW and the DGW for r=0.23m and for the broadside orientation are recorded with the same polarity. For r=0.5m, the DAW changes in amplitude from 0.52 to 1.9 mV reaching a minimum value at 70^0. Its shape has changed compared to the shape of the DAW for r=0.23m. More specifically, the minor lobes at approximately 90^0 and 270^0 are hard to discriminate because they are presented with a quite low value of amplitude. Despite this, the major lobe is still located at 180^0. At 0^0 and at 360^0 there is also a lobe of high amplitude. The DGW reaches a maximum amplitude of 1.57mV and a minimum of 0.7mV. Its shape generally follows the shape of the DAW with a major lobe clearly located at 180^0 and a lobe of high amplitude at 0^0 and at 360^0. A minor lobe in the trend of the DGW is probably located at ~90^0 but for its symmetrical part at 270^0 this is not observed. The RW has a higher amplitude range (~0.75-1.04mV) and it has the same polarity with the DAW and the DGW. For r=1m, the behavior of the DAW compared to the DGW starts to resemble to the behavior of those two responses in the synthetic data. More specifically, for r=1m, the DAW amplitude ranges

from 0.4 to 0.48mV. There is not a clear minimum in the trend of the DAW but there is a major lobe at 90^0 and at 270^0. The DGW amplitude ranges from 0.45 to 0.5mV. It is recorded with a reversed polarity compared to the DAW and its trend does not follow the trend of the DAW. A major lobe is probably located at 180^0. The RW amplitude ranges from 0.49 to 0.7mV.

The mean absolute normalized amplitude values in mV for the DW as a whole entity are presented in Figure 78 for the broadside antenna orientation and for all the circles. The DW in general maintains its shape with respect to the Tx-Rx distance. A major lobe is present in the results for all circles. For r=0.23m, there is the major lobe at 180^0, 0^0 and 360^0. The minor lobes are located at 90^0 and 270^0 as it was the case for the DAW and the DGW when they were treated as separate entities. For r=0.5m, the DW still has a major lobe at 180^0 characterizing its shape but its symmetrical part at 0^0 and 360^0 has lower values of amplitude. The minor lobes initially located at 90^0 and at 270^0 for r=0.23m, are not observed in the data of r=0.5m except from a small amplitude increase at 90^0. For r=1m, the DW is characterized by a lobe at 180^0 and the minor lobes at ~90^0 and 270^0 although they are not well shaped, they can be seen having almost equal amplitude to the major lobe at 180^0.

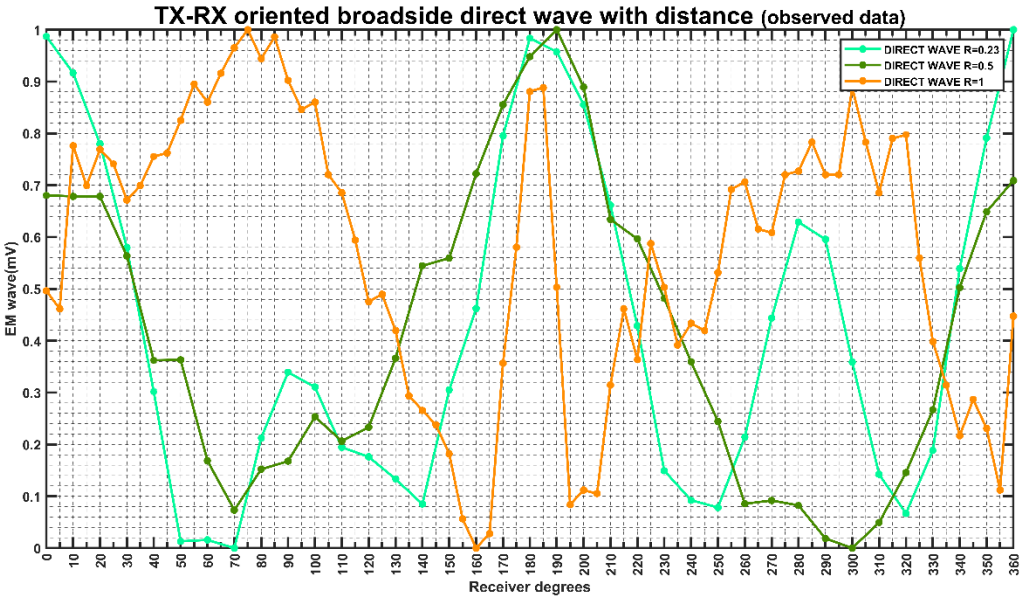

Figure 78: The normalized absolute mean values of the DW (y-axis) with respect to the angular step of the field collected traces (i.e., per 10^0 for r=0.23 and r=0.5m and per 5^0 for r=1m) as indicated in the x axis for the broadside antenna orientation and for the circles of r=0.23m (bright green line), r=0.5m (green line) and r=1m (orange line). The minor grid lines in the x axis are at every 5 degrees.

The normalized mean absolute amplitude values for the DW presented in Figure 78 were interpolated using the Kriging formula presented in Equation 8.1, to produce a plan view of the spatial amplitude distribution for the DW with distance from the Tx (Figure 79).

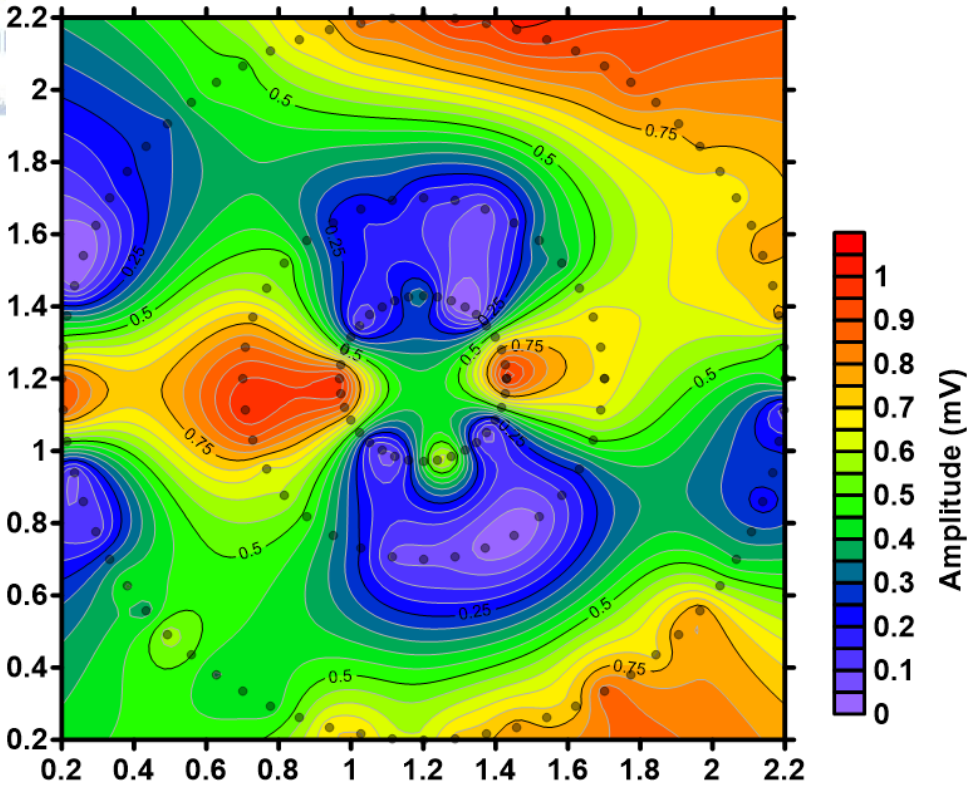

Figure 79: Field data normalized mean absolute amplitude values (mV) for the DW and for the broadside antenna orientation, interpolated using the Kriging method. The inner dotted circle is for r=0.23m, the middle dotted circle is for r=0.5m and the outer dotted circle is for r=1m. The x and the y axis are the relative coordinates of the circles in meters. The normalized mean absolute amplitude values are indicated by the rainbow color scale.

From the interpolated plan view values shown in Figure 79, the major lobe at 0^0 and 180^0 is obvious for r=0.23m. For the DW of r=0.5m, the major lobe is mainly located at 180^0 and there is an area of high amplitudes at the same position for r=1m. For r=0.23 and 0.5m the DW is characterized by weak strength at 90^0 and 270^0 degrees reaching a value of 0 at ~60^0. For r=1m, a zero value for the mean and normalized absolute amplitude is found at 160^0, 195^0 and 355^0.

The field data trace plots from 0^0 to 90^0 for the endfire antenna orientation and for all the circles are shown in Figure 80 for the observed data. The overall behaviour follows a similar logic to the one described above for the broadside antenna configuration.

The plots of the average absolute amplitude values for the three events and for all the circles are shown in Figure 81, for the endfire antenna configuration. The results for the average maximum values and the RMS values of amplitude of the DAW, the DGW and the RW over angular position can be found in Appendix C.

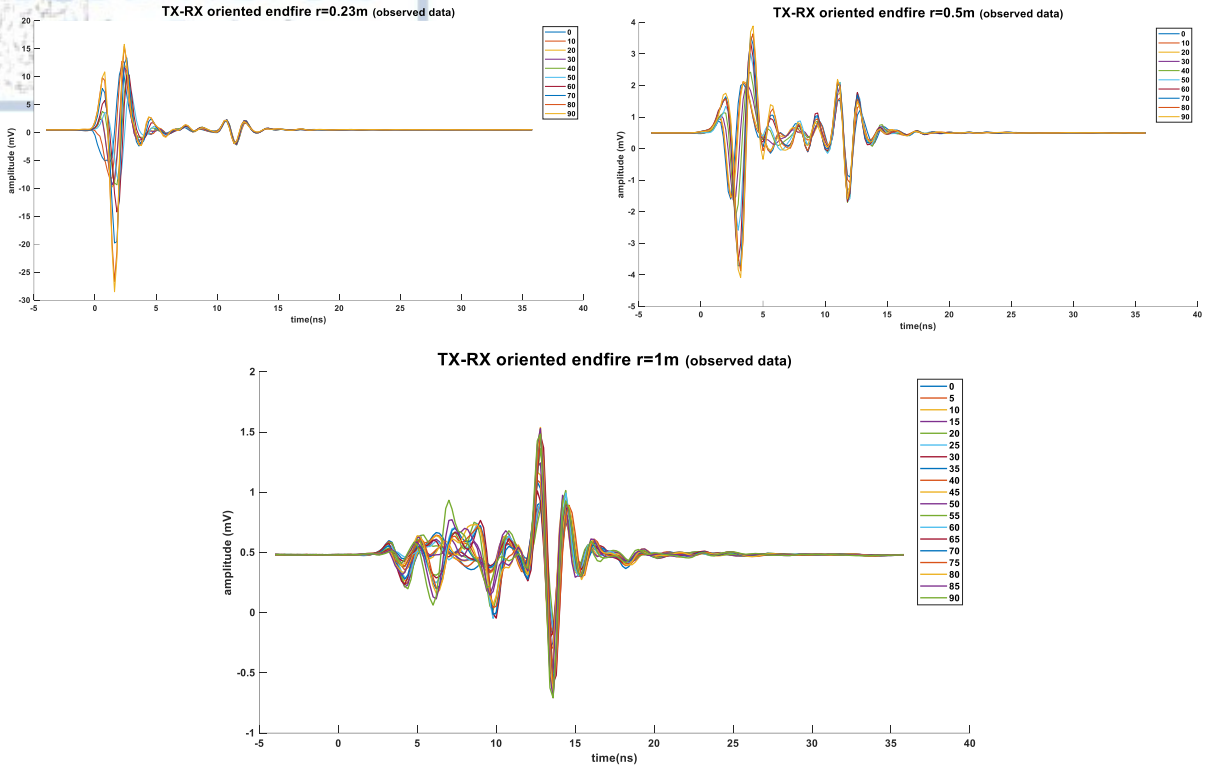

Figure 80: Field data trace plots for the traces collected from 0^0 to 90^0, for the endfire antenna orientation and for the circles of r=0.23m (top left), r=0.5m (top right) and for r=1m (bottom). In the x-axis the time in ns is indicated and the y-axis is the amplitude in mV. Each trace corresponds to a specific angular position around the Tx, as indicated by the legends.

For r=0.23m, the DAW (blue line of Figure 81-top left) is presented with a range of amplitude from 0.2 to 9mV and with a local minimum at 160^0. Three main amplitude lobes are observed at approximately 90^0, 180^0 and 270^0. The DGW amplitude ranges from 3.8 to 10mV. Its shape generally follows the shape of the DAW but the lobe at ~180^0 which seems to be the major one for the DAW, it is the minor lobe for the DGW. The shape of the DGW is characterized by major lobes at ~90^0 and 270^0. The RW for r=0.23m is quite unchangeable in terms of its amplitude (~1-1.02mV). For r=0.5m, the DAW amplitude ranges from 0.42 to 1.88mV with a local minimum at 210^0. Its shape is characterized by a major lobe at approximately 90^0 and 270^0 and there is also a minor lobe hard to discriminate at 180^0. The DGW amplitude ranges from 0.68 to 1.72mV and its trend generally follows the shape of the DAW. The DGW is formed by a major lobe located at 90^0 and 270^0 and no minor lobes are observed. The RW has a range of amplitudes of ~0.6-1mV. For r=1m, the DAW and the DGW seem to have a reversed shape in which the first has a local minimum at 270^0 and the second has a local maximum at the same position. The range in amplitude for the DAW for r=1m is 0.4 to 0.49 mV, for the DGW is 0.46 to 0.53mV and for the RW is 0.49 to 0.7mV.

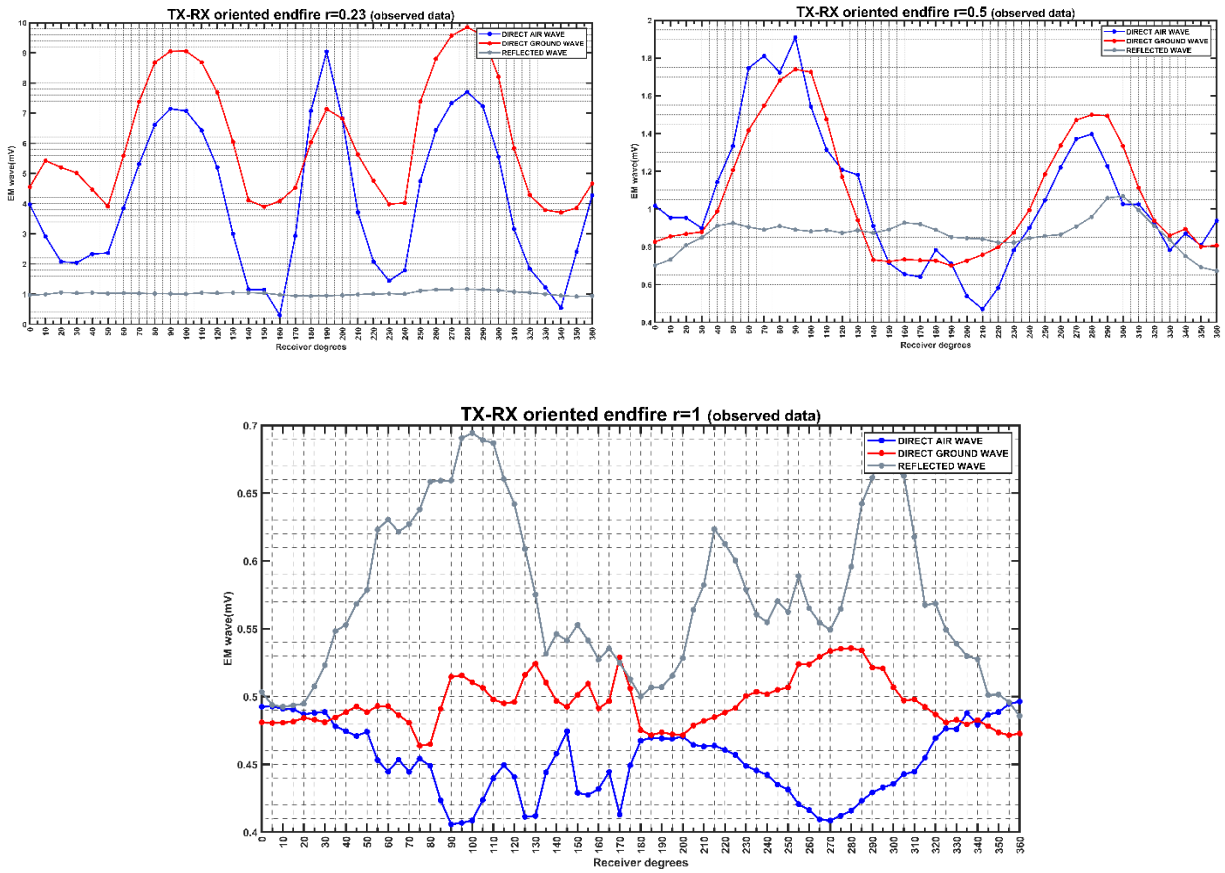

Figure 81: The field data mean absolute amplitude values in millivolts (y axis) for the DAW (blue line), the DGW (red line) and the RW (grey line) for the circles of r=0.23m (top left), r=0.5m (top right) and for r=1m (bottom) for the endfire antenna orientation over the angular position of the field collected traces (i.e., per 10^0 for r=0.23 and r=0.5m and per 5^0 for r=1m).

The normalized mean absolute amplitude values in mV for the DW as a whole entity is presented in Figure 82, for the endfire antenna orientation and for all the circles. From this plot, one can see that the DW for r=0.23m (bright green line) is characterized by a major lobe at 90^0 and 270^0 and a minor lobe at 180^0. For r=0.5m (green line), the major lobe is maintained at 90^0 and 270^0, but the minor lobe initially located at 180^0 (for r=0.23m), it is now hard to be observed, although there is a small amplitude increase at this position. For r=1m (orange line), the DW is not characterized by a specific trend.

The amplitude values presented in Figure 82 were interpolated using the Kriging formula to produce a plan view of the spatial amplitude distribution of the DW with distance from the source, as shown in Figure 83.

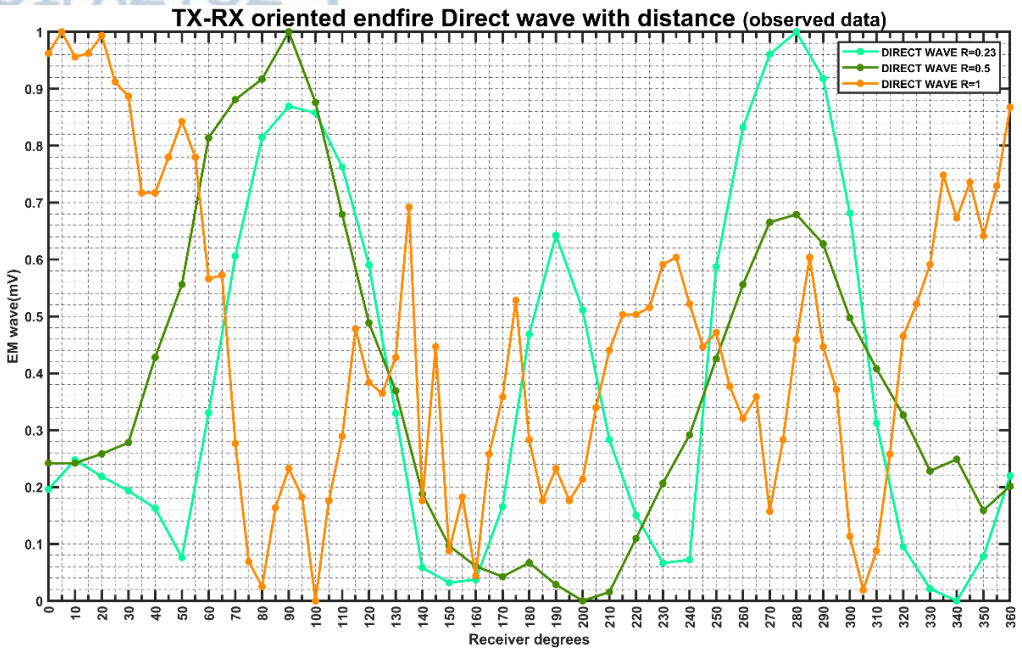

Figure 82: The normalized absolute mean values of the DW (y-axis) with respect to the angular step of the field collected traces (i.e., per 10^0 for r=0.23 and r=0.5m and per 5^0 for r=1m) as indicated in the x axis for the endfire antenna orientation and for the circles of r=0.23m (bright green line), r=0.5m (green line) and r=1m (orange line). The minor grid lines in the x axis are at every 5 degrees.

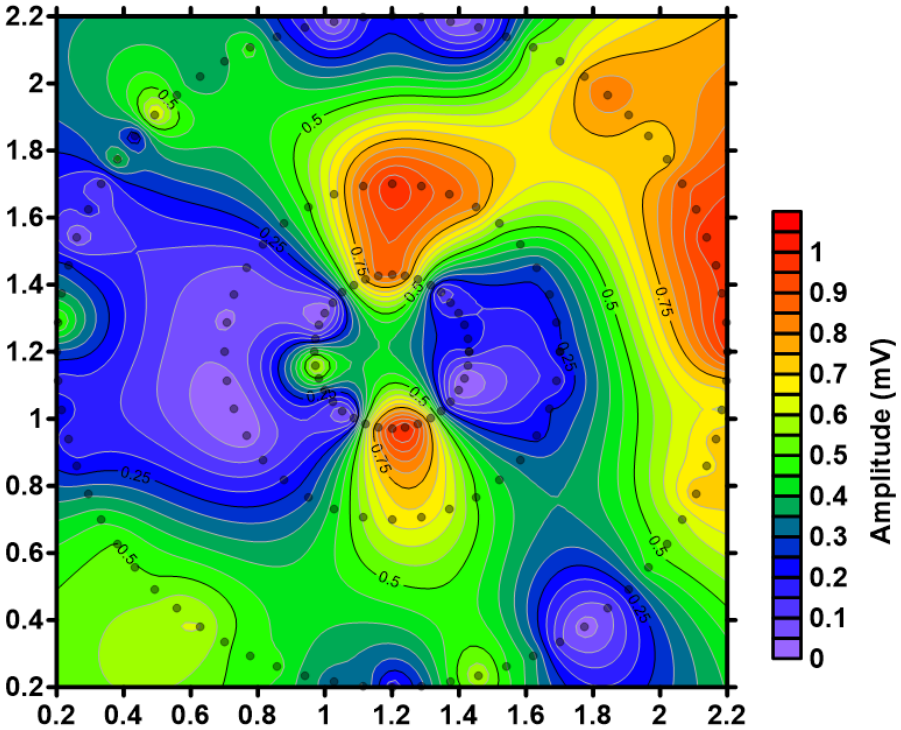

Figure 83: Field data normalized mean absolute amplitude values (mV) for the DW and for the endfire antenna orientation, interpolated using the Kriging method. The inner dotted circle is for r=0.23m, the middle dotted circle is for r=0.5m and the outer dotted circle is for r=1m. The x and the y axis are the relative coordinates of the circles in meters. The normalized mean absolute amplitude values are indicated by the rainbow color scale.

From the interpolated image of Figure 83 and for r=0.23m, the major lobe for the DW is roughly located at 90^0 and 270^0 and a minor lobe at approximately 180^0. The lowest amplitude values for r=0.23m (Figure 83-inner circle) are found from 0^0 to 50^0 for the first quadrant, between 140^0 and 170^0 for the second quadrant, from 210^0 to 240^0 for the third quadrant and between 320^0 and 360^0 for the fourth quadrant of the circle. For r=0.5m (Figure 83-middle circle), the DW has a major lobe at 90^0 and 270^0 and the minor lobe at 180^0 seen when r=0.23m is now not observed. The weak amplitude spots when r=0.5m are seen from 0^0 to 30^0, between 140^0 and 230^0 and between 330^0 and 360^0. For r=1m (Figure 83-outer circle), the DW has a minimum amplitude roughly at 90^0 and at 270^0 and also, from 160^0 to 140^0 and between 300^0 and 315^0. A minor lobe is probably seen at 175^0 and the maximum values of amplitude are at angles: 0^0-55^0, 115^0-135^0, 290^0 and 220^0-250^0.

7.Discussion

In this study the major aim was to examinate whether a Tx-Rx configuration exists where the direct wave becomes minimum while reflections from underground targets remain unchanged. For this reason, the EM signal's amplitude distribution around the Tx and Rx GPR transducers was studied in terms of the Tx-Rx separation, their forming angle and also, the antenna orientation. To do so, field measurements were collected and synthetic data were created in such a way to obtain GPR recordings in various Tx-Rx positions and Tx-Rx orientations. As the recorded GPR signals by the Rx are mainly characterized by the direct wave (it is the strongest response in a GPR record), we focused our study on this signal and its two counterparts: the direct air wave and the direct ground wave. It is known in advance from the concept of the antenna pattern, that there are some weak amplitude spots around the antennas and thus, there could be a position around the Tx-Rx pair where the direct wave has a local minimum in terms of amplitude strength. In this thesis, the angular positions where the direct wave is reaching minimum amplitude values will be attempted to be defined.

For the field measurements, a layered earth was spotted at the Agios Mammas area in Chalkidiki which hosted a horizontal reflector of approximately 0.75m depth. WARR measurements were performed to estimate the velocity of the upper layer and the arrival times of the direct air wave (DAW), direct ground wave (DGW) and the reflected wave (RW). The Tx was placed at the center of the horizontal part of the reflector and the Rx antenna was moved around the Tx, forming three concentric circles around it of radius r=0.23m, 0.5m and 1m. The antennas' centre frequency was 500MHz by Sensor & Software. Data were collected at reflection mode and were processed with EKKO_project and MATLAB to assess one trace per position with an angular step of 10^0 for r=0.23 and r=0.5m, and 5^0 for r=1m. The circular measurements were performed for both the broadside and the endfire antenna configurations.

For the synthetic data, a homogenous, lossless 3D half space was modelled with gprMax to have the same properties to the observed data. Data around three concentric circles of r=0.23, r=0.5 and r=1m were numerically calculated for both the endfire and broadside antenna orientations using an infinitesimal dipole EM source. Traces were obtained per 5 degrees for every circle and antenna orientation. Synthetic data were also produced in the same way as explained above only this time bare dipole antennas were modelled as the EM source (Tx) and the Rx. For the models including a bare dipole antennas, three semicircles of r=0.23, r=0.5 and r=1m were designed and data only for the broadside antenna configuration were modelled, with and angular step of 10^0. For all the traces calculated for a specific circle and a specific antenna orientation for both the observed and the synthetic data, the DAW, DGW and the RW events were cropped and the mean absolute, maximum absolute and RMS values of amplitude in millivolts (mV) were extracted.

In this chapter, a comparison between the observed and the synthetic data will be made and discussed. Starting with the broadside antenna orientation the results from the models where infinitesimal dipoles were used will be presented from 0^0 to 180^0 to match the data obtained from the models including the bare dipole antennas. For the observed field data, all the

quadrants of the circles will be presented separated in two parts: one at 0^0-180^0 and one at 180^0-360^0.

- ***Broadside antenna configuration***

Figure 84 shows the results for r=0.23m and for the broadside antenna orientation. The results for the synthetic data when point dipoles (Figure 84-top left) and when bare dipoles are used (Figure 84-top right) can be seen. Also, the observed data are depicted in the bottom part of the figure (0^0 to 180^0 in Figure 84-bottom left, and 180^0 to 360^0 in Figure 84-bottom right). For all these plots the DAW is depicted with a blue line, the DGW with a red line and the RW with a grey line.

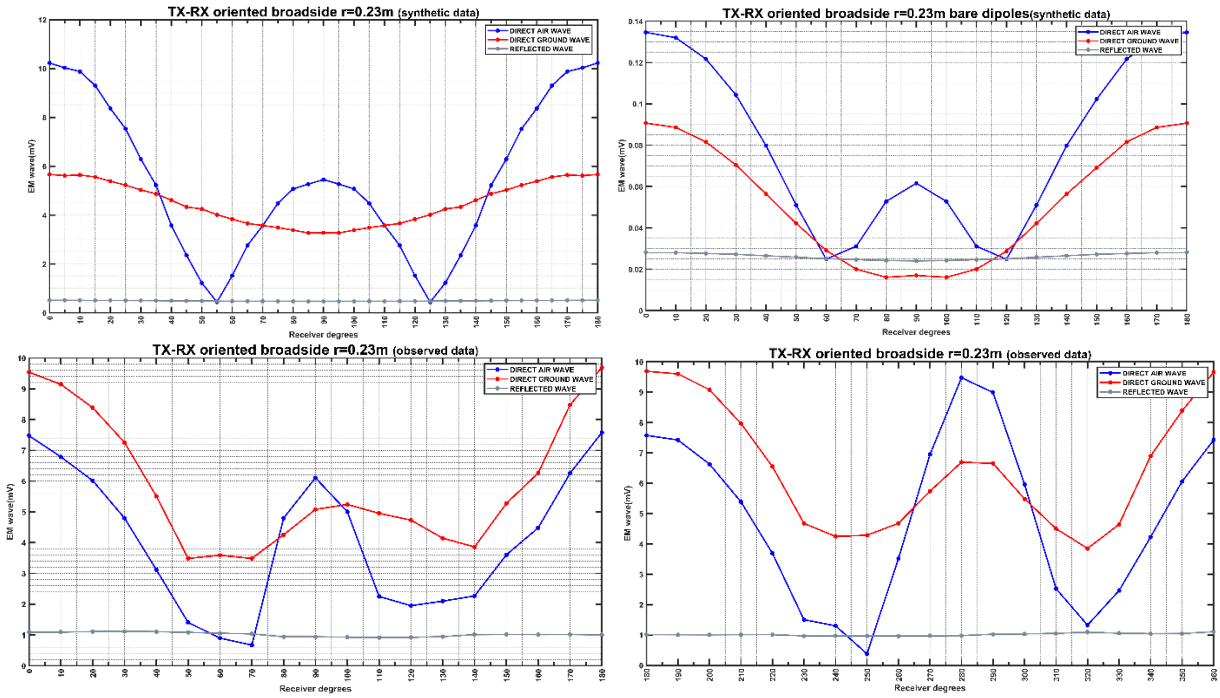

Figure 84: The mean absolute values of amplitude in mV for the DAW (blue line), the DGW (red line) and the RW (grey line) over the angular position for the broadside antenna orientation and for the circle with r=0.23m. The results are obtained from: modelled data employing infinitesimal dipoles (top left), modelled data using bare dipoles (top right) and observed data separated in two parts (i.e., from 0^0 to 180^0 (bottom left) and from 180^0 to 360^0 (bottom right).

For all the results shown in Figure 84, the DAW has a similar trend. A minor lobe is seen at 90^0 and a major lobe at 0^0 and at 180^0. The observed data are not entirely symmetrical, which makes sense as field conditions are never as clinical as the conditions employed by the numerical models. Even so, the shapes of the DAW, DGW and RW events are similar for both the 0^0-180^0 and 180^0-360^0 plots. The DGW for the point dipole (Figure 84-top left) has a shape characterized by a major lobe at 0^0 and 180^0, while the minor lobe at 90^0 of the DAW, cannot be observed. For the bare dipoles modelling case (Figure 84--top right), the DGW also has a major lobe at 0^0 and 180^0 and also, there is a small amplitude increase at 90^0 which could be considered as a minor lobe. For the observed data (Figure 84-bottom plots), the DGW roughly follows the shape trend of the DAW with a major lobe at 180^0 and minor lobes at 90^0 and 270^0. The RW for all the plots in this figure presents a quite unchangeable behavior with almost no variation in amplitude.

To summarize, for r=0.23m and for the broadside configuration, the synthetic data (point and bare dipole antennas) are close. All the three responses are presented with the same shape and behavior. The observed data are like the synthetic data considering the DAW response and the RW. The DGW in the observed data has a different behavior compared to the synthetic data and it generally follows the shape of the DAW, developing both the major and minor lobes at the same positions. The local minimum amplitude values in the DAW are found at slightly different angular positions when point dipoles are used (~55^0) than when bare dipoles are employed (~60^0). The local minimum for the DAW in the observed data is located at 70^0.

Figure 85 shows the results for r=0.5m and for the broadside antenna orientation. For both the point and bare dipole cases (Figure 85-top left and top right, respectively) the DAW and the DGW have a similar shape. The DAW has its major lobe at 180^0 and the minor lobe at 90^0 has become significantly higher in amplitude. The local minimum of the DAW when point dipoles are used has slightly shifted at 50^0 for r=0.5m from being at 55^0 when r=0.23m. The local minimum of the DAW for the bare dipoles case has remained at 60^0 for r=0.23 and r=0.5m. The DGW still has a major lobe at 180^0. For the observed data (Figure 85-bottom plots), the DAW has a shape characterized by a major lobe at 180^0, as it is the case for the synthetic data too. The local minimum has remained at 70^0 for r=0.23 and r=0.5m. A major difference between the observed and the synthetic data considering the DAW is that the minor lobe located for both cases at 90^0 is significantly lower in amplitude for the real data. The DGW is somehow following a similar trend for all data. The RW for all the plots of Figure 85 exhibits a higher range in amplitude compared to the range of this event for r=0.23m.

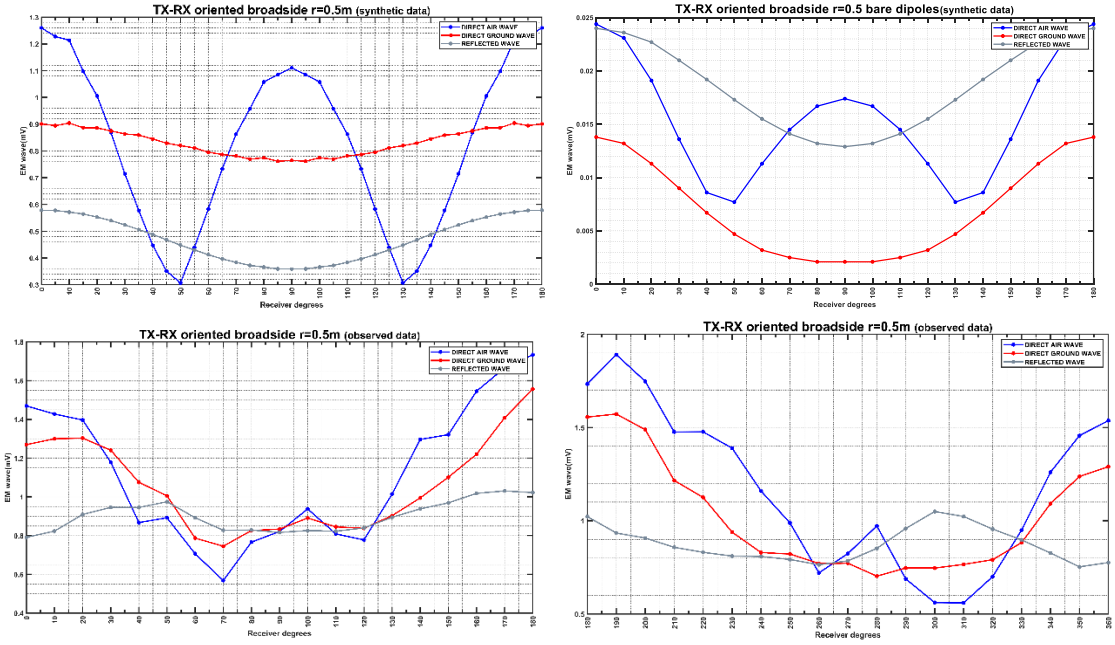

Figure 85: The mean absolute values of amplitude in mV for the DAW (blue line), the DGW (red line) and the RW (grey line) over the angular position for the broadside antenna orientation and for the circle with r=0.5m. The results are obtained from: modelled data employing infinitesimal dipoles (top left), modelled data using bare dipoles (top right) and observed data separated in two parts (i.e., from 0^0 to 180^0 (bottom left) and from 180^0 to 360^0 (bottom right).

Summarizing for r=0.5m, the DAW for all the results is presented with roughly the same shape including a major lobe at 180^0. For the synthetic data the side lobe at 90^0 is quite higher in amplitude than the side lobe at 90^0 for the observed data. The DGW for both the synthetic and field data does not seem to have any minor lobe. The RW although not as well and clearly shaped for the observed data, it generally shows a similar behavior to the synthetic data and also, it exhibits a higher range in amplitude compared to the case of r=0.23m.

Figure 86, shows the results for the case where r=1m and for the broadside antenna orientation. The DAW has the same behavior for both the synthetic and observed data. The major lobe in all cases is located at 90^0. For the synthetic data, the DAW has minor lobes at 0^0 and 180^0 and those lobes even though are not clearly observed in the field data, they can be marginally seen. The DGW also has a similar shape trend for both the synthetic and the observed data. The RW although it is not as well shaped for the real data, it has a high range in amplitude changes for all cases shown in Figure 86.

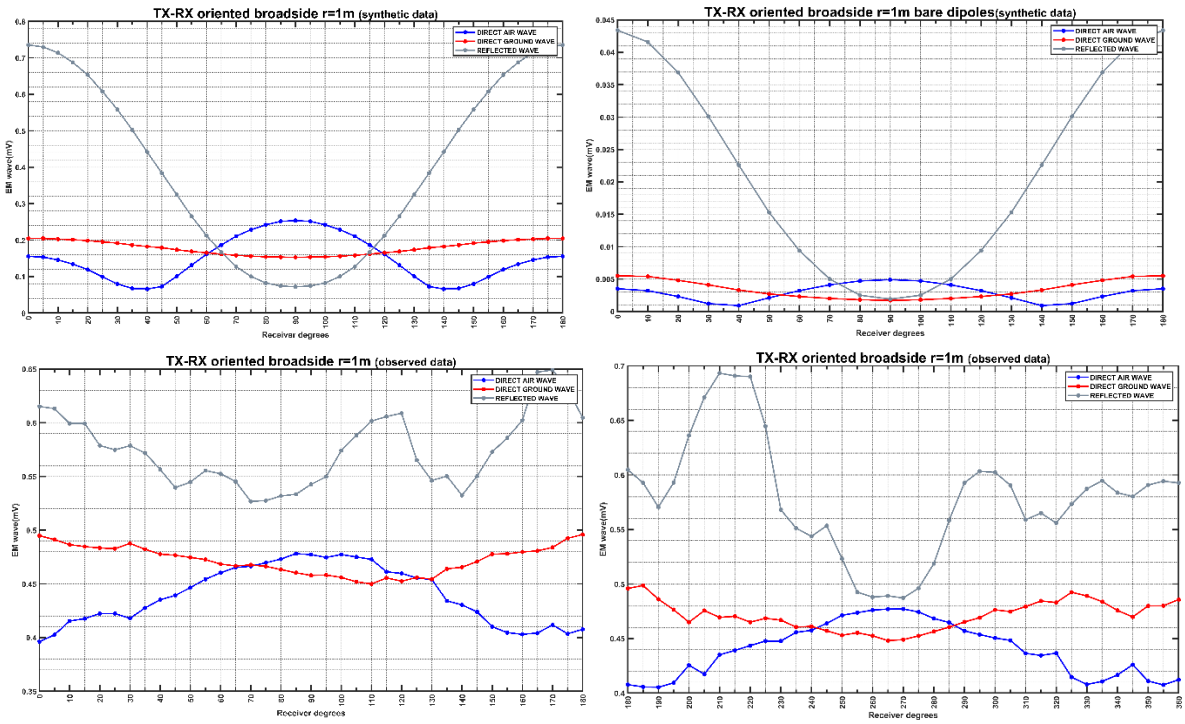

Figure 86: The mean absolute values of amplitude in mV for the DAW (blue line), the DGW (red line) and the RW (grey line) over the angular position for the broadside antenna orientation and for the circle with r=1m. The results are obtained from: modelled data employing infinitesimal dipoles (top left), modelled data using bare dipoles (top right) and observed data separated in two parts (i.e., from 0^0 to 180^0 (bottom left) and from 180^0 to 360^0 (bottom right).

- ***Endfire antenna configuration***

Figure 87 shows the results for r=0.23m and for the endfire antenna configuration for both the synthetic data when point dipoles are used (Figure 87-left) and for the observed data when a real GPR transducers are used (Figure 87-right). The DAW for both the synthetic and the observed

data is shown to have a quite similar trend. The major lobe is seen at 90^0 and 270^0 and a minor lobe at 180^0. The local amplitude minima are at similar angular positions for both the synthetic and the field data. The DGW for the synthetic data do not have minor lobes and a major lobe is located at 90^0 and 270^0. For the observed data, the DGW roughly follows the trend of the DAW. For both the synthetic and observed data the RW remains quite stable in amplitude.

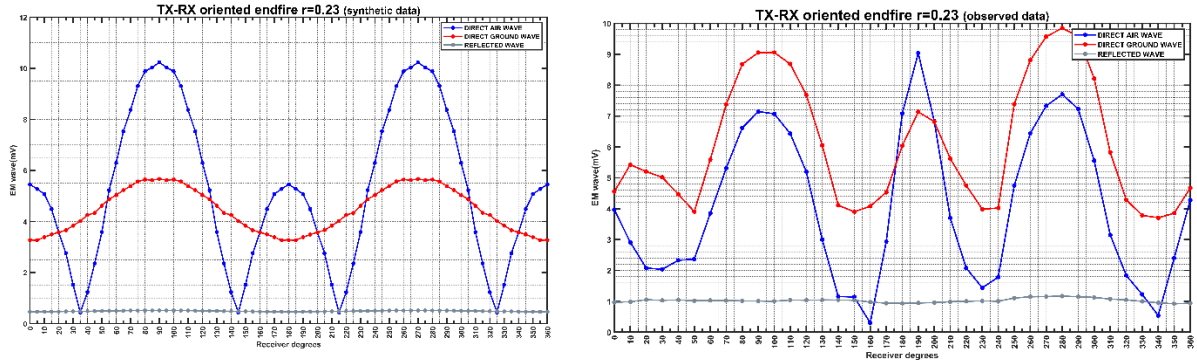

Figure 87: The mean absolute values of amplitude in mV for the DAW (blue line), the DGW (red line) and the RW (grey line) over the angular position for the endfire antenna orientation and r=0.23m. The results on the left plot are for the modelled data using infinitesimal dipoles and on the right plot for the field data.

Figure 88 shows the results for r=0.5m and for the endfire antenna orientation. The DAW for the synthetic data is shown to have a major lobe at 90^0 and 270^0, as it is the case for the field data too. A big difference is observed in the minor lobe at 180^0 of the DAW which has a high value of amplitude in the synthetic data but it is not as pronounced in the field data although there is an amplitude increase at this position too. The DGW for the synthetic data maintains a similar shape as for r=0.23m and also, for the field data is roughly following the shape of the DAW except from the minor lobe at ~180^0. The RW for both the synthetic and the observed data is shown to have a higher amplitude range compared to the RW for r=0.23m.

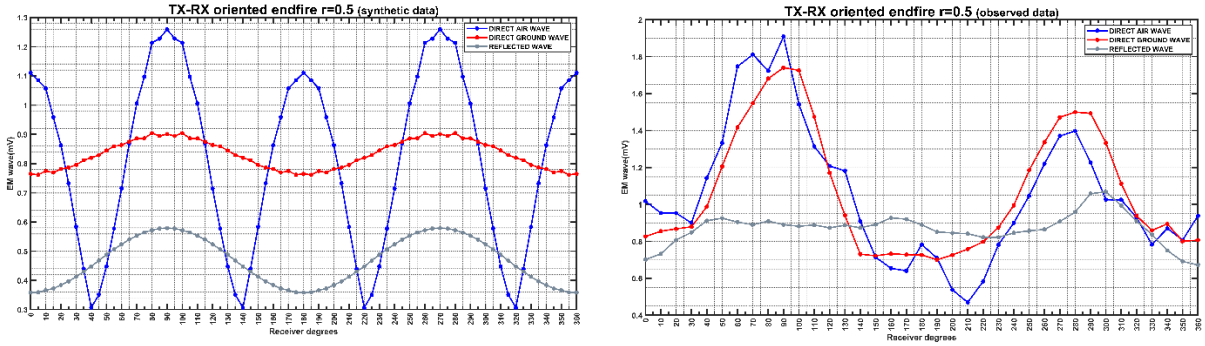

Figure 88: The mean absolute values of amplitude in mV for the DAW (blue line), the DGW (red line) and the RW (grey line) over the angular position for the endfire antenna orientation and r=0.5m. The results on the left plot are for the modelled data using infinitesimal dipoles and on the right plot for the field data.

Figure 89 shows the results for r=1m and for the endfire antenna orientation. The DAW for the synthetic data (Figure 89-left) has a major lobe at 0^0 and 180^0 and a minor lobe at 90^0 and 270^0

with a local minimum in amplitude at 50^0. The DAW for the field data is not as well shaped as in the case of the synthetic data, as it is expected. The DGW for the synthetic data maintains a similar shape as for the r=0.23 and r=0.5m cases. This event for the field data, although not as clinically shaped, it looks generally similar to the DGW of the synthetic data. The RW has a high amplitude range for both the synthetic and the field data.

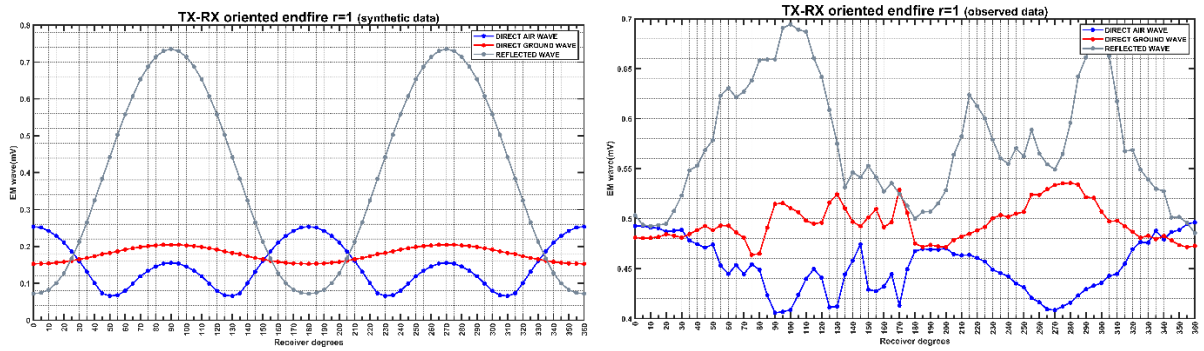

Figure 89: The mean absolute values of amplitude in mV for the DAW (blue line), the DGW (red line) and the RW (grey line) over the angular position for the endfire antenna orientation and r=1m. The results on the left plot are for the modelled data using infinitesimal dipoles and on the right plot for the field data.

8. Conclusions

To conclude, the synthetic data where point EM dipoles and also, bare dipole antennas were used to generate the GPR trace responses show a shape trend for the DAW, DGW and the RW which is perfectly symmetrical to the quadrants of the circles. For every antenna configuration/orientation, and for every radial distance, the numerical models employing infinitesimal dipoles and bare dipoles output similar results for every GPR trace that was studied in terms of its amplitude and shape. As expected, the observed data are not perfectly symmetrical, however, they exhibit a general, surprisingly good symmetry showing that the field conditions at the site we collected the GPR data were well understood and defined.

More specifically, for the data generated around a circle with radius r=0.23m and for the broadside antenna orientation, the synthetic data show that the DAW has a major lobe at 0^0 and 180^0 and a minor lobe at 90^0, with a local minimum at ~55^0-60^0. The DAW behavior for the observed data is also in agreement with the synthetic data considering its shape and also, it has a local minimum at ~70^0 (i.e., shifted ~10^0 compared to the results obtained from the bare dipoles). The RW also behaves the same way for all the cases studied as it remains almost invariant. The DGW is somehow different when comparing the synthetic and the observed data. For all data it has a major lobe at 0^0 and 180^0 however, for the observed data the DGW roughly follows the DAW shape pattern. So, for r=0.23m and the broadside antenna orientation, we can conclude that the reflected wave is almost stable in amplitude and that the DAW has its maximum of amplitude at 0^0 and 180^0 and its local minimum amplitude values are between 55^0 and 70^0. The DGW for all the cases at r=0.23m has a lower amplitude range compared to the DAW and it has a major lobe at 0^0 and 180^0.

For the data obtained around a circle with radius r=0.5m and for the broadside antenna orientation, for both the point and bare dipoles cases, the minor lobe at 90^0 has become significantly higher in amplitude and almost equal to the major lobe at 0^0 and 180^0. Local minima in the shape of the DAW for the synthetic data are located at ~50^0-60^0. The DGW exhibits a similar behavior as for r=0.23m case. For the field data, the major lobe in the shape of the DAW at 0^0 and 180^0 clearly dominates its shape and the minor lobes at 90^0 and 270^0 are present but quite lower in amplitude. So, for r=0.5m and the broadside antenna orientation we can conclude that the DAW still has a major lobe at 0^0 and 180^0 and that the minor lobes at 90^0 and 270^0 are behaving differently for the synthetic compared to the observed data. The local minima in the DAW generally range from 50^0 to 70^0 in angular position. The DGW in both the field and synthetic data is more similar in shape compared to the results for r=0.23m. The RW is shown to start to change for all the cases when compared to it being almost unchanged for the r=0.23m case.

For r=1m and for the broadside antenna orientation, the responses from both the synthetic and the field data have a similar behavior. Local minima in the DAW for the real data are not clearly observed because its trend is not as perfectly shaped. Despite this, for r=1m there seems to be the best match between synthetic and field data. The DAW has a major lobe at 90^0 and 270^0 and local minima according to the synthetic data are observed at 40^0. The DGW has a major lobe at

0^0 and 180^0 as it was the case for r=0.23 and r=0.5m maintaining its shape at every Tx-Rx distance. The RW presents a quite higher range in amplitude changes compared to the two other cases.

For the endfire antenna orientation, the DAW in respect to the Tx-Rx distance exhibits a shift at its major lobe angular position from 90^0 (r=0.23 and r=0.5m) to 180^0 (r=1m). This shift is obvious in the observed data when r=1m. The local amplitude minima in the DAW are slightly different for the synthetic and observed data but a range between 30^0 and 50^0 can be given. The DGW also behaves slightly differently for the synthetic and field data but there is a good agreement when r=1m. The RW for all cases of r=0.23m remains unchanged in amplitude and it gradually changes in amplitude around the circle when the Tx-Rx distance starts to increase.

For r=0.5, both for the broadside and for the endfire antenna orientations, the RW starts to change in amplitude and optimal local minima in the DW although they exist, they cannot clearly indicate an advantageous Tx-Rx position in which the RW is remains strong while the DW has its minimum value.

For r=1m, for both the broadside and the endfire antenna orientations the responses for the field data are not as clearly well shaped and thus, local minima in the trend of the DW are hard to define. Despite this, synthetic and field data are well related for all the compared events. An explanation for this could be that for a circle with radius of r=1m, the two antennas are well separated and signal paths are longer and not as much influenced by antenna structures.

As in actual GPR systems the Tx and Rx antennas are at near proximity to each other, the case where the Tx-Rx distance is equal to 0.23m is of bigger interest. For this case and for the broadside antenna configuration, we could say that at angular positions ranging from 50^0 to 70^0, there is an advantageous Tx-Rx position where the DAW null couples while the DGW does not. This configuration, even though it does not satisfy the ideal condition where both the DAW and DGW null couple (which would consequently lead to receiving enhanced shallow targets responses mostly free of the DW), it could be still used for other types of surveying, like for example, using the direct ground wave to extract moisture content from GPR data (e.g., Huisman et al., 2003).

An important fact that needs to be noted is that null coupling for the DW is expected on the assumption of static fields. We can assume that we are in this area (i.e., near field) when the circle radius is small. At large distances (i.e., 1.0 m circle radius or even at 0.5 m), we are no longer in the static field and the radiating fields mainly dominate. This could probably explain the fact that for the 0.5m or 1.0 m radius, null point positions deviate. This is a complicated problem that needs to be solved analytically and this is far beyond the scope of this thesis.

Bibliography

Annan, A. P. (2002). GPR—History, trends, and future developments. *Subsurface sensing technologies and applications*, *3*(4), 253-270.

Annan, A. P. (2005). GPR methods for hydrogeological studies. In *Hydrogeophysics* (pp. 185-213). Springer, Dordrecht.

Annan, A. P. (2005). Ground-penetrating radar. In *Near-surface geophysics* (pp. 357-438). Society of Exploration Geophysicists.

Annan, A. P., & Davis, J. L. (1997). Ground penetrating radar—coming of age at last. In *proceedings of Exploration* (Vol. 97, pp. 515-522).

Annan, P. (2003). Ground penetrating radar principles, procedures and applications. *Sensors & software*, *278*.

Archie, G. E. (1942). The electrical resistivity log as an aid in determining some reservoir characteristics. *Transactions of the AIME*, *146*(01), 54-62.

Baker, G. S., Jordan, T. E., & Pardy, J. (2007). An introduction to ground penetrating radar (GPR). *Special Papers-Geological Society of America*, *432*, 1.

Balanis, C. A. (1997). Fundamental parameters of antennas. *Antenna theory, analysis and design*, 28-102.

Balanis, C. A. (2012). *Advanced engineering electromagnetics*. John Wiley & Sons.

Balanis, C. A. (2015). *Antenna theory: analysis and design*. John wiley & sons.

Batayneh, A. T., Zumlot, T., Ghrefat, H., El-Waheidi, M. M., & Nazzal, Y. (2014). The use of ground penetrating radar for mapping rock stratigraphy and tectonics: implications for geotechnical engineering. *Journal of Earth Science*, *25*(5), 895-900.

Bébien, J., Dubois, R., & Gauthier, A. (1986). Example of ensialic ophiolites emplaced in a wrench zone: Innermost Hellenic ophiolite belt (Greek Macedonia). *Geology*, *14*(12), 1016-1019.

Berkhout, A. J. (1984). Seismic resolution, resolving power of acoustical echo techniques: Handbook of Geophysical Exploration, Seismic Exploration.

Brewster, M. L., & Annan, A. P. (1994). Ground-penetrating radar monitoring of a controlled DNAPL release: 200 MHz radar. *Geophysics*, *59*(8), 1211-1221.

Chen, C., & Zhang, J. (2009). A review on GPR applications in moisture content Determination and pavement condition assessment. In *Characterization, Modeling, and Performance of Geomaterials: Selected Papers From the 2009 GeoHunan International Conference* (pp. 138-143).

Cook, J. C. (1975). Radar transparencies of mine and tunnel rocks. *Geophysics*, *40*(5), 865-885.

Cook, K. L., & Van Nostrand, R. G. (1954). Interpretation of resistivity data over filled sinks. *Geophysics*, *19*(4), 761-790.

Diamanti, N., Redman, D., & Giannopoulos, A. (2010). A study of GPR pavement crack responses using field data and numerical modelling. In *Proceedings of the 13th International Conference on Ground Penetrating Radar (GPR2010), Lecce, Italy*.

Diamanti, N., & Annan, A. P. (2013). Characterizing the energy distribution around GPR antennas. *Journal of Applied Geophysics*, *99*, 83-90.

Diamanti, N., & Annan, A. P. (2019). Understanding the use of ground-penetrating radar for assessing clandestine tunnel detection. *The Leading Edge*, *38*(6), 453-459.

Diamanti, N., & Redman, D. (2012). Field observations and numerical models of GPR response from vertical pavement cracks. *Journal of Applied Geophysics*, *81*, 106-116.

Diamanti, N., Annan, P., & Redman, D. (2012, June). Quantifying GPR responses. In *2012 14th International Conference on Ground Penetrating Radar (GPR)* (pp. 237-242). IEEE.

Du, E., Zhao, L., Zou, D., Li, R., Wang, Z., Wu, X., ... & Sun, Z. (2020). Soil Moisture Calibration Equations for Active Layer GPR Detection—a Case Study Specially for the Qinghai–Tibet Plateau Permafrost Regions. *Remote Sensing*, *12*(4), 605.

Galagedara, L. W., Parkin, G. W., & Redman, J. D. (2003). An analysis of the ground-penetrating radar direct ground wave method for soil water content measurement. *Hydrological Processes*, *17*(18), 3615-3628.

Giannopoulos, A. (2005). Modelling ground penetrating radar by GprMax. *Construction and building materials*, *19*(10), 755-762.

Giannopoulos, A., & Diamanti, N. (2005, September). Modelling the effects of subsurface heterogeneity on ground penetrating radar signals. In *Near Surface 2005-11th European Meeting of Environmental and Engineering Geophysics* (pp. cp-13). European Association of Geoscientists & Engineers.

Giannopoulos, A., & Diamanti, N. (2008). Numerical modelling of ground-penetrating radar response from rough subsurface interfaces. *Near Surface Geophysics*, *6*(6), 357-369.

Goldstein, D. H. (2017). *Polarized light*. CRC press.

Grasmueck, M. (1996). 3-D ground-penetrating radar applied to fracture imaging in gneiss. *Geophysics*, *61*(4), 1050-1064.

Griffiths, D. J. (2005). Introduction to electrodynamics.

Grote, K., Anger, C., Kelly, B., Hubbard, S., & Rubin, Y. (2010). Characterization of soil water content variability and soil texture using GPR groundwave techniques. *Journal of Environmental & Engineering Geophysics*, *15*(3), 93-110.

Hatch, M. A., Heinson, G., Munday, T., Thiel, S., Lawrie, K., Clarke, J. D., & Mill, P. (2013). The importance of including conductivity and dielectric permittivity information when processing low-frequency GPR and high-frequency EMI data sets. *Journal of Applied Geophysics*, *96*, 77-86.

Holser, W. T., Brown, R. J. S., Roberts, F. A., Fredriksson, O. A., & Unterberger, R. R. (1972). Radar logging of a salt dome. *Geophysics*, *37*(5), 889-906.

HP, D. P. K. (1992). 85070A. Palo Alto. *CA: Research and Development Unit, Test and Measurements Laboratories, Hewlett Packard Corporation*.

Huisman, J.A., Hubbard, S.S., Redman, J.D., & Annan, A.P. (2003). Measuring soil water content with ground penetrating radar. *Vadose Zone Journal*, 2, 476–491.

Hülsenbeck & Co (1926) Verfahren zur elektrischen Bodenforschung German patent 48943

Hülsmeyer, C. (1904). Verfahren, um entfernte metallische Gegenstände mittels elektrischer Wellen einem Beobachter zu melden. *Eurpean Patent Office, Patentschrift DE165546*, *30*.

Kadioğlu, S., & Daniels, J. J. (2008). 3D visualization of integrated ground penetrating radar data and EM-61 data to determine buried objects and their characteristics. *Journal of Geophysics and Engineering*, *5*(4), 448-456.

Kallweit, R. S., & Wood, L. C. (1982). The limits of resolution of zero-phase wavelets. *Geophysics*, *47*(7), 1035-1046.

Kim, J. H. (2010). Dc2Dpro-2D Inversion of ERT data. *User's Manual. KIGAM, Korea*.

Klenk, P. T. P. (2012). *Developing ground-penetrating radar for quantitative soil hydrology* (Doctoral dissertation, Universitätsbibliothek Heidelberg).

Knapp, R. W. (1991). Fresnel zones in the light of broadband data. *Geophysics*, *56*(3), 354-359.

Knödel, K., Lange, G., & Voigt, H. J. (2007). *Environmental geology: Handbook of field methods and case studies*. Springer Science & Business Media.

Kockel, F., Mollat, H., & Walther, H. W. (1977). *Erläuterungen zur Geologischen Karte der Chalkidhiki und angrenzender Gebiete 1: 100 000 (Nord-Griechenland)* (p. 119). Hannover: Bundesanstalt für Geowissenschaften und Rohstoffe.

Kostaki, G., Kilias, A., Gawlick, H. J., & Schlagintweit, F. (2013). ? Kimmeridgian-Tithonian shallow-water platform clasts from mass flows on top of the Vardar/Axios ophiolites. *Bulletin of the Geological Society of Greece*, *47*(1), 184-193.

Kraus J.D. (1998). Antennas. McGraw-Hill International Editions.

Kunz, K. S., & Luebbers, R. J. (1993). *The finite difference time domain method for electromagnetics*. CRC press.

Lampe, B., & Holliger, K. (2003). Effects of fractal fluctuations in topographic relief, permittivity and conductivity on ground-penetrating radar antenna radiation. *Geophysics*, *68*(6), 1934-1944.

Loke, M. H., Chambers, J. E., Rucker, D. F., Kuras, O., & Wilkinson, P. B. (2013). Recent developments in the direct-current geoelectrical imaging method. *Journal of applied geophysics*, *95*, 135-156.

Löwy, H., & Leimbach, G. (1910). *Eine elektrodynamische Methode zur Erforschung des Erdinnern*. na.

Marcak, H., Tomecka-Suchoń, S., Czarny, R., Pysz, P., Akinsunmade, A., & Kril, T. (2018). GPR ground-wave parameters changes due to variation of soil moisture. In *E3S web of conferences* (Vol. 66, p. 01003). EDP Sciences.

Maxwell, J. C. (1873). *A treatise on electricity and magnetism* (Vol. 1). Oxford: Clarendon Press.

Meinhold, G., Kostopoulos, D., Reischmann, T., Frei, D., & BouDagher-Fadel, M. K. (2009). Geochemistry, provenance and stratigraphic age of metasedimentary rocks from the eastern Vardar suture zone, northern Greece. *Palaeogeography, Palaeoclimatology, Palaeoecology*, *277*(3-4), 199-225.

Mercier, J. (1966). Paleogeographie, orogenese, metamorphisme et magmatisme des zones internes des Hellenides en Macedoine (Grece); vue d'ensemble. *Bulletin de la Societe géologique de France*, *7*(7), 1020-1049.

Meyer, K., Erdogmus, E., Morcous, G., & Naughtin, M. (2008). Use of Ground Penetrating Radar for Accurate Concrete Thickness Measurements. In *AEI 2008: Building Integration Solutions* (pp. 1-10).

Millard, S. G., Shaari, A., & Bungey, J. H. (2002). Field pattern characteristics of GPR antennas. *NDT & E International*, *35*(7), 473-482.

Neal, A. (2004). Ground-penetrating radar and its use in sedimentology: principles, problems and progress. *Earth-science reviews*, *66*(3-4), 261-330.

Nivorlis, A. (2020). Multimethod characterization of a chlorinated solvents contaminated site and geoelectrical monitoring of in-situ bioremediation.

Nuzzo, L., Leucci, G., Negri, S., Carrozzo, M. T., & Quarta, T. (2002). Application of 3D visualization techniques in the analysis of GPR data for archaeology. *Annals of Geophysics*.

Olhoeft, G. R. (1998, May). Electrical, magnetic and geometric properties that determine ground penetrating radar performance. In *Proceedings of GPR* (Vol. 98, pp. 177-182).

Powers, M. H. (1997). Modeling frequency-dependent GPR. *The leading edge*, *16*(11), 1657-1662.

Radzevicius, S. J., & Daniels, J. J. (2000). Ground penetrating radar polarization and scattering from cylinders. *Journal of Applied Geophysics*, *45*(2), 111-125.

Reppert, P. M., Morgan, F. D., & Toksöz, M. N. (2000). Dielectric constant determination using ground-penetrating radar reflection coefficients. *Journal of Applied Geophysics*, *43*(2-4), 189-197.

Reynolds, J. M. (2011). *An introduction to applied and environmental geophysics*. John Wiley & Sons.

Rubin, Y., & Hubbard, S. S. (Eds.). (2006). *Hydrogeophysics* (Vol. 50). Springer Science & Business Media.

Francké, J. C., & Yelf, R. (2003, May). Applications of GPR for surface mining. In *Proceedings of the 2nd International Workshop onAdvanced Ground Penetrating Radar, 2003.* (pp. 115-119). IEEE.

Saad, R., Nawawi, M. N. M., & Mohamad, E. T. (2012). Groundwater detection in alluvium using 2-D electrical resistivity tomography (ERT). *Electronic Journal of Geotechnical Engineering*, *17*, 369-376.

Saarenketo, T. (1998). Electrical properties of water in clay and silty soils. *Journal of applied geophysics*, *40*(1-3), 73-88.

Sensors & Software Inc. (2005). pulseEKKO PRODUCT MANUAL.

Sensors & Software Inc. (2015). EKKO_Project with Processing, Bridge Deck Condition & Pavement Structure Modules, User's Guide.

Skolnik, M. I. (1980). Introduction to radar systems. *New York*.

Stern, W. (1929). Versuch einer elektrodynamischen Dickenmessung von Gletschereis. *Gerlands Beitrage zur Geophysik*, *27*, 292-333.

Stratton, J. A., & Chu, L. J. (1941). Steady-State Solutions of Electromagnetic Field Problems. I. Forced Oscillations of a Cylindrical Conductor. *Journal of Applied Physics*, *12*(3), 230-235.

Taflove, A. (1995). The Finite-Difference Time-Domain Method.

Thierbach, R. (1974). Electromagnetic reflections in salt deposits. *Journal of Geophysics*, *40*(1), 633-637.

Tsourlos, P. (1995). *Modelling, interpretation and inversion of multielectrode resistivity survey data* (Doctoral dissertation, University of York).

Tzanis, A. (2015). The Curvelet Transform in the analysis of 2-D GPR data: Signal enhancement and extraction of orientation-and-scale-dependent information. *Journal of Applied Geophysics*, *115*, 145-170.

Ulaby, F. T., Michielssen, E., & Ravaioli, U. (2015). *Fundamentals of applied electromagnetics*. Boston: Pearson.

Umenei, A. E. (2011). Understanding low frequency non-radiative power transfer. *Bearing a date of Jun*, *7*.

Unterberger, R. R. (1978). Radar propagation in rock salt. *Geophysical prospecting*, *26*(2), 312-328.

Van der Kruk, J., Diamanti, N., Giannopoulos, A., & Vereecken, H. (2012). Inversion of dispersive GPR pulse propagation in waveguides with heterogeneities and rough and dipping interfaces. *Journal of applied Geophysics*, *81*, 88-96.

Waite, A. H., & Schmidt, S. J. (1962). Gross errors in height indication from pulsed radar altimeters operating over thick ice or snow. *Proceedings of the IRE*, *50*(6), 1515-1520.
Ward, S. H., Hohmann, G. W., & Nabighian, M. (1991). Electromagnetic theory for geophysical exploration. *Society of Exploration Geophysics*, 121-223.

Warren, C., & Giannopoulos, A. (2011). Creating finite-difference time-domain models of commercial ground-penetrating radar antennas using Taguchi's optimization method. *Geophysics*, *76*(2), G37-G47.

Warren, C., Giannopoulos, A., & Giannakis, I. (2016). gprMax: Open source software to simulate electromagnetic wave propagation for Ground Penetrating Radar, Computer Physics Communications, 209, 163-170, 10.1016/j.cpc.2016.08.020.

Warren, C., & Giannopoulos, A. (2017). Characterisation of a ground penetrating radar antenna in lossless homogeneous and lossy heterogeneous environments. *Signal processing*, *132*, 221-226.

Wielopolski, L., Hendrey, G., Daniels, J. J., & McGuigan, M. (2000, April). Imaging tree root systems in situ. In *Eighth International Conference on Ground Penetrating Radar* (Vol. 4084, pp. 642-646). International Society for Optics and Photonics.

Yee, K. (1966). Numerical solution of initial boundary value problems involving Maxwell's equations in isotropic media. *IEEE Transactions on antennas and propagation*, *14*(3), 302-307.

Zohdy, A. A., Eaton, G. P., & Mabey, D. R. (1974). Application of surface geophysics to ground-water investigations.

Appendix A

In this appendix photos from the field measurements and the hardware supplement will be given.

Figure 90: The SmartCart GPR system from Sensors & Software (top left corner and bottom) and the SmartCart GPR system configured for operation with 500MHz transducers for the GPR grid data acquisition in the area of interest (top right corner).

Figure 91: Data acquisition for the WARR measurements with the pulseEKKO 500 SmartTow GPR system. Example for the broadside antenna orientation (top left corner) with antenna spacing equal to 0.275m (top right corner).

Figure 92: Data acquisition in the area of interest for the endfire antenna orientation and for the circles of r=0.23m (top), r=0.5m (middle), r=1m (bottom).

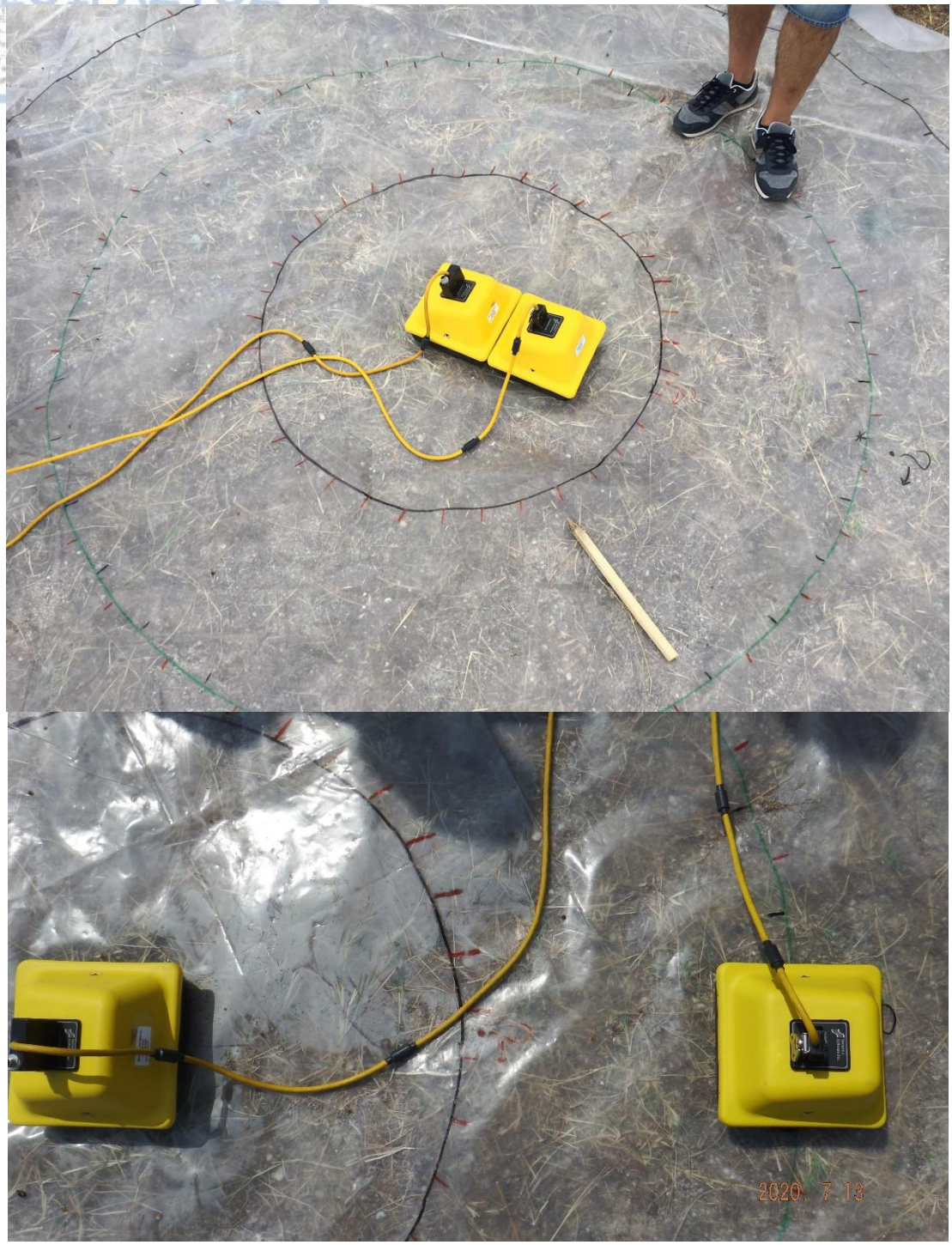

Figure 93: Data acquisition in the area of interest for the broadside antenna orientation and for the circles of r=0.23m (top), and r=1m (bottom).

Figure 94: Data acquisition for the ERT measurements in the area of interest. The electrodes are at a dipole-dipole arrangement and they are connected to the SyscalPro of Iris Instruments.

Appendix B

In this appendix photos from WARR measurements at various directions and using various antenna orientations will be given. All the measurements were performed using 500MHz antennas with antenna spacing equal to 0.275m and with the pulseEKKO 500 SmartTow GPR system of Sensors & Software.

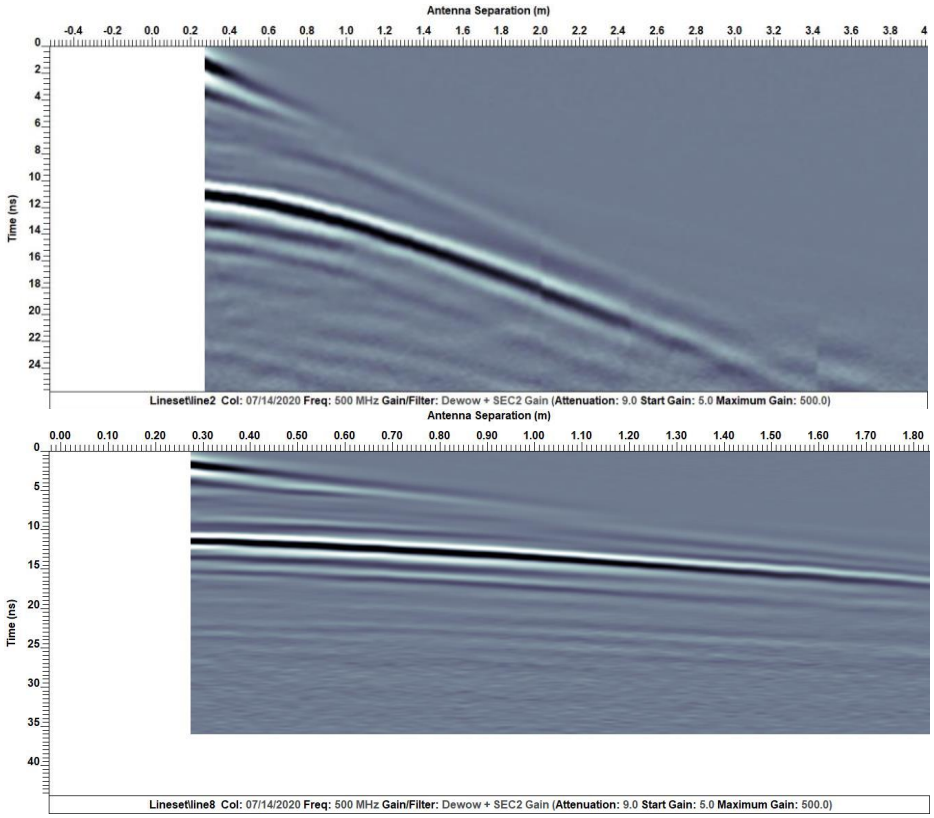

Figure 95: WARR measurements with the antennas-oriented broadside (top) at a SW-NE direction (middle) and WS-EN direction (bottom). In the x-axis is the antenna spacing in meters (m) and in the y-axis is the time in nanosecond (ns).

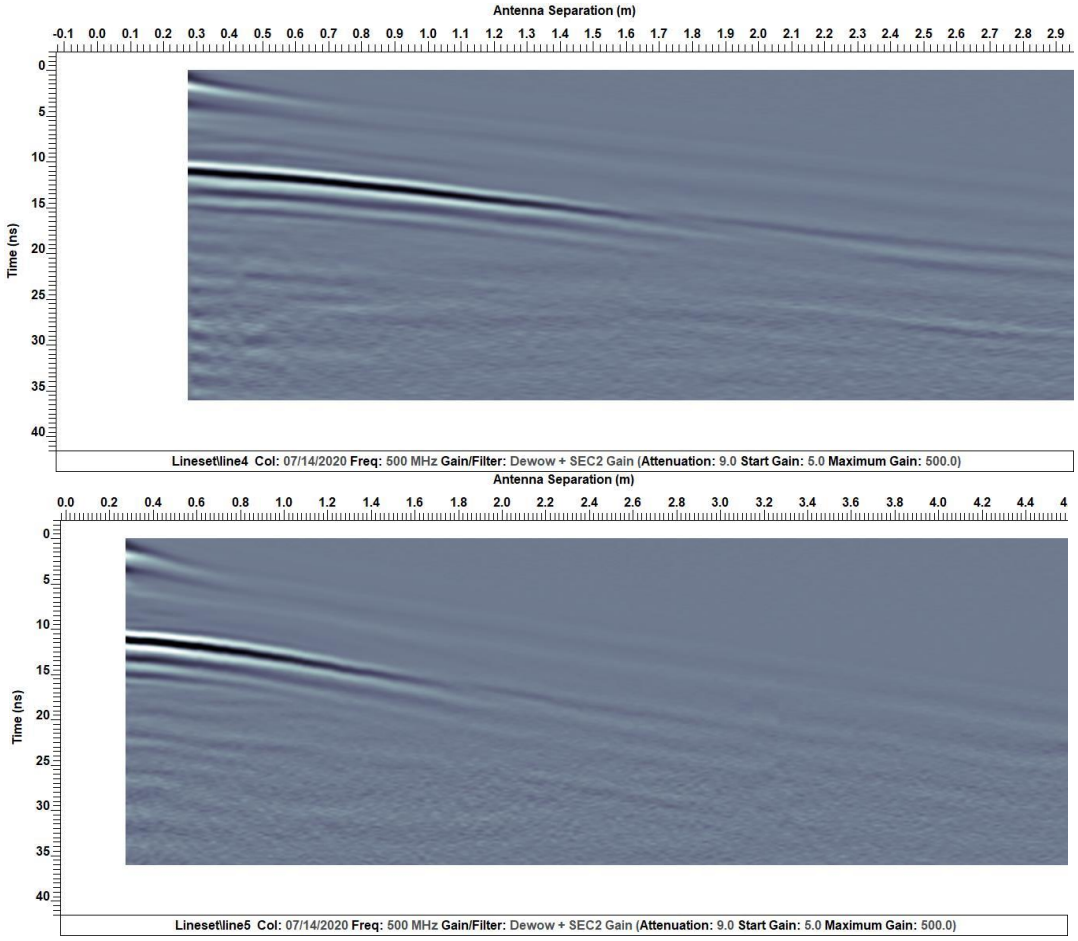

Figure 96: WARR measurements with the antennas-oriented endfire (top) at a SW-NE direction (middle) and WS-EN direction (bottom). In the x-axis is the antenna spacing in meters (m) and in the y-axis is the time in nanosecond (ns).

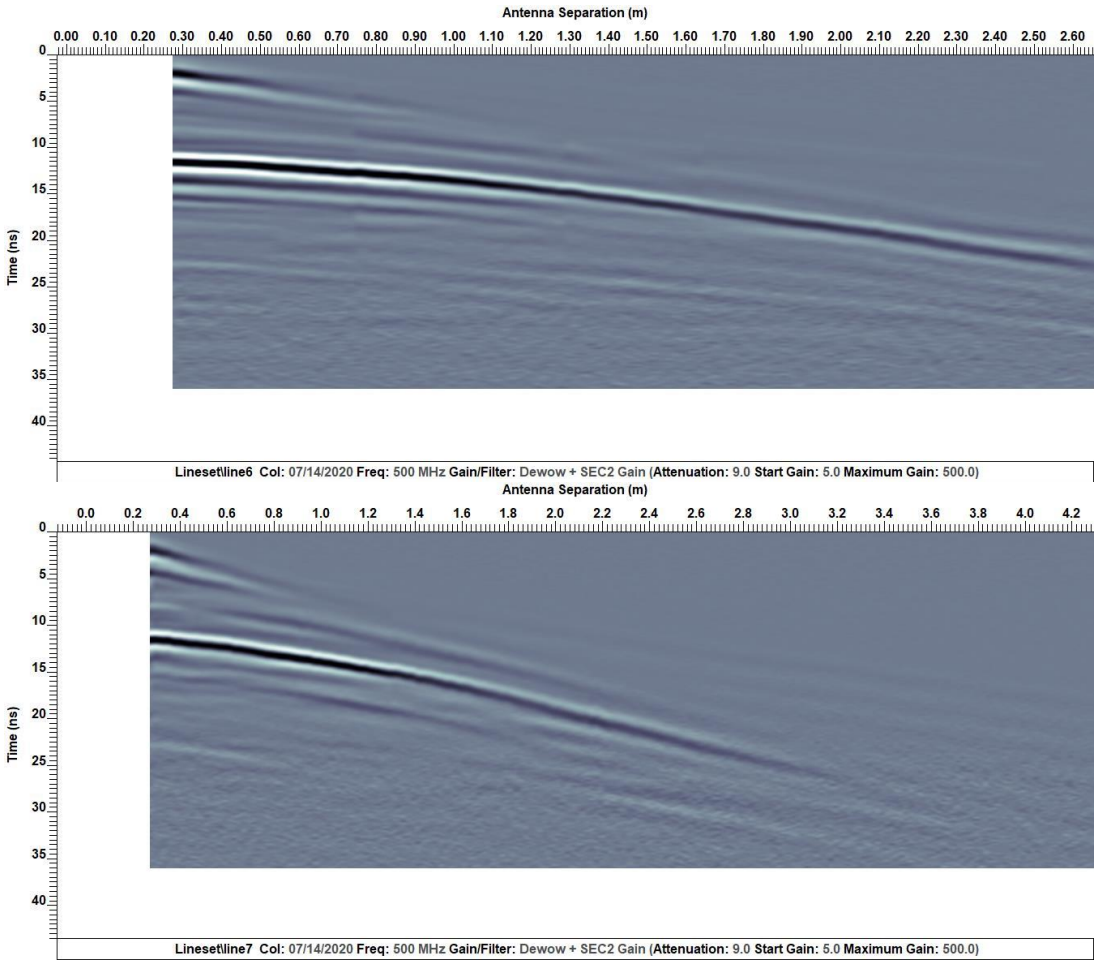

Figure 97: WARR measurements with the antennas-oriented cross at 45 degrees (top) at a NW-SE direction (middle) and NW-NE direction (bottom). In the x-axis is the antenna spacing in meters (m) and in the y-axis is the time in nanosecond (ns).

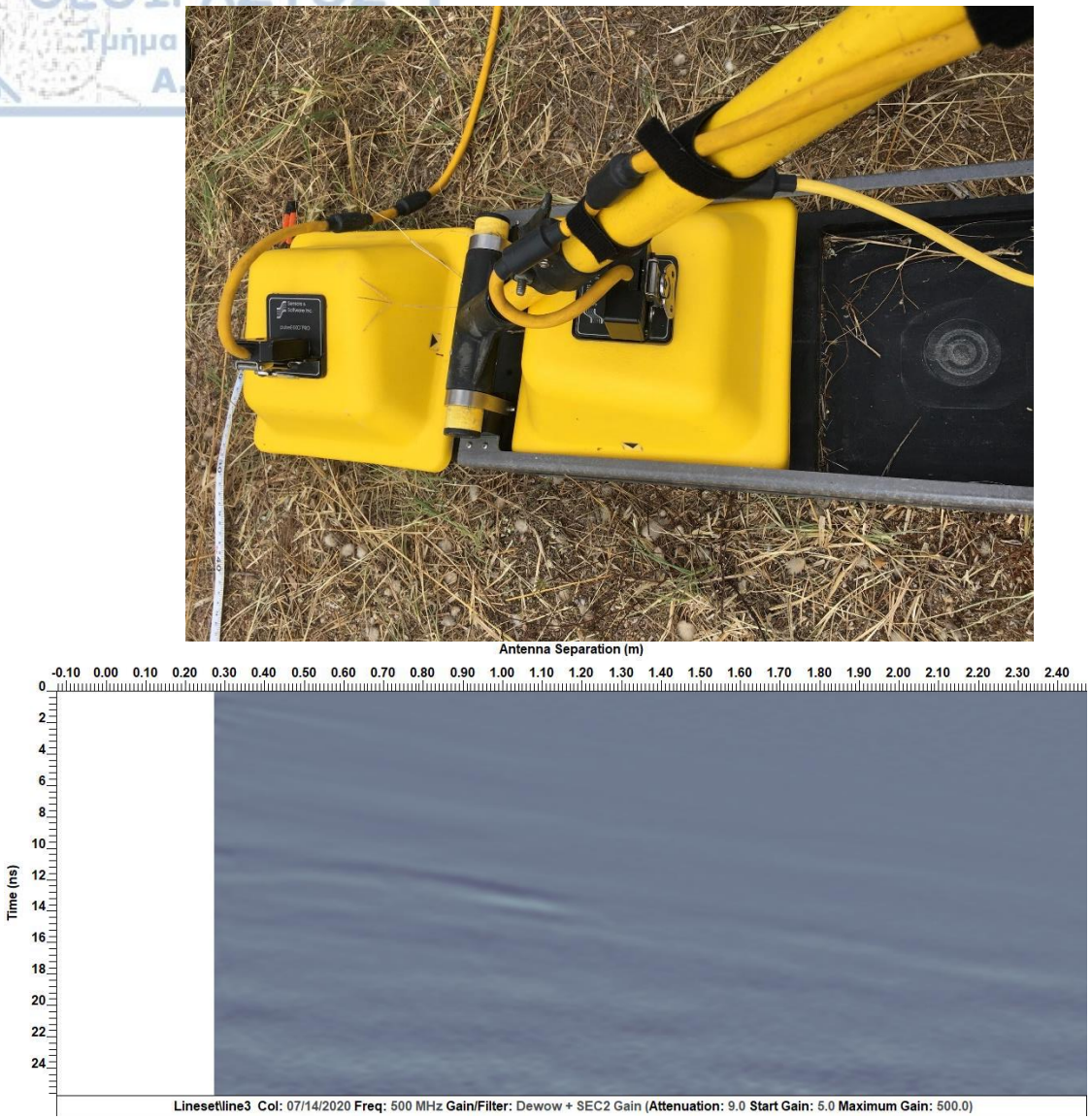

Figure 98: WARR measurements with the antennas-oriented cross at 90 degrees (top) at a SW-NE direction (bottom). In the x-axis is the antenna spacing in meters (m) and in the y-axis is the time in nanosecond (ns).

Appendix C

In this appendix, the plots from the synthetic and the observed data resulting from the traces analysis (from 0 to 360 degrees) for the direct and the reflected wave, using the values of the absolute mean, absolute maximum, and RMS of the amplitude in millivolts will be presented.

Synthetic data (point dipole)

- Broadside antenna orientation (synthetic data), circle of r=0.23m plots for the direct (as a whole entity -brown solid line) and reflected wave (grey solid line) versus the angle of the collected traces.

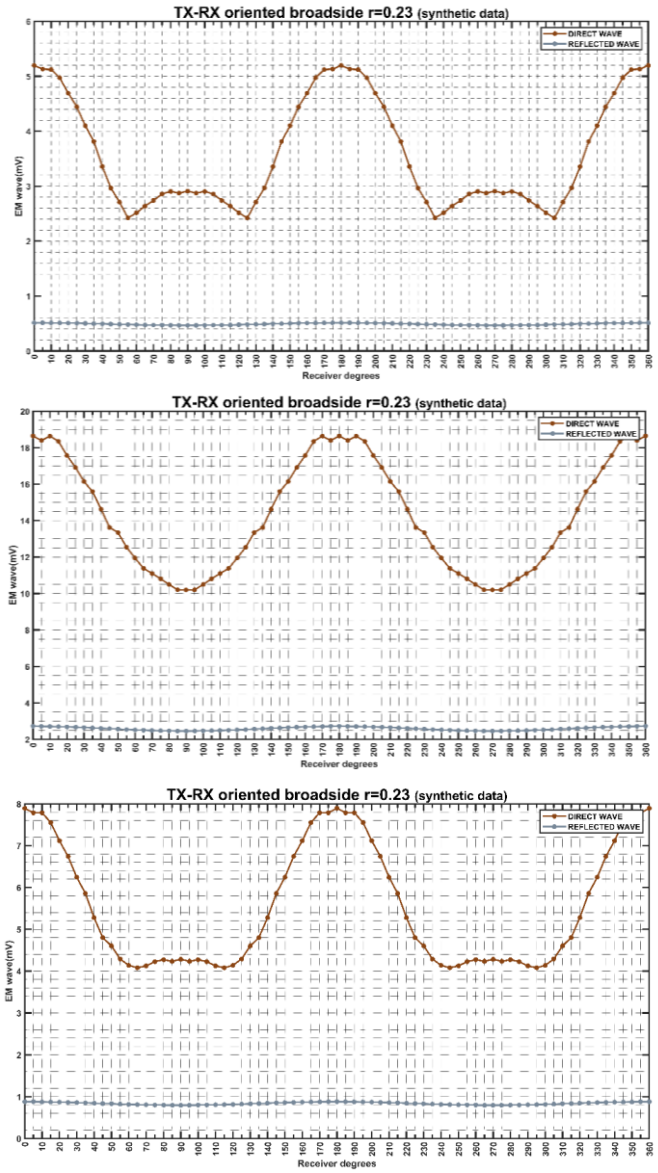

Figure 99: The mean of the absolute (top), the maximum of the absolute (middle), and the RMS (bottom) values of amplitude in millivolts (y axis) of the direct wave (brown solid line) and the reflected wave (grey solid line) for the circle of r=0.23m and for the broadside antenna orientation compared to the spatial step of the collected traces (i.e., per 5 degrees) as indicated in the x axis. The minor grid lines in the x axis are at every 5 degrees. The traces have been collected with point dipole antennas.

- Broadside antenna orientation (synthetic data), circle of r=0.23m plots for the direct (as two separated entities: the direct air wave -blue solid line- and the direct ground wave -red solid line-) and reflected wave (grey solid line) versus the angle of the collected traces. The results for the maximum absolute and RMS values of amplitude (mV) are given. The absolute mean values of amplitude have been presented in the main context.

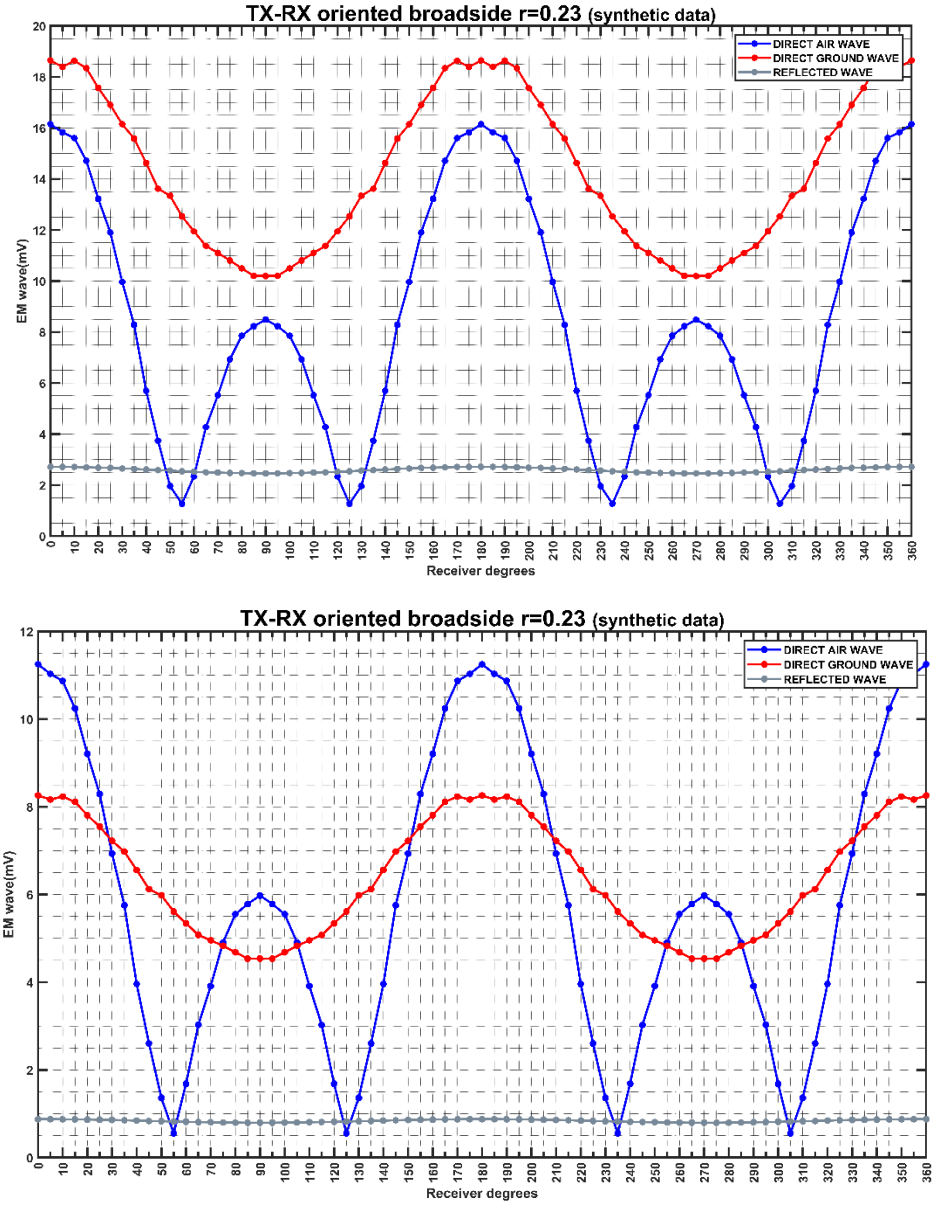

Figure 100: The maximum of the absolute (top), and the RMS (bottom) values of amplitude in millivolts (y axis) of the direct air wave (blue solid line) the direct ground wave (red solid line) and the reflected wave (grey solid line) for the circle of r=0.23m and for the broadside antenna orientation compared to the spatial step of the collected traces (i.e., per 5 degrees) as indicated in the x axis. The minor grid lines in the x axis are at every 5 degrees. The traces have been collected with point dipole antennas.

- Broadside antenna orientation (synthetic data), circle of r=0.5m plots for the direct (as a whole entity-brown solid line) and reflected wave (grey solid line) versus the angle of the collected traces.

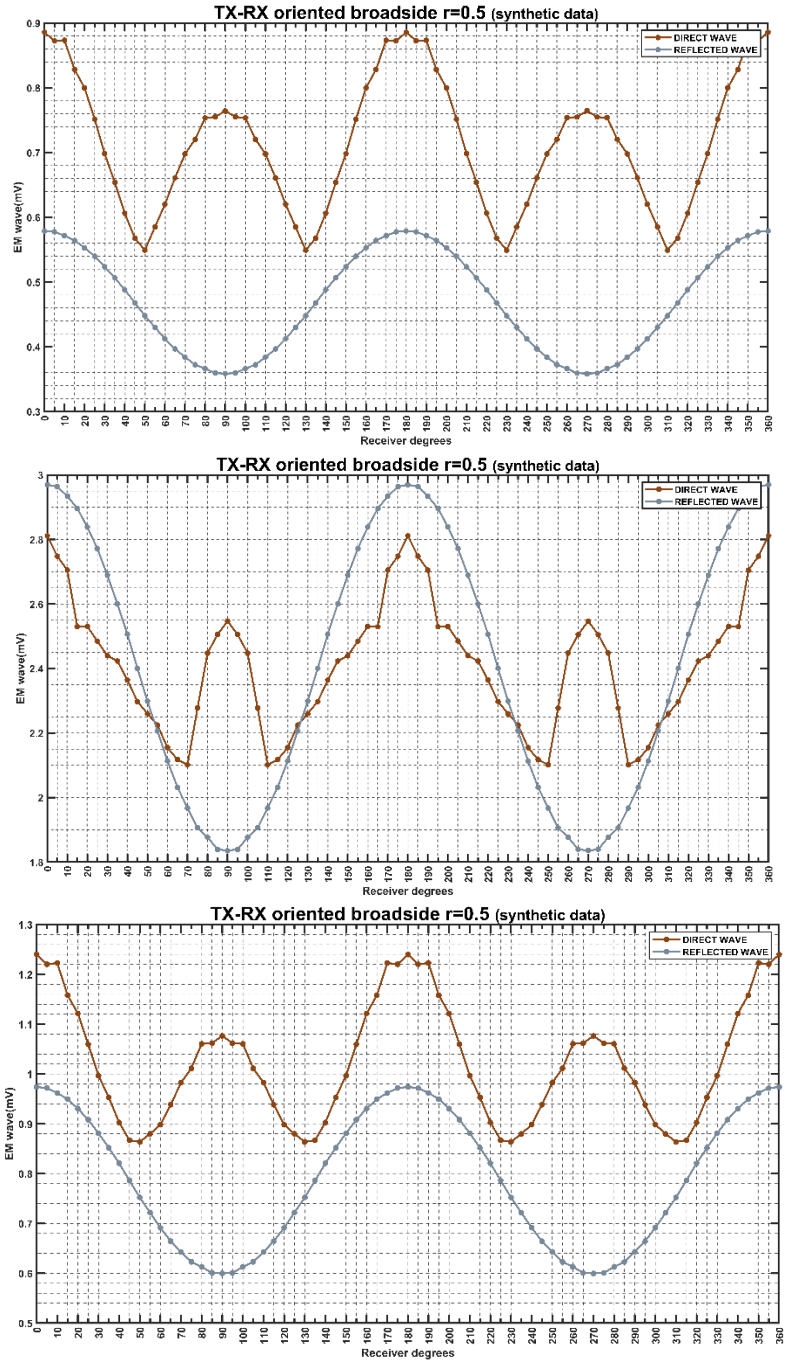

Figure 101: The mean of the absolute (top), the maximum of the absolute (middle), and the RMS (bottom) values of amplitude in millivolts (y axis) of the direct wave (brown solid line) and the reflected wave (grey solid line) for the circle of r=0.5m and for the broadside antenna orientation compared to the spatial step of the collected traces (i.e., per 5 degrees) as indicated in the x axis. The minor grid lines in the x axis are at every 5 degrees. The traces have been collected with point dipole antennas.

- Broadside antenna orientation (synthetic data), circle of r=0.5m plots for the direct (as two separated entities: the direct air wave -blue solid line- and the direct ground wave -red solid line-) and reflected wave (grey solid line) versus the angle of the collected traces. The results for the maximum absolute and RMS values of amplitude (mV) are given. The absolute mean values of amplitude have been presented in the main context.

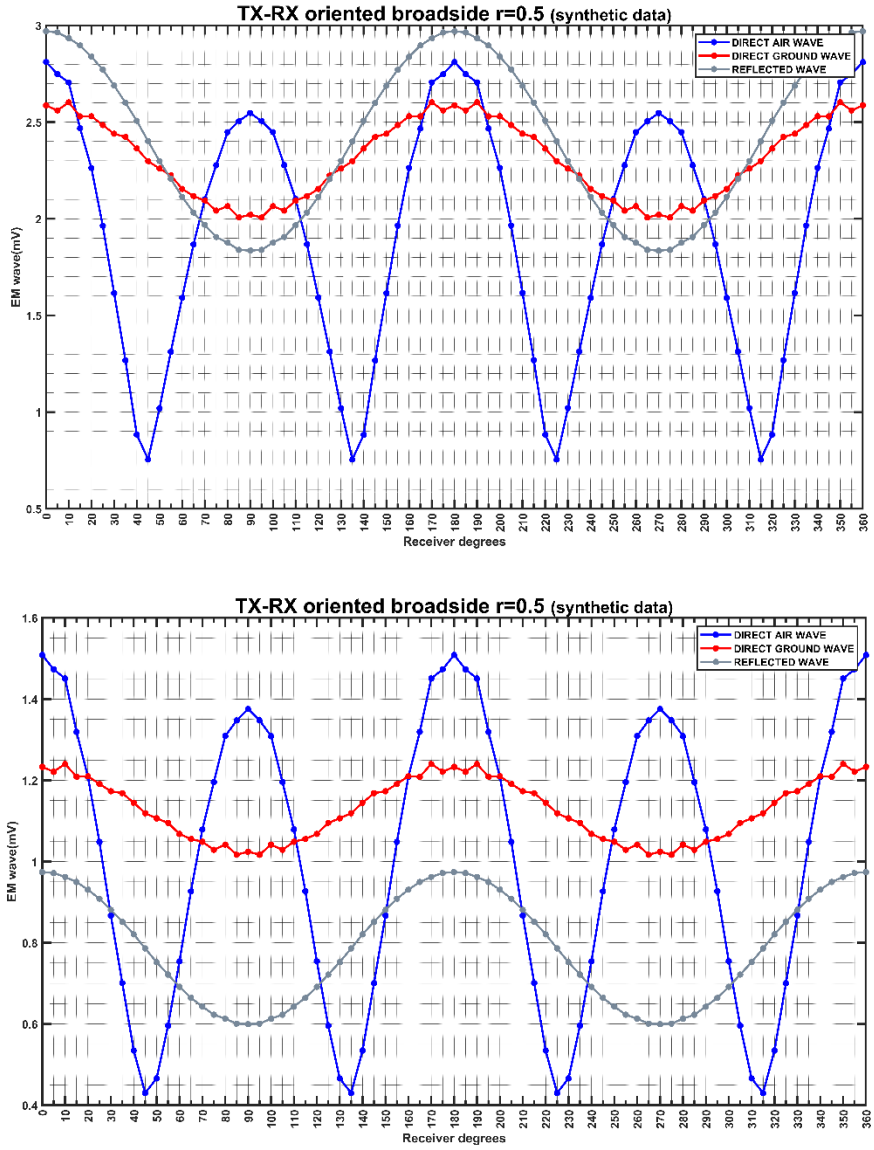

Figure 102: The maximum of the absolute (top), and the RMS (bottom) values of amplitude in millivolts (y axis) of the direct air wave (blue solid line) the direct ground wave (red solid line) and the reflected wave (grey solid line) for the circle of r=0.5m and for the broadside antenna orientation compared to the spatial step of the collected traces (i.e., per 5 degrees) as indicated in the x axis. The minor grid lines in the x axis are at every 5 degrees. The traces have been collected with point dipole antennas.

- Broadside antenna orientation (synthetic data), circle of r=1m plots for the direct (as a whole entity-brown solid line) and reflected wave (grey solid line) versus the angle of the collected traces.

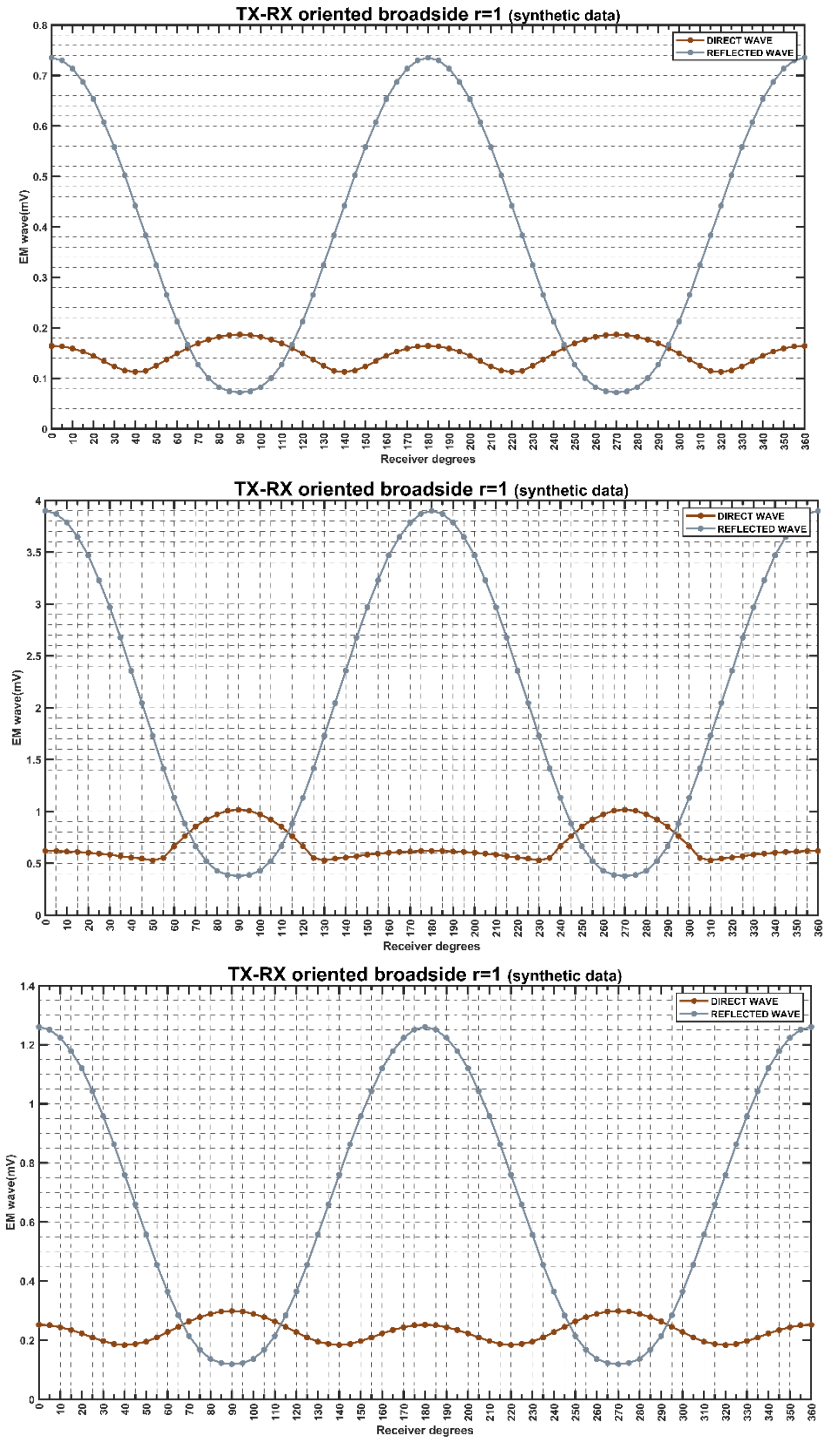

Figure 103: The mean of the absolute (top), the maximum of the absolute (middle), and the RMS (bottom) values of amplitude in millivolts (y axis) of the direct wave (brown solid line) and the reflected wave (grey solid line) for the circle of r=1m and for the broadside antenna orientation compared to the spatial step of the collected traces (i.e., per 5 degrees) as indicated in the x axis. The minor grid lines in the x axis are at every 5 degrees. The traces have been collected with point dipole antennas.

- Broadside antenna orientation (synthetic data), circle of r=1m plots for the direct (as two separated entities: the direct air wave -blue solid line- and the direct ground wave -red solid line-) and reflected wave (grey solid line) versus the angle of the collected traces. The results for the maximum absolute and RMS values of amplitude (mV) are given. The absolute mean values of amplitude have been presented in the main context.

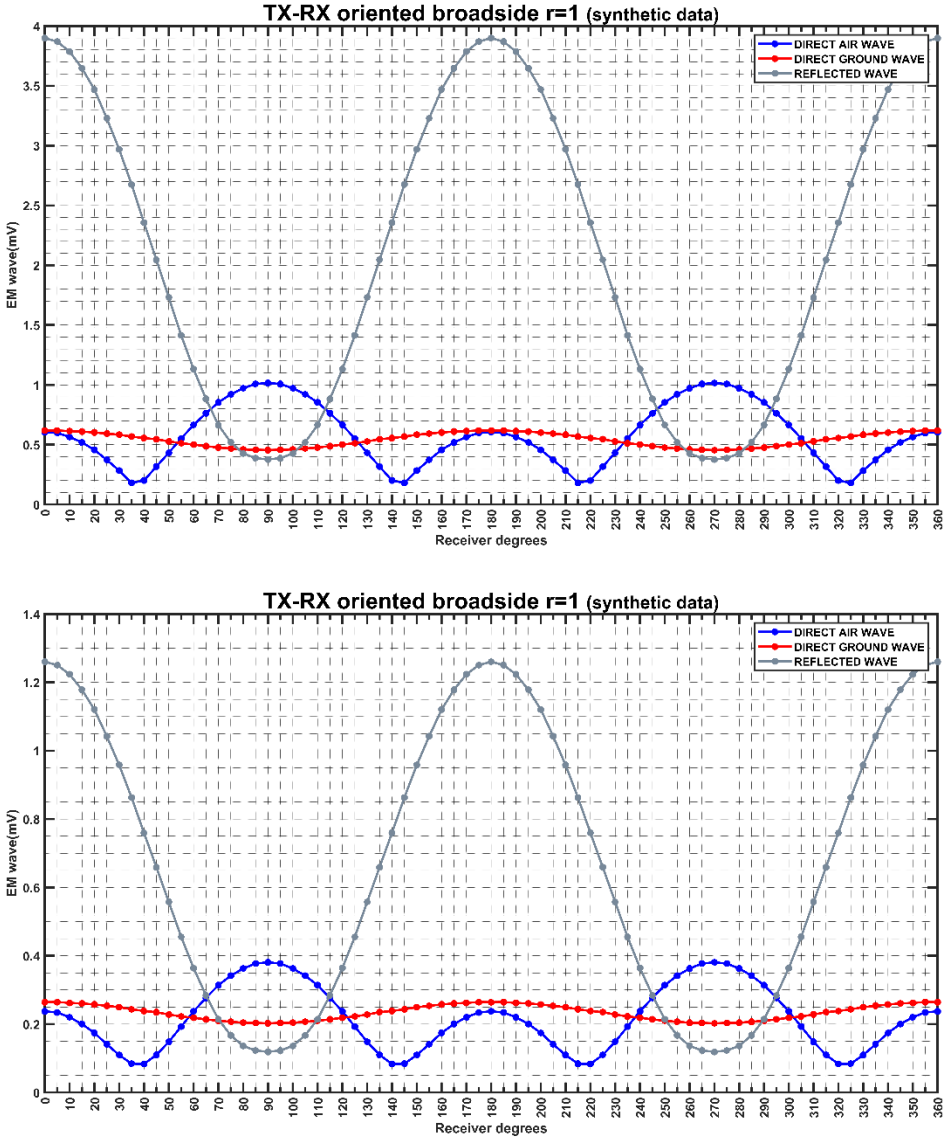

Figure 104: The maximum of the absolute (top), and the RMS (bottom) values of amplitude in millivolts (y axis) of the direct air wave (blue solid line) the direct ground wave (red solid line) and the reflected wave (grey solid line) for the circle of r=1m and for the broadside antenna orientation compared to the spatial step of the collected traces (i.e., per 5 degrees) as indicated in the x axis. The minor grid lines in the x axis are at every 5 degrees. The traces have been collected with point dipole antennas.

- Endfire antenna orientation (synthetic data), circle of r=0.23m plots for the direct (as a whole entity -brown solid line) and reflected wave (grey solid line) versus the angle of the collected traces.

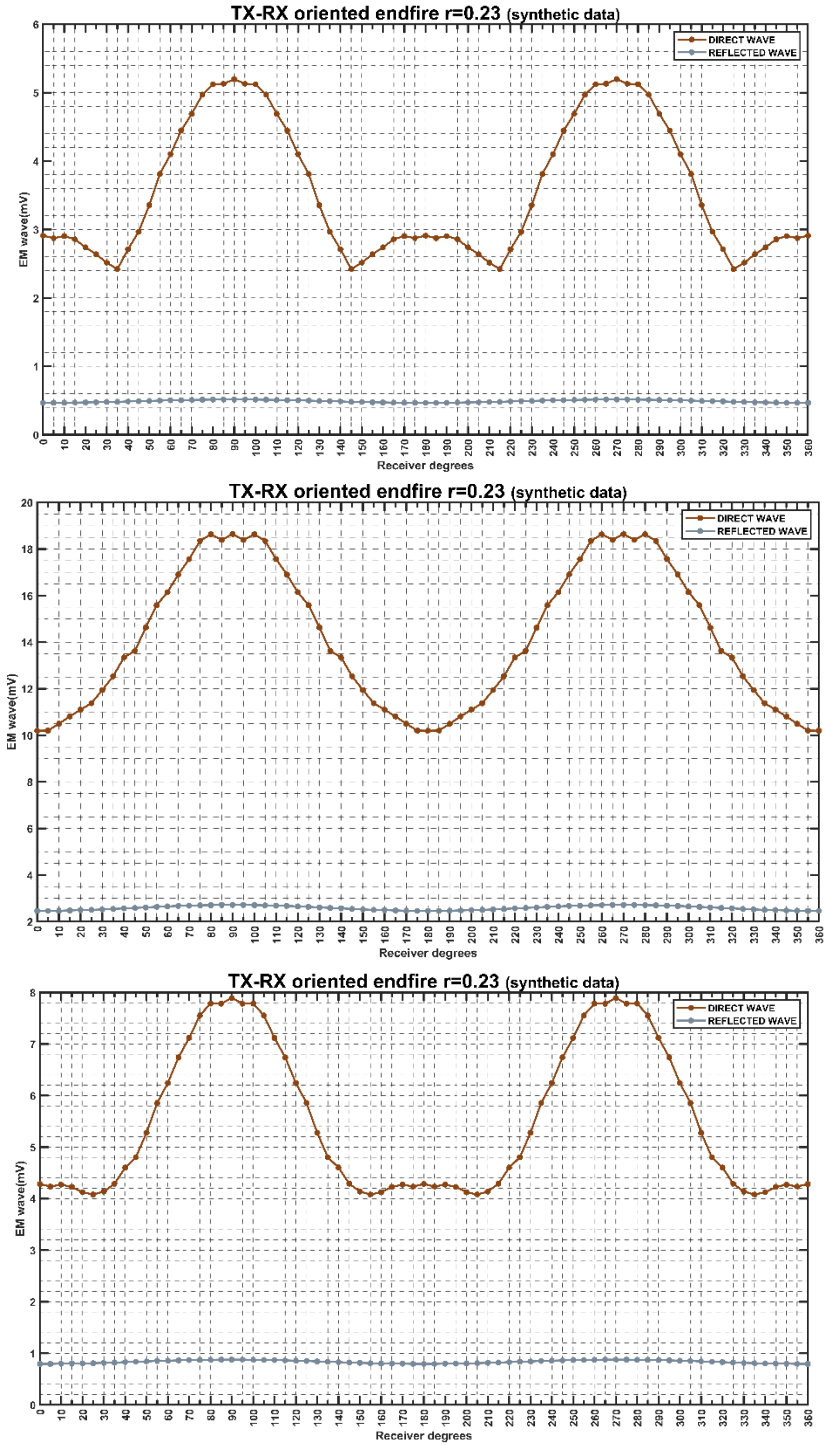

Figure 105: The mean of the absolute (top), the maximum of the absolute (middle), and the RMS (bottom) values of amplitude in millivolts (y axis) of the direct wave (brown solid line) and the reflected wave (grey solid line) for the circle of r=0.23m and for the endfire antenna orientation compared to the spatial step of the collected traces (i.e., per 5 degrees) as indicated in the x axis. The minor grid lines in the x axis are at every 5 degrees. The traces have been collected with point dipole antennas.

- Endfire antenna orientation (synthetic data), circle of r=0.23m plots for the direct (as two separated entities: the direct air wave -blue solid line- and the direct ground wave -red solid line-) and reflected wave (grey solid line) versus the angle of the collected traces. The results for the maximum absolute and RMS values of amplitude (mV) are given. The absolute mean values of amplitude have been presented in the main context.

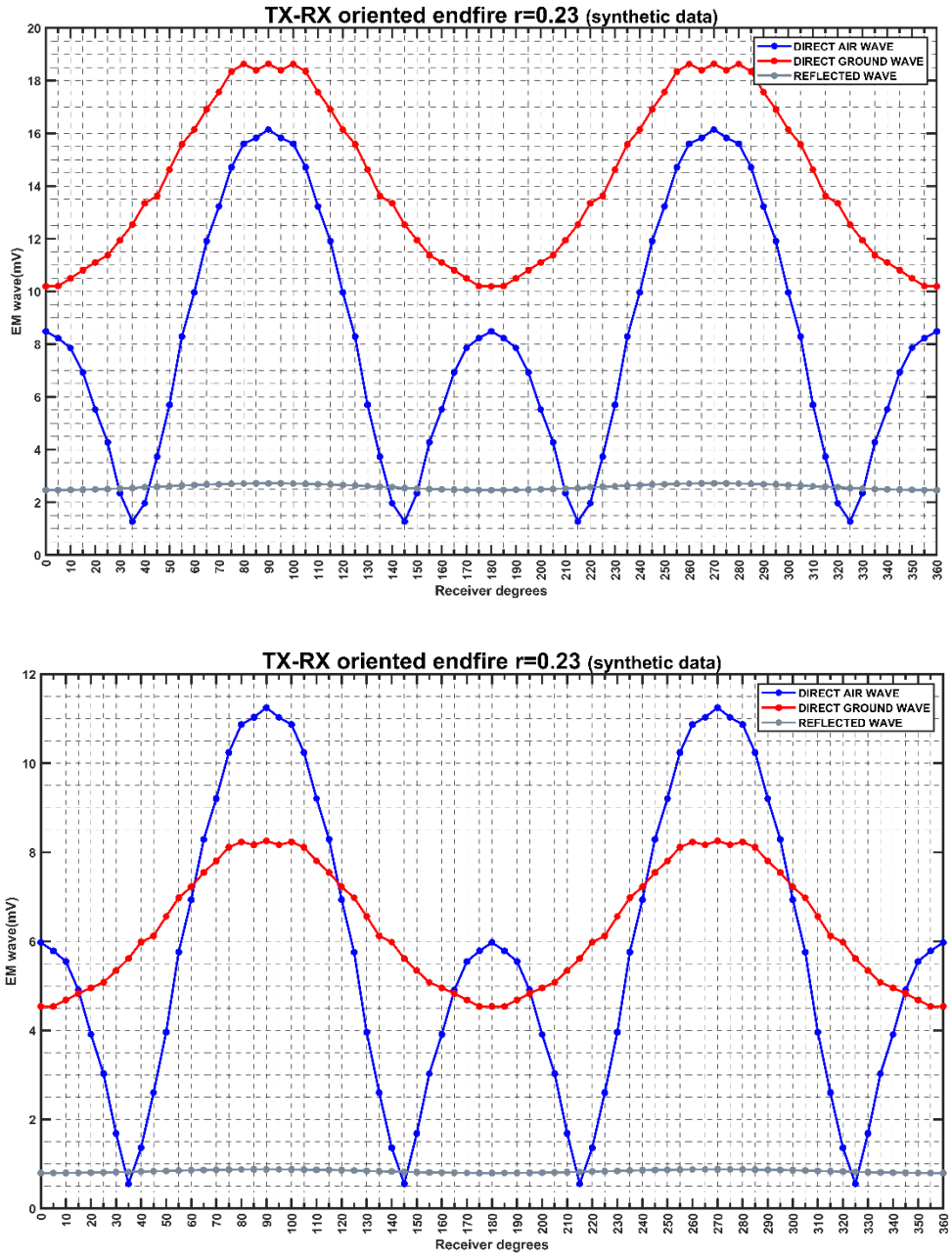

Figure 106: The maximum of the absolute (top), and the RMS (bottom) values of amplitude in millivolts (y axis) of the direct air wave (blue solid line) the direct ground wave (red solid line) and the reflected wave (grey solid line) for the circle of r=0.23m and for the endfire antenna orientation compared to the spatial step of the collected traces (i.e., per 5 degrees) as indicated in the x axis. The minor grid lines in the x axis are at every 5 degrees. The traces have been collected with point dipole antennas.

- Endfire antenna orientation (synthetic data), circle of r=0.5m plots for the direct (as a whole entity -brown solid line) and reflected wave (grey solid line) versus the angle of the collected traces.

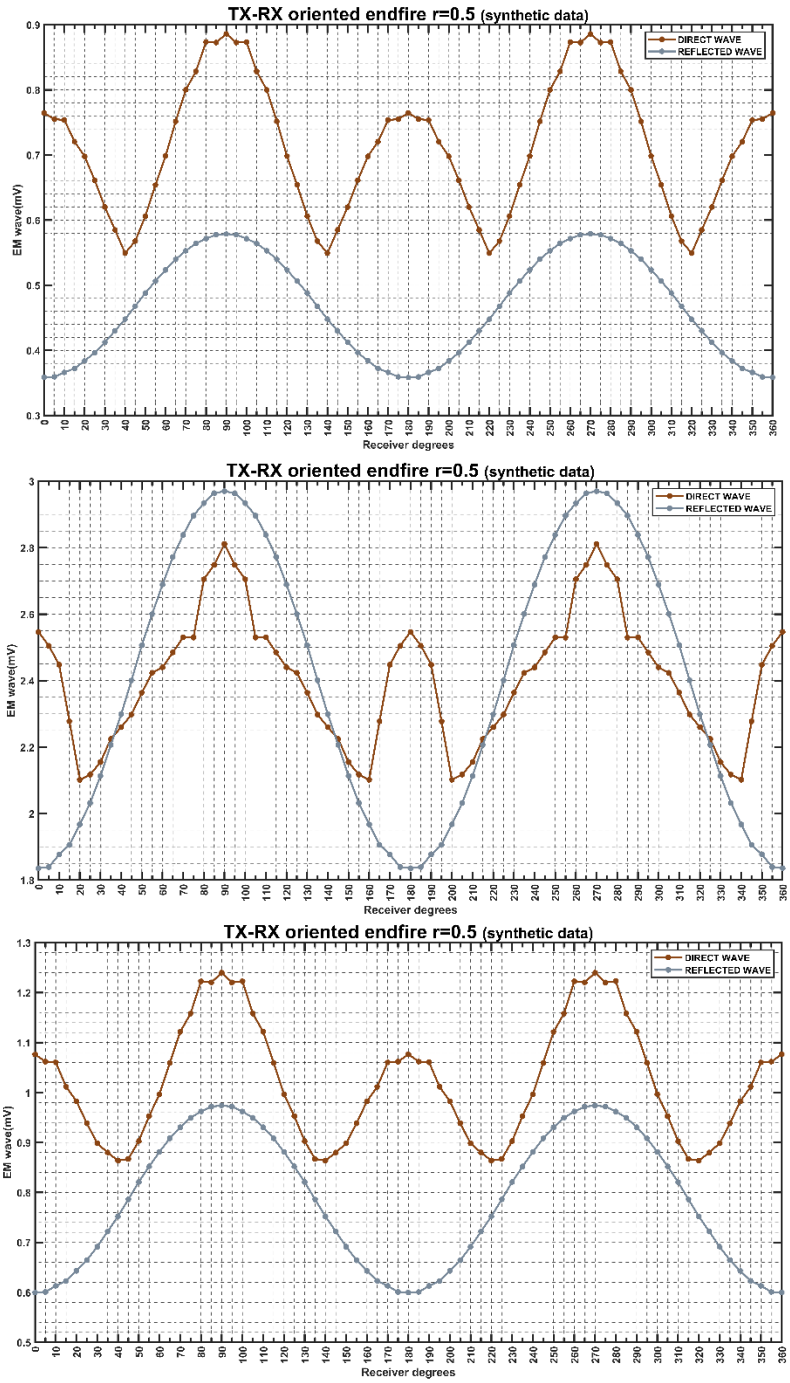

Figure 107: The mean of the absolute (top), the maximum of the absolute (middle), and the RMS (bottom) values of amplitude in millivolts (y axis) of the direct wave (brown solid line) and the reflected wave (grey solid line) for the circle of r=0.5m and for the endfire antenna orientation compared to the spatial step of the collected traces (i.e., per 5 degrees) as indicated in the x axis. The minor grid lines in the x axis are at every 5 degrees. The traces have been collected with point dipole antennas.

- Endfire antenna orientation (synthetic data), circle of r=0.5m plots for the direct (as two separated entities: the direct air wave -blue solid line- and the direct ground wave -red solid line-) and reflected wave (grey solid line) versus the angle of the collected traces. The results for the maximum absolute and RMS values of amplitude (mV) are given. The absolute mean values of amplitude have been presented in the main context.

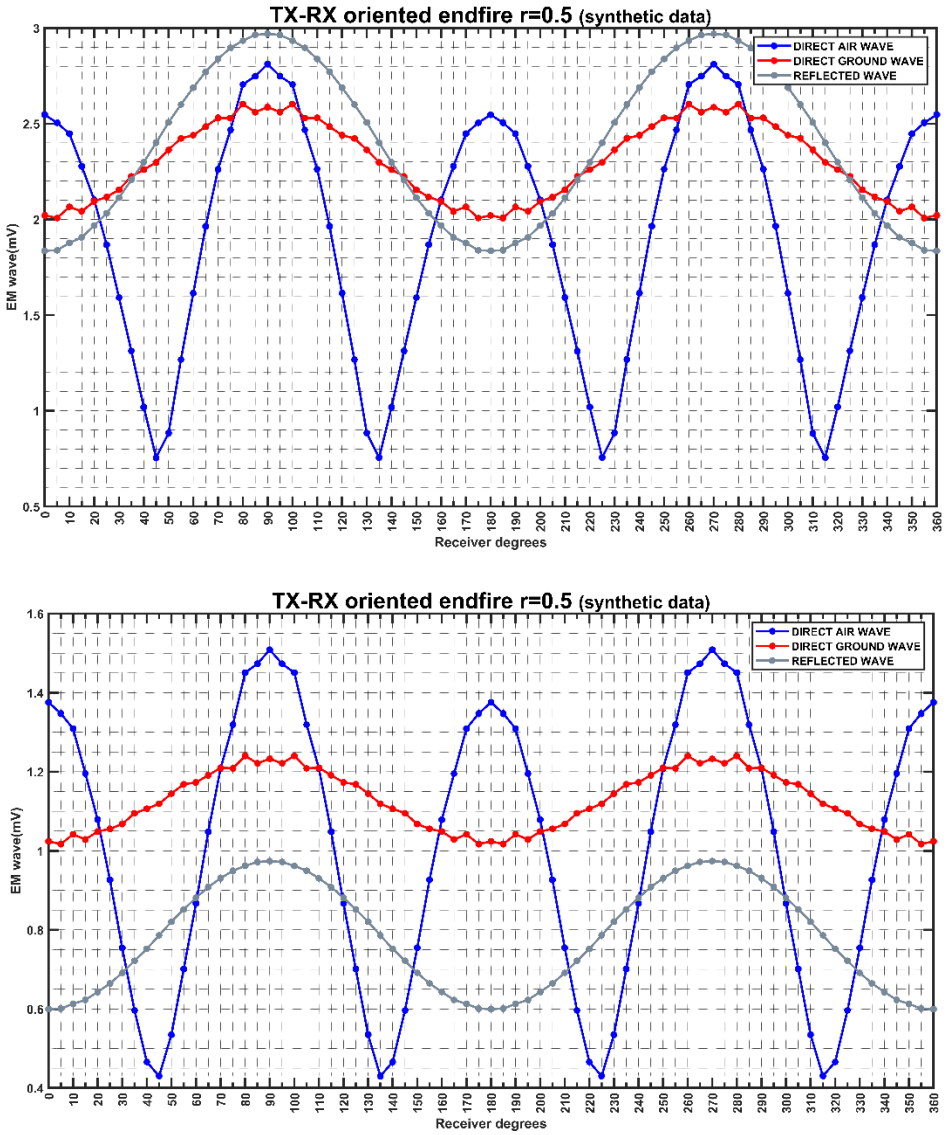

Figure 108: The maximum of the absolute (top), and the RMS (bottom) values of amplitude in millivolts (y axis) of the direct air wave (blue solid line) the direct ground wave (red solid line) and the reflected wave (grey solid line) for the circle of r=0.5m and for the endfire antenna orientation compared to the spatial step of the collected traces (i.e., per 5 degrees) as indicated in the x axis. The minor grid lines in the x axis are at every 5 degrees. The traces have been collected with point dipole antennas.

- Endfire antenna orientation (synthetic data), circle of r=1m plots for the direct (as a whole entity -brown solid line) and reflected wave (grey solid line) versus the angle of the collected traces.

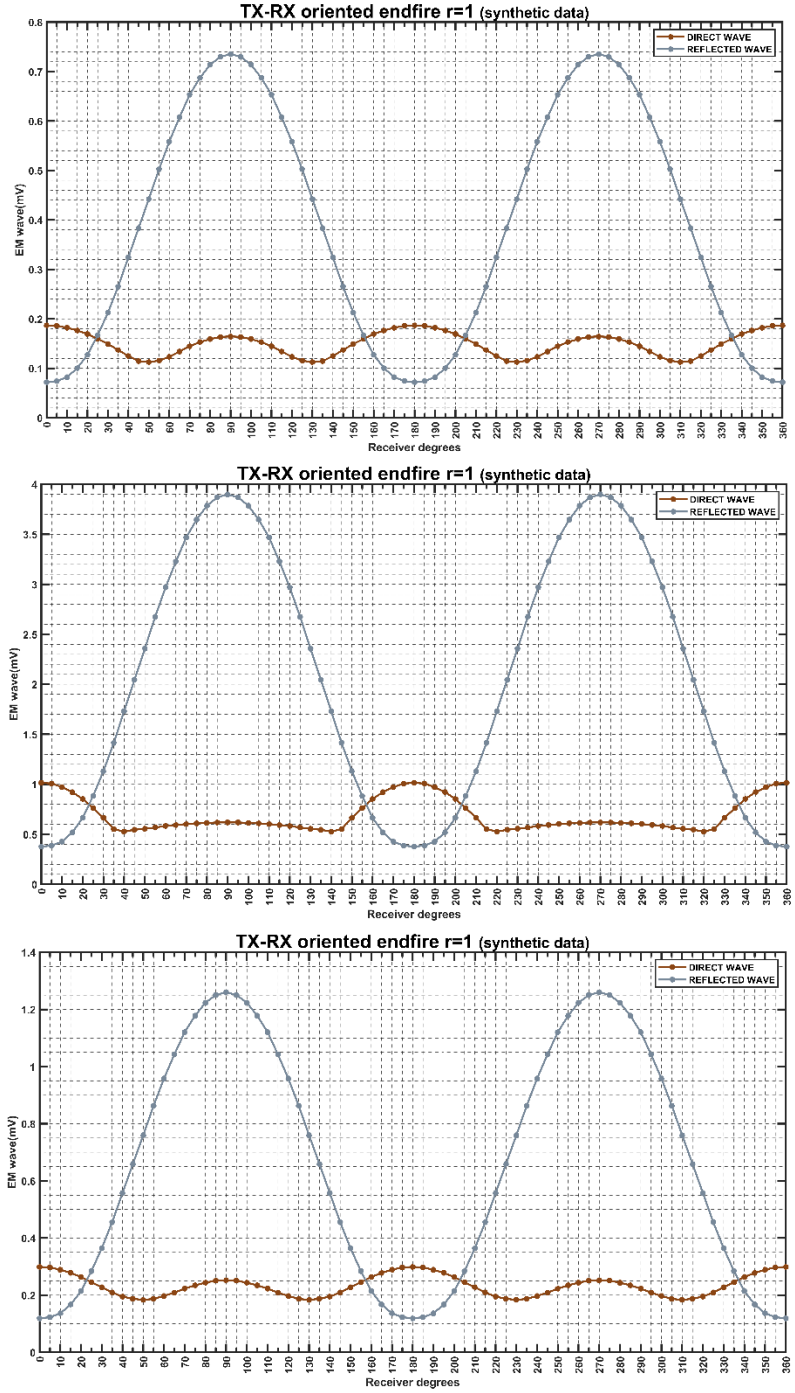

Figure 109: The mean of the absolute (top), the maximum of the absolute (middle), and the RMS (bottom) values of amplitude in millivolts (y axis) of the direct wave (brown solid line) and the reflected wave (grey solid line) for the circle of r=1m and for the endfire antenna orientation compared to the spatial step of the collected traces (i.e., per 5 degrees) as indicated in the x axis. The minor grid lines in the x axis are at every 5 degrees. The traces have been collected with point dipole antennas.

- Endfire antenna orientation (synthetic data), circle of r=1m plots for the direct (as two separated entities: the direct air wave -blue solid line- and the direct ground wave -red solid line-) and reflected wave (grey solid line) versus the angle of the collected traces. The results for the maximum absolute and RMS values of amplitude (mV) are given. The absolute mean values of amplitude have been presented in the main context.

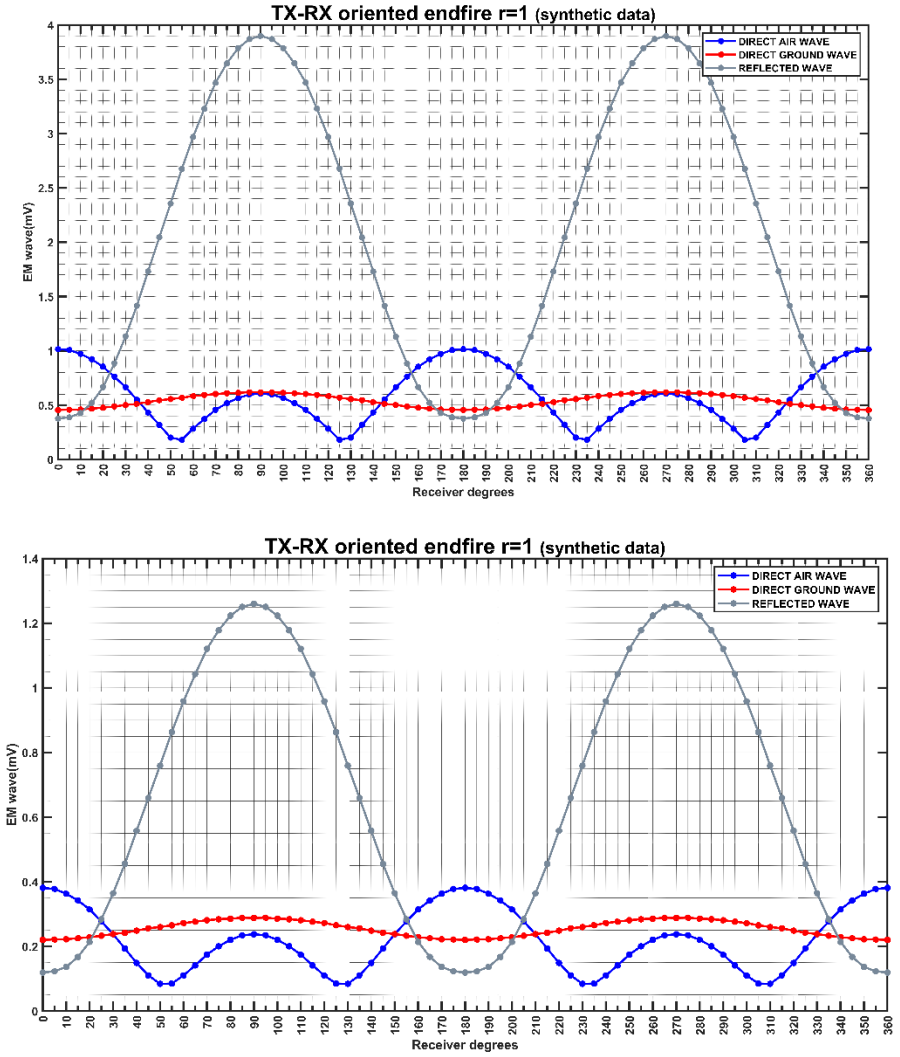

Figure 110: The maximum of the absolute (top), and the RMS (bottom) values of amplitude in millivolts (y axis) of the direct air wave (blue solid line) the direct ground wave (red solid line) and the reflected wave (grey solid line) for the circle of r=1m and for the endfire antenna orientation compared to the spatial step of the collected traces (i.e., per 5 degrees) as indicated in the x axis. The minor grid lines in the x axis are at every 5 degrees. The traces have been collected with point dipole antennas.

Synthetic data (bare dipole)

- Broadside antenna orientation (synthetic data), circle of r=0.23m plots for the direct (as a whole entity -brown solid line) and reflected wave (grey solid line) versus the angle of the collected traces.

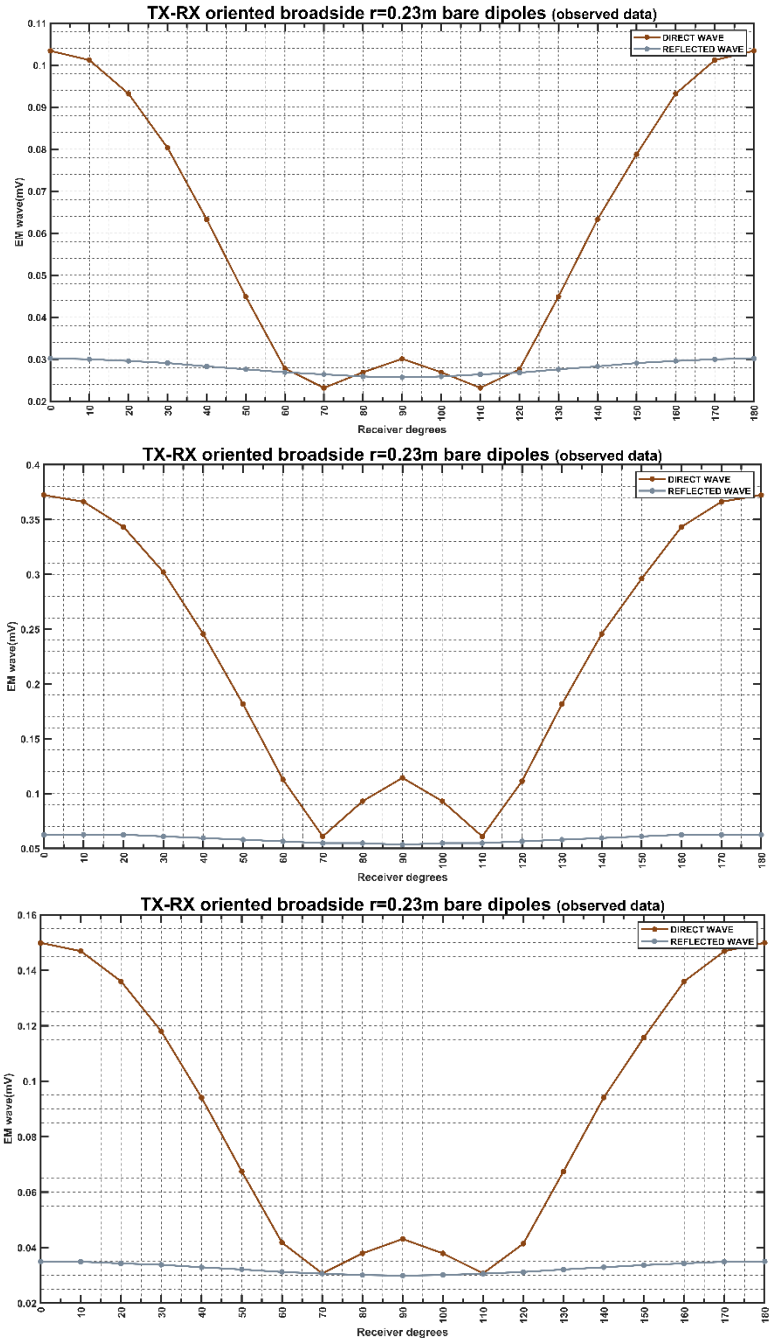

Figure 111: The mean of the absolute (top), the maximum of the absolute (middle), and the RMS (bottom) values of amplitude in millivolts (y axis) of the direct wave (brown solid line) and the reflected wave (grey solid line) for the circle of r=0.23m and for the broadside antenna orientation compared to the spatial step of the collected traces (i.e., per 5 degrees) as indicated in the x axis. The minor grid lines in the x axis are at every 5 degrees. The traces have been collected with bare dipole antennas.

- Broadside antenna orientation (synthetic data), circle of r=0.23m plots for the direct (as two separated entities: the direct air wave -blue solid line- and the direct ground wave -red solid line-) and reflected wave (grey solid line) versus the angle of the collected traces. The results for the maximum absolute and RMS values of amplitude (mV) are given. The absolute mean values of amplitude have been presented in the main context.

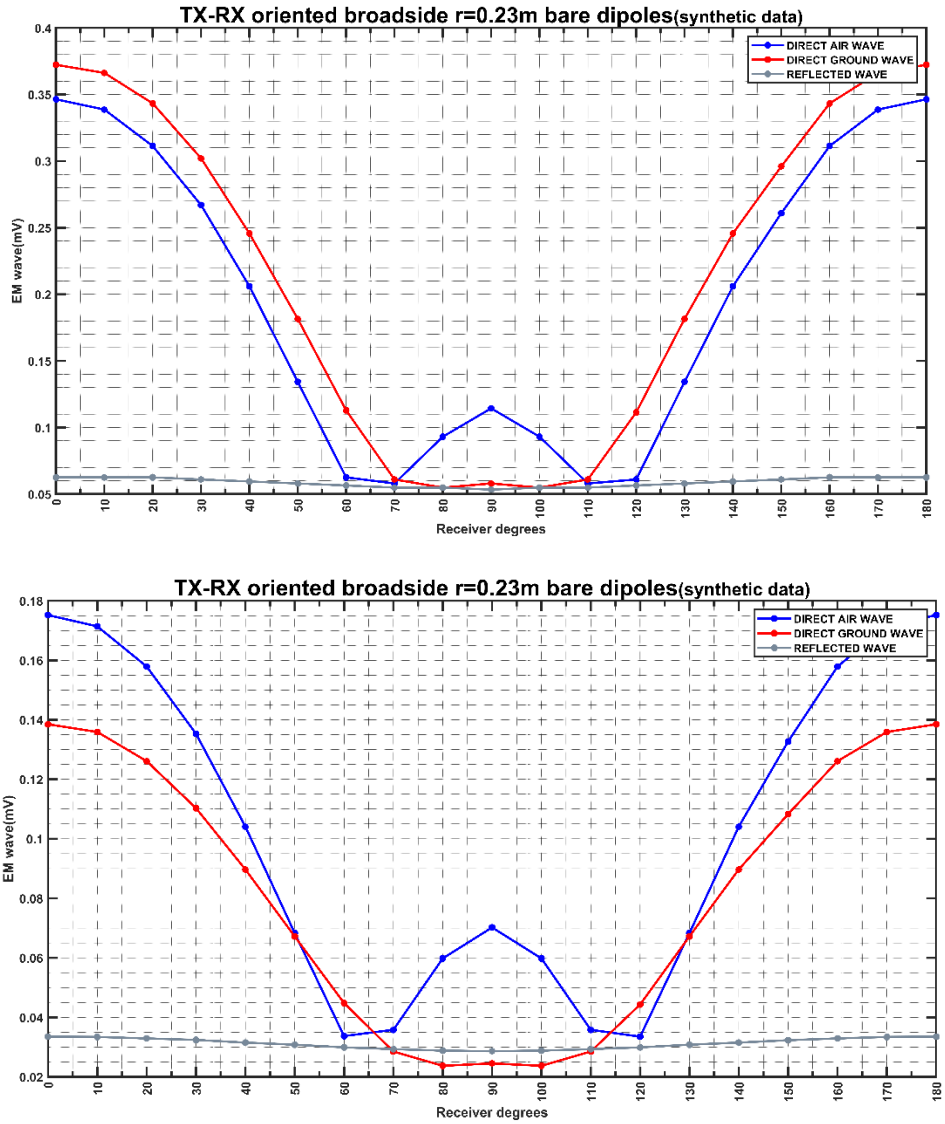

Figure 112: The maximum of the absolute (top), and the RMS (bottom) values of amplitude in millivolts (y axis) of the direct air wave (blue solid line) the direct ground wave (red solid line) and the reflected wave (grey solid line) for the circle of r=0.23m and for the broadside antenna orientation compared to the spatial step of the collected traces (i.e., per 5 degrees) as indicated in the x axis. The minor grid lines in the x axis are at every 5 degrees. The traces have been collected with bare dipole antennas.

- Broadside antenna orientation (synthetic data), circle of r=0.5m plots for the direct (as a whole entity -brown solid line) and reflected wave (grey solid line) versus the angle of the collected traces.

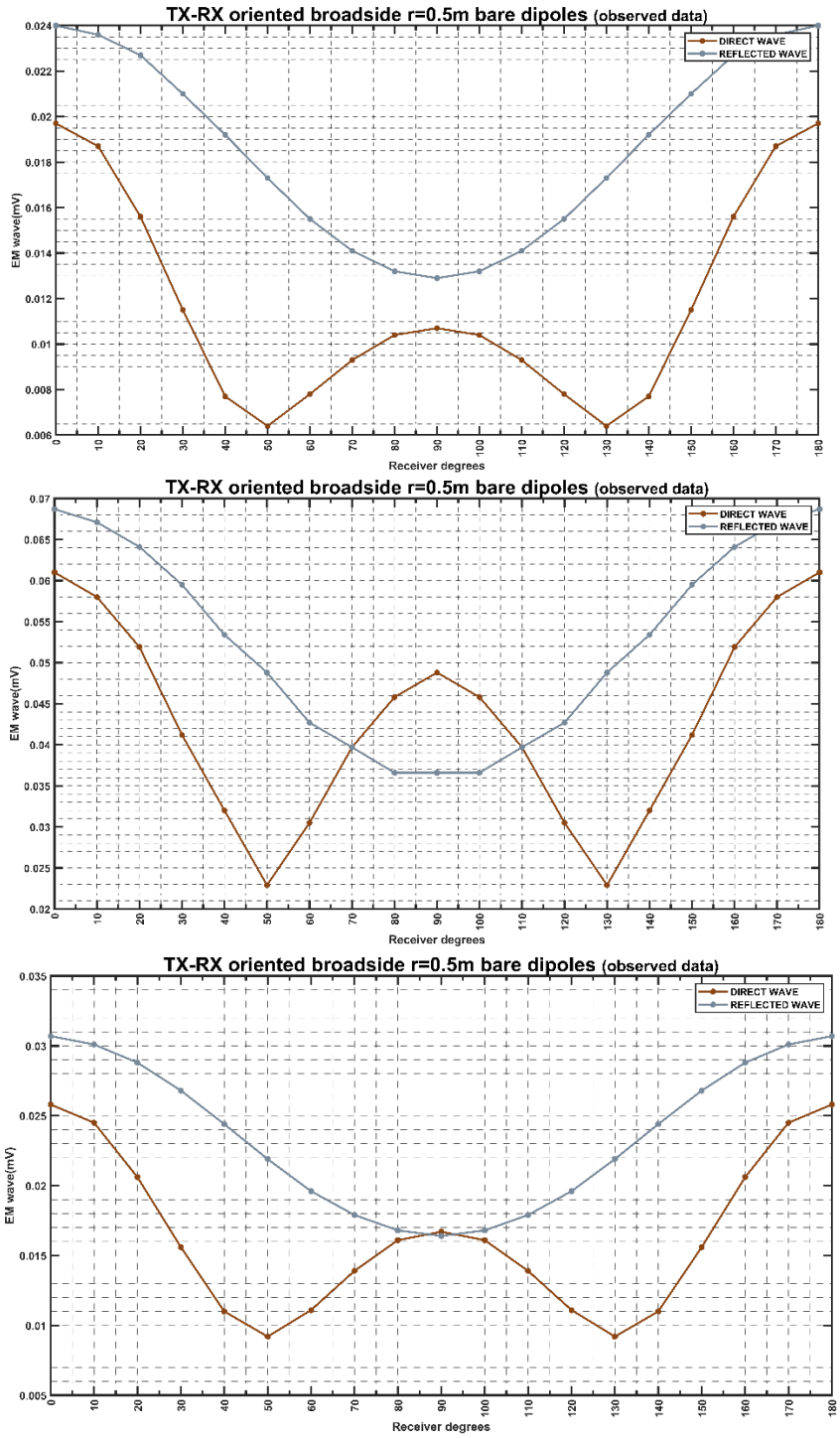

Figure 113: The mean of the absolute (top), the maximum of the absolute (middle), and the RMS (bottom) values of amplitude in millivolts (y axis) of the direct wave (brown solid line) and the reflected wave (grey solid line) for the circle of r=0.5m and for the broadside antenna orientation compared to the spatial step of the collected traces (i.e., per 5 degrees) as indicated in the x axis. The minor grid lines in the x axis are at every 5 degrees. The traces have been collected with bare dipole antennas.

- Broadside antenna orientation (synthetic data), circle of r=0.5m plots for the direct (as two separated entities: the direct air wave -blue solid line- and the direct ground wave -red solid line-) and reflected wave (grey solid line) versus the angle of the collected traces. The results for the maximum absolute and RMS values of amplitude (mV) are given. The absolute mean values of amplitude have been presented in the main context.

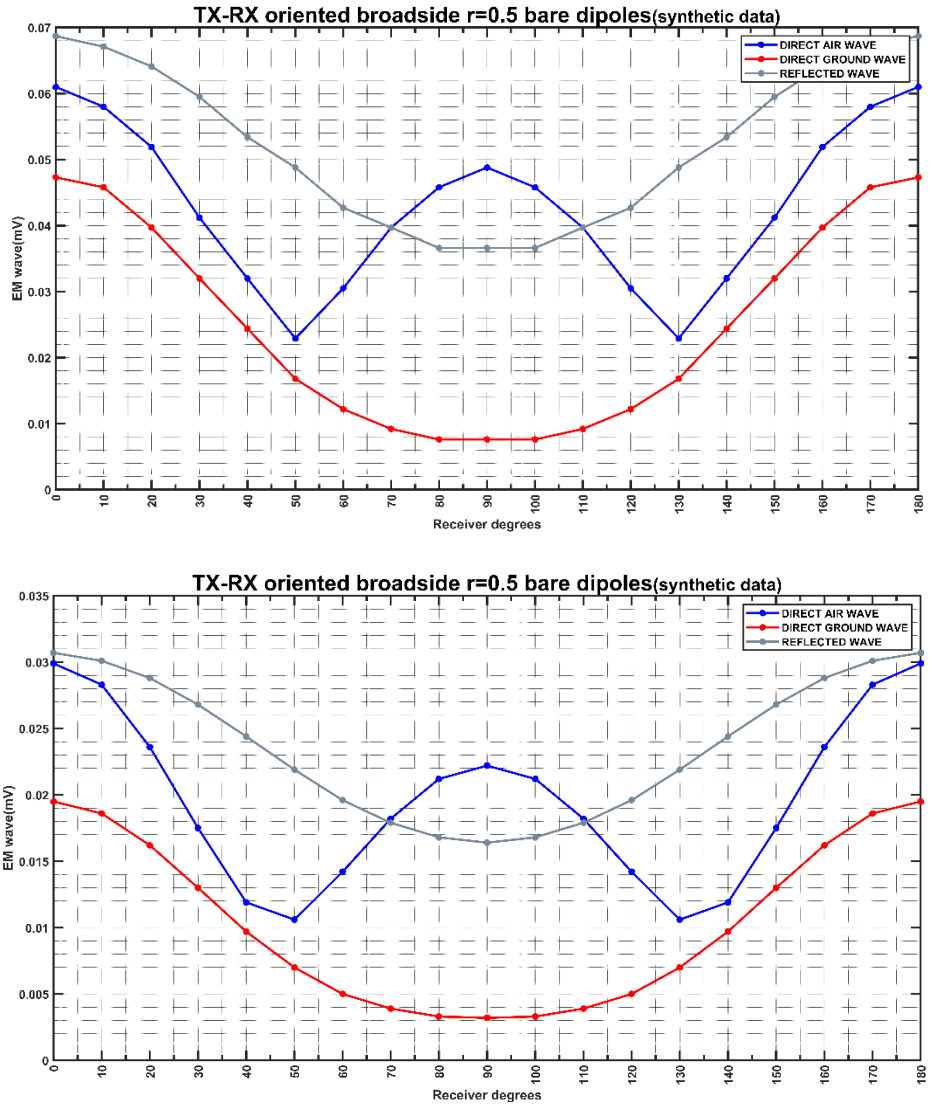

Figure 114: The maximum of the absolute (top), and the RMS (bottom) values of amplitude in millivolts (y axis) of the direct air wave (blue solid line) the direct ground wave (red solid line) and the reflected wave (grey solid line) for the circle of r=0.5m and for the broadside antenna orientation compared to the spatial step of the collected traces (i.e., per 5 degrees) as indicated in the x axis. The minor grid lines in the x axis are at every 5 degrees. The traces have been collected with bare dipole antennas.

- Broadside antenna orientation (synthetic data), circle of r=1m plots for the direct (as a whole entity -brown solid line) and reflected wave (grey solid line) versus the angle of the collected traces.

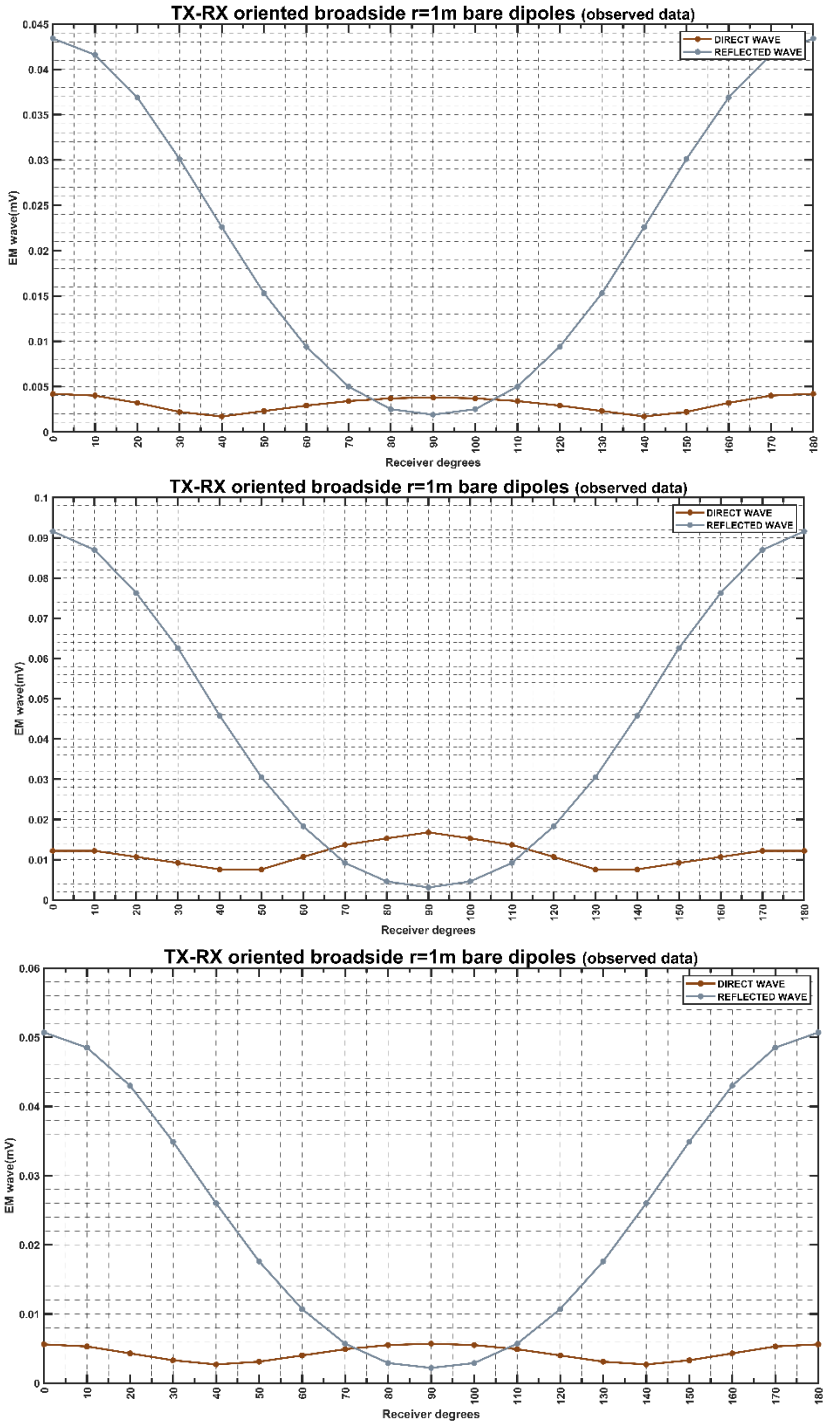

Figure 115: The mean of the absolute (top), the maximum of the absolute (middle), and the RMS (bottom) values of amplitude in millivolts (y axis) of the direct wave (brown solid line) and the reflected wave (grey solid line) for the circle of r=1m and for the broadside antenna orientation compared to the spatial step of the collected traces (i.e., per 5 degrees) as indicated in the x axis. The minor grid lines in the x axis are at every 5 degrees. The traces have been collected with bare dipole antennas.

- Broadside antenna orientation (synthetic data), circle of r=1m plots for the direct (as two separated entities: the direct air wave -blue solid line- and the direct ground wave -red solid line-) and reflected wave (grey solid line) versus the angle of the collected traces. The results for the maximum absolute and RMS values of amplitude (mV) are given. The absolute mean values of amplitude have been presented in the main context.

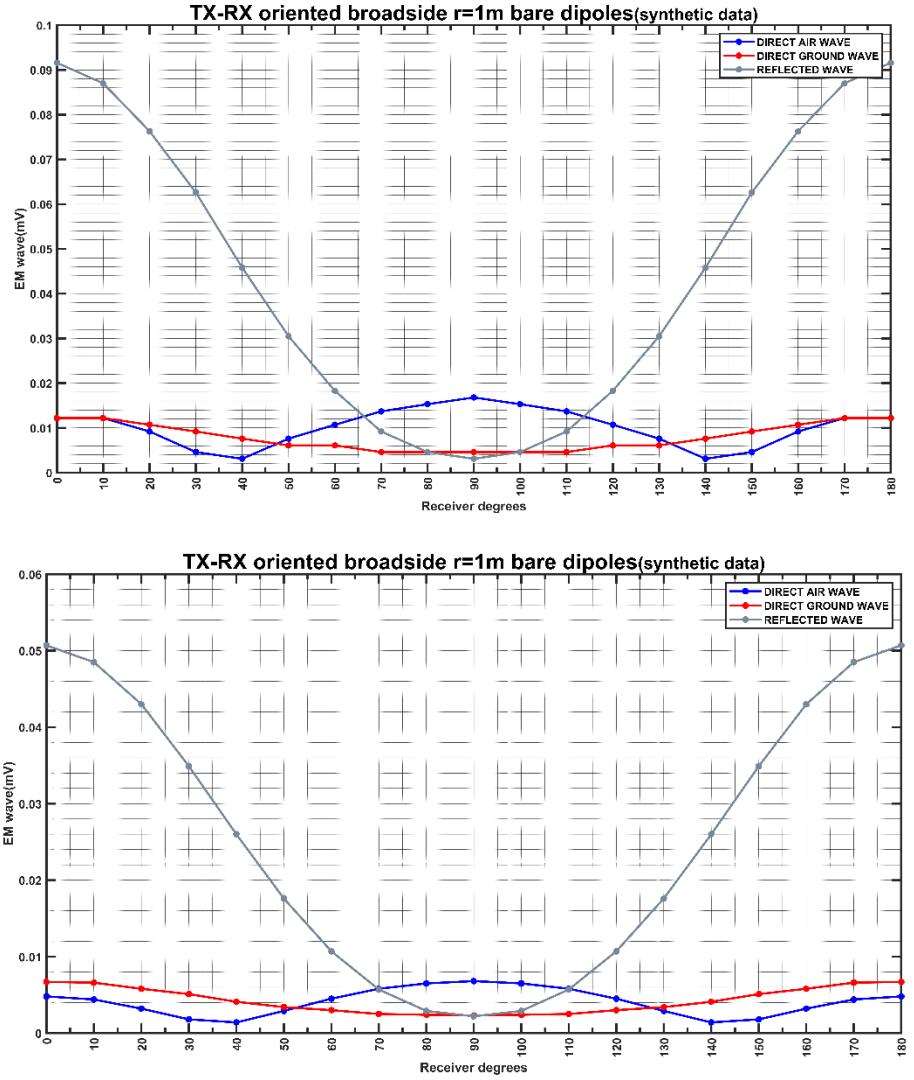

Figure 116: The maximum of the absolute (top), and the RMS (bottom) values of amplitude in millivolts (y axis) of the direct air wave (blue solid line) the direct ground wave (red solid line) and the reflected wave (grey solid line) for the circle of r=1m and for the broadside antenna orientation compared to the spatial step of the collected traces (i.e., per 5 degrees) as indicated in the x axis. The minor grid lines in the x axis are at every 5 degrees. The traces have been collected with bare dipole antennas.

Observed data

- Broadside antenna orientation (synthetic data), circle of r=0.23m plots for the direct (as a whole entity -brown solid line) and reflected wave (grey solid line) versus the angle of the collected traces.

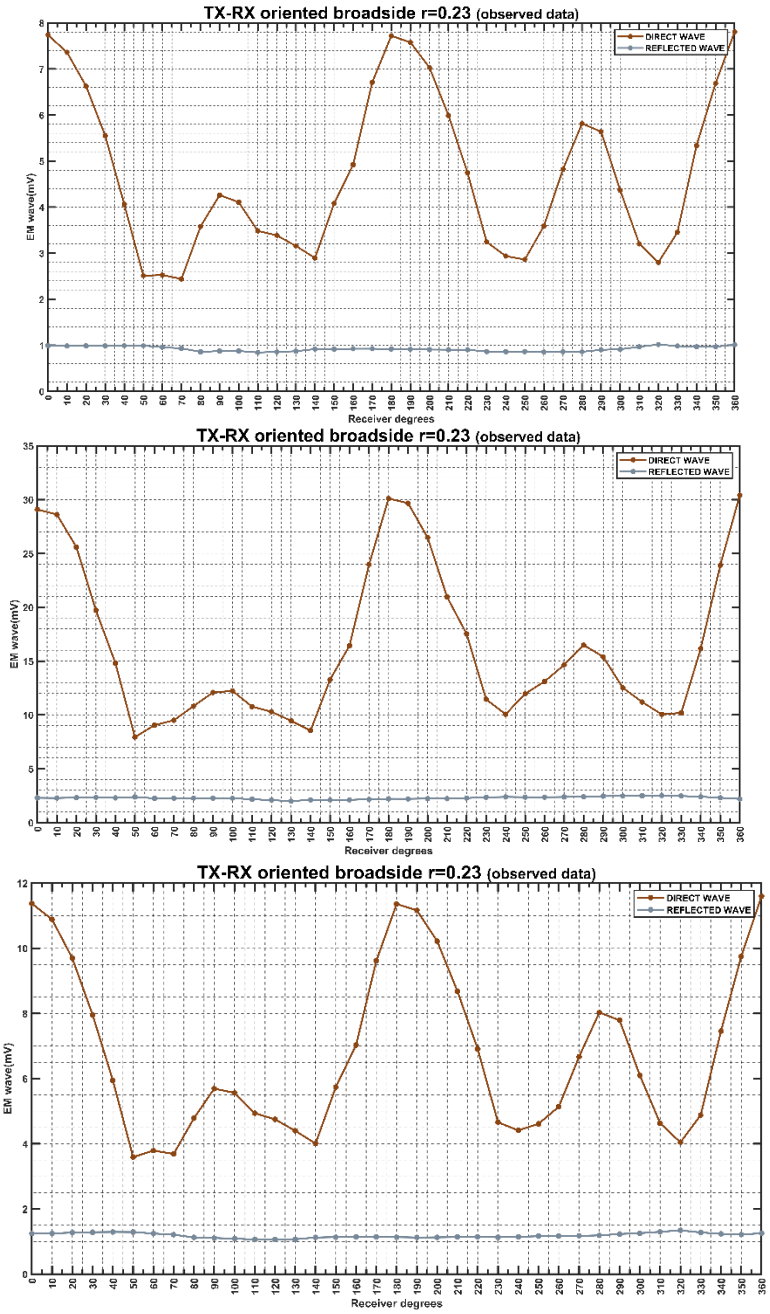

Figure 117: The mean of the absolute (top), the maximum of the absolute (middle), and the RMS (bottom) values of amplitude in millivolts (y axis) of the direct wave (brown solid line) and the reflected wave (grey solid line) for the circle of r=0.23m and for the broadside antenna orientation compared to the spatial step of the collected traces (i.e., per 10 degrees) as indicated in the x axis. The minor grid lines in the x axis are at every 5 degrees. The traces have been collected with the 500MHz antennas from Sensors & Software.

- Broadside antenna orientation (synthetic data), circle of r=0.23m plots for the direct (as two separated entities: the direct air wave -blue solid line- and the direct ground wave -red solid line-) and reflected wave (grey solid line) versus the angle of the collected traces. The results for the maximum absolute and RMS values of amplitude (mV) are given. The absolute mean values of amplitude have been presented in the main context.

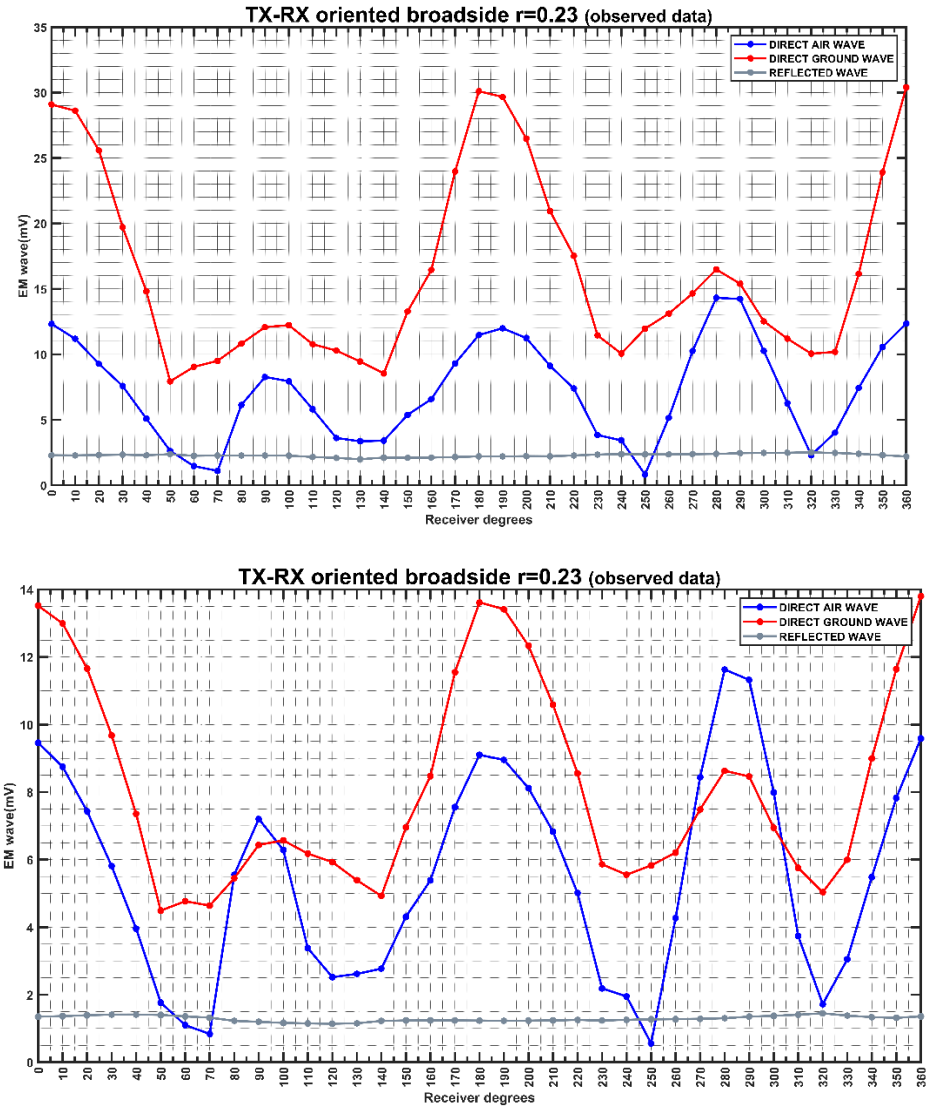

Figure 118: The maximum of the absolute (top), and the RMS (bottom) values of amplitude in millivolts (y axis) of the direct air wave (blue solid line) the direct ground wave (red solid line) and the reflected wave (grey solid line) for the circle of r=0.23m and for the broadside antenna orientation compared to the spatial step of the collected traces (i.e., per 10 degrees) as indicated in the x axis. The minor grid lines in the x axis are at every 5 degrees. The traces have been collected with the 500MHz antennas from Sensors & Software.

- Broadside antenna orientation (synthetic data), circle of r=0.5m plots for the direct (as a whole entity -brown solid line) and reflected wave (grey solid line) versus the angle of the collected traces.

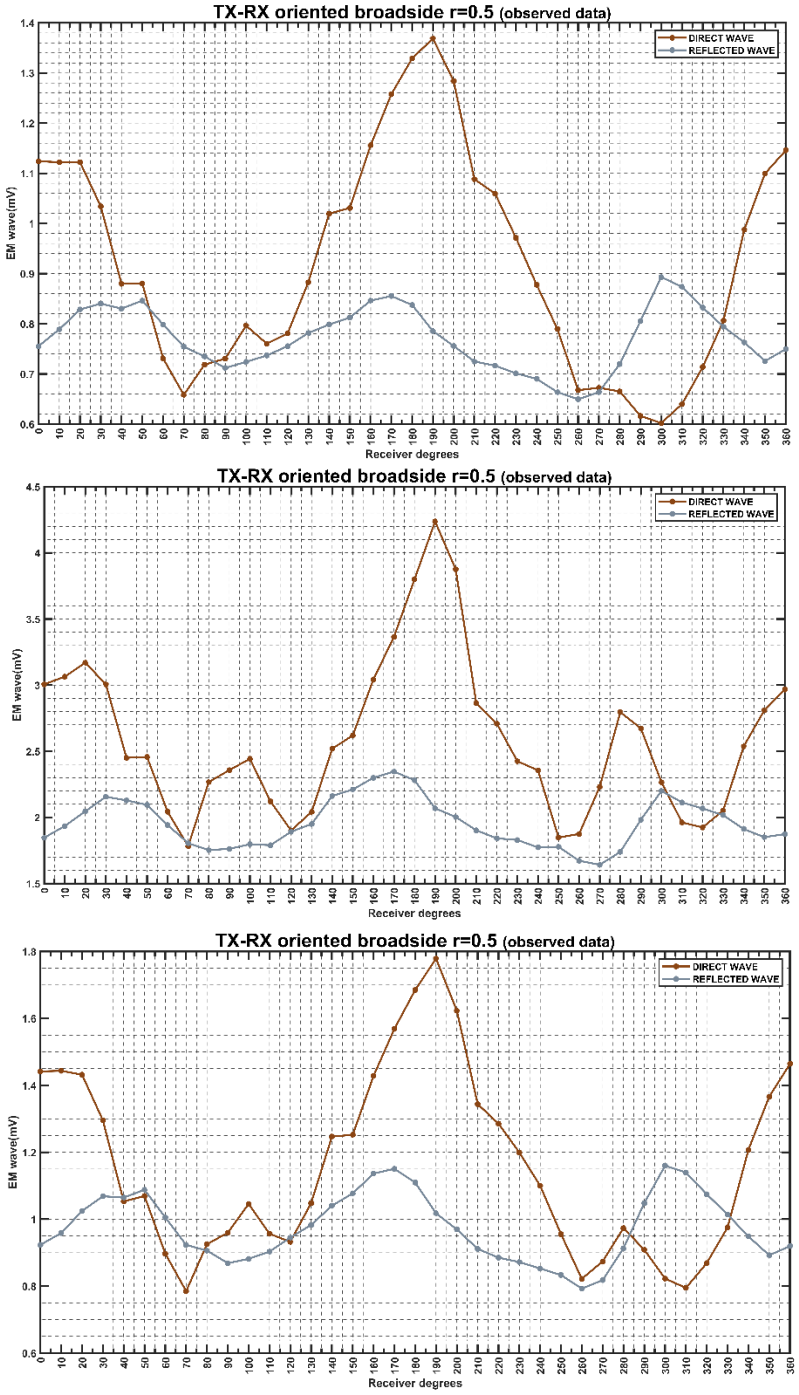

Figure 119: The mean of the absolute (top), the maximum of the absolute (middle), and the RMS (bottom) values of amplitude in millivolts (y axis) of the direct wave (brown solid line) and the reflected wave (grey solid line) for the circle of r=0.5m and for the broadside antenna orientation compared to the spatial step of the collected traces (i.e., per 10 degrees) as indicated in the x axis. The minor grid lines in the x axis are at every 5 degrees. The traces have been collected with the 500MHz antennas from Sensors & Software.

- Broadside antenna orientation (synthetic data), circle of r=0.5m plots for the direct (as two separated entities: the direct air wave -blue solid line- and the direct ground wave -red solid line-) and reflected wave (grey solid line) versus the angle of the collected traces. The results for the maximum absolute and RMS values of amplitude (mV) are given. The absolute mean values of amplitude have been presented in the main context.

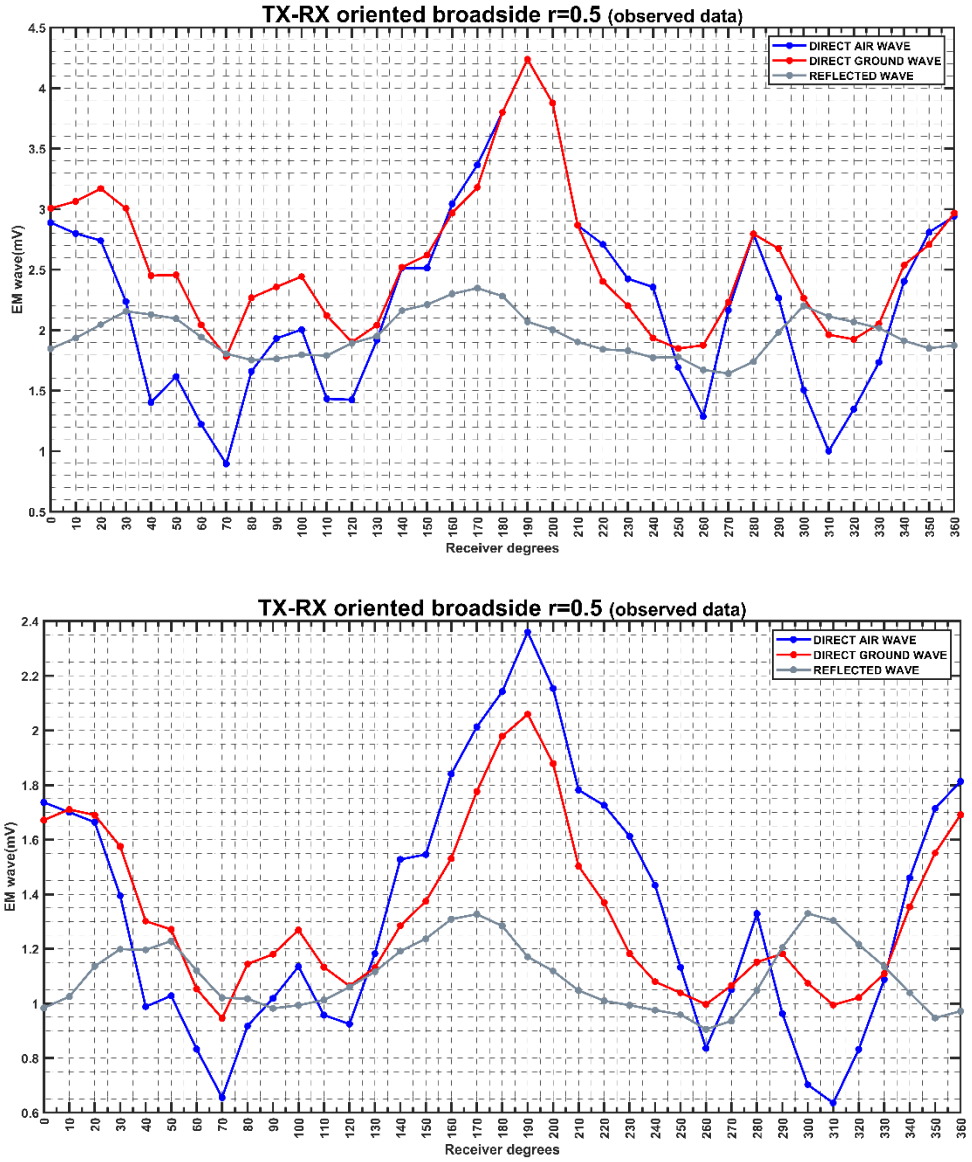

Figure 120: The maximum of the absolute (top), and the RMS (bottom) values of amplitude in millivolts (y axis) of the direct air wave (blue solid line) the direct ground wave (red solid line) and the reflected wave (grey solid line) for the circle of r=0.5m and for the broadside antenna orientation compared to the spatial step of the collected traces (i.e., per 10 degrees) as indicated in the x axis. The minor grid lines in the x axis are at every 5 degrees. The traces have been collected with the 500MHz antennas from Sensors & Software.

- Broadside antenna orientation (synthetic data), circle of r=1m plots for the direct (as a whole entity -brown solid line) and reflected wave (grey solid line) versus the angle of the collected traces.

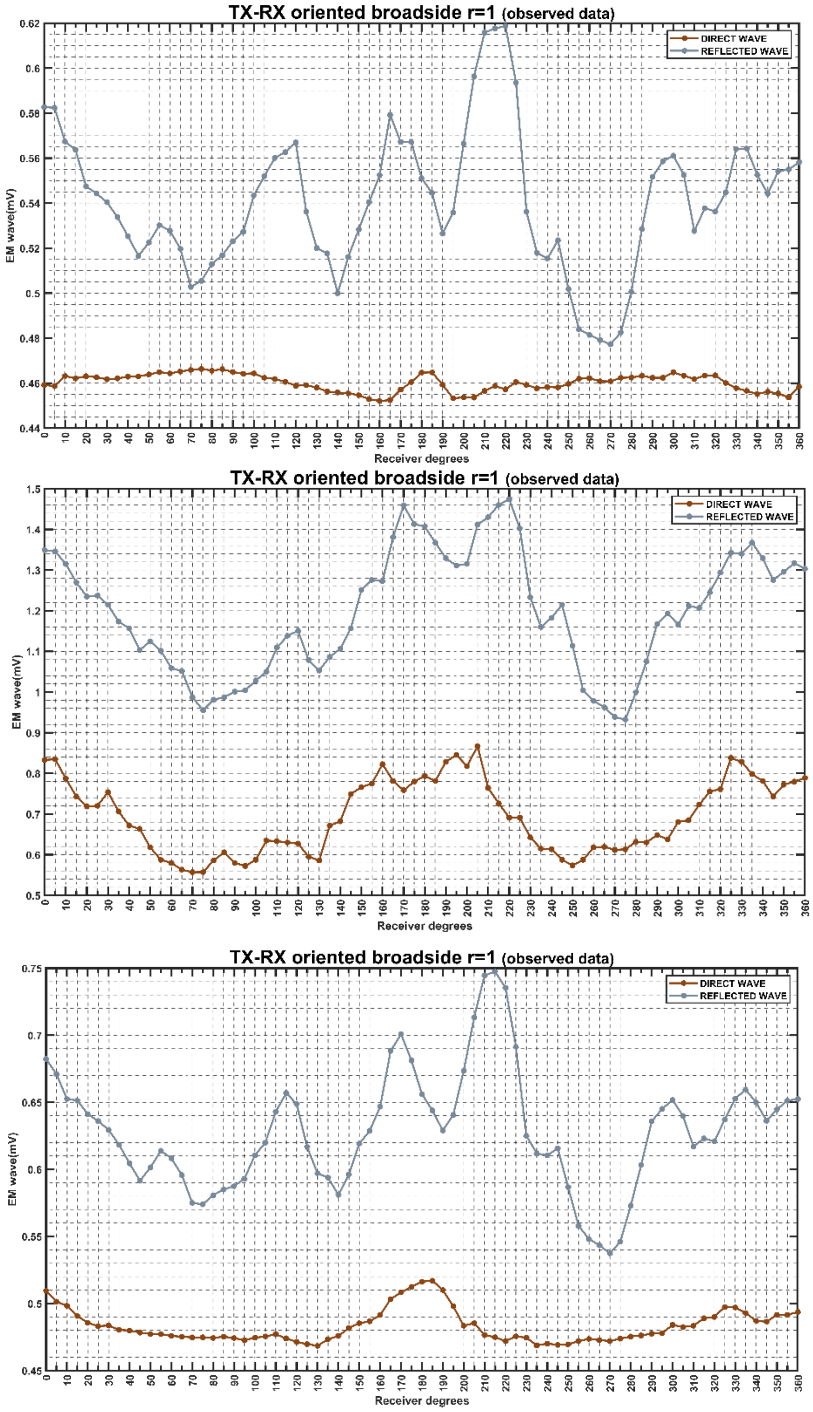

Figure 121: The mean of the absolute (top), the maximum of the absolute (middle), and the RMS (bottom) values of amplitude in millivolts (y axis) of the direct wave (brown solid line) and the reflected wave (grey solid line) for the circle of r=1m and for the broadside antenna orientation compared to the spatial step of the collected traces (i.e., per 5 degrees) as indicated in the x axis. The minor grid lines in the x axis are at every 5 degrees. The traces have been collected with the 500MHz antennas from Sensors & Software.

- Broadside antenna orientation (synthetic data), circle of r=1m plots for the direct (as two separated entities: the direct air wave -blue solid line- and the direct ground wave -red solid line-) and reflected wave (grey solid line) versus the angle of the collected traces. The results for the maximum absolute and RMS values of amplitude (mV) are given. The absolute mean values of amplitude have been presented in the main context.

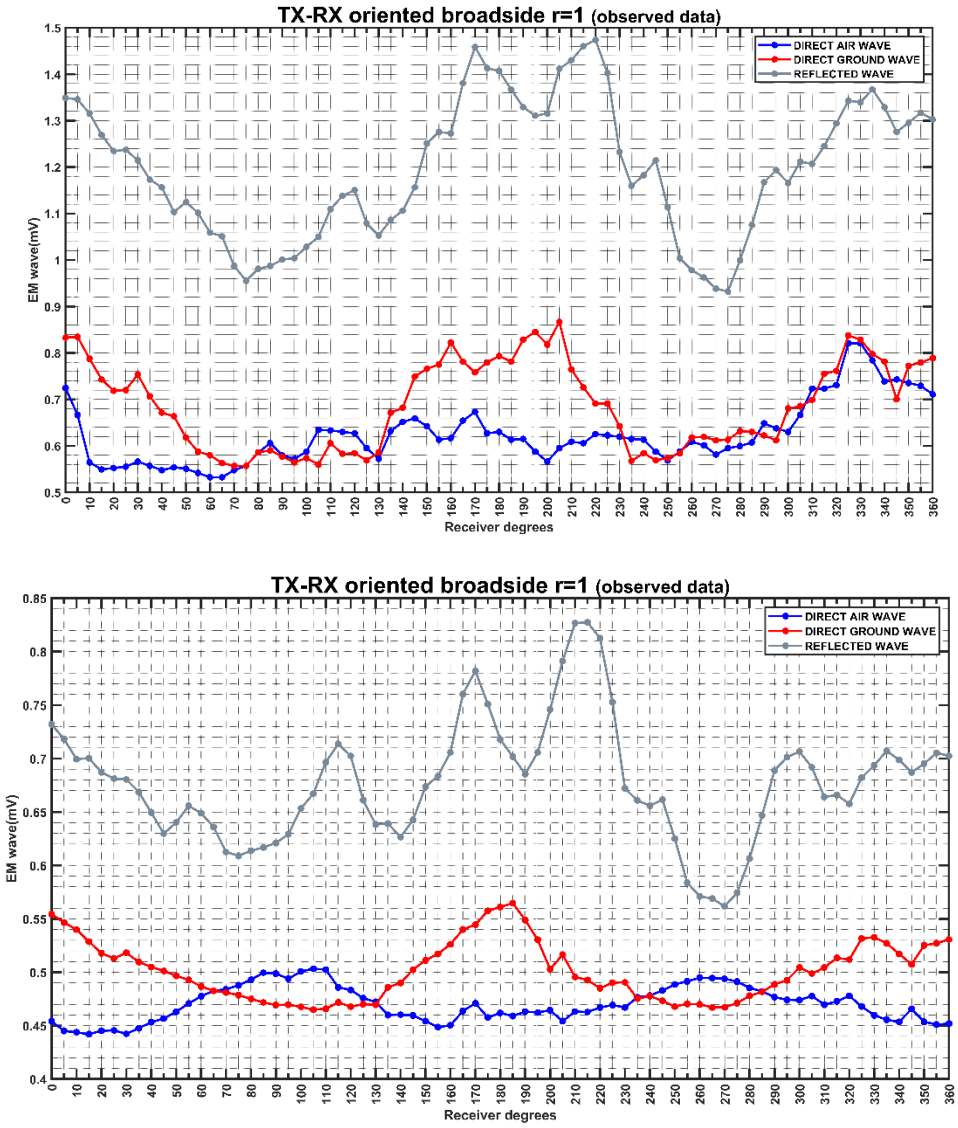

Figure 122: The maximum of the absolute (top), and the RMS (bottom) values of amplitude in millivolts (y axis) of the direct air wave (blue solid line) the direct ground wave (red solid line) and the reflected wave (grey solid line) for the circle of r=1m and for the broadside antenna orientation compared to the spatial step of the collected traces (i.e., per 5 degrees) as indicated in the x axis. The minor grid lines in the x axis are at every 5 degrees. The traces have been collected with the 500MHz antennas from Sensors & Software.

- Endfire antenna orientation (synthetic data), circle of r=0.23m plots for the direct (as a whole entity -brown solid line) and reflected wave (grey solid line) versus the angle of the collected traces.

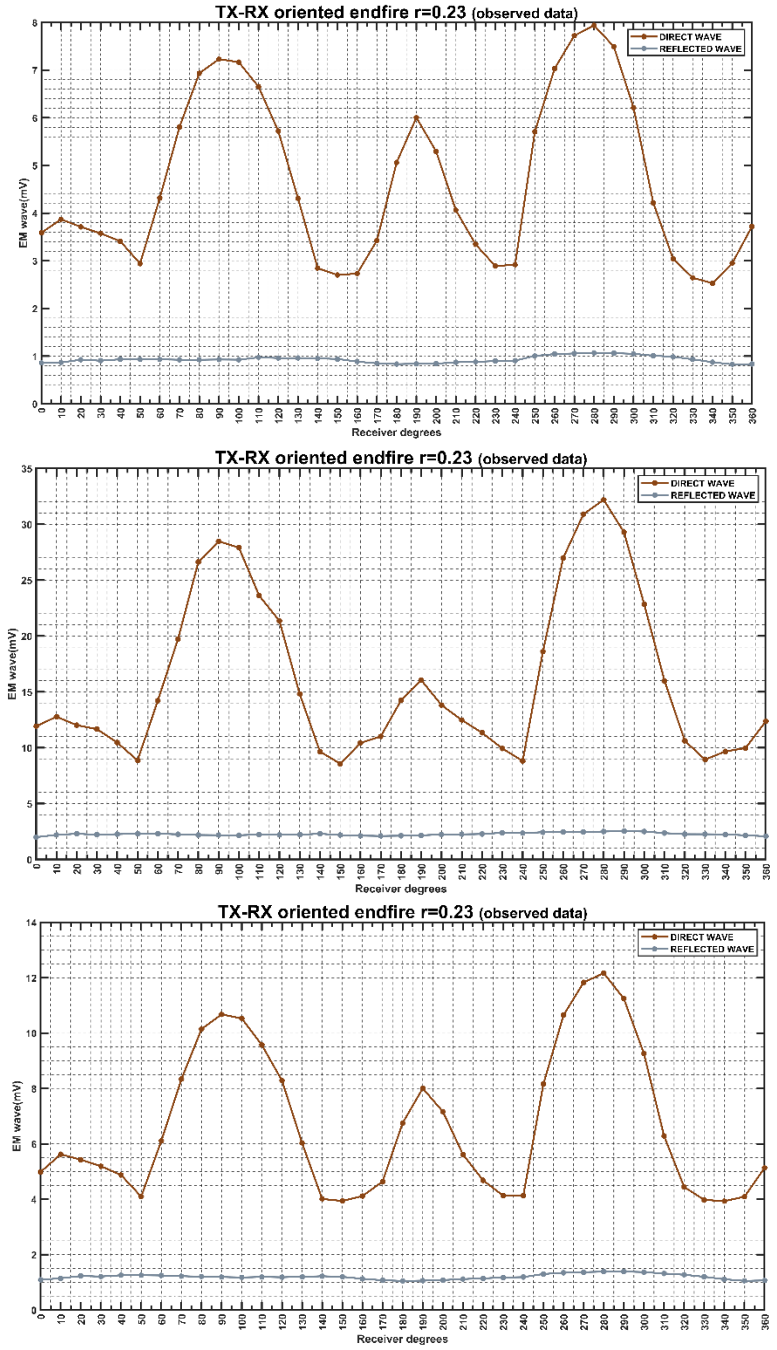

Figure 123: The mean of the absolute (top), the maximum of the absolute (middle), and the RMS (bottom) values of amplitude in millivolts (y axis) of the direct wave (brown solid line) and the reflected wave (grey solid line) for the circle of r=0.23m and for the endfire antenna orientation compared to the spatial step of the collected traces (i.e., per 10 degrees) as indicated in the x axis. The minor grid lines in the x axis are at every 5 degrees. The traces have been collected with the 500MHz antennas from Sensors & Software.

- Endfire antenna orientation (synthetic data), circle of r=0.23m plots for the direct (as two separated entities: the direct air wave -blue solid line- and the direct ground wave -red solid line-) and reflected wave (grey solid line) versus the angle of the collected traces. The results for the maximum absolute and RMS values of amplitude (mV) are given. The absolute mean values of amplitude have been presented in the main context.

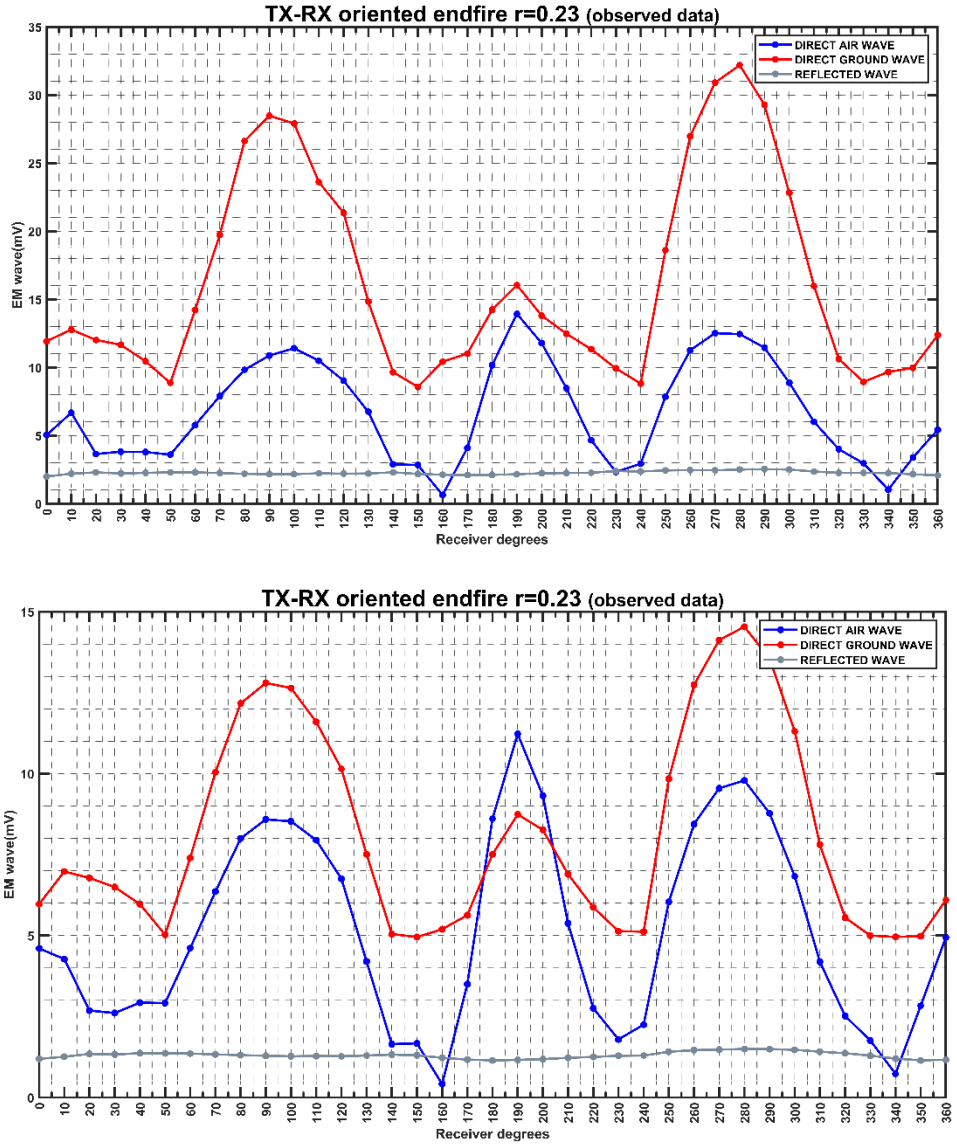

Figure 124: The maximum of the absolute (top), and the RMS (bottom) values of amplitude in millivolts (y axis) of the direct air wave (blue solid line) the direct ground wave (red solid line) and the reflected wave (grey solid line) for the circle of r=0.23m and for the endfire antenna orientation compared to the spatial step of the collected traces (i.e., per 10 degrees) as indicated in the x axis. The minor grid lines in the x axis are at every 5 degrees. The traces have been collected with the 500MHz antennas from Sensors & Software.

- Endfire antenna orientation (synthetic data), circle of r=0.5m plots for the direct (as a whole entity -brown solid line) and reflected wave (grey solid line) versus the angle of the collected traces.

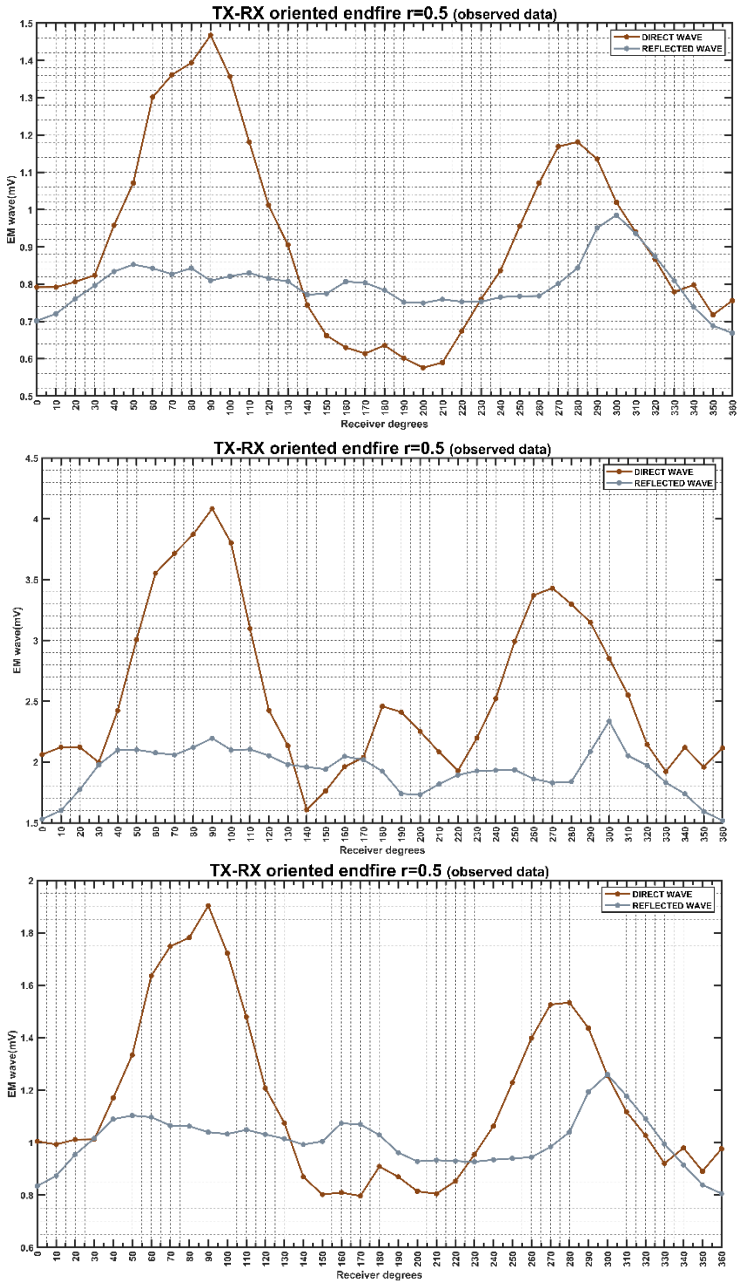

Figure 125: The mean of the absolute (top), the maximum of the absolute (middle), and the RMS (bottom) values of amplitude in millivolts (y axis) of the direct wave (brown solid line) and the reflected wave (grey solid line) for the circle of r=0.5m and for the endfire antenna orientation compared to the spatial step of the collected traces (i.e., per 10 degrees) as indicated in the x axis. The minor grid lines in the x axis are at every 5 degrees. The traces have been collected with the 500MHz antennas from Sensors & Software.

- Endfire antenna orientation (synthetic data), circle of r=0.5m plots for the direct (as two separated entities: the direct air wave -blue solid line- and the direct ground wave -red solid line-) and reflected wave (grey solid line) versus the angle of the collected traces. The results for the maximum absolute and RMS values of amplitude (mV) are given. The absolute mean values of amplitude have been presented in the main context.

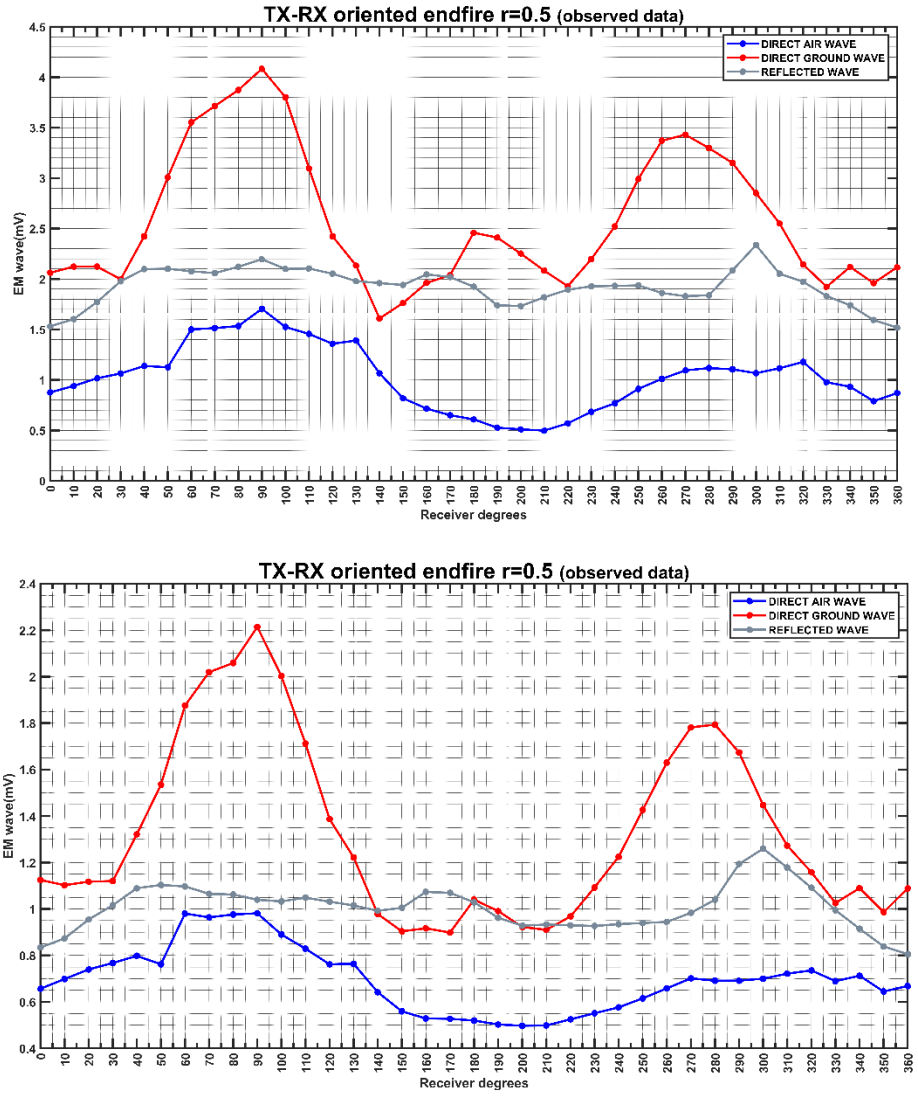

Figure 126: The maximum of the absolute (top), and the RMS (bottom) values of amplitude in millivolts (y axis) of the direct air wave (blue solid line) the direct ground wave (red solid line) and the reflected wave (grey solid line) for the circle of r=0.5m and for the endfire antenna orientation compared to the spatial step of the collected traces (i.e., per 10 degrees) as indicated in the x axis. The minor grid lines in the x axis are at every 5 degrees. The traces have been collected with the 500MHz antennas from Sensors & Software.

- Endfire antenna orientation (synthetic data), circle of r=1m plots for the direct (as a whole entity -brown solid line) and reflected wave (grey solid line) versus the angle of the collected traces.

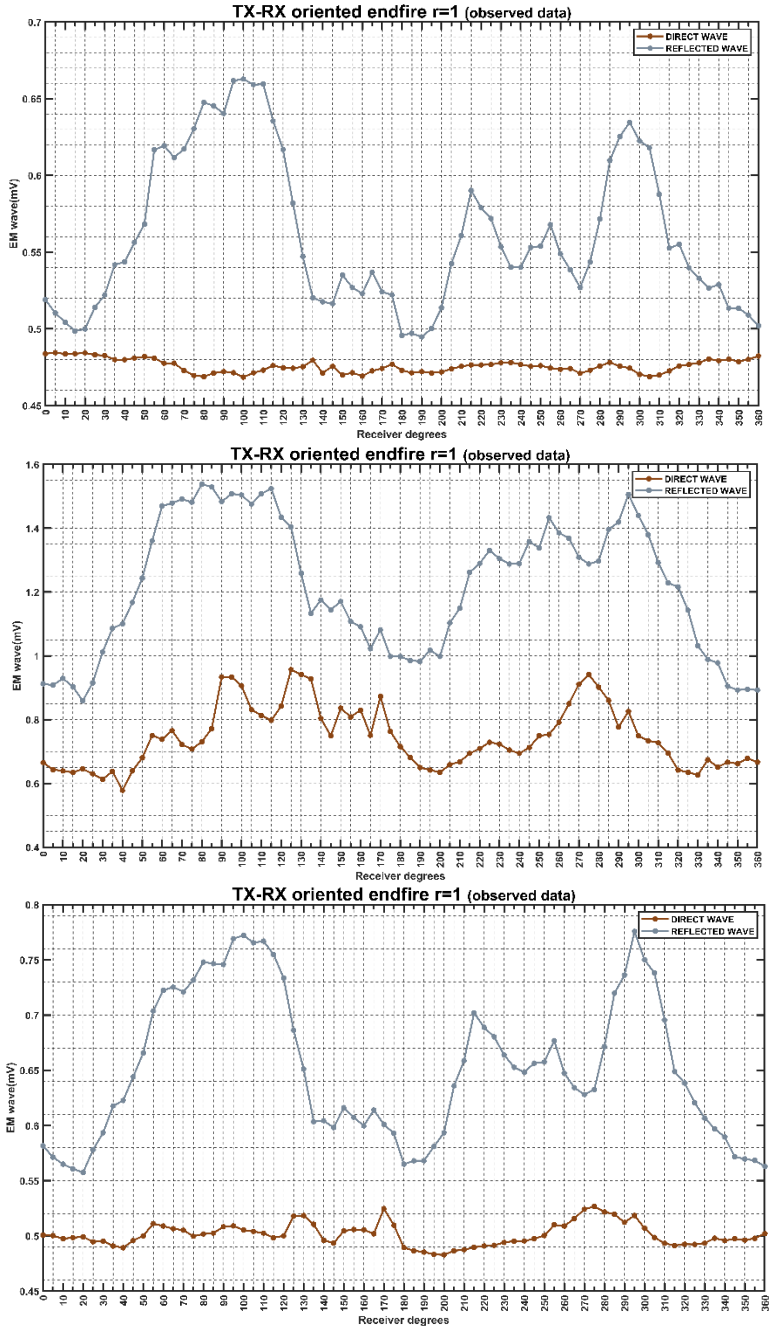

Figure 127: The mean of the absolute (top), the maximum of the absolute (middle), and the RMS (bottom) values of amplitude in millivolts (y axis) of the direct wave (brown solid line) and the reflected wave (grey solid line) for the circle of r=1m and for the endfire antenna orientation compared to the spatial step of the collected traces (i.e., per 10 degrees) as indicated in the x axis. The minor grid lines in the x axis are at every 5 degrees. The traces have been collected with the 500MHz antennas from Sensors & Software.

- Endfire antenna orientation (synthetic data), circle of r=1m plots for the direct (as two separated entities: the direct air wave -blue solid line- and the direct ground wave -red solid line-) and reflected wave (grey solid line) versus the angle of the collected traces. The results for the maximum absolute and RMS values of amplitude (mV) are given. The absolute mean values of amplitude have been presented in the main context.

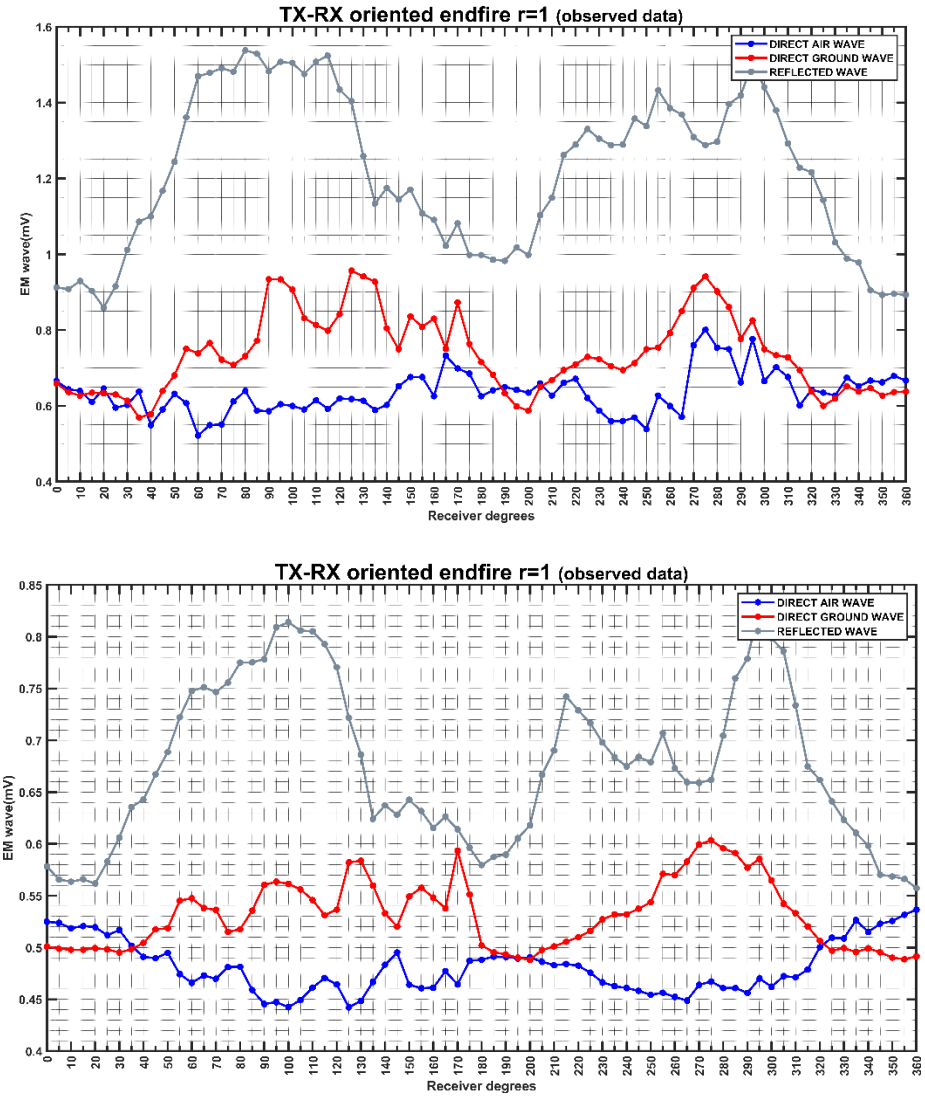

Figure 128: The maximum of the absolute (top), and the RMS (bottom) values of amplitude in millivolts (y axis) of the direct air wave (blue solid line) the direct ground wave (red solid line) and the reflected wave (grey solid line) for the circle of r=1m and for the endfire antenna orientation compared to the spatial step of the collected traces (i.e., per 10 degrees) as indicated in the x axis. The minor grid lines in the x axis are at every 5 degrees. The traces have been collected with the 500MHz antennas from Sensors & Software.